Comeld ™ Joints: Optimisation of Geometric Parameters of the Protrusions

By

Wei Tu

Department of Materials

Queen Mary, University of London

2011

DECLARATION

I declare that the work performed is entirely by myself during the course of my Ph.D. studies at the Queen Mary, University of London and has not been submitted for a degree at this or any other university.

Wei Tu

ABSTRACT

Current and future structural applications for composite laminates frequently involve design solutions combining composite laminates and metal; the materials must be joined. Two conventional means of joining are available: mechanical joining and adhesive bonding. Both methods have critical disadvantages.

A novel surface treatment for metals developed at TWI, Surfi-Sculpt ™ leads to the formation of surface protrusions on metal surfaces. These protrusions are typically 1.0 mm high and 0.6 mm diameter. The surface modified metal can be bonded with composite laminates to form a Comeld ™ joint. These joints can be described as a combination of mechanical fastening and adhesive bonding. There are many possible variables which could be applied to the metal surface. The variables include the shape, height, orientation and distribution (distribution pattern and density) of the protrusions.

The aim of this work was to optimise the protrusions with respect to their geometry and distribution using the finite element modelling method for the Comeld ™ joint under tensile loading with titanium alloy and cross-ply carbon prepreg composites. The simulations require multi-scale modelling techniques to transfer results between the global model, which is the reflection of the whole joint, and the unit cell models containing a protrusion. The two-dimensional simulations focused on the protrusion geometric parameters whereas the three-dimensional simulations focused on the protrusion spatial arrangement including the distribution pattern and density. Modelling of the entire joint geometry with two and three-dimensional global models was carried out using smeared properties for the adhesive layer which includes the protrusions.

These models yield results for both quasi-static properties and stress distributions for these joints. Results from the simulations show critical effects on stress distributions arising from changing protrusion geometry. These joints show significant advantages over conventional joining technologies and their application would allow improved performance for combinations of metal and composite laminates.

ACKNOWLEDGEMENTS

I would like to express my sincere gratitude to my supervisors, Professor Felicity J Guild, Dr PH Wen and Professor P J Hogg for their guidance throughout the project. Sincere appreciation is also extended to the project collaboration partners from TWI, Dr. Faye Smith (previous project leader) and Dr. Philippe Bastid for their invaluable advice and help throughout the course of this Ph.D.

Many thanks to all the technicians in Department of Materials, Queen Mary, University of London, especially Mr Colin Langdown without whom I would have had a much harder time as well as Raymond Lam and Steve Wicks for IT support.

I would also like to thank my colleagues in Room 235 for their suggestions and support, in particular Chootum, Rob, Mohamed.

I am indebted to the TWI Ltd and the Materials Department for the financial support throughout the course of the Ph.D. programme.

Finally, I would like to express thanks to my family, friends and last but not least my wife Jia, for her continuous support and encouragement throughout this study.

POSTER, PRESENTATION AND PUBLICATIONS

Finite Element Model of Comeld ™ Joints, presentation at The Welding Institute (TWI), Cambridgeshire UK, 24th May 2005

Finite Element Modelling of Comeld ™ Joints, presentation at TWI, Cambridgeshire, UK, 22ed July 2005

Finite Element Modelling of Comeld ™ Joints, presentation at SAMPE/IOM3 Annual Student Seminar, 22ed November 2005

Finite Element Modelling of Comeld ™ Joints, poster presented (by Prof. F J Guild) at Adhesion Society Annual Meeting, Tampa, Florida, USA, 18th February 2007

Comeld ™ Joints: A Novel Technique for Bonding Composites and Metal, paper presented (by Prof. F J Guild) at Adhesion Society Annual Meeting, Tampa, Florida, USA, 18th February 2007

Comeld ™ Joints - Optimisation of the proggle* geometry and density, presentation at TWI, Cambridgeshire UK, 21st February 2007

Comeld ™ Joints: A Novel Technique for Bonding Composites and Metal, poster presented at The Ninth Great British Research and R&D Show, the House of Commons, London, UK, 18th March 2007

Comeld ™ Joints – Optimisation of Protrusion Geometry and Density, presentation at Deformation and Fracture of Composites 9, Sheffield, UK, 10th April 2007

Finite Element Modelling of Comeld ™ Joints, poster presented at International Materials Research Conference 2008, Chongqing, China, 9th June 2008

Adhesive Joints between Metals and Composites - Simulation of Comeld™ Joints, Presentation by F.J. Guild, IMechE and IMarEST, Singapore, Jan 2010

Multi-region mesh free method for Comeld™ joints, Computational Materials Science, Volume 48, Issue 3, Pages 481-489, May 2010

The Optimisation of Comeld ™ Joints: a Novel Technique for Bonding Composites and Metal, Proceedings of the World Congress on Engineering 2010 Vol II, WCE 2010, June 30 - July 2010

Optimisation of the protrusion geometry in Comeld ™ joints, Composites Science and Technology, Volume 71, Issue 6, Pages 868-876, April 2011

The Optimisation of Comeld™ Joints between Composites and Metal, Presented by F.J. Guild, DFC11, Cambridge, UK, April 2011

* stands for surface patterns on the metal part of the joint, and later changed to protrusion

CONTENTS

List of Figures

List of Tables

SYMBOLS

σ	Stress
σ_0	Load
a	Crack length
r	Radius of crack tip
U_a	Change in elastic strain energy of a loaded plate of unit thickness
E	Young's modulus
π	Pi
γ_e	Surface energy per unit area
U	Total energy
U_0	Total energy of the plate and its loading system
U_p	Potential energy
U_γ	Energy of the creation of a crack surface area
Q	Work performed by the loading system during introduction of the crack
G	Energy release rate
G_c	Critical value of energy release rate
K	Stress intensity factor
K_c	Critical value of stress intensity factor
Y	Geometric factor
J	Decrease in potential energy per increment of crack extension
ν	Poisson's Ratio
W	Strain energy density
T	Traction
A	Area of plate
u	Displacement

s	Crack extension increment
Γ	Perimeter
x_1, x_2	Coordinates of the moved coordinate system
F	Force
k	Stiffness of spring
C	Compliance
S	Stiffness

1 INTRODUCTION

Composites are gaining widespread use in the applications for industries such as automobiles and aircraft, for their superior weight reduction to isotropic materials such as metals since the composites are typically manufactured from low density constituents and can also be tailored to suit a particular application. Extensive research has been done for composite materials and they are now being exploited as primary structures, for instance in the automobile industry, where before they were mainly utilised as secondary load carrying structures. A very important use of composites in developing high performance automobiles or aircraft is for light weight due to their tailorability coupled with high-strength and stiffness-to-weight ratios, environmental, corrosion and fatigue resistance.

However, in general, the uptake in structural applications for composites has been slow. In many large-scale applications, a total composite solution may be unrealistic; it would be extremely difficult in moulding the complex geometries. Then the connection of dissimilar material components becomes a very important aspect. There is an intrinsic dilemma for the design of composite joints, since the two alternatives of mechanical or adhesive bonding both show significant disadvantages. There has been vast amount of research on joints with adhesive or mechanical bonding mechanism.

The most promising way forward may be a combination of adhesive and mechanical bonding. This combination of joining methods may be attained following the development of Surfi-Sculpt ^{TM} technology by TWI. The Surfi-Sculpt ^{TM} technology as a new method for the surface treatment on the metal surfaces, bonding of the sculpted metal surface to composite laminates forms a Comeld ^{TM} joint; this enables the combination of mechanical and adhesive bonding at the same time. However, very little work has focussed on this method. Limited work on stitching and z-pinning through-the-thickness reinforcement joints indicates some improvement over

conventional adhesive joining system. Comeld ™ joint takes advantages from both adhesive and mechanical joints to improve metal-composite joint performance. From the preliminary studies of this technology, subjected to tensile loading, higher maximum load and extension were found (see Chapter 2, section 2.4). More energy can be absorbed before ultimate failure occurs compared to the conventional adhesive joints. Potentially, any connection between metal and composite can be considered to be replaced by the Comeld ™ joint.

This programme sought to explore the effect of geometric parameters, in order to optimise the design of the joining system prior to failure initiation. As the costs and time required for development of this new technology can be expected to be high, it would be more convenient to employ finite element analysis to study the various key geometric parameters in order to establish their effects on joint performance. The main objective of this work was to carry out a FEA study on the effects of the various geometric parameters of the surface treatment technique in order to optimise the design of the joining system prior to failure initiation.

2
LITERATURE REVIEW

Composite material is often made up of at least two constituents. Many materials are effectively composites. In many cases, a strong and stiff component is present, often in elongated form, embedded in a softer constituent forming the matrix. Commonly, such composite materials show marked anisotropy, i.e. their properties vary significantly when measured in different directions [Hull, 1981].

The applications of polymer matrix composites in automobile, aeroplane and various industries are widespread due to increased requirements of safety and improvement in energy efficiency. Those applications include airframe applications such as the Boeing 777 aircraft which extended the use of advanced composites to main flaps, passenger floor beams, horizontal stabilisers, and vertical fins; helicopter applications such as tail rotor flex beam, fuselage and blades; Formula 1 cars, energy absorption components; and automobile bumpers, boot panels, tail fins, and fuel tanks, etc.; extensively in rail vehicle cab ends, internal fittings, lightweight panels, the filament wound passenger coach body shells, etc.; offshore pipe lines, pressure vessels, and tanks; flywheels; wind turbine blades; ships and marine structures; sporting equipment; medical devices; and many aspects of civil engineering and many more.

2.1 Joining

With the widespread applications of polymer matrix composites, making individual components is just the first step; assembly and joining separate components made of different materials introduces problems. Conventionally, joining techniques include mechanical fastening, adhesive bonding and fusion bonding (welding, soldering or brazing) of thermoplastic composites. The technology for joining metals is quite mature including a number of processes, including riveting, bolting, welding, adhesive bonding, brazing, and soldering [Vinson, 1989]. However, the technology for joining composites is less well understood, but still important. In structures made

of or consisting of polymer matrix composites, the components must be joined to retain the structural integrity in the face of both mechanical (static and dynamic) and environmental loads including temperature and humidity [Vinson, 1989].

In general, joining is required when there is need to

(i) produce larger physical size,
(ii) create "un-mouldable" geometries,
(iii) co-join two dissimilar materials, or
(iv) preserve a degree of access [Meyer, 1990].

For structural applications [Stokes, 1989], the important issues for joint performance regardless of the joining technology used include the strength of the joint under static and dynamic loads, the resistance of the joint to impact loads, the effect of resin ageing, residual stresses, creep, foreign fillers such as particulates, fibres, and bond heating sources, and the influence of environmental factors such as temperature, moisture, and solvents. Each of these issues must be addressed when selecting the proper joint design with as much if not more respect as is the case in material selection for the overall structure [Tierney et al., 2000].

2.1.1 Mechanical fastening

Typical assemblies include threaded and unthreaded fasteners with interlocking design features, and metallic and thermoplastic riveted assemblies [Stokes, 1989]. These fastenings can either be permanent or consist of joints that can be opened or closed. Mechanical fastening offers the following advantages [Ueng et al., 1985]: (i) no need of surface preparation, (ii) they are insensitive to or adversely affected by thermal cycling loads or high humidity environments, (iii) they can easily be disassembled without structural or surface damage, and (iv) they are readily accessible for visual inspection for damage/wear. The unique characteristics of composite structures raise many difficulties associated with mechanical fastening [Tierney et al., 2000] including some of the following disadvantages: (i) cyclic loading, in-plane shear, and transverse pulling forces can lead to high stress

concentrations; (ii) cold flow can cause deformation of fasteners or holes and can lead to fastener loosening or pull-out, and joint failure; (iii) fastener tear-out or pull-through can also be observed especially with thin adherend materials; (iv) stress profiles are complex and multiple failure mechanisms are possible; and (v) increased weight, part count, and costs. Mechanical fasteners can fail in a variety of modes, including tension, shear, bolt, and cleavage-tension failure, as well as from bolt pull through [Vinson, 1989; Hart-Smith, 1978; Hart-Smith, 1986]. In the case of vibration, mechanically fastened components can show fretting due to small relative movement between the components, while adhesive bonding eliminates and even serve to damp the vibration. Furthermore, the failure mode for any given joint is highly dependent on geometry, and still may vary with the fibre orientation or laminate stacking sequence. For instance, connecting composite components with pinned or bolted joints may reduce costs and desired for its simplicity, however, drilled holes often lead to the reduction of the load carrying capacity due to the stress concentration occurring around the boundary of the holes. Special attention must be given for the design of bolted joints to avoid catastrophic failure. These mechanical fastened joints normally suffer with three failure modes, which are net-tension, shear-out and bearing, reported by İçten et al. [İçten et al., 2006] and Karakuzu et al. [Karakuzu et al., 2006]; onset of non-linearity can occur due to local failure mechanism, such as delaminations at edges of holes.

Despite weight, mechanically fastened joints containing composite materials can be designed to compete with adhesively bonded joints. Mechanically fastened joints can also be disassembled relatively easily in comparison to adhesively bonded joints, which make them attractive for inspection, repair and recycling purposes amongst others. This means that, in industry sectors used to dealing with metals, mechanical fasteners have been commonly used to join composite materials to themselves and other materials.

2.1.2 Adhesive bonding

Adhesive bonding is used widely for joining sheet materials for load-bearing engineering applications, and also for transferring loads in large structures for civil engineering. The development of adhesive bonding has depended heavily on understanding of the chemistry involved [Stokes, 1989]. A vast research has been done for adhesive bonding of composites, and several key issues have been identified [Hart-Smith, 1986; Wegman, 1989; Venables, 1984; Shaffer et al., 1991]. These include adhesive selection, surface preparation of the composite adherends, wetting, mechanisms of bonding, durability, and bonding of dissimilar materials. Generally, adhesive bonded joints are stiffer than mechanically fastened polymers or composites, due to more uniformly distributed loadings over large areas resulting in lower stresses and fewer stress concentrations. The strength of the adhesive material usually determines the maximum bond stress, and the chemical structure and temperature of the adhesive ultimately determines the mechanical behaviour of the joint during its operating life [Tierney et al., 2000].

According to Comyn [Comyn, 1997], there are six theories of adhesion, physical adsorption, chemical bonding, diffusion, electrostatic, mechanical interlocking and weak boundary theories. Physical adsorption contributes to all the adhesive bonds. It involves van der Waals forces across the interface. Chemical bonding invokes the formation of covalent, ionic or hydrogen bonds across the interface to contribute. The diffusion theory can be recognised as polymers in contact may inter-diffuse which results in the removal of the initial boundary. The electrostatic theory commonly exists with metal-metal joints which form a force of attraction by allowing the transfer of electrons. The weak boundary theory points out the effect of contamination forming weak boundary layers.

Epoxides are the most widely used structural adhesives, which are also used as matrix resins for composites. Epoxide resins can be mixed with a wide range of hardeners to connect dissimilar components. During the application of epoxide adhesives there is no volatile formed on hardening with very low shrinkage, but contact may cause skin diseases [Comyn, 1997].

2.1.3 Brief comparison of mechanical and adhesive bonding

Advantages and disadvantages of adhesive bonding compared to mechanical fastening are shown Table.2.1.

Table.2.1 *Advantages and disadvantages of adhesive bonding compared to mechanical fastening [Smith, 2004]*

Advantages	Disadvantages
• Can form lightweight, strong and stiff structures. • Ability to join dissimilar materials • Ability to efficiently join thin-sheet materials • Improved stress distribution • Good fatigue properties due to improved stress distribution • Galvanic corrosion minimised by non-conducting interlayer • Smooth surface finish • Bonding process can be automated	• Cannot be easily dissembled • Residual stresses may be created due to mismatches in coefficient of thermal expansion • Limits to thicknesses joined with simple configurations • Sensitive to peel or through-thickness stress • Poor resistance to elevated temperature • Prone to environmental degradation under severe conditions • Flammability and toxicity problems • Inspection can be difficult • Needs of surface preparation

2.1.4 Stresses in adhesive joint

Fig.2.1 shows some typical classifications of joint which are commonly found in practice. One of the most commonly used configurations is Fig.2.1 (a), single-lap joint, where the stress state is complex. As shown in Fig.2.2, the loads in the single-lap joint are not collinear, and a bending moment exists where the joint will rotate. Clearly there is peel stress at the ends of the joint in addition to shear in the adhesive layer. The adherends are bent instead of in simple tension.

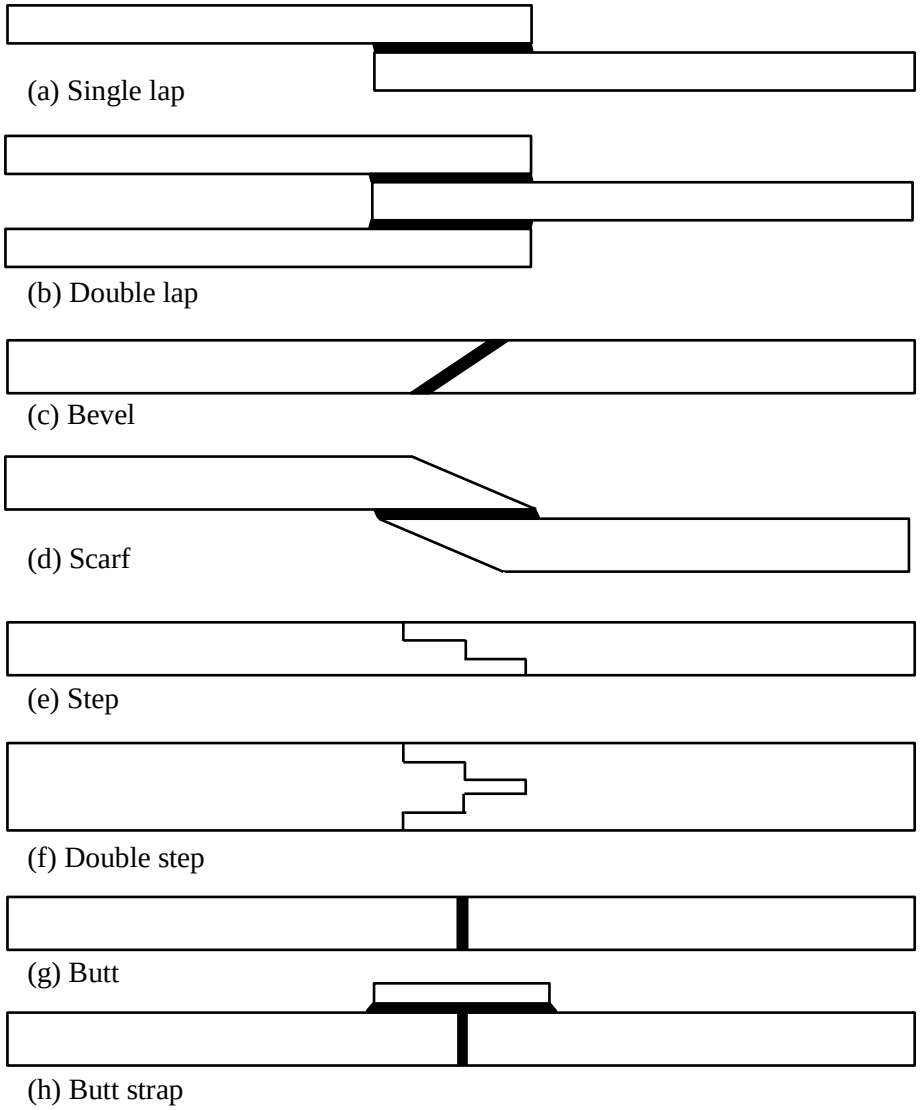

Fig.2.1 *Some common adhesive joints*

Single lap joints will have the highest shear and bending stresses, whereas scarf joints will have the lowest bending stresses. The joints are often scarfed or stepped to reduce stiffness discontinuities and resulting stress concentrations at the joint edges. Double lap joints are often used to reduce bending or peel stresses at the joint edges. A variety of failure modes exist for adhesively bonded materials. The most common failures are: (i) cohesive failure within the adhesive layer, (ii) interfacial failure at the adhesive-adherend interface, (iii) failure of the matrix on the surface of the adherend, (iv) inter-laminar failure in the adherend laminate, (v) transverse failure of the surface lamina due to matrix failure or to interfacial failure, and (vi) longitudinal failure of the surface lamina. [Tierney et al., 2000]

Fig.2.2 *Single-lap joint under loads*

For single-lap joint, in 1938, the shear lag model was proposed by Volkersen for analysing shear stress within adhesive joint. Ignoring the effects of adherends bending, the axial displacements of adherends in the single lap joint were considered. Volkersen developed a second order differential equation for the shear stress, known as differential shear, as a function of distance along the bondline. [Adams et.al. 1997] Assuming shear deformation occurs in the adhesive layer with linear elasticity, the length of joint is `l`, the second order differential equation is shown in the form [Adams et.al. 1997; Dillard, 2002],

$$\tau(x) = A\ cosh\ \omega x + B\ sinh\ \omega x$$

Eq.2.1

$$\omega = \sqrt{\frac{G}{h}\left(\frac{E_1 t_1 + E_2 t_2}{E_1 t_1 E_2 t_2}\right)}$$

Eq.2.2

where E_i is the Young's modulus and t_i is the thickness of each adherend, G is the shear modulus of the adhesive layer and h is the thickness.

In single-lap joints, adherend bending and peel stresses exist and they often account for failure. The shear lag model would be more appropriate to be applied to several joint geometries other than single lap, such as half of a double-lap joint, where the bending is less pronounced.

The governing differential equation will be useful for several different geometries and loading scenarios. Depending on the configuration being considered, the boundary conditions needed to be solved for the coefficients A and B. The final solution can be

determined for the shear lag model with boundary conditions, in the case of mechanically applied axial load, P (load per unit width), resulting in

$$\tau(x) = \frac{P\omega}{2sinh\left(\frac{\omega l}{2}\right)} cosh\ \omega x + \frac{P\omega}{2cosh\left(\frac{\omega l}{2}\right)} \left(\frac{E_2 t_2 - E_1 t_1}{E_1 t_1 + E_2 t_2}\right) sinh\ \omega x$$

Eq.2.3

For the balanced adherend case, $E_i\ t_i$ for the upper and lower adherends is the same, the coefficient for the hyperbolic sine term becomes zero, and the shear stress symmetrically distributed about the centre of the joint.

Adams et.al. has provided illustration for the shear stress distributions within joints consisting of either rigid or extensible adherends, see Fig.2.3.

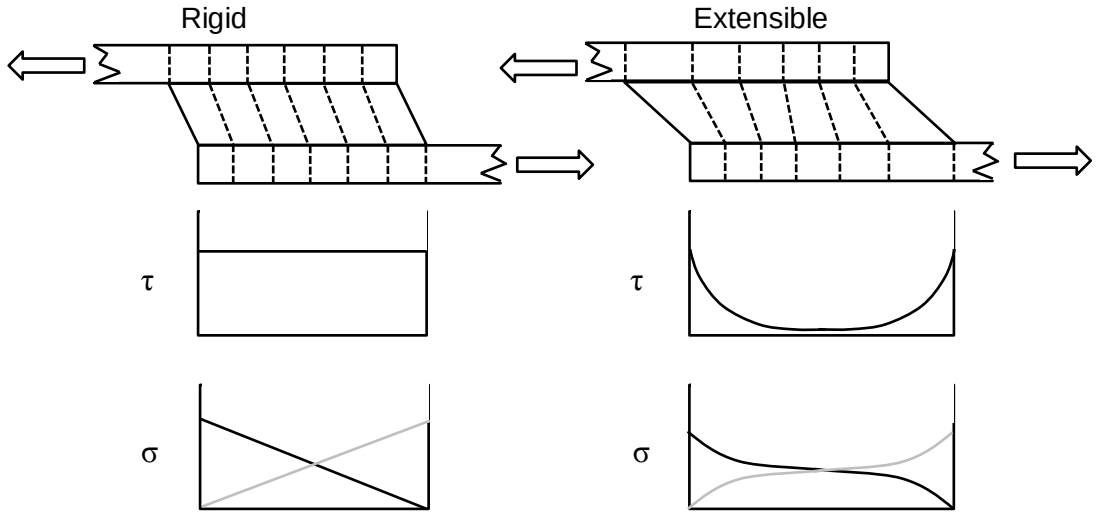

Fig.2.3 *Schematic diagram of the loaded lap joints with the effect of adherend extensibility on adhesive shear stress, τ, and adherend axial stresses, σ. [Adams et.al. 1997]*

Gained from the Volkersen shear lag result, there are peaks in the shear stress anywhere there are relative changes in the stiffness of the adherends, and thus near joint ends, large shear stress peaks are expected. For situations where the adherends

are not balanced, the shear stress distribution is skewed to result in higher shear stresses at the end of the stiffest adherend.

Accounting for the bending moment, joint rotation, the joint displacements are no longer proportional to the applied load. Goland and Reissner developed bending moment factor, k, which relates the bending moment on the adherend to the in-plan loading. [Adams et.al. 1997] For equal thickness adherends was of the form

$$k_{GR} = \left[1 + 2\sqrt{2}\, tanh(\frac{\theta}{2\sqrt{2}})\right]^{-1}$$

Eq.2.4

where

$$\theta = l\sqrt{\frac{3P(1-\nu^2)}{bEt^3}}$$

where ν is the Poisson's ratio, b is the width of the joint. This form is believed to give the best fit over a range of conditions.

Hart-Smith and Zhao et.al. showed some alternative forms of the bending moment factor, [Adams et.al. 1997]

$$k_{HS} = [1 + \theta + \theta^2/6]^{-1}$$

Eq.2.5

$$k_Z = [1 + \theta]^{-1}$$

Eq.2.6

2.2 Classical laminate theory [Daniel et.al, 1994] and orthotropic material stiffness matrix in ABAQUS

2.2.1 Anisotropic and orthotropic elasticity

For anisotropic material, a point in a general continuum can be represented by nine stress components σ_{ij}, where i, j = 1, 2, 3, acting on sides of an elementary cube with sides parallel to 1, 2, and 3 axes, see Fig.2.4. The state of deformation is represented by nine strain components, ε_{ij}. The stress and strain components are related by the generalised Hooke's law shown with Eq.2.7.

$$\sigma_{ij} = C_{ijkl}\,\varepsilon_{kl}$$

(i, j, k, l = 1, 2, 3)

$$\varepsilon_{ij} = S_{ijkl}\,\sigma_{kl}$$

Eq.2.7

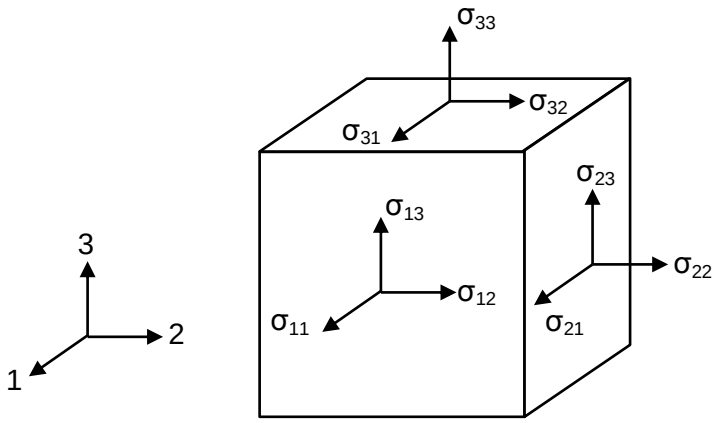

Fig.2.4 *Stress states at a point in a general continuum*

where C_{ijkl} represents the stiffness components, S_{ijkl} represents the compliance components, and i, j, k, l = 1, 2, 3.

The compliance matrix [S_{ijkl}] is the inverse of the stiffness matrix [C_{ijkl}]. The system of strain tensors

$$\sigma_{ij} = \sigma_{ji}$$

$$\varepsilon_{ij} = \varepsilon_{ji}$$

Eq.2.8

reduces the number of independent elastic constant to 36.

The contracted notation for the stress strain, stiffness and compliance tensors are shown as follows (i, j = 1, 2, 3),

$$\sigma_{ii} = \sigma_i$$

$$\sigma_{23} = \tau_{23} = \sigma_4 = \tau_4$$

$$\sigma_{31} = \tau_{31} = \sigma_5 = \tau_5$$

$$\sigma_{12} = \tau_{12} = \sigma_6 = \tau_6$$

and

$$\varepsilon_{ii} = \varepsilon_i$$

$$2\varepsilon_{23} = \gamma_{23} = \varepsilon_4 = \gamma_4$$

$$2\varepsilon_{31} = \gamma_{31} = \varepsilon_5 = \gamma_5$$

$$2\varepsilon_{12} = \gamma_{12} = \varepsilon_6 = \gamma_6$$

and

$C_{iiii} = C_{ii}$, $C_{iijj} = C_{ij}$, $C_{ii23} = 2C_{i4}$, $C_{ii31} = 2C_{i5}$, $C_{ii12} = 2C_{i6}$, $C_{23ii} = C_{4i}$, $C_{31ii} = C_{5i}$, $C_{12ii} = C_{6i}$, $C_{2323} = 2C_{44}$, $C_{2331} = 2C_{45}$, $C_{2312} = 2C_{46}$, $C_{3123} = 2C_{54}$, $C_{3131} = 2C_{55}$, $C_{3112} = 2C_{56}$, $C_{1223} = 2C_{64}$, $C_{1231} = 2C_{65}$, $C_{1212} = 2C_{66}$

Eq.2.9

Therefore, the stress-strain relationship can be written as

$$\sigma_i = C_{ij}\,\varepsilon_j$$

(i, j, k, l = 1, 2, 3, 4, 5, 6)

$$\varepsilon_i = S_{ij}\,\sigma_j$$

Eq.2.10

In the case of orthotropic material (where material symmetry follows mutually perpendicular planes), the stress-strain relations in general have the same form as Eq.2.10 with reduced number of independent elastic constants. This is clearly seen when the reference system of coordinates is along principal planes of material symmetry. Then,

$$\begin{bmatrix}\sigma_1\\ \sigma_2\\ \sigma_3\\ \tau_4\\ \tau_5\\ \tau_6\end{bmatrix} = \begin{bmatrix} C_{11} & C_{12} & C_{13} & & & \\ C_{12} & C_{22} & C_{23} & & 0 & \\ C_{13} & C_{23} & C_{33} & & & \\ & & & C_{44} & 0 & 0 \\ & 0 & & 0 & C_{55} & 0 \\ & & & 0 & 0 & C_{66} \end{bmatrix} \begin{bmatrix}\varepsilon_1\\ \varepsilon_2\\ \varepsilon_3\\ \gamma_4\\ \gamma_5\\ \gamma_6\end{bmatrix}$$

$$\begin{bmatrix}\varepsilon_1\\ \varepsilon_2\\ \varepsilon_3\\ \gamma_4\\ \gamma_5\\ \gamma_6\end{bmatrix} = \begin{bmatrix} S_{11} & S_{12} & S_{13} & & & \\ S_{12} & S_{22} & S_{23} & & 0 & \\ S_{13} & S_{23} & S_{33} & & & \\ & & & S_{44} & 0 & 0 \\ & 0 & & 0 & S_{55} & 0 \\ & & & 0 & 0 & S_{66} \end{bmatrix} \begin{bmatrix}\sigma_1\\ \sigma_2\\ \sigma_3\\ \tau_4\\ \tau_5\\ \tau_6\end{bmatrix}$$

Eq.2.11

And when one of the principal planes is a plane of isotropy, i.e., transverse isotropic material, the number of independent elastic constants reduced to five. The stress-strain relations are therefore simplified by noting that subscripts 2 and 3 (2-3 plane of isotropy) are interchangeable in Eq.2.11. And also subscripts 5 and 6 are interchangeable. Furthermore, stiffness C_{44} (or compliance S_{44}) is not independent and the form can be obtained

$$C_{44} = \frac{C_{22} - C_{33}}{2}$$

Eq.2.12

Thus Eq.2.11 reduces to

$$\begin{bmatrix}\sigma_1\\ \sigma_2\\ \sigma_3\\ \tau_4\\ \tau_5\\ \tau_6\end{bmatrix} = \begin{bmatrix} C_{11} & C_{12} & C_{12} & & & \\ C_{12} & C_{22} & C_{23} & & 0 & \\ C_{12} & C_{23} & C_{22} & & & \\ & & & \frac{C_{22}-C_{33}}{2} & 0 & 0 \\ & 0 & & 0 & C_{55} & 0 \\ & & & 0 & 0 & C_{66} \end{bmatrix} \begin{bmatrix}\varepsilon_1\\ \varepsilon_2\\ \varepsilon_3\\ \gamma_4\\ \gamma_5\\ \gamma_6\end{bmatrix}$$

$$\begin{bmatrix}\varepsilon_1\\ \varepsilon_2\\ \varepsilon_3\\ \gamma_4\\ \gamma_5\\ \gamma_6\end{bmatrix} = \begin{bmatrix} S_{11} & S_{12} & S_{12} & & & \\ S_{12} & S_{22} & S_{23} & & 0 & \\ S_{12} & S_{23} & S_{22} & & & \\ & & & 2(S_{22}-S_{33}) & 0 & 0 \\ & 0 & & 0 & S_{55} & 0 \\ & & & 0 & 0 & S_{66} \end{bmatrix} \begin{bmatrix}\sigma_1\\ \sigma_2\\ \sigma_3\\ \tau_4\\ \tau_5\\ \tau_6\end{bmatrix}$$

Eq.2.13

Converting the relations in Eq.2.11 to engineering constants as follows,

$$\begin{bmatrix}\varepsilon_1\\ \varepsilon_2\\ \varepsilon_3\\ \gamma_4\\ \gamma_5\\ \gamma_6\end{bmatrix} = \begin{bmatrix} \frac{1}{E_1} & -\frac{\nu_{21}}{E_2} & -\frac{\nu_{31}}{E_3} & & & \\ -\frac{\nu_{12}}{E_1} & \frac{1}{E_2} & -\frac{\nu_{32}}{E_3} & & 0 & \\ -\frac{\nu_{13}}{E_1} & -\frac{\nu_{23}}{E_2} & \frac{1}{E_3} & & & \\ & & & \frac{1}{G_{23}} & 0 & 0 \\ & 0 & & 0 & \frac{1}{G_{31}} & 0 \\ & & & 0 & 0 & \frac{1}{G_{12}} \end{bmatrix} \begin{bmatrix}\sigma_1\\ \sigma_2\\ \sigma_3\\ \tau_4\\ \tau_5\\ \tau_6\end{bmatrix}$$

Eq.2.14

With unidirectional thin lamina, it is assumed that it is under plane stress conditions, and therefore, $\sigma_3 = 0$, $\tau_{23} = \tau_4 = 0$, $\tau_{13} = \tau_5 = 0$, and then

$$\begin{bmatrix}\sigma_1\\ \sigma_2\\ \tau_6\end{bmatrix} = \begin{bmatrix}Q_{11} & Q_{12} & 0\\ Q_{12} & Q_{22} & 0\\ 0 & 0 & Q_{66}\end{bmatrix}\begin{bmatrix}\varepsilon_1\\ \varepsilon_2\\ \gamma_6\end{bmatrix}$$

$$\begin{bmatrix}\varepsilon_1\\ \varepsilon_2\\ \gamma_6\end{bmatrix} = \begin{bmatrix}S_{11} & S_{12} & 0\\ S_{12} & S_{22} & 0\\ 0 & 0 & S_{66}\end{bmatrix}\begin{bmatrix}\sigma_1\\ \sigma_2\\ \tau_6\end{bmatrix}$$

Eq.2.15

where $Q_{ij} = C_{ij} - C_{i3}C_{j3}/C_{33}$ (i, j = 1, 2, 6). The engineering constants would then be expressed by noting that $S_{11} = 1/E_1$, $S_{22} = 1/E_2$, $S_{12} = -\nu_{12}/E_1 = -\nu_{21}/E_2$, $S_{66} = 1/G_{12}$, and $Q_{11} = E_1/(1-\nu_{12}\,\nu_{21})$, $Q_{22} = E_2/(1-\nu_{12}\,\nu_{)}$, $Q_{12} = \nu_{12}E_2/(1-\nu_{12}\,\nu_{21}) = \nu_{21}E_1/(1-\nu_{12}\,\nu_{21})$, $Q_{66} = G_{12.}$ Thus, there are only four independent constants, E_1, E_2, G_{12} and $\nu_{12.}$

2.2.2 Laminate elasticity

A laminate is an organised stack of uni-directional composite plies. The stack is defined by the fibre directions of each ply. The overall behaviour of a multidirectional laminate is a function of the stack sequence and materials properties. The classical laminate theory can predict the behaviour of the laminate with the following assumptions:

1. Each layer of the laminate is quasi-homogeneous and orthotropic.
2. The laminate and its layers are in the plane stress state.
3. All displacements are continuous and small compared with the laminate thickness.
4. In-plane displacements vary linearly through the laminate thickness.
5. Transverse shear strains are negligible.
6. Strain-displacement and stress-strain relations are linear.
7. Transverse normal strain is negligible compared with the in-plane strains.

The strain-displacement relations can be then obtained as

$$\begin{bmatrix}\varepsilon_x\\ \varepsilon_y\\ \gamma_s\end{bmatrix} = \begin{bmatrix}\varepsilon_x^o\\ \varepsilon_y^o\\ \gamma_s^o\end{bmatrix} + z\begin{bmatrix}k_x\\ k_y\\ k_s\end{bmatrix}$$

Eq.2.16

where z is the coordinate variable of a general point of the cross section, k_i, i = x, y, and s (xy) is the curvatures of the laminate, ε_i^o is the strain on the reference plane.

The stress-strain relations for layer k can then be written as

$$\begin{bmatrix}\sigma_x\\ \sigma_y\\ \tau_s\end{bmatrix}_k = \begin{bmatrix}Q_{xx} & Q_{xy} & Q_{xs}\\ Q_{yx} & Q_{yy} & Q_{ys}\\ Q_{sx} & Q_{sy} & Q_{ss}\end{bmatrix}_k \begin{bmatrix}\varepsilon_x^o\\ \varepsilon_y^o\\ \gamma_s^o\end{bmatrix} + z\begin{bmatrix}Q_{xx} & Q_{xy} & Q_{xs}\\ Q_{yx} & Q_{yy} & Q_{ys}\\ Q_{sx} & Q_{sy} & Q_{ss}\end{bmatrix}_k \begin{bmatrix}k_x\\ k_y\\ k_s\end{bmatrix}$$

Eq.2.17

or, in brief,

$$[\sigma]_{x,y}^k = [Q]_{x,y}^k\,[\varepsilon^o]_{x,y} + z\,[Q]_{x,y}^k\,[k]_{x,y}$$

It is obvious that whereas the strains vary linearly through the thickness, the stresses do not. The reason is the discontinuous variation of the stiff matrix from layer to layer and this may also be true for the stresses.

The force and moment resultants can be obtained as

$$\begin{bmatrix}N_x\\ N_y\\ N_s\end{bmatrix} = \sum_{k=1}^{n}\int_{h_{k-1}}^{h_k}\begin{bmatrix}\sigma_x\\ \sigma_y\\ \tau_s\end{bmatrix}_k dz$$

Eq.2.18

and

$$\begin{bmatrix} M_x \\ M_y \\ M_s \end{bmatrix} = \sum_{k=1}^{n} \int_{h_{k-1}}^{h_k} \begin{bmatrix} \sigma_x \\ \sigma_y \\ \tau_s \end{bmatrix}_k zdz$$

Eq.2.19

where N_i and M_i (i = x, y, s) are the force and moment resultants, h_k and h_{k-1} are the z-coordinates of the upper and lower surfaces of layer k.

For the general load-deformation relations, the stiffness, reference plane strains and curvatures are taken outside the integration operation since they are not functions of z, as the curvature and reference plane strains are the same for all plies. Thus, the full form of the force-deformation relations can be obtained as

$$\begin{bmatrix} N_x \\ N_y \\ N_s \\ -- \\ M_x \\ M_y \\ M_s \end{bmatrix} = \left[\begin{array}{ccc|ccc} A_{xx} & A_{xy} & A_{xs} & B_{xx} & B_{xy} & B_{xs} \\ A_{yx} & A_{yy} & A_{ys} & B_{yx} & B_{yy} & B_{ys} \\ A_{sx} & A_{sy} & A_{ss} & B_{sx} & B_{sy} & B_{ss} \\ -- & -- & -- & -- & -- & -- \\ B_{xx} & B_{xy} & B_{xs} & D_{xx} & D_{xy} & D_{xs} \\ B_{yx} & B_{yy} & B_{ys} & D_{yx} & D_{yy} & D_{ys} \\ B_{sx} & B_{sy} & B_{ss} & D_{sx} & D_{sy} & D_{ss} \end{array}\right] \begin{bmatrix} \varepsilon_x^o \\ \varepsilon_y^o \\ \gamma_s^o \\ -- \\ k_x \\ k_y \\ k_s \end{bmatrix}$$

Eq.2.20

or in brief

$$\begin{bmatrix} N \\ -- \\ M \end{bmatrix} = \left[\begin{array}{c|c} A & B \\ -- & -- \\ B & D \end{array}\right] \begin{bmatrix} \varepsilon^o \\ -- \\ k \end{bmatrix}$$

Eq.2.21

where

$$A_{ij} = \sum_{k=1}^{n} Q_{ij}^k \, (h_k - h_{k-1})$$

$$B_{ij} = \frac{1}{2}\sum_{k=1}^{n} Q_{ij}^{k}\,(h_k^2 - h_{k-1}^2)$$

$$D_{ij} = \frac{1}{3}\sum_{k=1}^{n} Q_{ij}^{k}\,(h_k^3 - h_{k-1}^3)$$

Eq.2.22

with i, j = x, y, s

Note that the [A], [B] and [D] matrices are symmetric and they are functions of the geometry, material properties and stacking sequence of individual plies. They are the average elastic parameters of the multidirectional laminate as A_{ij} are extensional stiffnesses, relating in-plane loads to in-plane strains; B_{ij} are coupling stiffnesses, relating in-plane loads to curvatures and moments to in-plane strains; D_{ij} are bending or flexural laminate stiffnesses, relating moments to curvatures.

In the case of symmetric laminates with special orthotropic layers, such as crossply laminates, the coupling stiffness $B_{ij} = 0$, the load-deformation relations are reduced to

$$\begin{bmatrix} N_x \\ N_y \\ N_s \end{bmatrix} = \begin{bmatrix} A_{xx} & A_{xy} & 0 \\ A_{yx} & A_{yy} & 0 \\ 0 & 0 & A_{ss} \end{bmatrix} \begin{bmatrix} \varepsilon_x^o \\ \varepsilon_y^o \\ \gamma_s^o \end{bmatrix}$$

$$\begin{bmatrix} M_x \\ M_y \\ M_s \end{bmatrix} = \begin{bmatrix} D_{xx} & D_{xy} & 0 \\ D_{yx} & D_{yy} & 0 \\ 0 & 0 & D_{ss} \end{bmatrix} \begin{bmatrix} k_x \\ k_y \\ k_s \end{bmatrix}$$

Eq.2.23

2.2.3 Orthotropic elasticity in ABAQUS

In ABAQUS, the stress-strain relationship is described with Eq.2.24. The definition of orthotropic elasticity can be achieved by specifying the terms in the elastic stiffness matrix, which is designated as the ABAQUS D matrix [ABAQUS, 2005].

$$\begin{Bmatrix}\sigma_{11}\\ \sigma_{22}\\ \sigma_{33}\\ \tau_{12}\\ \tau_{13}\\ \tau_{23}\end{Bmatrix} = \begin{bmatrix} D_{1111} & D_{1122} & D_{1133} & & & \\ & D_{2222} & D_{2233} & & 0 & \\ & & D_{3333} & & & \\ & & & D_{1212} & 0 & 0 \\ & sym & & & D_{1313} & 0 \\ & & & & & D_{2323} \end{bmatrix} \begin{Bmatrix}\varepsilon_{11}\\ \varepsilon_{22}\\ \varepsilon_{33}\\ \gamma_{12}\\ \gamma_{13}\\ \gamma_{23}\end{Bmatrix}$$

Eq.2.24

where

$D_{1111} = E_1 (1 - \nu_{23} \nu_{32}) \gamma$

$D_{2222} = E_2 (1 - \nu_{13} \nu_{31}) \gamma$

$D_{3333} = E_3 (1 - \nu_{12} \nu_{21}) \gamma$

$D_{1122} = E_1 (\nu_{21} + \nu_{31} \nu_{23}) \gamma = E_2 (\nu_{12} + \nu_{32} \nu_{13}) \gamma$

$D_{1133} = E_1 (\nu_{31} + \nu_{21} \nu_{32}) \gamma = E_3 (\nu_{13} + \nu_{12} \nu_{23}) \gamma$

$D_{2233} = E_2 (\nu_{32} + \nu_{12} \nu_{31}) \gamma = E_3 (\nu_{23} + \nu_{21} \nu_{13}) \gamma$

$D_{1212} = G_{12}$

$D_{1313} = G_{13}$

$D_{2323} = G_{23}$

with

$\gamma = 1/(1- \nu_{12} \nu_{21} - \nu_{23} \nu_{32} - \nu_{13} \nu_{31} - 2\nu_{21} \nu_{32} \nu_{13})$

Note that this ABAQUS orthotropic material stiffness matrix is for the continuum orthotropic material, and it is different to the D matrix in the classical laminate theory.

2.3 Fracture of Composites

Fracture of a fibre-reinforced composite is often controlled by numerous micro-cracks distributed throughout the material. A vast amount of research has been conducted to assess the suitability of simple fracture mechanics to composite materials, and it has been shown that the compliance relationships for a fibre reinforced material in the fibre direction are significantly different to an isotropic elastic continuum. In many cases, when the composite structure behaves globally in a linear and elastic manner while the local material separation process at the crack tip exhibits nonlinear behaviour.

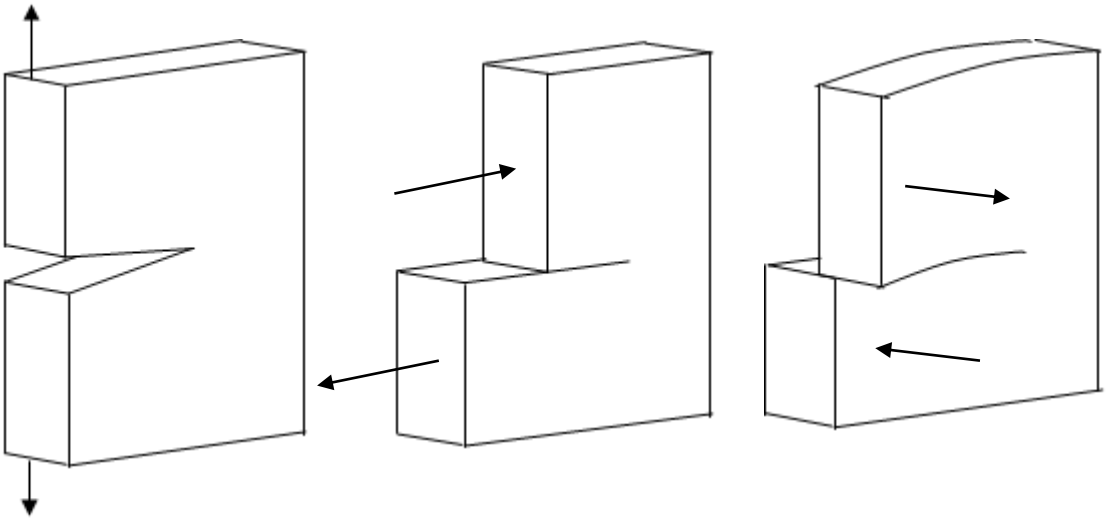

Fig.2.5 *The three modes of crack surface displacements*

There are three modes of crack opening, mode I opening, mode II shearing or sliding and mode III tearing, Fig.2.5. All crack growth may be expressed as one or combinations of these three modes.

Fig.2.6 shows various failure mechanisms in fibre reinforced composites [Anderson, 2005]. Loading in fibre direction can produce matrix cracking, fibre bridging, fibre rupture, fibre pullout, and debonding at the fibre/matrix interface. Out-of-plane stresses can lead to interlaminar separation or delaminations in composite laminates

because fibres are not strengthening in this direction. Compressive loads can cause fibre microbuckling, and macroscopic delamination buckling.

Out-of-plane tensile stress leads to delamination resulting also from the structural geometry. Mismatch in Poisson's ratios between plies results in the shear stresses between plies near the ply interface, which produce a bending moment balanced by a stress in the out-of-plane direction. As stated above that fracture mechanics is appropriate for composites in certain situations, delamination is one of the situations. Delamination can occur in both Mode I and Mode II conditions. According to Anderson and Hunston [Anderson, 2005; Hunston et al., 1987], for brittle matrix, the composite has a higher toughness than the neat resin, but reversed for high toughness matrices. Delamination can occur in Mode II, but the critical value of G, G_{IIc}, is typically 2 to 10 times higher than the corresponding G_{Ic}, in brittle matrices [Anderson, 2005]. For example, Dávila et al. reported the values of G_c for graphite/epoxy composite, are 268 J/m^2 for G_{Ic} and 1450 J/m^2 for G_{IIc} [Dávila et al., 2001]; Bonhomme et al. reported the values of G_c for AS4/8552 carbon prepreg composites are 302.1 J/m^2 for G_{Ic} and 1098.5 J/m^2 for G_{IIc} [Bonhomme et al., 2009]; and Meziere et al reported the values of G_c for T300-914 unidirectional carbon prepreg are 129 J/m^2 for G_{Ic} and 220 J/m^2 for G_{IIc} [Meziere et al., 2000]. There is some evidence that as a result of improved matrix toughness, G_{Ic} increases, and the ratio between G_{IIc} and G_{Ic} reduces, for example, the values of G_c for AS4/APC2 are 969 J/m^2 for G_{Ic} and 1719 J/m^2 for G_{IIc}; the values of G_c for AS4/APC2 are around 1330 J/m^2 for G_{Ic} and 1765 J/m^2 for G_{IIc} [O'Brian, 1984; Russell et al., 1987; Camanho et al., 2002].

Under tensile loading for the cross-ply laminates, for example $[0/90]_s$, the cross-ply undergoes the same axial deformation. Due to the difference in Poisson's ratios, the 0 and 90 degree layers will deform differently in the transverse direction when acting independently. Bonded together in the laminate, the 0 and 90 degree layers must have the same transverse deformation. This is achieved through interlaminar shear stresses, which is tension in the transverse direction for 0 degree layer (mainly on the matrix), and compression in the fibre direction for 90 degree layer. The interlaminar shear stresses vary across the width of the specimen, which will be zero over the central

region and reaching peak value near the edge of the specimen [Daniel et al., 1994]. At the edge of the specimen, transverse shear stress could contribute to the failure of cross-ply composites.

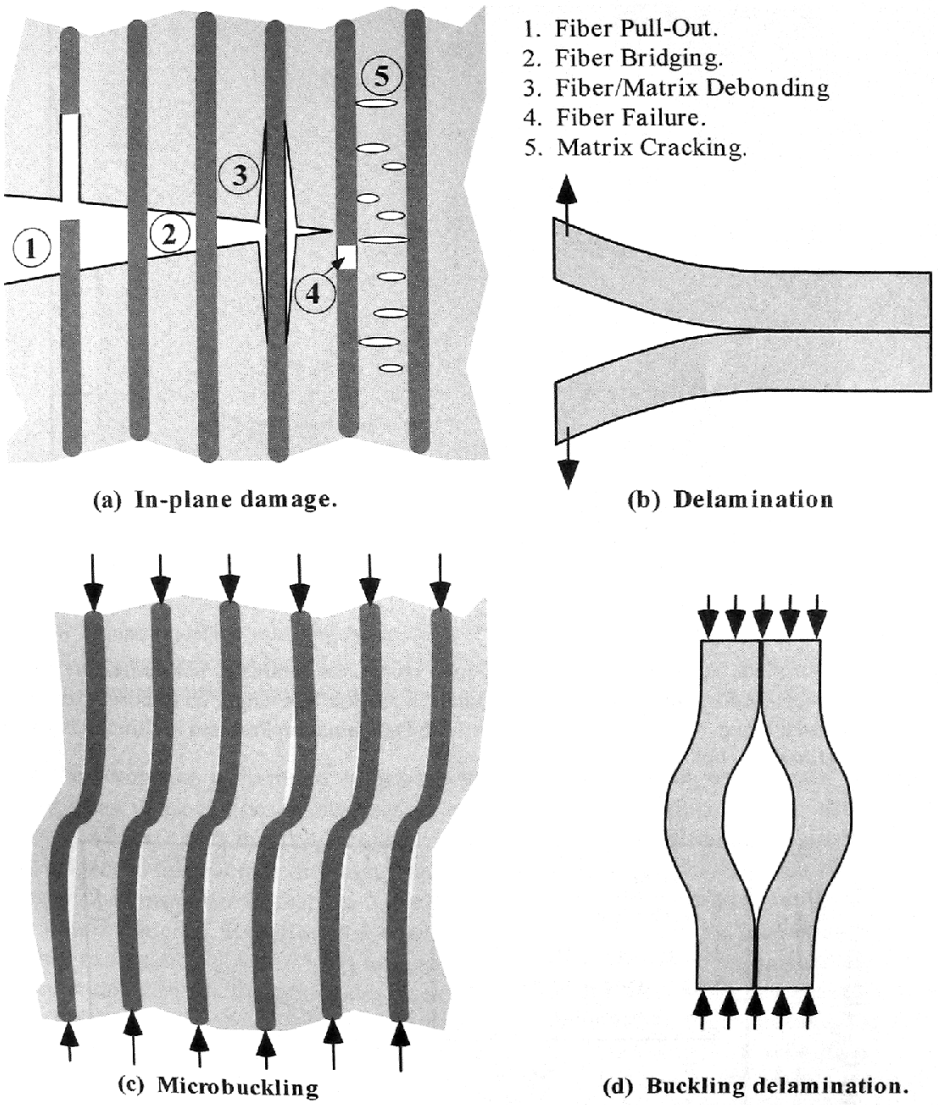

Fig.2.6 *Examples of damage and fracture mechanisms in fibre reinforced composites [Anderson, 2005]*

Foye and Baker [Foye et al., 1970] published a landmark report in which strength and failure mode dependence as a function of stacking sequence was observed. Further research has been done by Pagano and Pipes [Pagano et al., 1971]. The effect of stacking sequence on the interlaminar stress σ_z has been shown in Fig.2.7 [Pagano et al., 1971]. It is obvious that carefully designed laminate stack can effectively reduce

stress in the through-thickness direction. In general, for designing laminar composites, minimizing stress σ_z is one of the key desired factors.

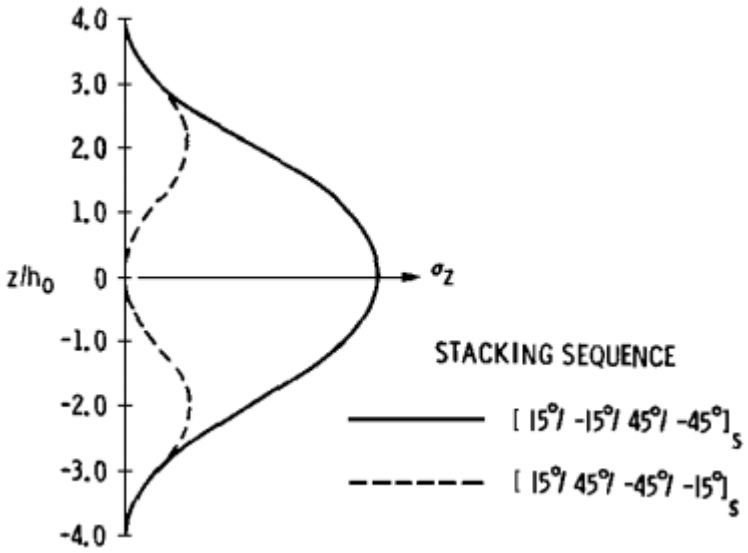

Fig.2.7 *Effect of stacking sequence on stress in cross thickness direction [Pagano et al., 1971]*

Rice [Rice, 1968] introduced J integral energy balance approach as a technique of the fracture mechanism for the free edge problem. The J integral method is able to accommodate thermal effects by incorporating the free thermal strains into the strain energy density [Yang et al., 1998; Schapery et al., 1990]. The effect of the delamination on ultimate failure is complicated. There is not any generic explanation to address this. This should be considered as a structural problem, which will depend on structural configuration, stacking sequence, and damage modes and progression ultimately [Pagano et al., 2000].

There has been extensive research carried out on the delamination failure of composite laminates and composite adhesive joints for static or cyclic loadings with respect to fibre distribution [Melro et al., 2008], different loading modes, crack propagation [Hadavinia et al., 2003; Guild et al., 2001; Potter et al., 2001], fracture toughness [Pinho et al., 2006], failure [Pinho et al., 2006], crack path selection [Chen et al., 2001; Chen et al., 2002], design for improved performances [Silva et al., 2007],

and finite element studies on the fracture [Guild et al., 2001; Pinho et al., 2006; Blackman et al., 2003], etc.

As previously mentioned, lap joints often have significant amount of shear and bending stresses. This is caused by the discontinuities of material stiffness and joint geometry. Stepped joints can reduce these stiffness discontinuities and resulting in reduced shear and bending or peel stresses at the joint edges.

A search of published literature revealed that very little research has been carried out on stepped joints. The stresses in stepped joints were reported by Hart-Smith [Hart-Smith, 1981]. It is also reported [Hart-Smith, 1981; Adams et al., 2000] that the stepped joint strength can be improved by matching stiffness of adherends, obtaining symmetric transverse or shear stress distribution along the stepped joint, which peaks at the ends of the overlap.

2.4 Comeld ™ joints

This work is focused on a novel joint system, called Comeld ™, connecting metal and composite components with the application of a new surface treatment technique, called Surfi-Sculpt ™, on the metal surface.

Comeld ™ joints are designed to take advantages of both mechanical and adhesive bonds. It is the combination of adhesive bonding and mechanical keying provided by the surface texture. This joining system is designed to improve conventional metal-composites joints.

Surfi-Sculpt ™ technology has been developed by TWI which uses an electron beam to create various surface textures through the manipulation of the electron beam. This technique is applicable to a wide range of metals, allows the creation of a range of surface textures, which can be precisely controlled. Some of these surface textures are included in Fig.2.8. Comeld ™ is the application uses Surfi-Sculpt ™ to create protrusions and cavities on and in the metal onto which the composite is laid and cured, forming the Comeld ™ joint.

Typical Surfi-Sculpt ™ metal surfaces are shown in Fig.2.8 [www.twi.co.uk]. To create a Comeld ™ joint, the metallic part is machined to form the required shape, Fig.2.9. And then Surfi-Sculpt ™ surface treatment is applied to create certain surface textures, examples are shown in Fig.2.10 [Smith, 2004].

The composite material is then laid-up onto the treated metal surface. Processing routes that can be used with Comeld ™ joining includes hand lay-up, spray lay-up, resin vacuum infusion, autoclave compaction etc. However, surface treatment on metal parts is required, such as etching. Various examples of Comeld ™ joints are shown in Fig.2.11 [Smith, 2004]. Fig.2.12 shows a close-up image of fibres located around the protrusions [Smith, 2004].

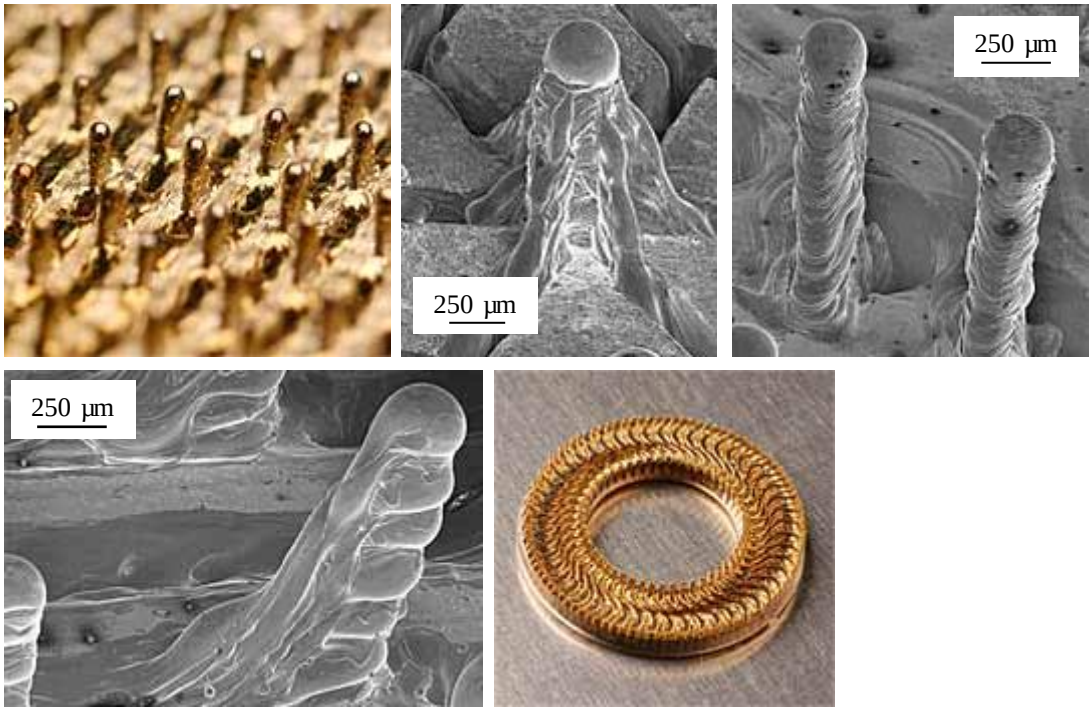

Fig.2.8 *Examples of Surfi-Sculpt ™ treatment on different metals [www.twi.co.uk]*

Fig.2.9 *Metal parts of Comeld ™ joints, (a) double-sided joints, (b) single-sided joints*

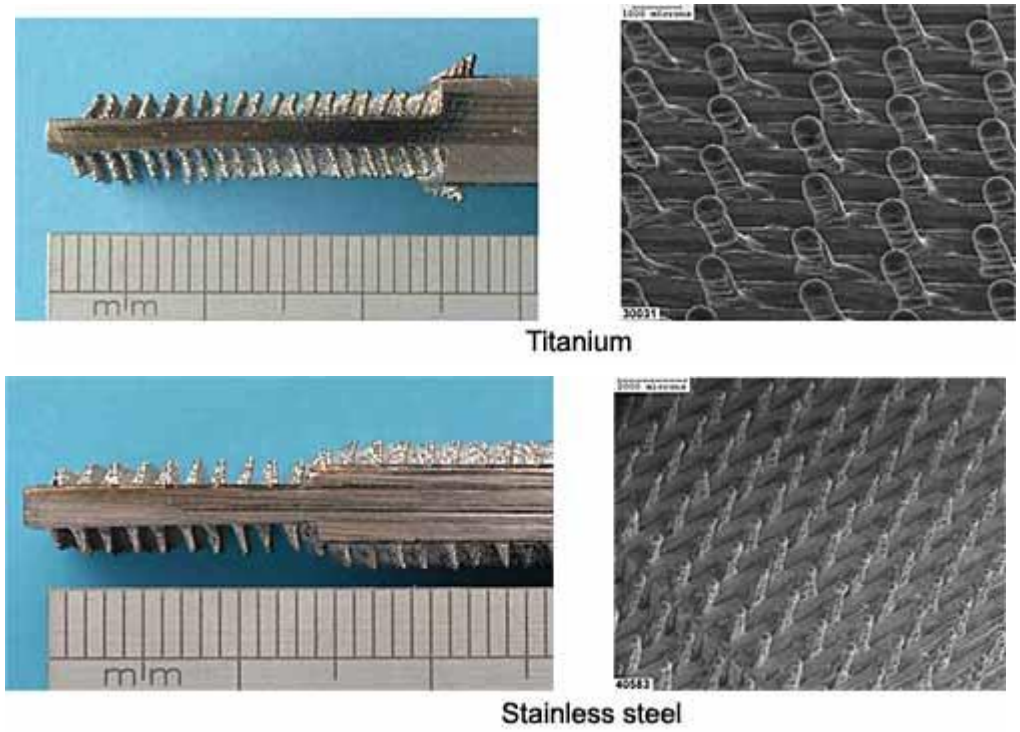

Fig.2.10 *Examples of Surfi-Sculpt [TM] treatment for Comeld [TM] joints [Smith, 2004]*

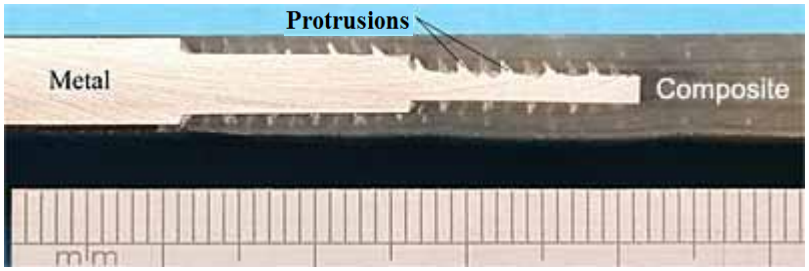

Stainless steel/non-crimp glass fabric reinforced vinyl ester

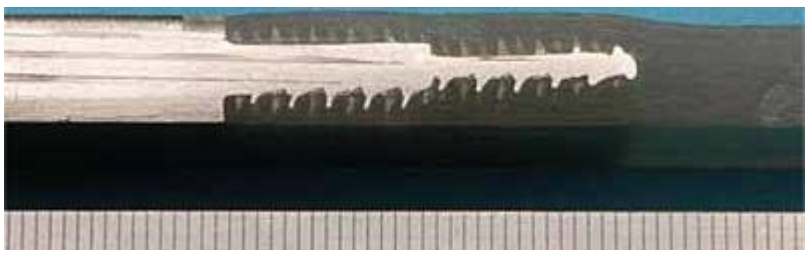

Stainless steel/woven glass fabric reinforced polyester

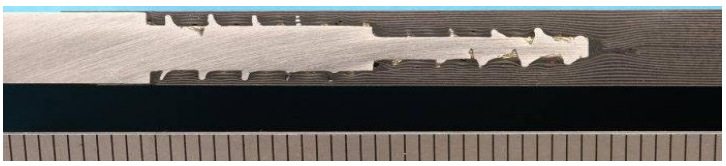

Titanium alloy/carbon fibre prepreg

Fig.2.11 *Various combination of Comeld [TM] joints (scale, mm) [Smith, 2004]*

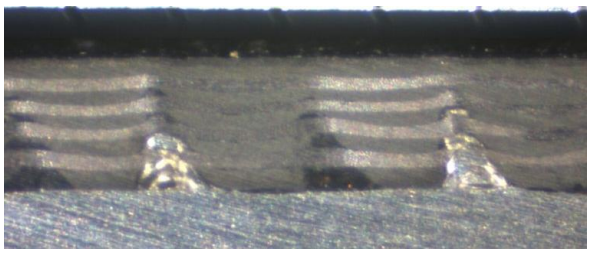

Fig.2.12 *Micrograph showing fibres located around protrusions within Comeld ™ joints [Smith, 2004]*

To compare the results under tension, the control samples were made [Smith, 2004] using exactly the same material (stainless steel and titanium) and processing but did not have the Surfi-Sculpt ™ treatment applied. Fig.2.13 (a) [Smith, 2004] shows that for GFRP/stainless steel double step joints, the Comeld ™ samples failed at a much higher load than the control joints and absorbed three times as much energy as the control specimens before failure; Fig.2.13 (b) shows that for CFRP/titanium double step joints, the Comeld ™ samples and the control samples failed at approximately the same load, however, the Comeld ™ joint absorbed three times as much energy as the control joint before failure.

(a)

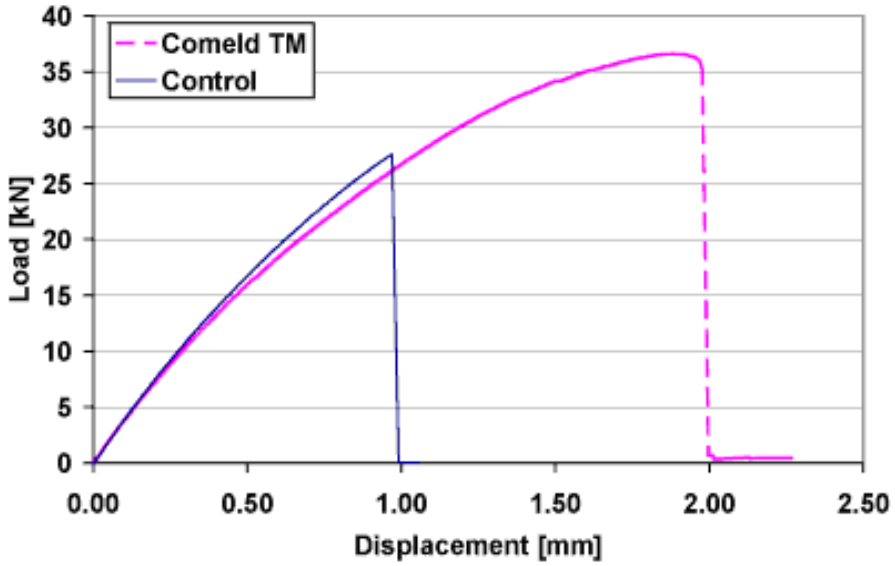

(b)

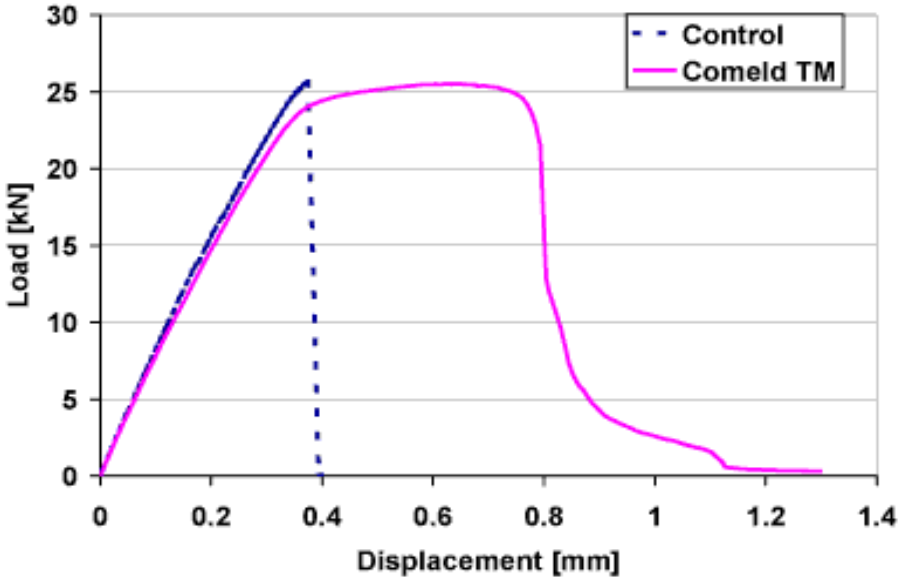

Fig.2.13 *Results of tensile testing on (a) GFRP/stainless steel, (b) CFRP/titanium double step joints [Keller et al., 2004]*

The explanation for the different behaviours under tensile loading of GFRP/stainless steel and CFRP/titanium can be obtained by observing the way in which the specimens failed. The typical failure of the control and Comeld ^{TM} samples are shown in Fig.2.14 and Fig.2.15. The control specimens for both material combinations failed at the composite-metal interface (resin is used as adhesives) [Smith, 2004].

The GFRP/stainless steel Comeld ™ joints failed within the composite, due to the presence of the protrusions; the interface is no longer the weakest part and can carry more load. After failure, composite material was observed to be attached to the protrusions. Shear failure also occurred in those regions without the protrusions. Closer inspections show the protrusions had undergone plastic deformation during failure of the specimen. For CFRP/titanium Comeld ™ specimens, the interaction of the composite with the protrusions made the interface no longer the weakest part, and in this case titanium failed before the composite. The high level of Surfi-Sculpt ™ treatment applied to the section to be joined meant that the metal had significantly reduced cross-section area, which decreased the load carrying capability of the titanium, and resulted in the unexpectedly low failure load [Kellar et al., 2004 (patent)].

(a)

(b)

Fig.2.14 *Failure in control samples, (a) GFRP/stainless steel, (b) CFRP/titanium (scale, mm) [Smith, 2004]*

(a)

(b)

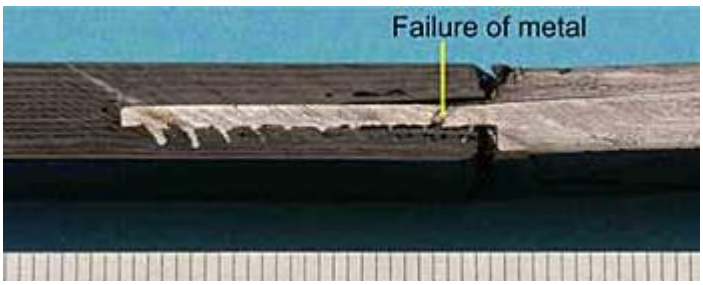

Fig.2.15 *Failure in Comeld™ samples, (a) GFRP/stainless steel, (b) CFRP/titanium (scale, mm) [Smith, 2004]*

The results from the research conducted on Comeld ™ joints suggest that the technique offers certain advantages in joining dissimilar materials compared with bonding and bolting. However, further research is required to investigate the joining mechanisms and failure behaviour of protrusions. In addition, there are many possible variables which could be adjusted with Surfi-Sculpt ™ technology. The variables include the distribution, radius, height and orientation of the protrusions. Therefore, finite element analysis of the Comeld ™ joining system is required to gain better understanding of the mechanism of the protrusions, and to optimise the detailed geometries of the joining system.

2.5 Finite element method

Finite element analysis (FEA), also called finite element method (FEM), is a method for numerical solution of field problems [Cook, 2002]. FEA can be used as an analytical tool to solve scientific and engineering problems. Structures can be divided to small pieces called finite elements, which are interconnected at joints known as nodes. After the physical nature of a problem has been understood, a model for analysis can be devised. A numerical model may describe an approximate behaviour of a geometric model, and is an idealisation. To consider a three-dimensional

structure subjected to external loads, such as mechanical loads or thermal loads, the mathematical model is discretised by dividing the structure into a mesh of finite elements, and then can be represented by finite number of nodal quantities and interpolation within each element. The value of a field variable is assumed to vary over each element in a predefined manner, while the variable distribution through the whole structure is adequately approximated with the chosen number and type of elements, which have influence on the overall accuracy of the results. Therefore, choosing appropriate element type and number is essential. The principle is to calculate not only the relationship between the external loads and the corresponding internal forces which together satisfy the equilibrium conditions of the structure, but also with the displacements of sets of nodes and the corresponding deformations which satisfy the compatibility.

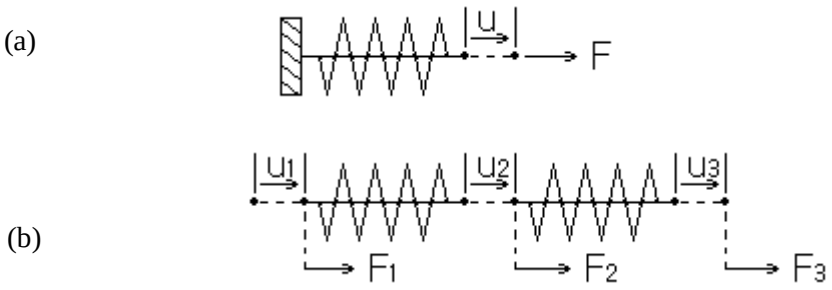

Fig.2.16 *(a) Single spring, fixed at left end; (b) system of two springs*

2.5.1 Example of Springs

Considering a simple stress analysis example [Barber, 2005], a problem of single spring, with stiffness ***k*** under loading force ***F***, assume the force displacement relation is linear, i.e. linear elastic spring. The force, ***F***, displacement, ***u*** relation can be expressed as,

$$F = ku \qquad \textbf{Eq.2.25}$$

The single spring is fixed at one end and free to move in the other to accommodate the resulting displacement associated with the external force. For this linear elastic spring, the displacement is proportional to the force applied, Fig.2.16 (a).

For a system of two springs, the stiffness of each spring is not necessarily the same. Considering each spring as one element defined by the two ends, and the stiffness of the springs are k_1, and k_2 respectively. At equilibrium, it follows that,

$F_1 + F_2 + F_3 = 0$ ***Eq.2.26***

where

$F_1 = k_1 (u_1 - u_2)$ ***Eq.2.27***

$F_3 = k_2 (u_3 - u_2)$ ***Eq.2.28***

Therefore, $F_2 = -k_1u_1 + (k_1 + k_2)\, u_2 - k_2u_3$.

The matrix form of the relations can be expressed as

$\boldsymbol{F = KU}$ ***Eq.2.29***

$$\begin{bmatrix} F_1 \\ F_2 \\ F_3 \end{bmatrix} = \begin{bmatrix} k_1 & -k_1 & 0 \\ -k_1 & k_1 + k_2 & -k_2 \\ 0 & -k_2 & k_2 \end{bmatrix} \begin{bmatrix} u_1 \\ u_2 \\ u_3 \end{bmatrix}$$ ***Eq.2.30***

Consider force acting on each spring separately, and the matrix can be expressed respectively as

$$\begin{bmatrix} F_1 \\ F_2 \\ 0 \end{bmatrix} = \begin{bmatrix} k_1 & -k_1 & 0 \\ -k_1 & k_1 & 0 \\ 0 & 0 & 0 \end{bmatrix} \begin{bmatrix} u_1 \\ u_2 \\ u_3 \end{bmatrix}$$ ***Eq.2.31***

$$\begin{bmatrix} 0 \\ F_2 \\ F_3 \end{bmatrix} = \begin{bmatrix} 0 & 0 & 0 \\ 0 & k_2 & -k_2 \\ 0 & -k_2 & k_2 \end{bmatrix} \begin{bmatrix} u_1 \\ u_2 \\ u_3 \end{bmatrix}$$ ***Eq.2.32***

therefore, Eq.2.30 can be derived from considering each spring separately by simply adding Eq.2.31 and Eq.2.32 together. This example shows how the principles of the individual elements were combined to determine the overall response of the system. For more springs in the system, the connectivity of those elements becomes complicated, and the relevant force equations can be derived by minimising the potential energy of the system. For FE method, before the equation can be solved, some form of boundary condition must be applied. In term of stress problems, this means that the body must be constrained to prevent it from performing unrestricted rigid body motion (as stated in the example of the single spring, one end is fixed). For thermal problems, the temperature must be defined at one or more of the nodes.

This approach can be used to solve both static and dynamic stress analyses and also steady state and transient thermal analyses. Clearly, large range of problems can be adopted for analysis by FEM, and certainly many of these problems were previously insoluble until the finite element method became available. Increasingly, the complexities and approximations of the algorithms used by many commercial FEA software packages are becoming less apparent to end users. Certain aspects of the analysis have been automated by employing more sophisticated pre-processors and post-processors that can be used to generate and interrogate the analysis results. The so called solvers have become concealed as commercial packages. Pre-processors can now easily generate highly complex models with little amount of input from the engineer, while the post-processors are able to produce equally impressive and convincing graphical output. Although finite element method can produce accurate and reliable results when used correctly, and it is important to underline that FEM is only an approximate technique. The validity and accuracy of the model and its solution highly rely on an accurate understanding and representation of the problem together with the correct analysis procedures. [Fagan, 1992; Fenner, 1987]

2.5.2 Geometric simplification with symmetry

A numerical model can be developed with geometric shape and description of the behaviour. All variables including geometry, loads, material properties, and boundary

conditions are idealised based on the importance in obtaining the required results, which could be recognised as simplification of the real problem. The overall cost of carrying out finite element analyses includes savings in time and effort in both model development and analysis. Saving can be achieved by careful model design, while maintaining the model result accuracy. This can usually be made by approximating the dimensionality of the problem, and by taking advantage of any symmetry in the body. There are four types of symmetry recognised that could be used to simplify the problem, and could be encountered in engineering problems: axial; planar; cyclic and repetitive. [Busfield, 2000]

1. Axial symmetry. If a shape can be defined by rotating a cross-section about a line (e.g. a cone) then it is said to be axial symmetric or axisymmetric. Axial symmetric models are two-dimensional models of the identical shape distributing around an axis in radial direction, Fig.2.17 (a).

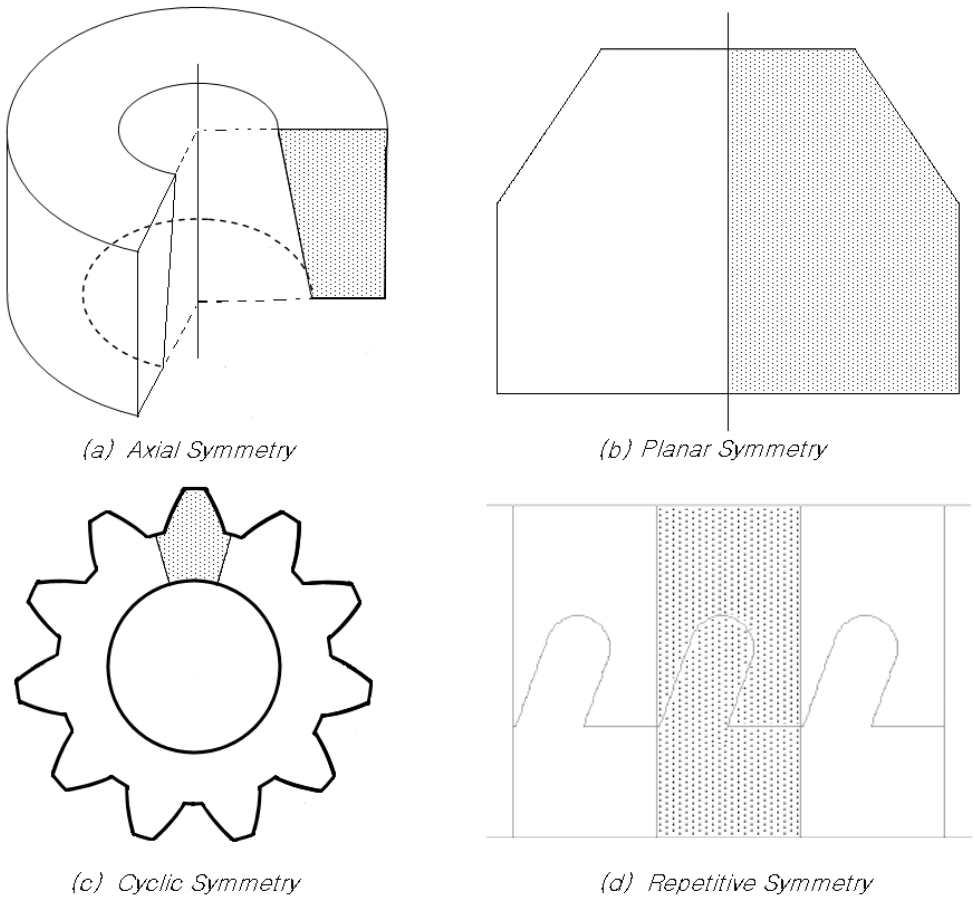

Fig.2.17 *A schematic drawing to demonstrate the four types of symmetry*

2. Planar symmetry. With planar symmetry, the axis of symmetry of a two-dimensional figure is a line such that, if a perpendicular is constructed, any two points lying on the perpendicular at equal distances from the axis of symmetry are identical, i.e. if the shape were to be folded in half over the axis, the two halves would be identical: the two halves are each other's mirror image, Fig.2.17 (b).

3. Cyclic symmetry. The cyclic symmetric structure is composed of a series of identical sectors that are arranged circumferentially to form a ring, which is present for example in gears, spline fittings, a turbine disc with blades attached and propellers, Fig.2.17 (c).

4. Repetitive symmetry. Repetitive symmetry is present as part of a structure is repeated regularly in a linear sequence. Depending on the nature of boundary conditions, it is possible to model only the repeating section. This technique is used in this project, to obtain simplification, Fig.2.17 (d).

These four types of symmetry can be used in combination to achieve the simplification of real engineering problems. In this project, planar symmetry and repetitive symmetry are employed to investigate the Comeld ^{TM} joint.

Unit cell models can be used for the repetitive symmetry, when the periodic boundary conditions can be identified. Periodic boundary conditions are a set of boundary conditions that are often used to simulate a large system by modelling a small part that is far from its edge. Unit cell models have been used widely as an important technique for numerically solve problems for elastic constants estimation, composite laminate structures, micro-mechanical analysis, crystalline structures, chemical molecular simulation, etc. and even for the video game industry. For composite research, the unit cell models are used extensively [Byström et al., 2000; He et al., 2007].

2.5.3 Analysis Procedures

The stages involved in producing or developing an FE model are detailed below.

First, to determine the type of model to be employed which is capable of representing the behaviour of the component or system most accurately by using all available approximations simplifying the model, such as approximation of the geometries within tolerance (for example, use two dimensional instead of three dimensional model).

Second, to mesh the model into finite elements and specify the material properties, boundary conditions, step definitions, and output variables required. Generate the input file. Select proper element type based on the first step, for example, shell elements, beam elements, two-dimensional continuum elements or three dimensional elements.

Third, the input file can be submitted to a dedicated equation solver software. The externally applied load vectors and the stiffness matrix are calculated for each element in the model. These values can then be combined together to determine the single force vector and the stiffness matrix, {F} and [k], for all the elements in the analysis; following which, a matrix solution is performed to evaluate the simultaneous equations $\boldsymbol{F} = \boldsymbol{kU}$ adopting a potential energy minimisation technique.

Fourth, having calculated the nodal displacement in all degrees of freedom, the stress and strains are evaluated and tabulated. The tabulated results can be examined and interpreted by using a ready to use graphical post-processing software package.

Then, for a given analysis, the mesh size sensitivity studies are important. Increase mesh density until a consistent solution is obtained. Element size sensitivity study can be employed to obtain both the efficiency and accuracy. Note that the mesh sensitivity studies were carried out for all models presented in this work; the development and analysis of these studies were lengthy.

Lastly, assumptions used in the model should be questioned. For example, is the model correct? Do the boundary conditions employed accurately describe the physical nature of the behaviour? Is the simplification of the model itself within the tolerance?

2.5.4 Selection of elements

Fig.2.18 [ABAQUS, 2005] shows the element families that are used most commonly in a stress analysis. One of the major distinctions between different element families is the geometry type that each family assumes.

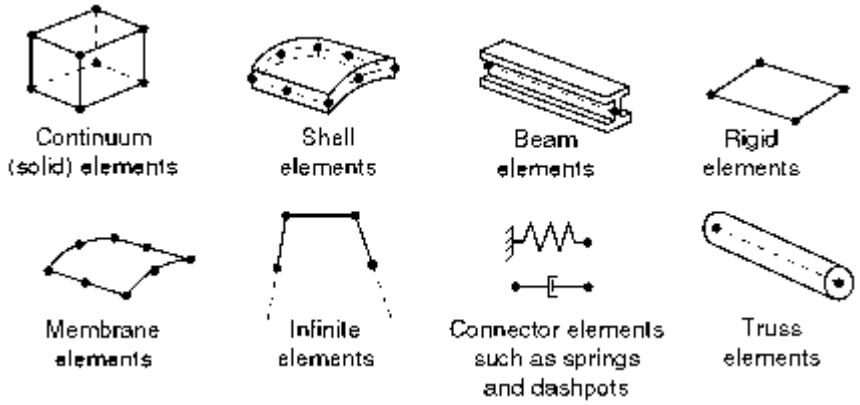

Fig.2.18 *Families of elements in ABAQUS [ABAQUS, 2005]*

There are various types of elements that could be used in a finite element analysis to describe the component or system's geometry. The shapes of these elements vary from a single point with no dimensions to a full three-dimensional shape. All the finite element work presented in this work used mainly the ABAQUS v6.5 software, and with the assistance of I-DEAS 11, to solve problems and post-process the results. The elements used in this work consist of triangular and rectangular two-dimensional and 8-nodes brick shaped three-dimensional elements, Fig.2.19 [ABAQUS, 2005].

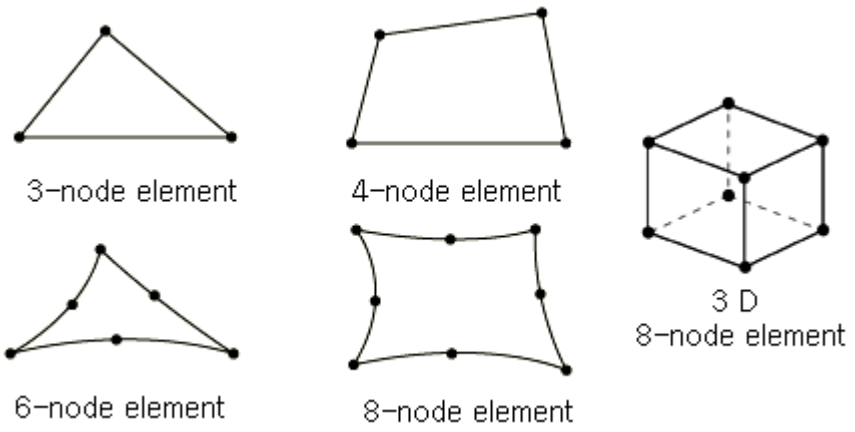

Fig.2.19 *Shape of elements used in this project [ABAQUS, 2005]*

It is also possible to use either first or second order elements. The difference between the two is the first order elements offer linear displacement interpolation between adjacent nodes. As an example, the behaviour of a point in between the adjacent nodes will be described by averaging the displacement behaviour of each node. Second order elements offer a quadratic interpolation of the position between nodes. The behaviour of one point along the edge of an element is described by a quadratic relationship. First order elements can induce the problem of hourglass and shear locking, if the elements distortion and applied strain are small, the second order elements are capable of producing a more reliable stress distribution, while consuming more resources during the analysis. First order elements are preferred for large strain analyses, due to its capability of undertaking larger element distortions before failure to a converged solution.

Additionally, there are two common types of element integration options that are available for continuum mechanics problems. They are the normal and reduced integration elements, Fig.2.20 [ABAQUS, 2005]. The former performs calculations at several locations which are distributed throughout each element, which can generate result with increased accuracy, although consuming more resources and sometimes resulting in convergence problems, whilst the latter performs the calculations at fewer points faster and is acceptable for most simulations.

Reduced integration first and second order two-dimensional elements and reduced integration three-dimensional stress elements were used for this project.

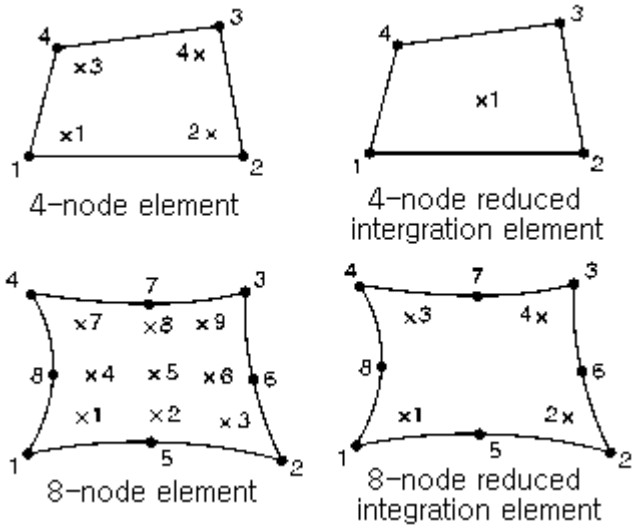

Fig.2.20 *Normal and reduced integration elements [ABAQUS, 2005]*

Commonly used two-dimensional elements include plain stress, plain strain, and generalised plan strain elements. According to ABAQUS Analysis User Manual, "Plane stress element can be used when the thickness of a body or domain is small relative to its lateral (in-plane) dimensions. The stresses are functions of planar coordinates alone, and the out-of-plane normal and shear stresses are equal to zero. Plane stress elements must be defined in the ***X***-***Y*** plane, and all loading and deformation are also restricted to this plane. This modelling method generally applies to thin, flat bodies. For anisotropic materials the Z-axis must be a principal material direction." [ABAQUS, 2005]

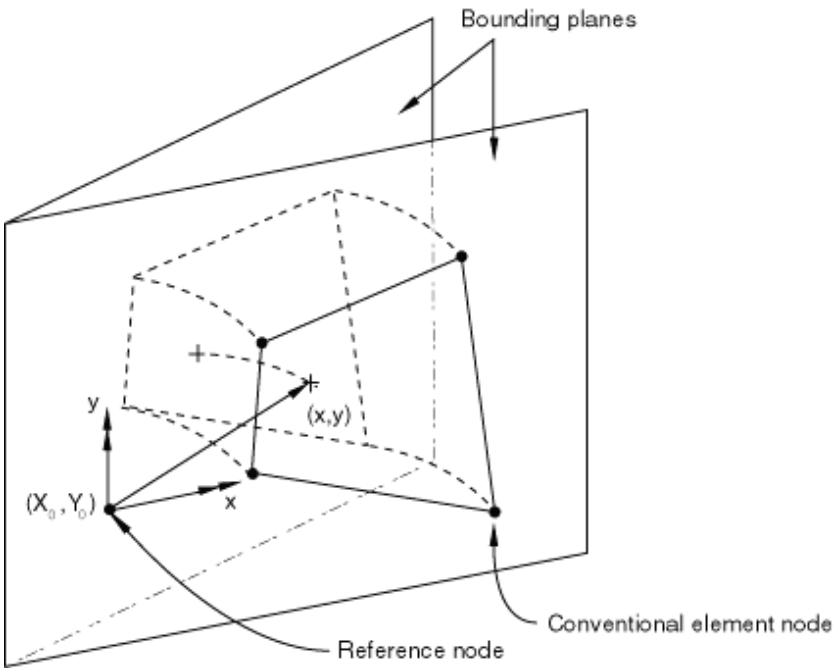

Fig.2.21 *Generalised plane strain elements [ABAQUS, 2005]*

According to ABAQUS Analysis User Manual, "Plane str**a**in elements can be used when it can be assumed that the strains in a loaded body or domain are functions of planar coordinates alone and the out-of-plane normal and shear strains are equal to zero. Plane strain elements must be defined in the ***X***–***Y*** plane, and all loading and deformation are also restricted to this plane. This modeling method is generally used for bodies that are very thick relative to their lateral dimensions, such as shafts, concrete dams, or walls. Plane strain theory might also apply to a typical slice of an underground tunnel that lies along the ***Z***-axis. For anisotropic materials the ***Z***-axis must be a principal material direction. Since plane strain theory assumes zero strain in the thickness direction, isotropic thermal expansion may cause large stresses in the thickness direction." [ABAQUS, 2005]

According to ABAQUS Analysis User Manual, "Generalised plane strain elements provide for the modeling of cases in ABAQUS/Standard where the structure has constant curvature (and, hence, no gradients of solution variables) with respect to one material direction - the 'axial' direction of the model. The formulation, thus, involves a model that lies between two planes that can move with respect to each other and, hence, cause strain in the axial direction of the model that varies linearly with respect

to position in the planes, the variation being due to the change in curvature. In the initial configuration the bounding planes can be parallel or at an angle to each other, the latter case allowing the modeling of initial curvature of the model in the axial direction." The concept is illustrated in Fig.2.21 [ABAQUS, 2005]. Generalised plane strain elements are typically used to model a section of a long structure that is free to expand axially or is subjected to axial loading. [ABAQUS, 2005]

Beyond the curved components, according to Le Page et al. [Le Page et al., 2004] and Taliercio, [Taliercio, 2005], it is proved that generalised plane strain elements may well be used when the effect of variability in fibre architecture in the through-width (becomes through thickness in two dimensional finite element model) direction is not included [Le Page et al., 2004], which allows a 'slice' to be analysed without imposing the severe constraint of plane strain; and it works with the cross section of parallel fibres [Taliercio, 2005].

2.5.5 Submodelling [ABAQUS, 2005]

Submodelling is the technique to study a local part of a model with a refined mesh, based on interpolation of the solution from an initial global model onto appropriate parts of the boundary of the submodel. The method is most useful when it is necessary to obtain an accurate, detailed solution in the local region. The response at the boundary of the local region is defined by the solution for the global model and together with loads applied to the local region it determines the solution in the submodel. The technique relies on the global model defining this submodel boundary response with sufficient accuracy.

Submodelling can be applied quite generally using ABAQUS. With a few restrictions different element types can be used in the submodel compared to those used to model the corresponding region in the global model. Both the global model and the submodel can use solid elements, or they can both use shell elements. The material response defined for the submodel may also be different from that defined for the global model. Both the global model and the submodel can have nonlinear response

and can be analysed for any sequence of analysis procedures. The procedures do not have to be the same for both models.

The submodel is a separate analysis. The only link between the submodel and the global model is the transfer of the time-dependent values of variables to the relevant driven variables of the submodel. The only information in the global model available to the submodel analysis is the file output data written during the global model analysis. These data contain, by default, the undeformed coordinates of all global model nodes and element information for all elements in the global model.

Node-based submodelling is the most commonly used technique. With this technique global model responses are used to prescribe boundary conditions at the driven nodes in the submodel. It can be used to drive a local part of the model by nodal results, such as displacements results from the global mesh.

2.5.6 Meshfree methods

Among computational simulation techniques, finite element method (FEM) is often used to model and investigate physical phenomena in an engineering system. The simulation requires solving the complex differential or partial differential equations that govern these phenomena. The spatial domain is often discretised into meshes. As introduced previously, a mesh is defined as a net formed by connecting nodes in a predefined manner. By using a properly predefined mesh and by applying a proper principle, complex differential or partial differential governing equations can be approximated by a set of algebraic equations for the mesh. The system of algebraic equations for the whole problem domain can be formed by assembling sets of algebraic equations for all the meshes. [Liu, 2003]

The mesh free method can be used to establish a system of algebraic equations for the whole problem domain without the predefined mesh. In recent years, meshfree methods have gained attention. The trend in computational mechanics has been to focus on increasingly demanding problems that require the ability to treat large deformations, advanced materials, complex geometry, nonlinear material behaviour,

discontinuities and singularities, etc. Meshfree methods use a set of nodes scattered within the problem domain and on the boundaries of the domain to represent (not discretise) the problem domain and its boundaries. The information on the relationship between the nodes is not required, i.e. a mesh is not formed, at least for field variable interpolation. These means that meshfree methods eliminate some or all of the traditional mesh-based view of the computational domain and rely on a particle (either Lagrangian or Eularian) view of the field problem. [Liu, 2003]

There are a number of meshfree methods summarised by Liu [Liu, 2009], such as the element free Galerkin (EFG/EFGM) method developed by Belytschko et al. in 1994, the meshless local Petrov-Galerkin (MLPG) method developed by Atluri and Zhu in 1998, the diffuse element method (DEM) developed by Nayroles, Touzot and Villon in 1992, the point interpolation method (PIM) developed by Liu, G. R. and Gu in 1999, the point assembly method (PAM) developed by Liu, G. R. in 1999, the finite point method developed by Onate et al. in 1996, the finite difference method with arbitrary irregular grids developed by Liszka, Orkisz and Jensen in 1980, smooth particle hydrodynamics (SPH) developed by Lucy in 1977 and Gingold and Monaghan in 1977, reproducing kernel particle method developed by Liu, W. K. et al. in 1993, and so forth. They all share the same feature that predefined meshes are not used at least for field variable interpolation. The methodology is still in a rapid development stage.

2.6 Similar through-thickness techniques

Comeld ™ joints may be comparable with some transverse reinforcement techniques. Similar through-thickness techniques include z-pinning, stitching, bolted adhesive joint, tufting, etc. The use of both adhesive and mechanical bonds can take advantages of both methods, and these can be done before the curing processes for the composites. Previous work done on similar techniques for improving adhesive joints by adding mechanical keying effect was only conducted for composite-to-composite lap joints. Among which, z-pinning may be comparable with Comeld ™ technique.

Some trends can be identified for some geometric parameters including size, angle, distribution density of the reinforcements (inserted z-fibres and metallic rods). As a novel joining technique, the Comeld ™ joining system enables metal-to-composite joining with through-thickness reinforcement. For the present development of the joining system, understanding of the geometric parameters influence on the mechanical performance of the joint is the aim of this work.

The z-fibre technique is designed for composite-to-composite joint, which employs fibres in the through-thickness directions for the composite laminate joints to improve the through-thickness mechanical properties and delamination resistance. The manufacture process employs ultrasonically assisted z-pin insertion of thin fibrous composite or metallic rods (to various lengths, spacing and patterns) that have high axial stiffness, strength and fatigue endurance on top of laminates for the through thickness direction, with a layer of low density foam on top of the laminates allowing z-pins to penetrate, and this preformed layer can be sheared away to complete the z-pinned laminates before curing process. With vast amount of research done for the technology, both numerical or experimental, it proved that the inter-laminar strength for Mode I, II [Partridge et al., 2005; Grassi et al., 2003; Steeves et al., 2006] and mixed-mode improved significantly for static and cyclic loads compared to conventional laminate composites [Carti é et al., 2006[a]; Zhang et al., 2008]. According to Mouritz [A.P. Mouritz, 2007], z-pinning not only improves the delamination toughness, but also transforms the crack propagation from an unstable to stable process especially in brittle matrix laminates.

This technology can be used for joining laminate composites during the joint components' manufacturing process. For instance, after the prepreg laminates have been laid up, the insertion of fibres in through thickness direction can be performed to create the z-pinned joint ready for curing process. Composite T-joints reinforced using z-pinning technology have improved the delamination resistance and joint strength for simple and mixed-mode loading conditions. The improvements in the through thickness direction have been attributed to large scale bridging effects [Carti é et al., 2006[b]; Rugg et al., 2002]. It is observed that the z-pinning may slightly reduce the in-plane stiffness properties [Lenzi et al., 2007; Chang et al., 2006], which might

be caused by the in-plane fibres misalignment around the z-fibre insertion and the formation of resin rich regions around the z-fibre.

Similarly to the z-pinned joints design, the Comeld ™ joining system is designed to enable improvements for metal-composites joints. The difference is mainly because the protrusions are created from the metal joint surfaces, where it is an insertion process in the case of z-pinning technology. There are many possible variables which could be adjusted with Surfi-Sculpt ™ technology. These variables include the protrusion distribution pattern and density, protrusion radius, height and orientation, etc. The aim of this work is to study the influence on these geometric parameters of the protrusions to optimise the design of the joining system.

As mentioned previously, little relevant information has been obtained after extensive literature research, and only some z-pinning related research has been done with some investigation of z-fibre geometric parameters. The effects of z-fibre density, diameter and insertion depth have been studied [Grassi et al., 2003]. Rugg et. al. include the effect of the z-fibre density with mixed mode delamination investigation [Rugg et al., 2002]. Another similar technique of insertion of metallic rods revealed an effect of the angle of those metallic rods for improving lap joints performances [Rugg et al., 1998; Carti é et al., 2004]. Recent research using metal spikes welded on the joint step metal surface has been reported by Ucsnik et al. [Ucsnik et al., 2010]. Improvements in ultimate load and maximum deformation were found despite failure of the spikes at the metal surface.

3
THE FINITE ELEMENT METHODS

3.1 Introduction

The overall aim of this work is to improve the performance of the Comeld ™ joining system. The finite element (FE) investigation is focused on the individual protrusions influence on the Comeld ™ joint stress status under loading using several different FE modelling techniques. There are many parameters that can be studied to investigate the protrusions, which include the geometric parameters of the individual protrusions such as the protrusion shape, angle, height, size; and the spatial arrangement parameters of the protrusions, including the protrusion distribution density and protrusion pattern.

Two finite element methods have been employed to investigate the geometric and spatial effects of the protrusions of the joints. Firstly, two-dimensional modelling (2D) was used to investigate the effects of change of geometric parameters of the protrusions including shape, angle and protrusion height; secondly, three-dimensional modelling (3D) was used to investigate the effects of change of spatial arrangement of the protrusions along with the protrusion distribution. However, for both these two methods, a series of 3D models were produced initially for material characterisation purposes as explained in sections 3.2.3 and 3.2.4.

This chapter describes the finite element modelling methods that were used to simulate and predict the joint behaviour for different protrusion parameters, the mesh control and the element type used for the finite element methods, both 2D and 3D models, and the materials characterisation models.

3.2 Material Properties

The materials used for the unit cell models are carbon fibre/epoxy cross ply AS4/8552 prepreg $[0/90]_{12S}$, and aerospace grade titanium alloy Ti-6Al-4V (Ti64). The linear elastic material properties are obtained from materials handbook and the prepreg data sheets. For Ti64, the plasticity data is available and therefore has been used in the 2D models.

3.2.1 The titanium alloy material properties characterisation

The Ti64 material properties are shown below [Bastid, 2005], see Table.3.1 and Fig.3.1

Table.3.1 *Titanium material properties*

E [GPa]	ν	σ_y [MPa]
114	0.336	960

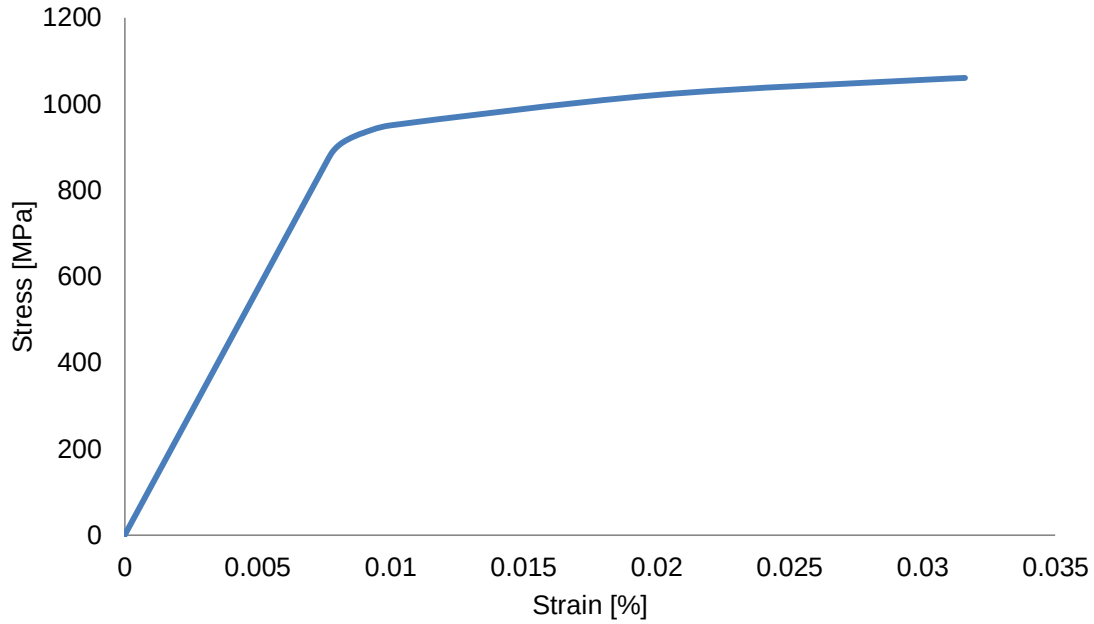

Fig.3.1 *Stress-strain behaviour of the titanium alloy.*

3.2.2 The prepreg material properties

The uni-directional prepreg material properties are shown below, see Table.3.2.

Table.3.2 *The uni-directional carbon prepreg, AS4/8552**

E_1 [GPa]	E_2 [GPa]	E_3 [GPa]	ν_{12}	ν_{13}	ν_{23}	G_{12} [GPa]	G_{13} [GPa]	G_{23}^{**} [GPa]
112.4	9.38	9.38	0.32	0.32	0.4	5.28	5.28	3.35

Axial tensile strength [MPa]	Transverse tensile strength [MPa]	0 °ILSS strength [MPa]	In-plane shear strength [MPa]	Neat resin strength [MPa]
2207	81	128	114	121

where, for 0 degree ply, 1 is the fibre direction, 2 and 3 are the transverse directions. G_{23} is calculated with E_2 and ν_{23} since the original data for G and ν are not compatible mathematically. The strength data is from the Hexcel materials data sheet.

* - The unidirectional prepreg is AS4/8552 from Hexcel, and the properties are approved by TWI and are taken from literature [McGowan et al., 1998].

** - The shear modulus was modified to satisfy the material transverse isotropy fulfilling the relationship $E_{23}=2G_{23}(1+\nu_{23})$

The material properties of composite regions in the models have been assigned accordingly based on the model design (some models have a homogenised region and others have layered region for the composite partition). The models with layered composite partitions have been assigned with the prepreg properties in the relative directions, which are 0 and 90 degrees.

3.2.3 The homogenised composite material properties

To obtain the homogenised properties, layered three-dimensional models for the cross-ply composite region have been created to simulate $[0/90]_{2S}$ lay-up and the model design is shown in Fig.3.2, containing four layers of cross-ply composites, where the thickness of the composite layer is identical with the carbon prepreg ply. The dimensions of the model are not important because there is not any detailed geometry involved. The symmetry plane is (1, 3) plane at the bottom in Fig.3.2

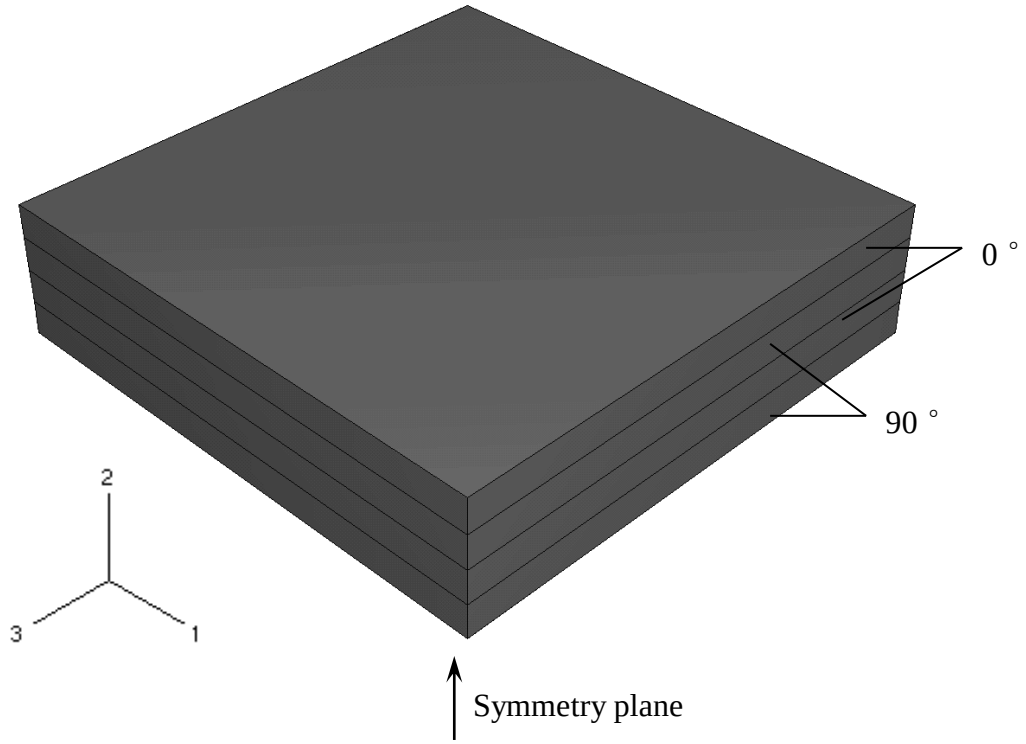

Fig.3.2 *The simulation of [0/90]$_{2S}$ cross-ply*

The layered models have been assigned the unidirectional prepreg properties oriented in one or three directions to simulate the cross-ply $[0/90]_{2S}$ homogenised material response to loads. The prepreg material properties are discussed in the materials characterisation section 3.2.2.

3.2.3.1 Three-dimensional composite properties model boundary conditions

The composite layer interfaces have been assumed to have perfect bonding, because the analysis conducted is elastic (elastic material properties). The model has been loaded in 1, 2 and 3-directions separately with 0.1% strain.

Finite element analysis has been carried out on series of elastic static three-dimensional analyses. The homogenised properties have been obtained based on the classic laminate theory and simulation. The obtained homogenised cross-ply composites properties data are shown in Table.3.3. The fibre axis of the 0 and 90 degrees UD prepreg lie in 1-direction and 3-direction respectively, therefore the layer

is orthotropic. When values could be obtained from both finite element analysis and classic laminate theory (software used was ESAComp 2.1), the values were found identical. However, some values were only be obtained by one method. The homogenised properties for the cross ply material are shown in Table.3.3.

Table.3.3 *The engineering constants of the cross ply material*

E_1 [GPa]	E_2 [GPa]	E_3 [GPa]	G_{12} [GPa]	G_{13} [GPa]	G_{23} [GPa]
61.21	10.68	61.21	4.31	5.28	4.31

ν_{12}	ν_{13}	ν_{21}	ν_{23}	ν_{31}	ν_{32}
0.41	0.049	0.072	0.072	0.049	0.41

For the shear modulus of the composites, the data have been obtained by using the classic laminate theory. For orthotropic material properties application in the ABAQUS, these engineering constants must be converted to the orthotropic material stiffness matrix. The values of the orthotropic material stiffness matrix were calculated for the layer and are shown in Table.3.4. Note that the definition of the orthotropic material stiffness matrix used in ABAQUS is not the same as the D matrix defined in the classical laminate theory (see section 2.2).

The material stiffness matrix of the homogenised cross ply material will be applied for the composite partitions in the homogenised 2D global models and 2D unit cell models.

Table.3.4 *The stiffness matrix for orthotropic material in ABAQUS*

D_{ijkl},								
1111	2222	3333	1122	1133	2233	1212	1313	2323
64.44	11.06	62.76	6.532	26.76	2.457	4.31	5.28	4.31

3.2.4 The protrusion layer homogenised material properties

3.2.4.1 Three-dimensional protrusion layer properties model design

The 3D model for the protrusion layer was designed based on the protrusion distribution density of the Comeld ™ joint specimens. The protrusion distribution

density is calculated by the number of the protrusions on the joint step divided by the joint step area, the average value of which is 0.54 per square millimetre, i.e. one protrusion per 1.85 square millimetres. The measurement was done by dividing the area of the joint step with the number of protrusions. The typical radius and height of the protrusions are 0.58 mm and 1.0 mm. If assuming square array arrangements, the repeatable unit cell would be 1.36 mm square and 3 mm as height. This was measured by dividing the number of the protrusions on the steps by the area of the step.

These models have been designed for the material characterisation purposes, therefore, the shape of the protrusions was simplified in these models to be cylindrical. Considering the repetitive protrusions on the joint steps and the symmetrical features over the cylindrical protrusion shape, the typical protrusion layer model contains 1/8 protrusion with the radius of the quarter cylinder calculated retaining the same volume fraction of the protrusion. The radius of the cylinder is calculated as 0.21 mm. The schematic model design is shown below in Fig.3.3.

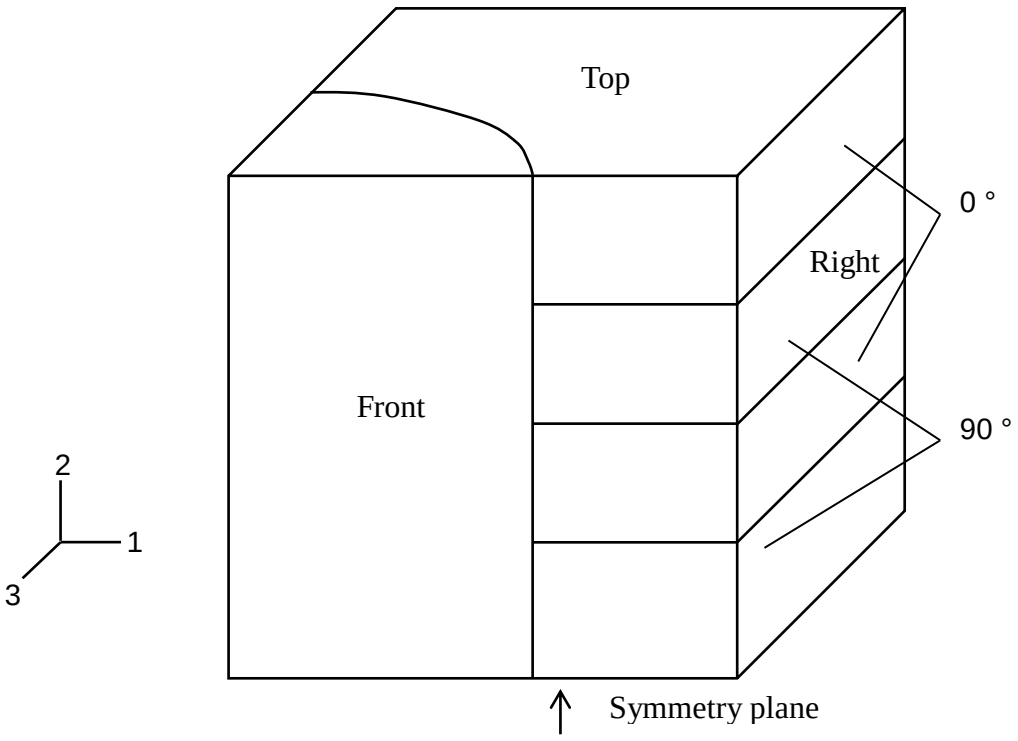

Fig.3.3 *Schematic 3D model of the protrusion layer*

The layered models have been assigned the unidirectional prepreg properties oriented in 1 or 3 directions. The metal region is assigned with Ti64 properties. The prepreg material properties are discussed in the materials characterisation section 3.2.2.

3.2.4.2 Three-dimensional protrusion layer properties model boundary conditions

The composite layer interfaces and the composite to metal interfaces have been assumed to have perfect bonding, because the analysis conducted is elastic (elastic material properties). The model has been loaded in 1, 2 and 3-directions separately with 0.1% strain.

The protrusion layer consists of protrusions and composite with certain volume fraction based on the protrusion distribution density. The analyses for the homogenised properties are based on assumption that the protrusion is perpendicular to the joint surface.

The surfaces in Fig.3.3 are loaded separately in 1, 2 and 3-directions respectively. The reaction forces were calculated for 1, 2 and 3-direction loadings respectively and based on which the engineering constants of the protrusion layer have been obtained, see Table.3.5.

Table.3.5 *The engineering constants of the protrusion layer*

E_1 [GPa]	E_2 [GPa]	E_3 [GPa]
65.18	24.53	65.17

ν_{12}	ν_{13}	ν_{21}	ν_{23}	ν_{31}	ν_{32}
0.30	0.080	0.11	0.11	0.080	0.30

As discussed before, the fibre axis of the 0 and 90 degrees UD prepreg lie in 1-direction and 3-direction respectively, and following the assumption of the protrusion layer, all protrusions are in 2-direction, therefore the protrusion layer is orthotropic. And again the orthotropic material stiffness matrix can be calculated for application in ABAQUS.

The stiffness matrix for orthotropic material properties was calculated for the protrusion layer and is shown in Table.3.6 [ABAQUS, 2005]

The stiffness matrix for the homogenised orthotropic material properties of the protrusion layer will be applied for the protrusion layer partitions of all the 2D global models.

Table.3.6 *The stiffness matrix for orthotropic material in ABAQUS*

D_{ijkl},								
1111	2222	3333	1122	1133	2233	1212	1313	2323
69.41	25.73	67.61	10.46	21.95	4.54	4.31	5.28	4.31

3.3 Two Dimensional Modelling methods

Geometries of the protrusion are shown in Fig.3.4. The definition of the protrusion angle and shape is also included. The hill shape protrusion with different angle was configured keeping the same volume fraction as the protrusion in the composite. The unit cell is then taken as the cross section of the configuration.

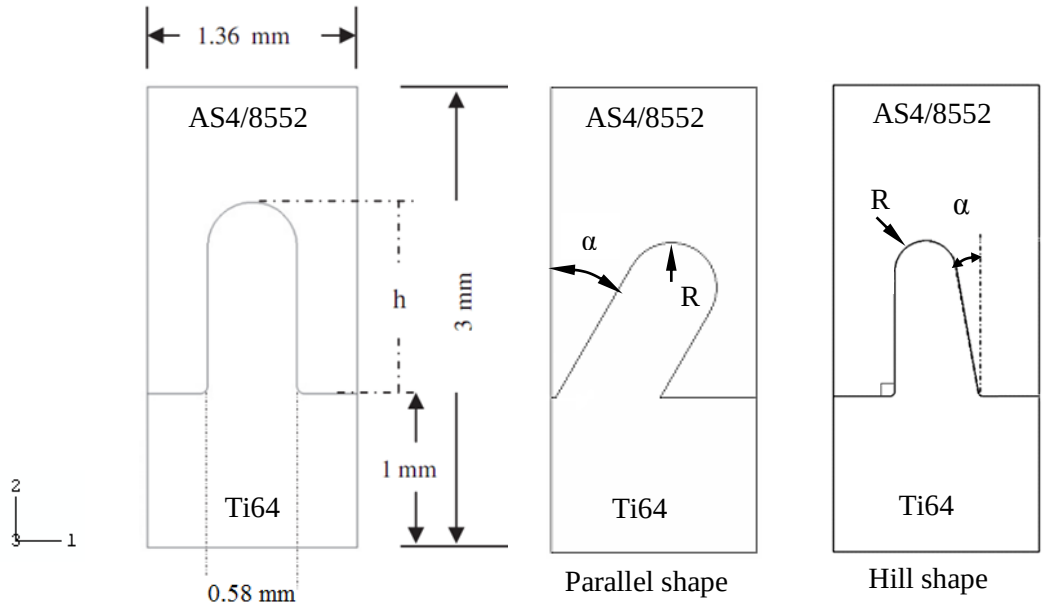

Fig.3.4 *Geometries of the unit cell models for different protrusion angle and shape*

The 2D modelling investigates the geometric parameters influence on the stress states locally around the individual protrusion. A large number of protrusions are located on

the metal surface with certain patterns (can be varied), therefore, there are two clear cases to be considered: repetitive protrusion in the middle of the joint step and the protrusion next to the step edges. The flow chart of the modelling scheme is shown in Fig.3.5. To investigate the protrusions on the joint step, two different cases were investigated, and they are the protrusions in the middle of the joint step and on the joint step edge. In this section, the two-dimensional global model was analysed, see section 3.3.1; and the finite element model methods are discussed in the cases of repetitive protrusions, see 3.3.2, and protrusions on the step edge, see 3.3.3. The results will be presented in Chapter 4. The elements used for the two dimensional analyses were plane strain quadrilateral element.

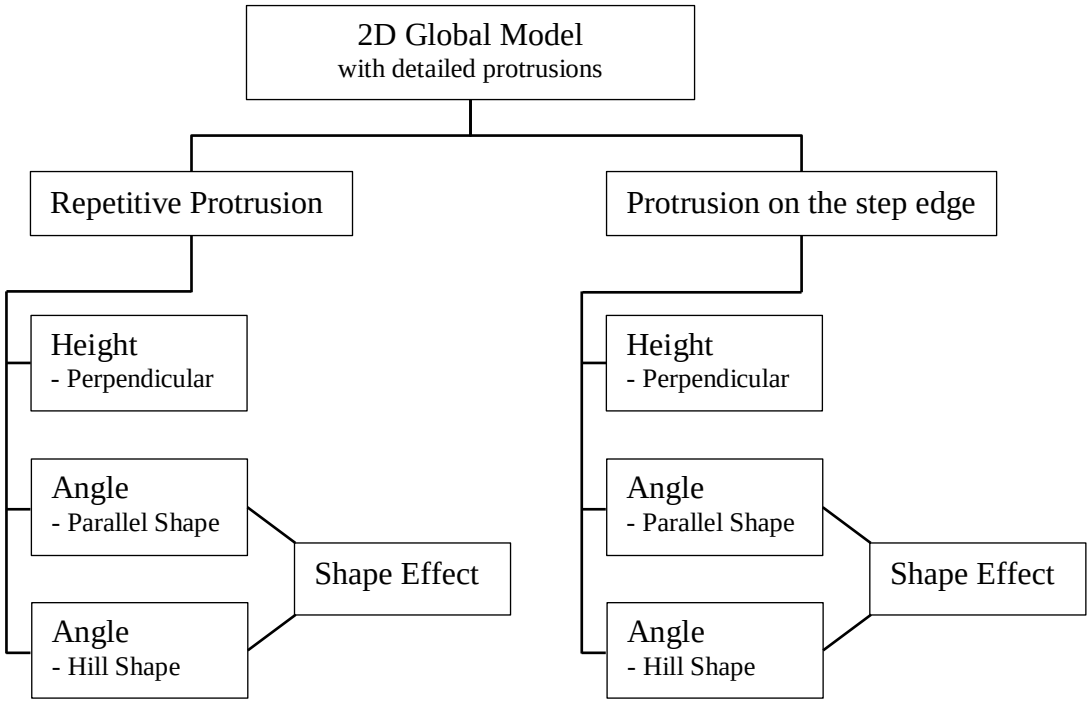

Fig.3.5 *Flow chart for two-dimensional analysis*

3.3.1 Two dimensional global model

Due to symmetry of double step joints, only half of the joint needs to be analysed. The schematic diagram for the global model with detailed protrusions is shown in Fig.3.6. The global model is 3 mm thick and 150 mm long, with 15 mm long and 1 mm deep steps. There are 11 protrusions on the steps. With dotted rectangles, the

positions of the repetitive protrusion (the seventh from the step edge) and protrusion on the joint step edge are marked. The number of elements used for the global model is around 280,000. Mesh density study was carried out with four times the number of elements. Identical results were obtained. The mesh density studies were also carried out for other models.

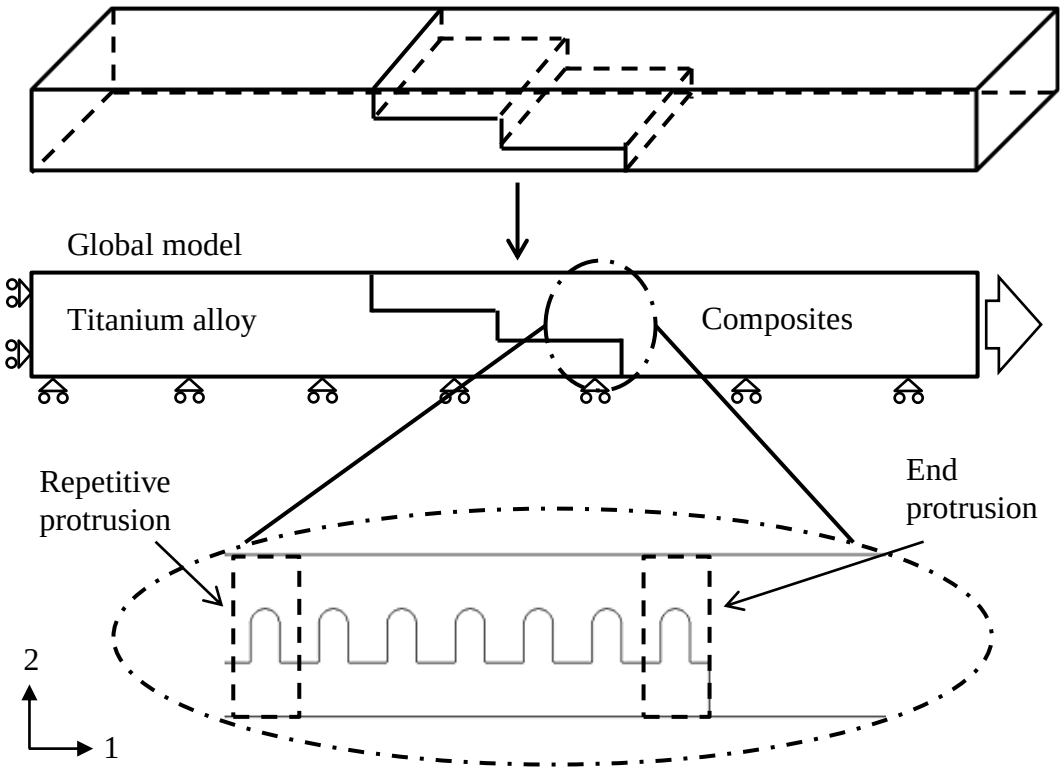

Fig.3.6 *Schematic diagram of the global model with detailed protrusions*

The global model was loaded with 1 MPa pressure on the right edge, and appropriate constraints were applied according to the symmetry, see Fig.3.6. The left edge of the global model was constrained in the axial direction and free to move in the through-thickness direction, and the bottom edge of the global model was constrained in the through the thickness direction and free to move in the axial direction.

3.3.2 Repetitive Protrusions

The 2D modelling investigates the geometric parameters influence on the stress states locally around the individual protrusion. Considering the large number protrusions

located on the metal surface with certain patterns, a repetitive cell as shown in Fig.3.7 can be used for the analysis. 2D models are based on the repetitive condition and include only one protrusion. These unit cell models are used to investigate the geometric parameters effects. In Fig.3.7, R represents the radius of the protrusion and h_p is the height of the protrusion; h_b is the height of the metal base which is 1mm; L is the width of the unit cell, 1.36 mm; H represents the unit cell height is taken to 3 mm; the protrusion angle is α. The material applied for the global models are titanium alloy, Ti64, and cross-ply prepreg composites, AS4/8552 (homogenised). For the angle effect, the protrusion height h_p was kept as 1 mm and the three dimensional volume of the protrusion was kept the same throughout the angle analysis. The number of elements used for the angle effect is around 8,000 and the number of elements used for the height effect is around 9,800.

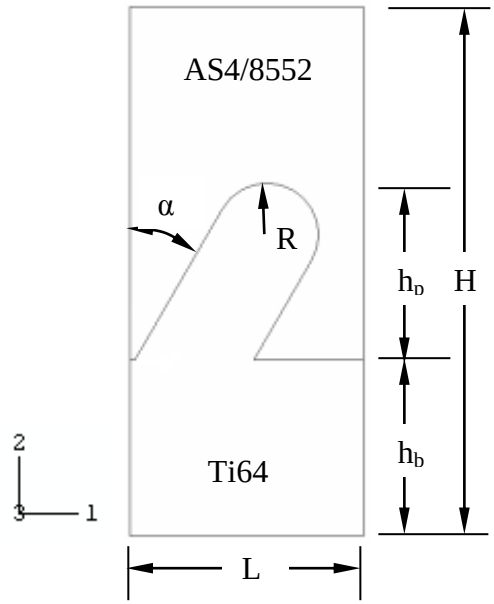

Fig.3.7 *Geometry of a unit cell model with protrusion*

By considering the symmetry of structure, the displacement and traction for both sides of the unit cell can be presented, as shown in Fig.3.7, as

$$u_1(L,x_2)-u_1(0,x_2)=U_0$$
$$u_2(L,x_2)-u_2(0,x_2)=0 \qquad \textbf{Eq.3.1}$$

and

$$t_1(L,x_2)+t_1(0,x_2)=0$$
$$t_2(L,x_2)+t_2(0,x_2)=0$$

Eq.3.2

where U_0 denotes the relative movement between these two sides as shown in Fig.3.8, which is constant. The boundary conditions on bottom are

$$u_2(x_1,0)=0$$
$$t_1(x_1,0)=0$$

Eq.3.3

and the top is free.

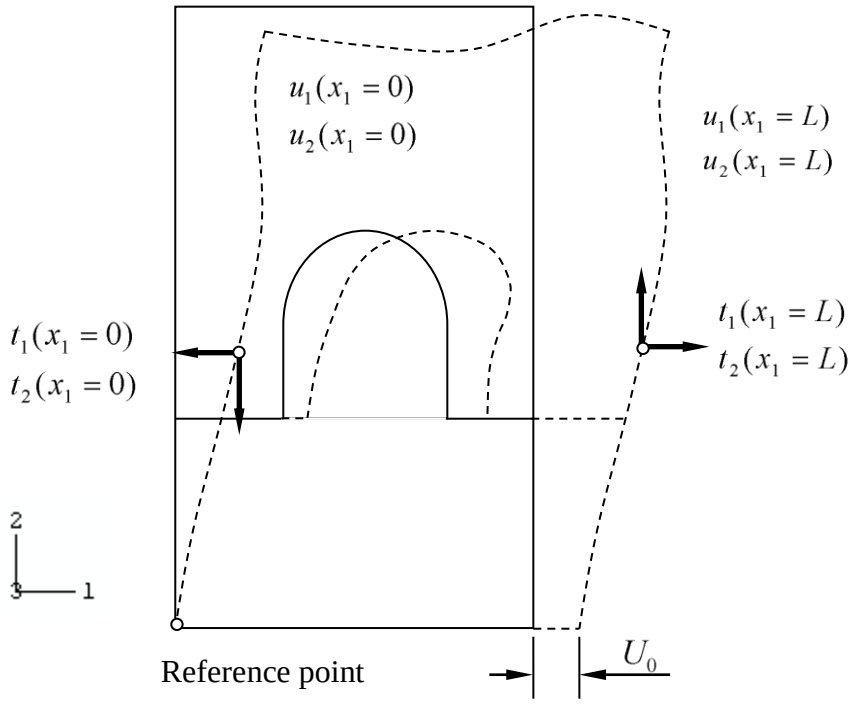

Fig.3.8 *Deformation and boundary conditions on the unit cell*

The constant U_0 should be determined by the equilibrium condition

$$U_0 = F_0 / \int_0^H t_1^*(L,y)dy$$

Eq.3.4

where F_0 is the applied force at the end and $t_1^*(L, y)$ is the traction distribution for a unit relative movement $U_0 = 1$.

The detailed study for the boundary conditions can be found in the published paper reproduced in Appendix A. The model was loaded with concentrated force on the right corner node, and the force was redistributed on the right edge equivalent to 1 MPa according to the repetitive symmetry.

Results of the composite region around the repetitive protrusion

The deformed shape of the perpendicular and angled protrusion for the unit cell model is shown in Fig.3.9.

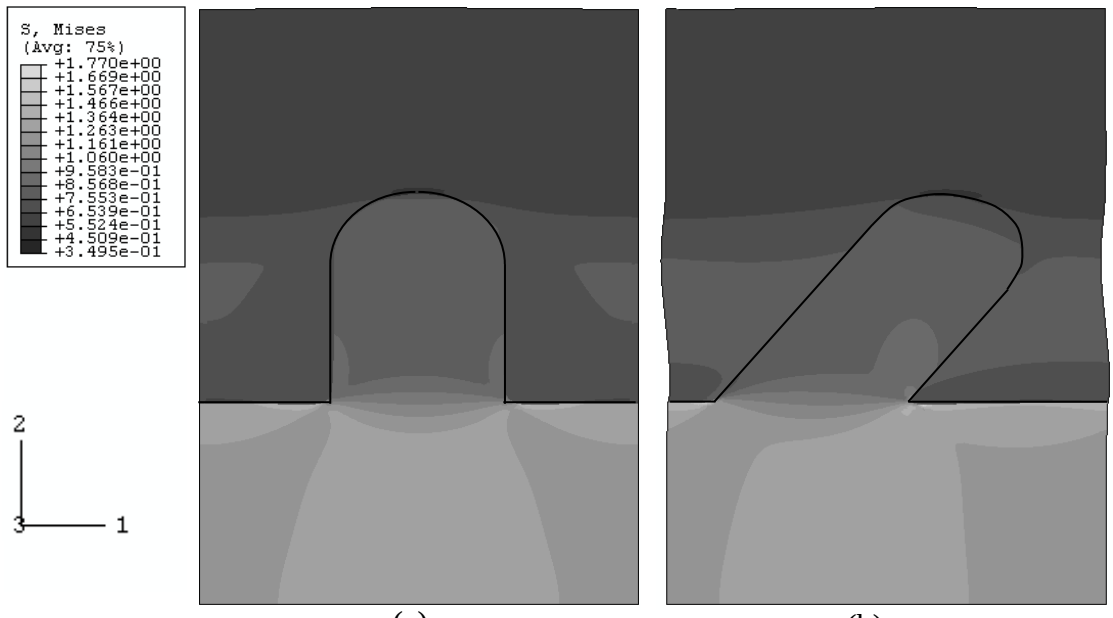

Fig.3.9 *Deformed shape with von Mises stress concentration contour results (a) perpendicular protrusion, and (b) 30 degree protrusion (the deformation scale factor is 20,000).*

The perpendicular protrusion unit cell model deforms symmetrically, while the 30 degree protrusion unit cell model deforms with repetitively curved side edges. The load applied is 1 MPa. However, the deformation in 1-direction of the 30 degree

protrusion unit cell model is very small (roughly 4% of the average deformation of the side in 1-direction), see Fig.3.9 (b). Therefore, the simplification that the 30 degree protrusion unit cell model side edges are straight may be applied under repetitive boundary conditions and tensile loading.

The stress concentrations of the protrusion region are compared with the global model result and shown in Fig.3.10, Fig.3.11 and Fig.3.12 for axial, peel and shear stress. The maximum stress concentrations are marked in the figures. The maximum stress concentrations are also listed in Table.3.7, Table.3.8 and Table.3.9. Stress distributions for all the stress components are similar for the global model and the unit cell model. Minus sign indicates compression for the peel stress and change of direction for shear stress.

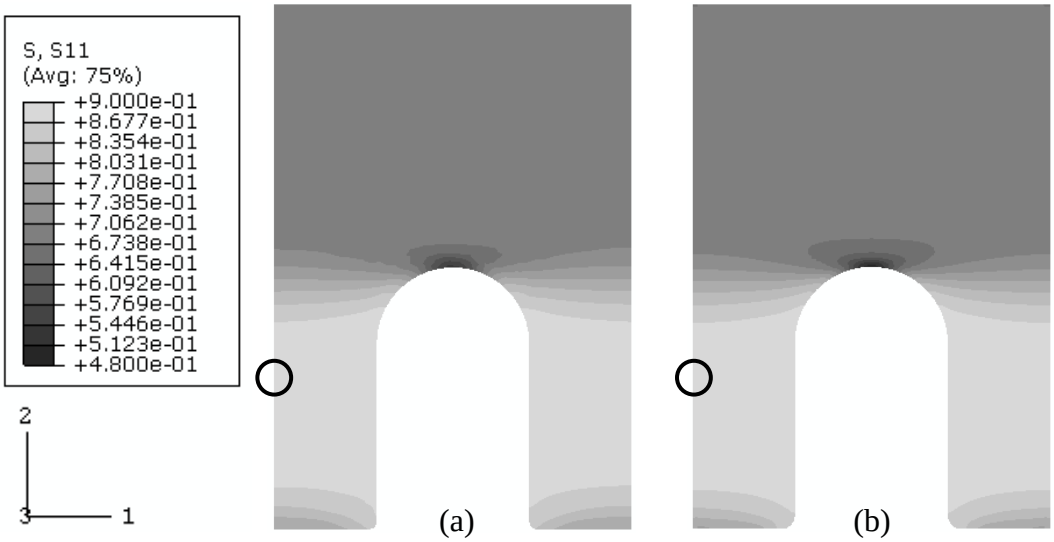

Fig.3.10 *Axial stress concentration contour results of the composite region for the global model with detailed geometries (a); unit cell model (b)*

Table.3.7 *Maximum concentration of axial stresses for the composite region*

	Global Model	Unit cell Model
σ_{11}/σ	8.95e-1	8.95e-1

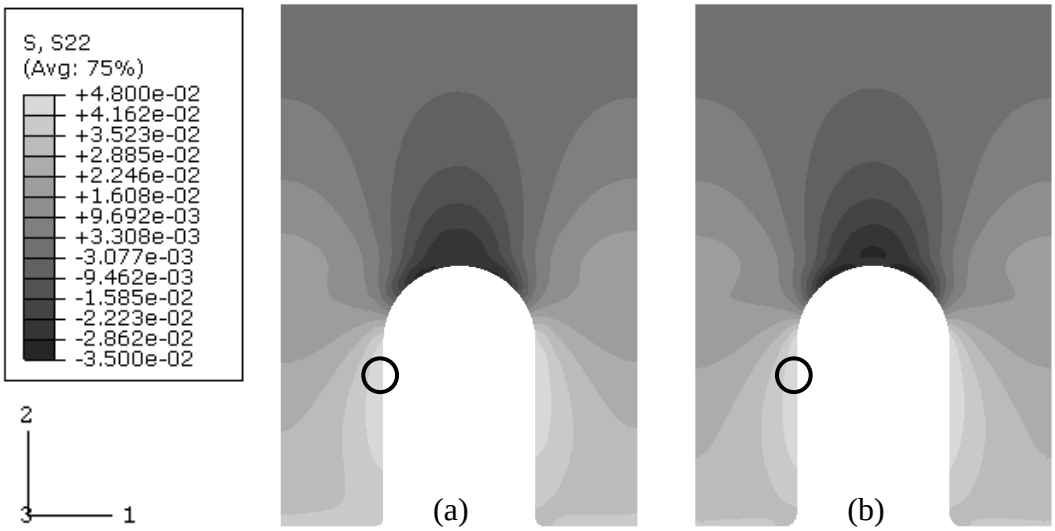

Fig.3.11 *Peel stress concentration contour results of the composite region for the global model with detailed geometries (a); unit cell model (b)*

Table.3.8 *Maximum concentration of peel stresses for the composite region*

	Global Model	Unit cell Model
σ_{22}/σ	4.66e-2	4.75e-2 (+1.9%)

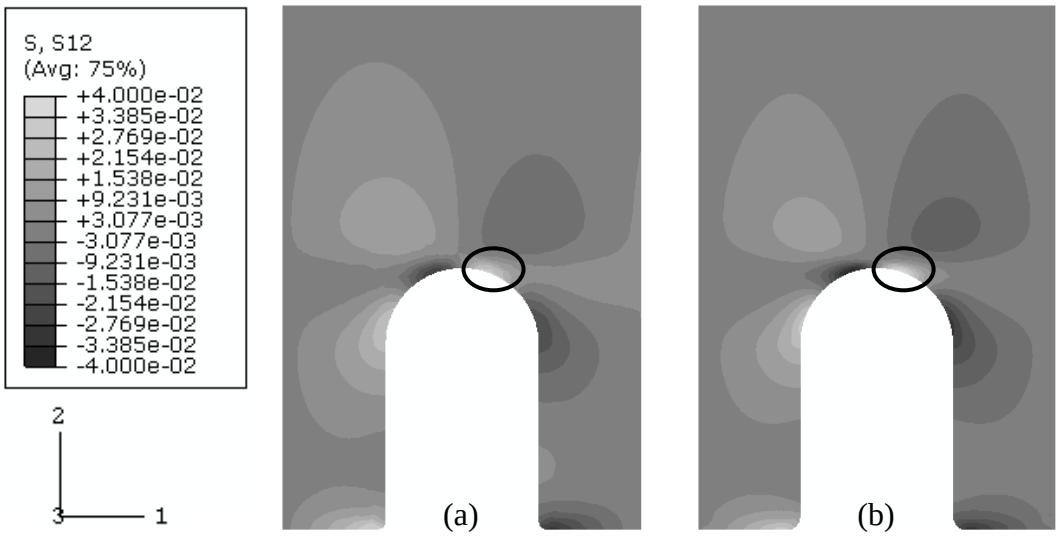

Fig.3.12 *Shear stress concentration contour results of the composite region for the global model with detailed geometries (a); unit cell model (b)*

Table.3.9 *Maximum concentration of shear stresses for composite region*

	Global Model	Unit cell Model
σ_{12}/σ	3.46e-2	3.97e-2 (+14.7%)

Stress distributions are almost symmetrical for the protrusion from the global model. Only in the case of shear stress, the stress distribution is slightly unsymmetrical. The values of the maximum stress concentrations are similar for the global and unit cell models, as well as the location of the maximum stress.

These results show that the unit cell model and the global model are in agreement for the repetitive protrusions.

3.3.3 Protrusions on the joint step edge

To study stress distribution around the end protrusion on the Comeld ™ joint first step edge, simply repetitive boundary conditions cannot be applied anymore. Therefore, new models need to be developed to study the end protrusion. The global model with detailed protrusions can be used as reference to check the new models. Several strategies were developed to study the end protrusion for the global tensile loading condition.

3.3.3.1 Perpendicular protrusions

For the perpendicular protrusion case, there are three strategies based on multiple protrusions and the unit cell models. They are listed and described below.

Strategy A

To recreate the correct local loading condition, two set of models are developed, shown in Fig.3.13 (a) and (b). Model 1 includes two protrusions with detailed geometry and composite with two units of protrusion unit cell model width. Model 2 includes one protrusion with detailed geometry, one unit cell model width region with homogenised protrusion properties and homogenised composite region with two units of protrusion width. The boundary conditions applied are the same for these two

models, which are shown in Fig.3.13 (a) and (b). The left edge of the entire model was constrained in 1-direction and free to move in 2-direction, this is to represent that repetitive boundary conditions resulting in straight side for the perpendicular protrusions; bottom edge, the symmetry line, was constrained with symmetry in 2-direction; the right edge of the entire model was loaded with uniform pressure of 1 MPa. The number of elements used is around 40,000.

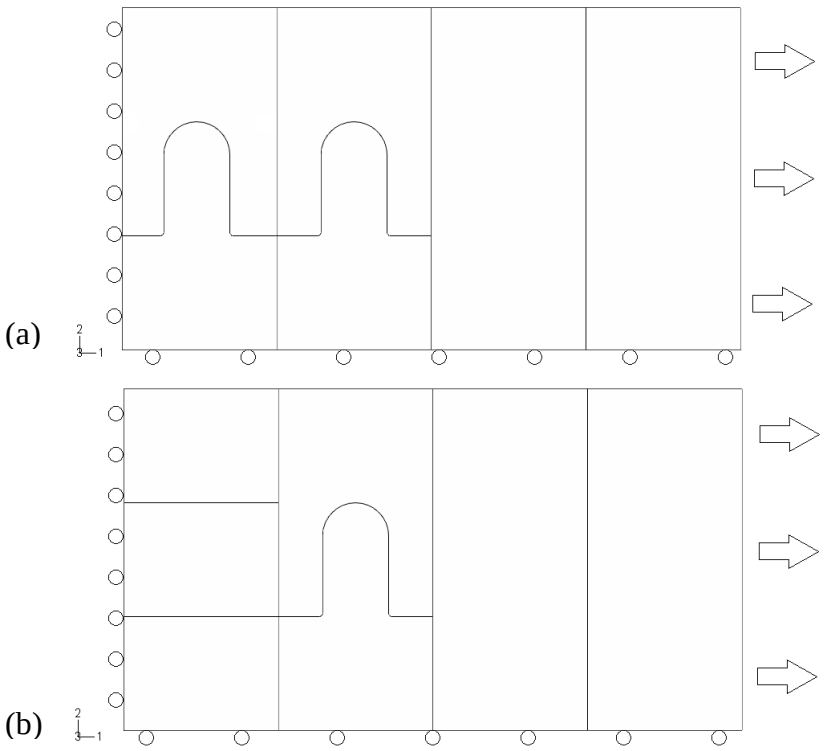

Fig.3.13 *Schematic illustration of Strategy A, Model 1 (a) and Model 2 (b)*

Strategy B

To simulate the end protrusion, a line of 6 protrusions is created, where the right hand side represents the edge of the step and left hand side represents the middle of the step, see Fig.3.14. This line of protrusions includes detailed protrusion geometries. The boundary conditions applied are, the left edge was constrained in 1-direction (similarly to Strategy A, for the representation of the repetitive boundary conditions), and free to move in 2-direction; bottom edge, the symmetry line, was constrained in 2-direction with symmetry. Load was applied on the right edge of the entire model.

The load applied was extracted from the global model as described in Appendix B. The number of elements used is around 60,000.

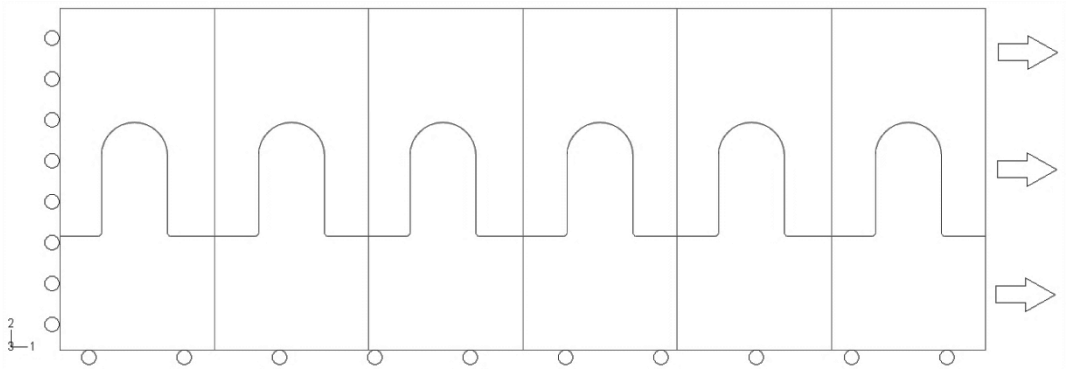

Fig.3.14 *Schematic illustration of Strategy B*

Strategy C

By applying different boundary conditions, a single unit cell model can be considered to study the end protrusion, see Fig.3.15. For the purpose of representing the end protrusion, the unit cell models from the repetitive simulations were used with repetitive boundary conditions on the left edge and extracted load from the global model as described above. The number of elements used is around 10,000.

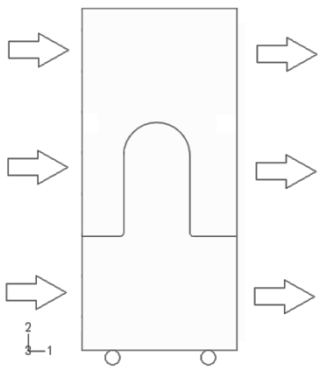

Fig.3.15 *Schematic illustration of Strategy C*

Results of the composite region around the end protrusion

The stress contour results are shown in Fig.3.16 to Fig.3.18 for the composite regions of the end protrusion in various strategies. The locations of the maximum stresses are marked with circle on each of the contour results. The maximum values are listed in

Table.3.10 to Table.3.15. For peel and shear stresses, minus values indicate change in stress direction.

For the composite region of the end protrusion, stress components for the axial, peel and shear stress are compared. Specific regions were selected at different areas of stress concentration to examine the modelling strategies in detail.

Fig.3.16 shows the axial stress contour results of different strategies. With the same scale, stress distributions are similar to the global model end protrusion except Strategy C, Fig.3.16 (e). Four regions from the global model result were chosen to compare the local stress concentration, see Fig.3.16 (a). The stress values for the different regions are listed in Table.3.10. The maximum stress values are in different regions for different strategies. In region I, II and III, all strategies show good agreement with the global model in terms of location and value of the stress concentration; the difference is less than 5%. For region IV, all strategies show more than 5% differences compared with the global model. This may be caused by the interface; load is transferred from right hand side into the joining system, therefore, different boundary conditions will result in different stress concentration. That is most obvious at this location.

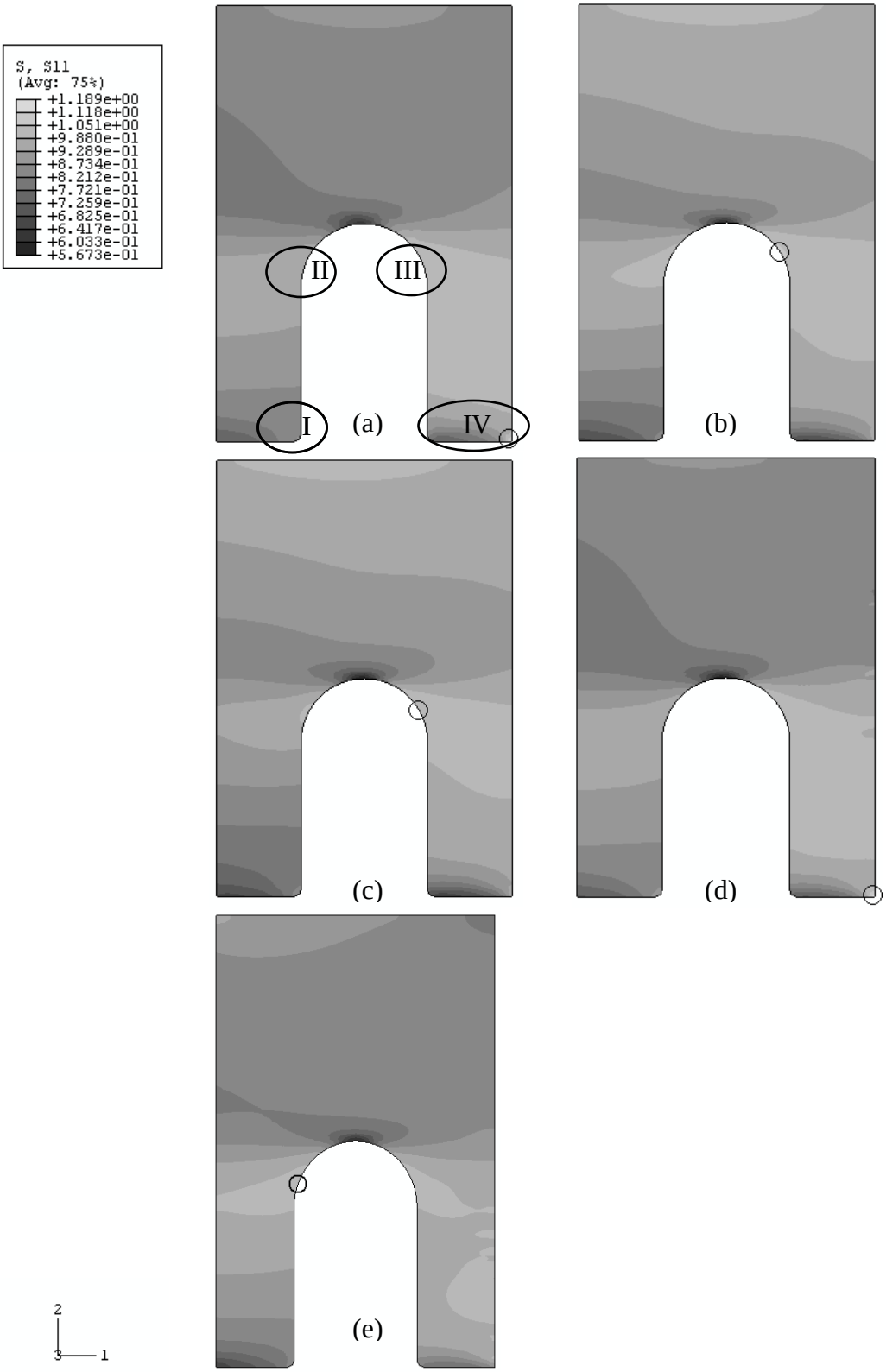

Fig.3.16 *Axial stress concentration contour results of the top of protrusion region for the global model with detailed geometries (a); Strategy A Model 1 (b); Strategy A Model 2 (c); Strategy B (d); Strategy C (e).*

Table.3.10 *Maximum concentration of axial stresses for the top of protrusion region of various models*

	Global Model	Strategy A Model 1	Strategy A Model 2	Strategy B	Strategy C
σ_{11}/σ Zone I	0.876	0.836 (-4.6%)	0.839 (-4.2%)	0.893 (+1.9%)	0.835 (-4.7%)
σ_{11}/σ Zone II	0.984	1.014 (+3.0%)	0.999 (+1.5%)	0.988 (+0.4%)	1.012 (+2.8%)
σ_{11}/σ Zone III	1.027	1.057 (+2.9%)	1.048 (+2.0%)	1.026 (-0.1%)	1.010 (-1.7%)
σ_{11}/σ Zone IV	1.130	0.962 (-14.9%)	0.962 (-14.9%)	1.189 (+5.2%)	1.002 (-11.3%)

For peel stress, the stress distributions appear to be similar for Fig.3.17 (a), (b), (c) and (d), but the locations of the maximum stress values differed. Similarly, two stress concentration regions from the global model were selected and compared, see Fig.3.17 (a). The maximum values of the peel stress concentration for the selected regions are listed in Table.3.11. Strategy C shows different stress distribution to the global model, and also shows large difference in stress concentration, more than 50%, for Zone I, and little difference, less than 2%, for Zone II. This suggests Strategy C is not stable or not accurate for the peel stress to represent the end protrusion in the global model. Strategy A Model 2 displays large difference in Zone II, 35.7%, indicating this model is not accurate or stable for representing the global model end protrusion. Around the top of the protrusion, the maximum stress is in compression and therefore is considered not important for the failure process.

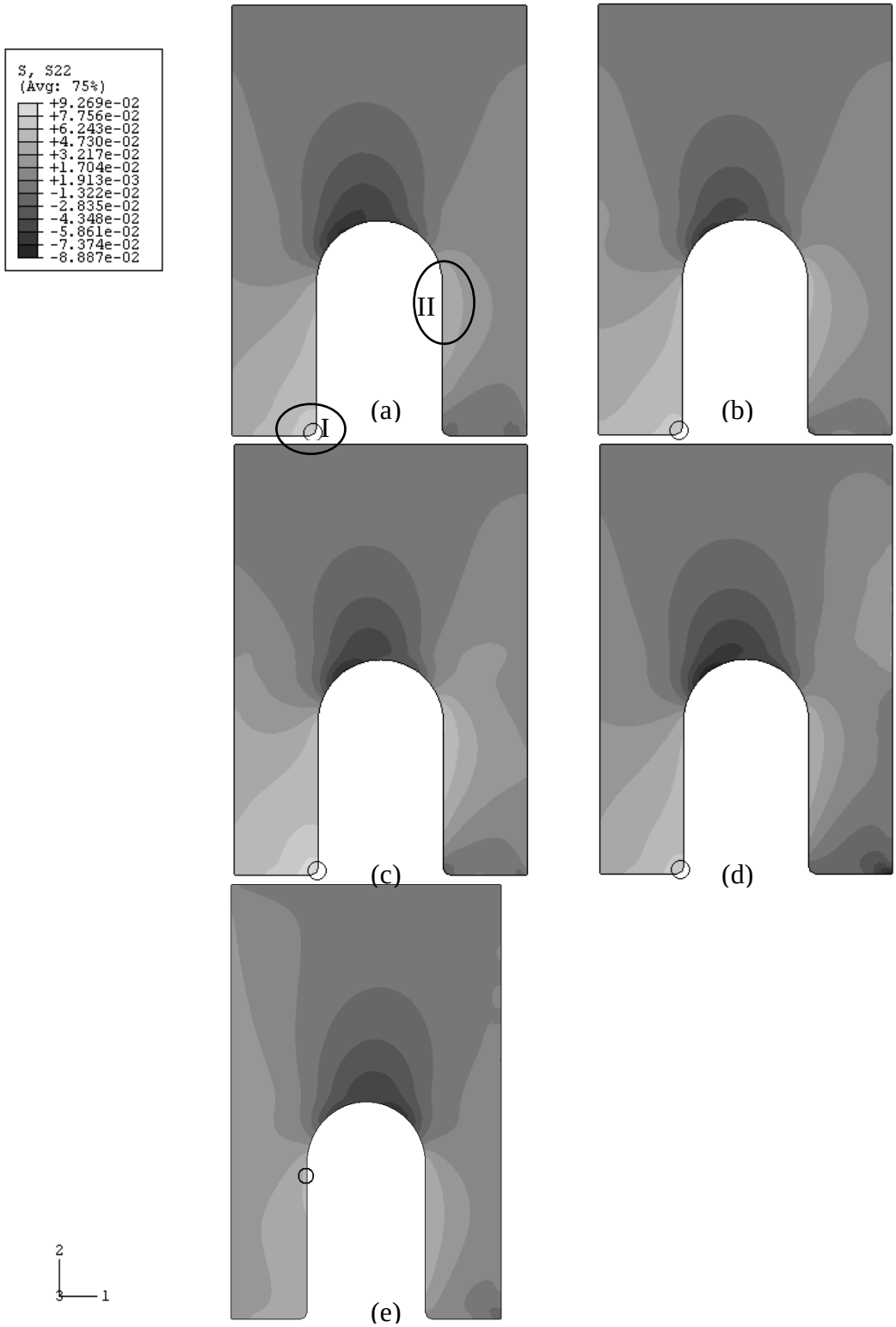

Fig.3.17 *Peel stress concentration contour results of the top of protrusion region for the global model with detailed geometries (a); Strategy A Model 1 (b); Strategy A Model 2 (c); Strategy B (d); Strategy C (e).*

Table.3.11 *Maximum concentration of peel stresses for the top of protrusion region of various models*

	Global Model	Strategy A Model 1	Strategy A Model 2	Strategy B	Strategy C
σ_{22}/σ Zone I	8.023e-2	7.625e-2 (-4.9%)	9.269e-2 (+15.5%)	7.581e-2 (-5.5%)	3.956e-2 (-50.7%)
σ_{22}/σ Zone II	4.788e-2	5.296e-2 (+10.6%)	6.496e-2 (+35.7%)	4.764e-2 (-0.5%)	4.709e-2 (-1.6%)

For shear stress, shown in Fig.3.18, location of the maximum stress values and stress distributions are similar to each other, however they are different compared to the global model end protrusion. Four regions from the global model were selected, see Fig.3.18 (a). The maximum values of the shear stress for these regions are listed in Table.3.12. For Strategy A Model 2, Fig.3.18 (c), the maximum values difference for the four regions can be as high as 37.3%. Strategy A Model 1 and Strategy B results show less difference in these regions, 12.7% and 9.3% respectively. The comparison of results for the different zones is shown in Fig.3.19.

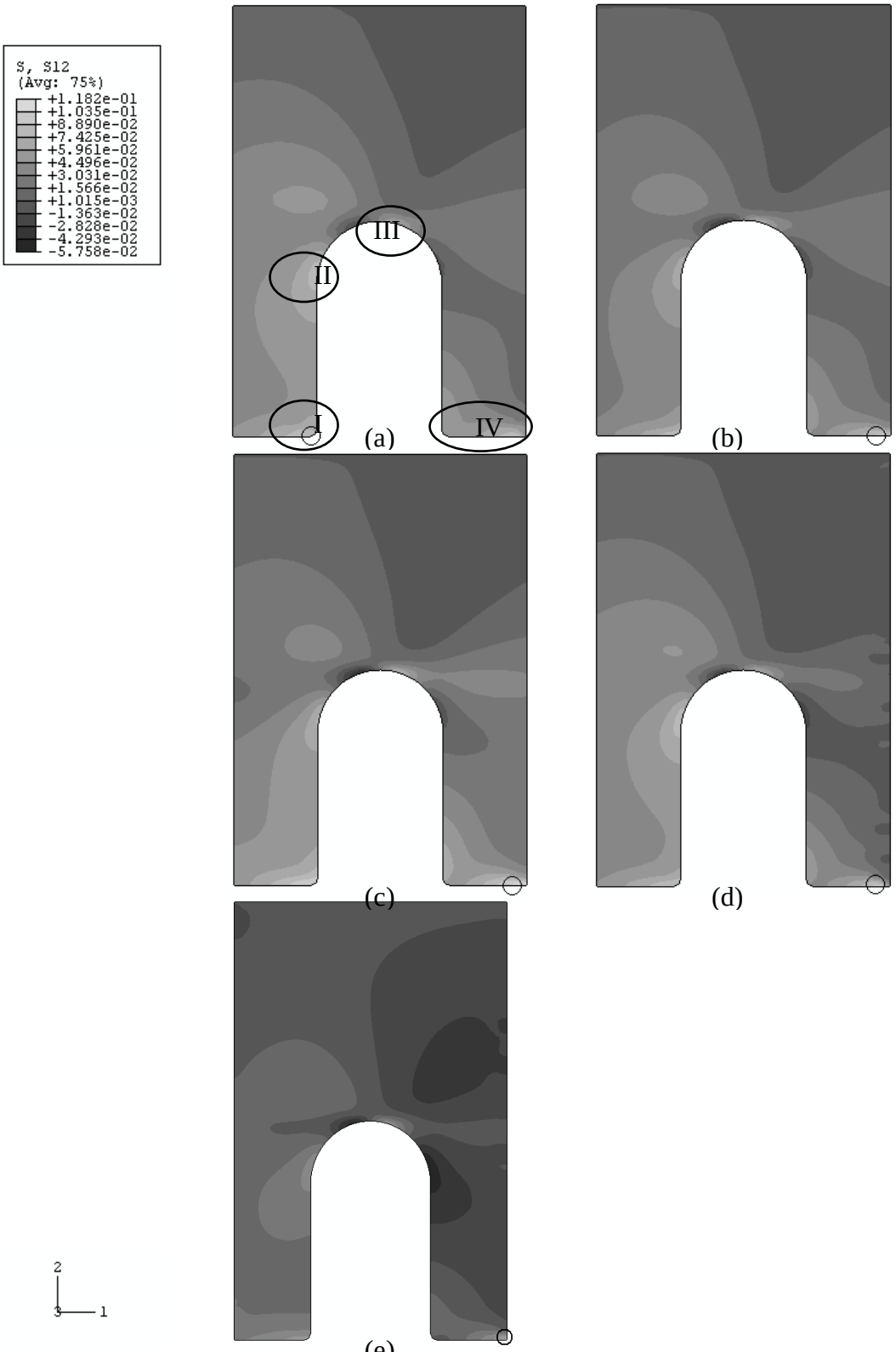

Fig.3.18 *Shear stress concentration contour results of the top of protrusion region for the global model with detailed geometries (a); Strategy A Model 1 (b); Strategy A Model 2 (c); Strategy B (d); Strategy C (e).*

Table.3.12 *Maximum concentration of shear stresses for the top of protrusion region of various models*

	Global Model	Strategy A Model 1	Strategy A Model 2	Strategy B	Strategy C
σ_{12}/σ Zone I	8.739e-2	8.225e-2 (-5.9%)	1.051e-1 (+20.3%)	8.919e-2 (+2.1%)	5.307e-2 (-39.3%)
σ_{12}/σ Zone II	8.423e-2	7.283e-2 (-13.5%)	7.748e-2 (-8.0%)	8.720e-2 (+3.5%)	4.170e-2 (-50.5%)
σ_{12}/σ Zone III	6.033e-2	7.039e-2 (+16.7%)	7.560e-2 (+25.3%)	6.819e-2 (+13.0%)	4.229e-2 (-29.9%)
σ_{12}/σ Zone IV	8.606e-2	9.869e-2 (+14.7%)	1.182e-1 (+37.3%)	1.019e-1 (+18.4%)	6.680e-2 (-22.4%)

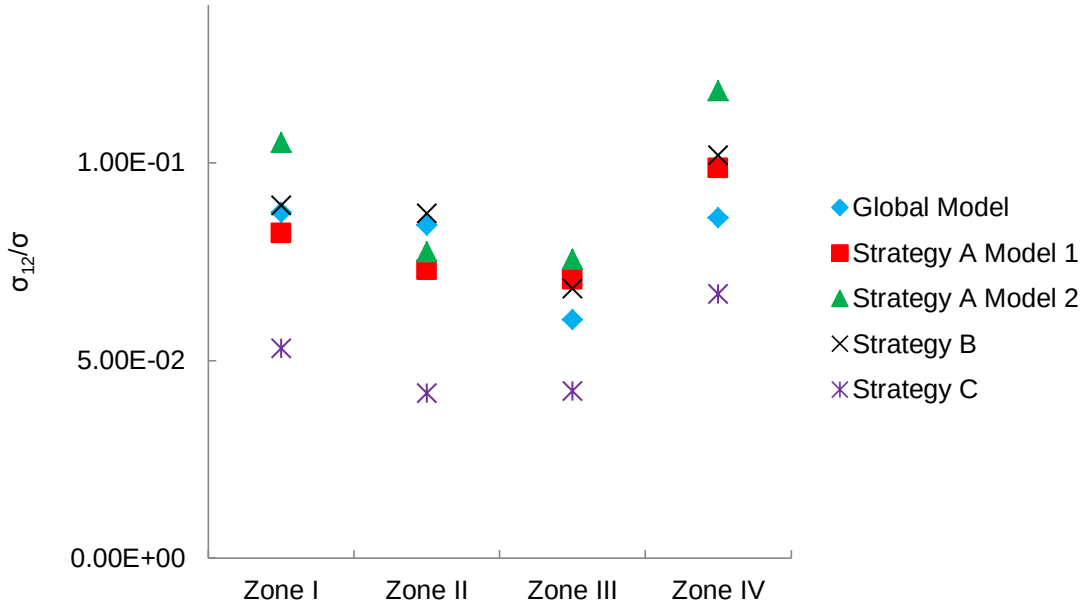

Fig.3.19 *Shear stress concentration contour results comparisons for the marked zones.*

The stress concentration results show that for the perpendicular protrusions, Strategy C is not suitable to represent the end protrusion from the global model; Strategy A Model 1 seems to be the best strategy to simulate the perpendicular end protrusion behaviour of the joint under tension. The consideration is whether this strategy is also the best to simulate angled end protrusions.

3.3.3.2 Protrusions at 30 degrees against the loading direction

Due to the poor results presented by Strategy C, it is abandoned for further analysis. Only Strategy A and B are studied in this part. Similarly to the perpendicular case, global model with detailed 30 degree protrusions was created and analysed as before.

Strategy A

To recreate the correct local loading condition, two set of models are developed similar to models shown in Fig.3.13 (a) and (b), but with 30 degree protrusion. Model 1 includes two protrusions with detailed geometry and composite with two units of protrusion width. Model 2 includes one protrusion with detailed geometry, one unit width region with homogenised protrusion region and two units of protrusion width homogenised composite. The boundary conditions applied are the same for these two models. The left edge of the entire model was constrained in 1-direction; bottom edge, the symmetry line, was constrained with symmetry in 2-direction; the right edge of the entire model was loaded with uniform pressure of 1 MPa.

Strategy B

A line of 6 protrusions at 30 degrees is created, where the right hand side represents the edge of the step and left hand side represents the middle of the step, similar to Fig.3.14. This line of protrusions includes detailed protrusion geometries. The boundary conditions applied are, the left edge was constrained in 1-direction; bottom edge, the symmetry line, was constrained in 2-direction with symmetry. Load was applied on the right edge of the entire model. The load applied was extracted from the global model as described in Appendix B.

Results of the composite region around the end protrusion

The stress concentration contour results are shown in Fig.3.20 to Fig.3.22 for the composite region around top of the protrusion. The locations of the maximum stresses are marked with circle on each of the contour results. The maximum values are listed

in Table.3.13 to Table.3.15. For peel and shear stresses, minus values indicate change in stress direction.

For the composite region of the end protrusion at 30 degrees, similarly, stress components for the axial, peel and shear stress are compared. Specific regions were selected from the stress concentrations in the global model. These comparisons were used to examine the modelling strategies further.

Fig.3.20 shows the axial stress contour results of different strategies. Stress distributions are similar to the global model end protrusion. Four regions from the global model result were chosen to compare the local stress concentration, see Fig.3.20 (a). The stress values for different region are listed in Table.3.13. The maximum stress values locate in different regions for different strategies. In region I, II and III, all strategies show good agreement with the global model in terms of location and value of the stress concentration; the difference is less than 4%. For region IV, all strategies show more than 9% differences compared with the global model. Again, this may be caused by the interface; load is transferred from right hand side into the joining system, therefore, different boundary conditions will result in different stress concentration which is most obvious at this location.

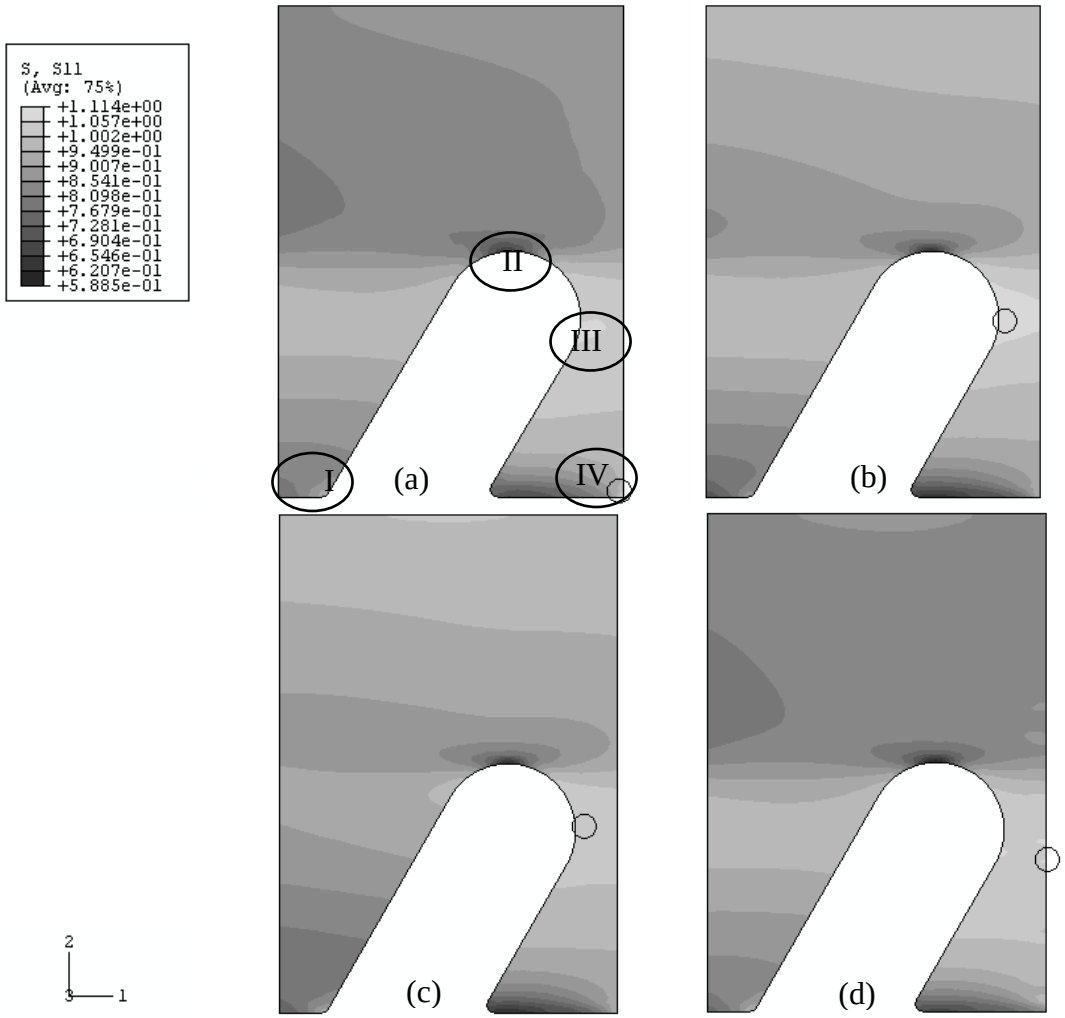

Fig.3.20 *Axial stress concentration contour results of the top of protrusion region for the global model with detailed geometries (a); Strategy A Model 1 (b); Strategy A Model 2 (c); Strategy B (d).*

Table.3.13 *Maximum concentration of axial stresses for the top of protrusion region of various models*

	Global Model	Strategy A Model 1	Strategy A Model 2	Strategy B
σ_{11}/σ Zone I	9.292e-1	8.957e-1 (-3.6%)	9.292e-1 (0%)	9.526e-1 (+2.5%)
σ_{11}/σ Zone II	9.709e-1	9.972e-1 (+2.7%)	9.757e-1 (+0.5%)	9.729e-1 (+0.2%)
σ_{11}/σ Zone III	1.060	1.067 (+0.7%)	1.053 (-0.7%)	1.058 (-0.2%)
σ_{11}/σ Zone IV	1.114	9.579e-1 (-14.0%)	9.701e-1 (-12.9%)	1.007 (-9.6%)

For peel stress, see Fig.3.21, the stress distributions appear to be similar as well as the locations of the maximum stress values. Similarly, two regions from the global model were selected, see Fig.3.21 (a). The maximum values of the peel stress for the selected regions are listed in Table.3.14. Strategy A Model 2 shows a big difference in Zone I and II, about 15%, indicating this model is not accurate or stable for representing the global model end protrusion. Strategy A Model 1 shows smaller variation with the global model results for Zone I and a slight bigger difference in Zone II, 12.6%. Strategy B shows similar results in Zone I and II compared to the global model.

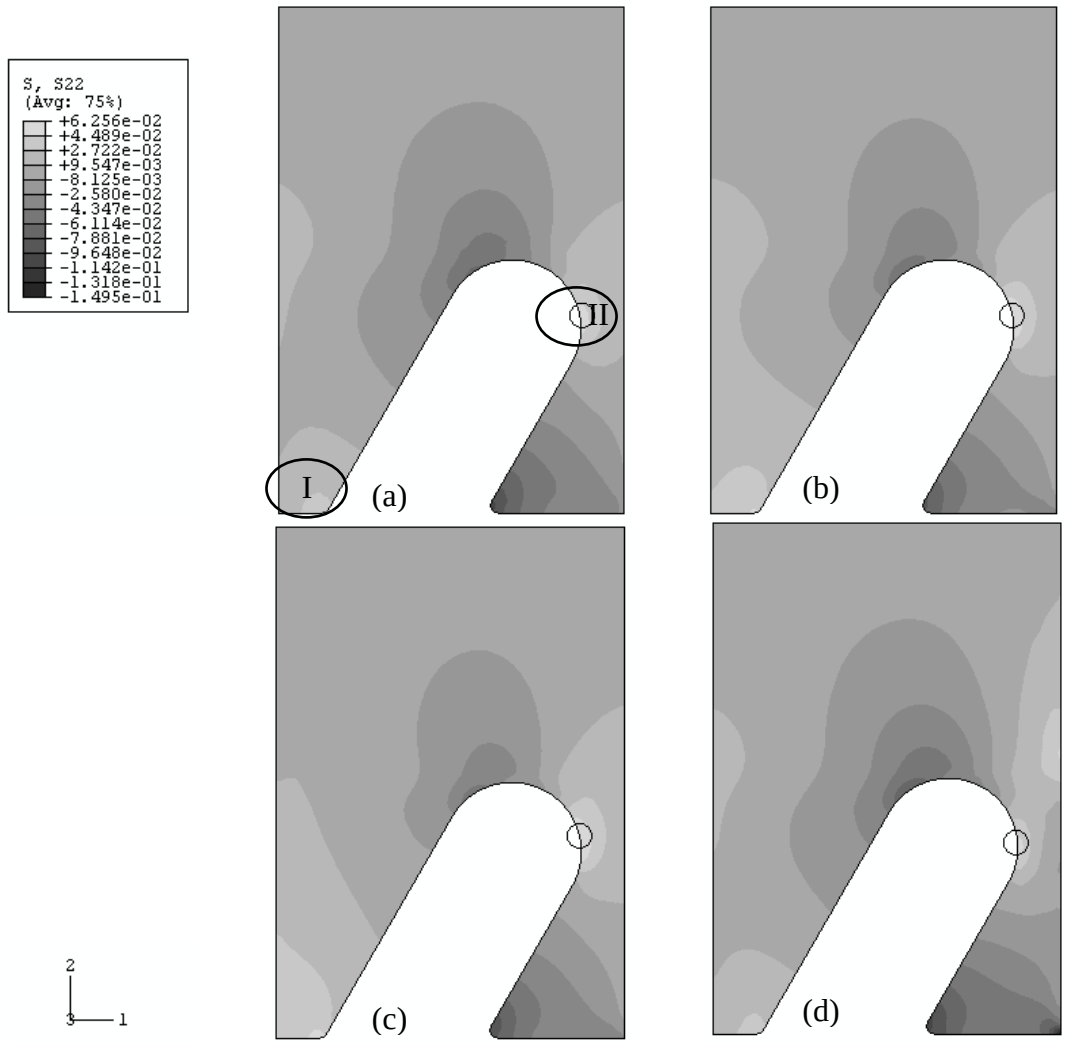

Fig.3.21 *Peel stress concentration contour results of the top of protrusion region for the global model with detailed geometries (a); Strategy A Model 1 (b); Strategy A Model 2 (c); Strategy B (d).*

Table.3.14 *Maximum concentration of peel stresses for the top of protrusion region of various models*

	Global Model	Strategy A Model 1	Strategy A Model 2	Strategy B
σ_{22}/σ Zone I	4.265e-2	4.601e-2 (+7.9%)	4.908e-2 (+15.1%)	3.990e-2 (-6.4%)
σ_{22}/σ Zone II	5.423e-2	6.108e-2 (+12.6%)	6.256e-2 (+15.4%)	5.379e-2 (-0.8%)

For shear stress, shown in Fig.3.22, location of the maximum stress values vary, but the stress distributions are similar to the global model end protrusion. Four regions from the global model were selected, see Fig.3.22 (a). The maximum values of the shear stress for these regions are listed in Table.3.15. For Strategy A Model 1, Fig.3.22 (b), the maximum values difference for the four regions varies from -1.2 and -2.2% in Zone I and III, 17.5% in Zone IV, to 30% in Zone II. Strategy A Model 2 shows higher maximum values in these zones, with more than 10% in Zone I II and IV, 3.6% in Zone III. Strategy B shows smaller variations for Zone I and IV, 7.5% and 0.5%, and large variations for Zone II and III, 12.4% and 45.5.%. The comparisons of results for different zones are shown in Fig.3.23.

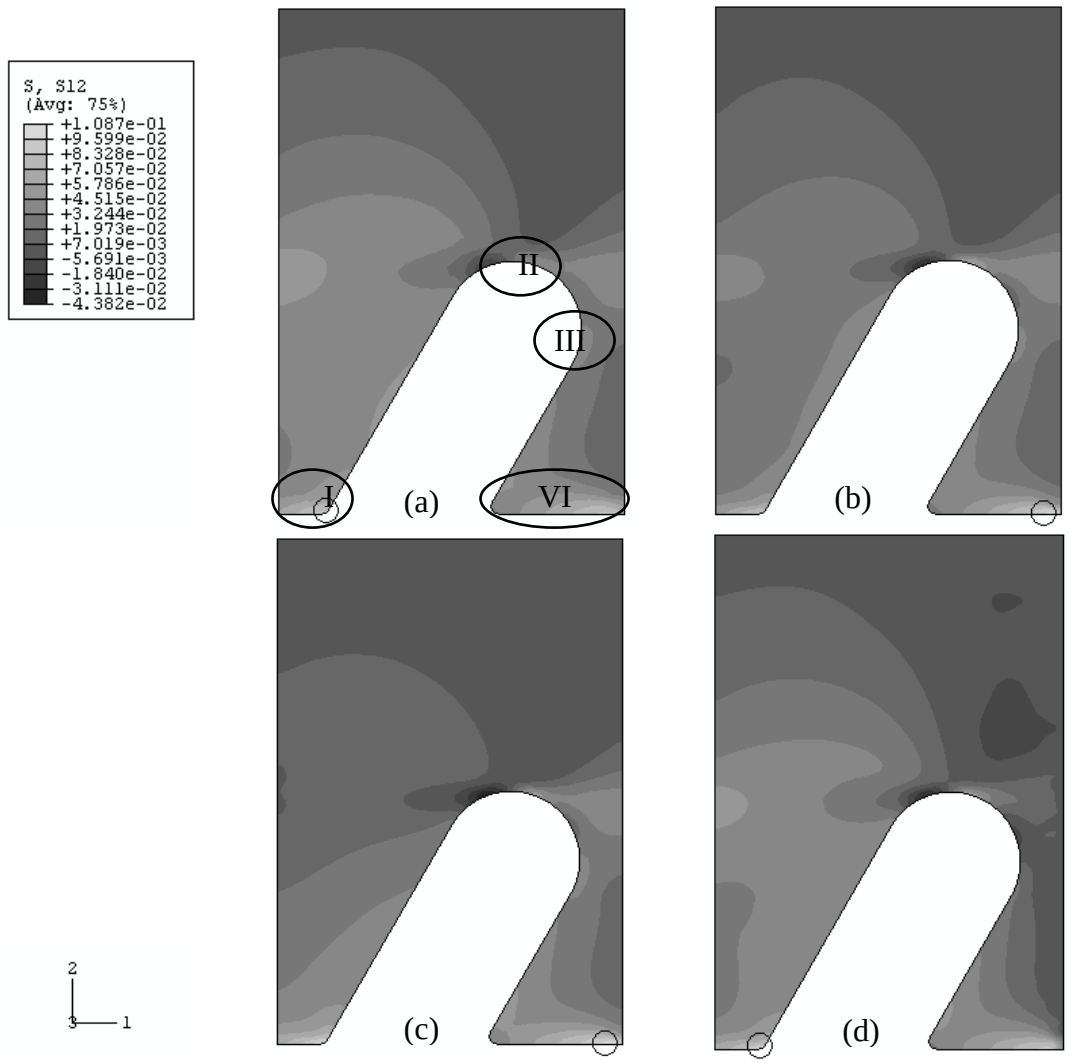

Fig.3.22 *Shear stress concentration contour results of the top of protrusion region for the global model with detailed geometries (a); Strategy A Model 1 (b); Strategy A Model 2 (c); Strategy B (d).*

Table.3.15 *Maximum concentration of shear stresses for the top of protrusion region of various models*

	Global Model	Strategy A Model 1	Strategy A Model 2	Strategy B
σ_{12}/σ Zone I	8.852e-2	8.657e-2 (-2.2%)	9.956e-2 (+12.5%)	9.517e-2 (+7.5%)
σ_{12}/σ Zone II	4.853e-2	6.310e-2 (+30.0%)	5.408e-2 (+11.4%)	5.453e-2 (+12.4%)
σ_{12}/σ Zone III	4.166e-2	4.118e-2 (-1.2%)	4.316e-2 (+3.6%)	2.272e-2 (-45.5%)
σ_{12}/σ Zone IV	8.833e-2	1.038e-1 (+17.5%)	1.087e-1 (+23.1%)	8.790e-2 (-0.5%)

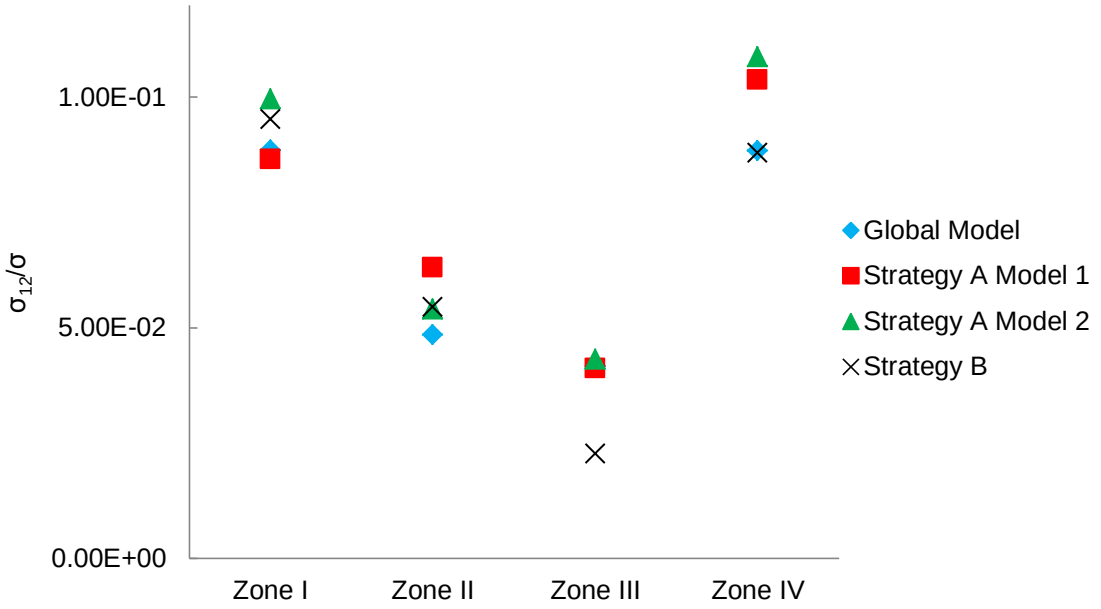

Fig.3.23 *Shear stress concentration contour results comparisons for the marked zones.*

The stress concentration results show that Strategy B is not suitable to represent the end protrusion from the global model; Strategy A Model 1 seems to be the best strategy to simulate the 30 degree end protrusion behaviour of the joint under tension.

Stress profiles of both edges of the end protrusion

To gather further proof for the strategy selection, the stress concentration profile are taken from top to the bottom of the protrusion models (left and right edges). For the axial stress, all strategies shows resonably good agreement with the global model results. However, for the peel and shear stress profiles, the stress concentration profiles shows difference between the strategies.

Peel stress concentration on both sides are examined in Fig.3.24 and Fig.3.25. On the left side, before the joint step except for Strategy A Model 2, all other strategies were close to the global model result. When it reached the titanium alloy region, stress for Strategy A models have similar shapes compare with the global model, but show higher concentrations, whereas Strategy B shows lower concentrations with a similar shape. Strategy A Model 2 displays a very different stress concentration on the left

side of the model. This is considered due to the homogenised composite region for simplification.

On the right side, Strategy A models show a reasonable agreement with the global model, whereas Strategy B shows much more variations, see Fig.3.24. These are considered to be caused by the loading on the right side of the model.

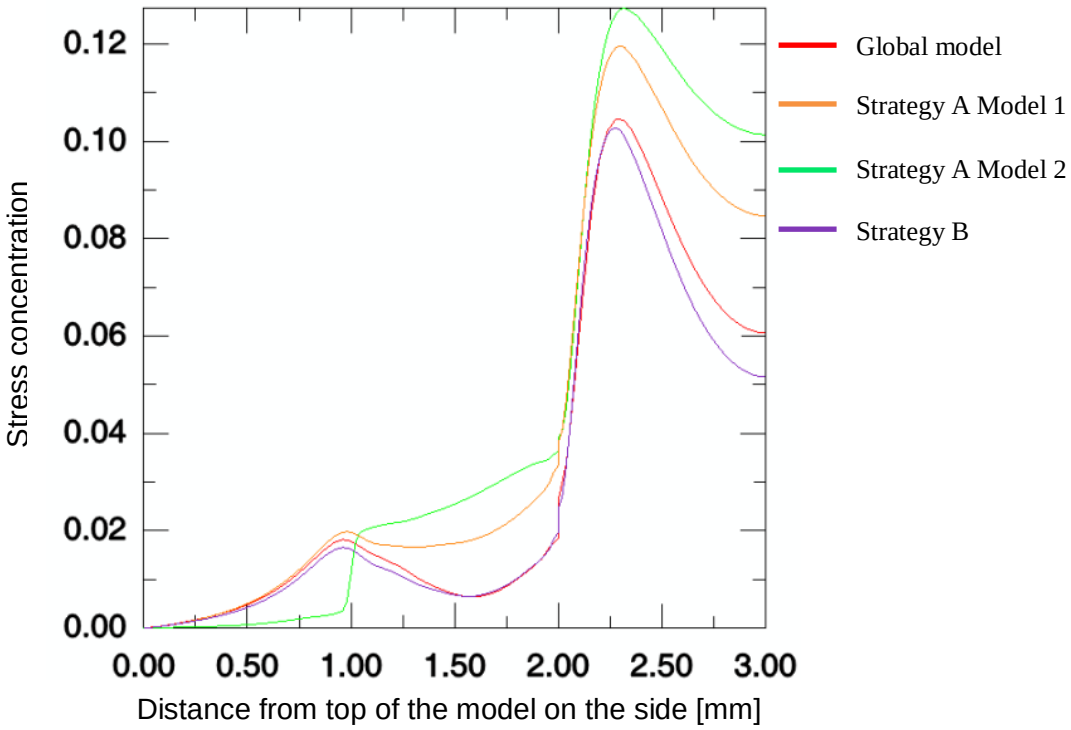

Fig.3.24 *Peel stress concentration on the left side of the end protrusion at 30 degrees for the global model and all the strategies.*

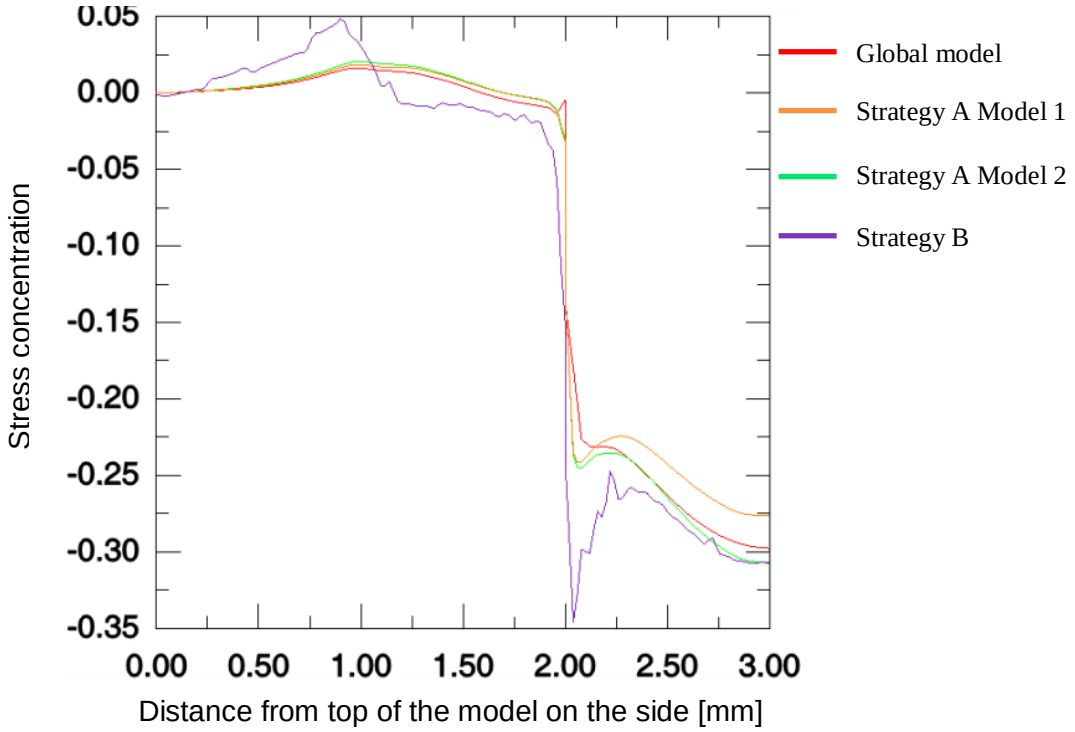

Fig.3.25 *Peel stress concentration on the right side of the end protrusion at 30 degrees for the global model and all the strategies.*

Shear stress concentration on both left and right side is shown in Fig.3.26 and Fig.3.27. On the left side, Strategy A Model 2 shows a different response to the load. Strategy B shows a very close results with the global model end protrusion, and Strategy A Model 1 shows a very good agreement with slightly lower concentrations than the global model end protrusion.

On the right side, Strategy B shows a very different stress profile compare with the global model results. Strategy A models show very good agreement with the global model, where the maximum concentration at around 2 mm are both higher than the global model results.

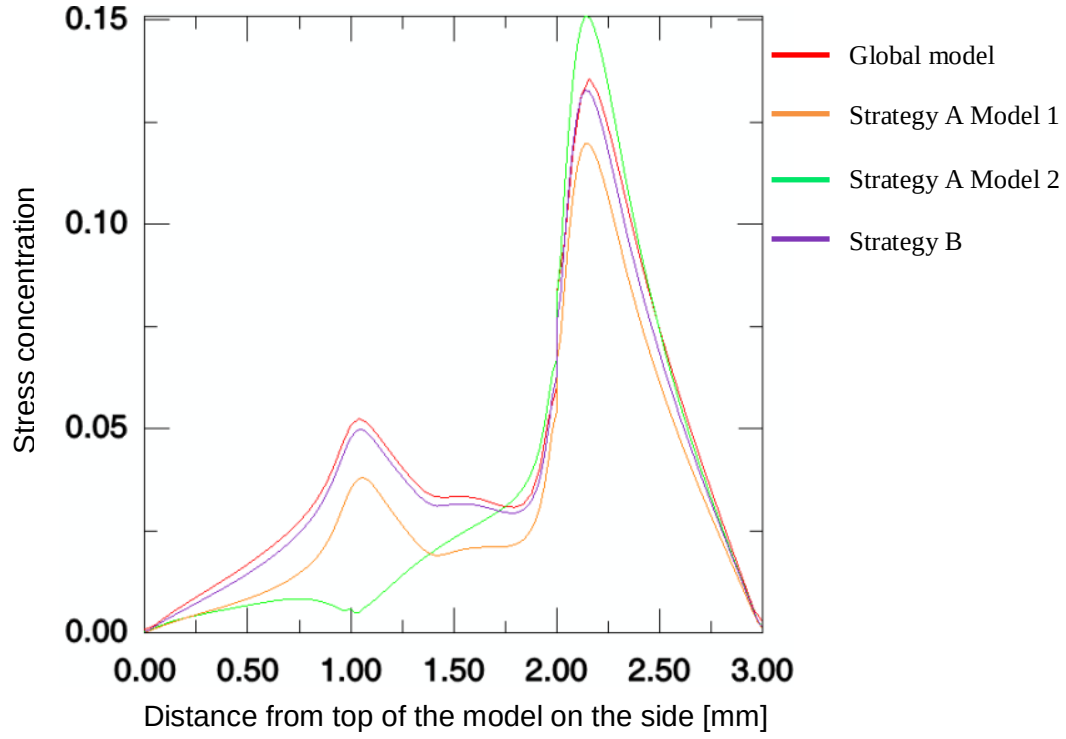

Fig.3.26 *Shear stress concentration on the left side of the end protrusion at 30 degrees for the global model and all the strategies.*

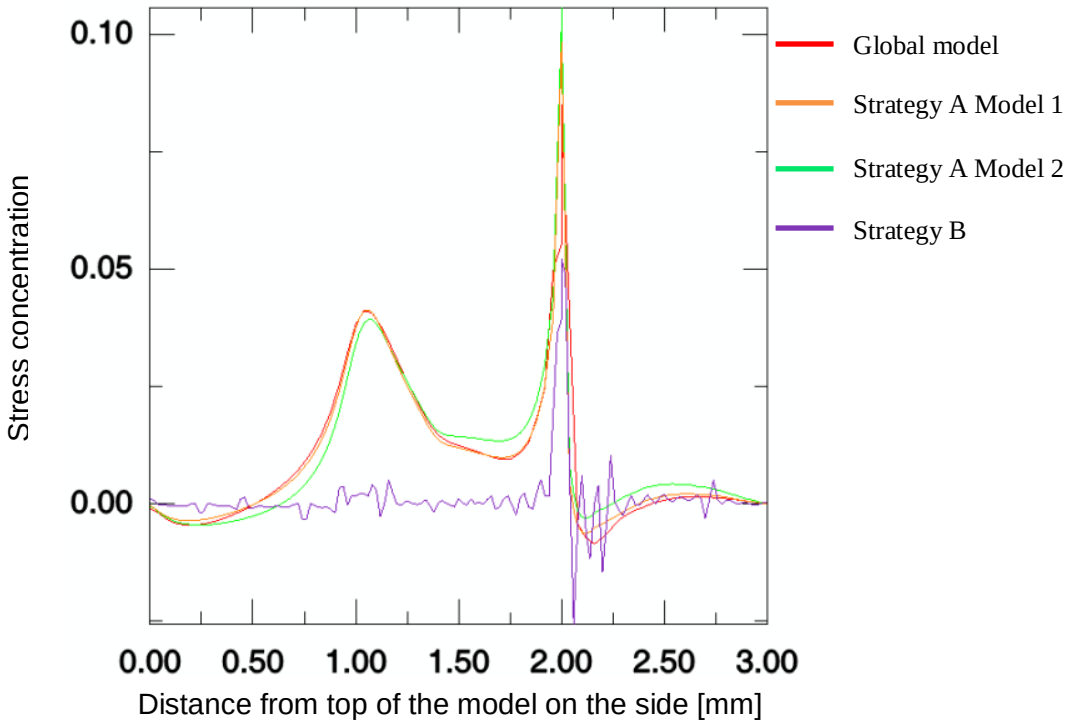

Fig.3.27 *Shear stress concentration on the right side of the end protrusion at 30 degrees for the global model and all the strategies.*

Other stress profiles on the side edges are shown in Appendix C, C.2 and C.4.

3.3.3.3 Strategy selection

For the perpendicular protrusion case, with the stress contour results of the whole model and the composite region, Strategy A Model 1 and Strategy B can be selected as the variations were small. Strategy A Model 1 is the favourite for this case, because the stress profiles on right side for Strategy B shows very different stress states compared to the global model end protrusion results (see Fig.3.25 and Fig.3.27). This is caused by the load was put on this particular side for Strategy B. Strategy A Model 2 and Strategy C are considered not suitable, because their large variation with the composite region contour results and the stress profiles along both sides. Particularly, Strategy C is abandoned for analysis of the 30 degree protrusion case. For the 30 degree protrusion case, the same conclusions can be drawn.

By careful examination of different modelling strategies with stress contours for the whole model (see Appendix C C.1 and C.3) and the composite region, and the stress profiles on both sides of the end protrusion, Strategy A Model 1 was selected to carry out further studies for the end protrusion.

3.4 Three Dimensional Modelling methods

The 3D modelling investigates the spatial arrangement and spacing influence on the stress states locally around the individual protrusion. Elements used in these analyses are hexahedral stress elements. The flow chart of 3D modelling is shown in Fig.3.28.

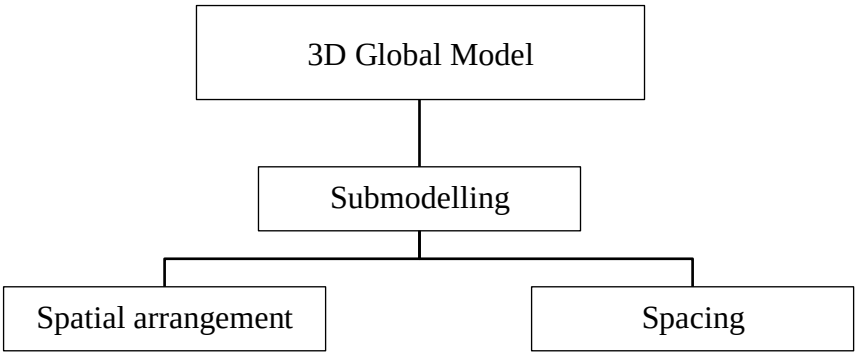

Fig.3.28 *Flow chart for three-dimensional analysis*

3.4.1 Three-dimensional global model and submodel design

To investigate the protrusions spatial distribution and density effects, three-dimensional global model and submodels were created.

The geometry of the cross section of the 3D global model with normal in 3-direction is the same as the 2D global model mentioned in section 2.1, and it is with half the width, 12.5 mm, of the real specimens because of symmetry, see Fig.3.29.

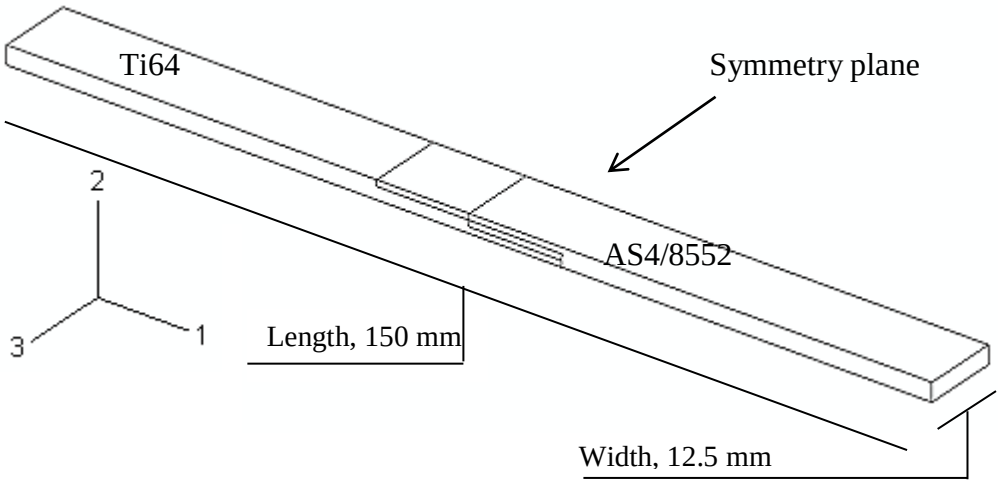

Fig.3.29 *Geometry of the 3D global model with protrusion layers (half the width of the specimen)*

The 3D global model cross-section (1-2 plane) has the same geometries with the 2D global model and with width of 12.5 mm in the 3-direction (which is the half of the

specimen width). For the cross-section geometries, the length of the model is 150 mm, and the thickness is 3 mm. The heights of the steps are the same, 1 mm. The composite part consists of cross-ply unidirectional carbon prepreg, AS4/8552, as $[0/90]_{12}$. The global model has been created and analysed with linear elastic material properties.

To simulate the protrusion spatial distribution, submodels have been designed from the specific region, the dotted rectangle area (and the grey regular tetrahedron) in Fig.3.30 and with the same coordinate system as the 3D global model.

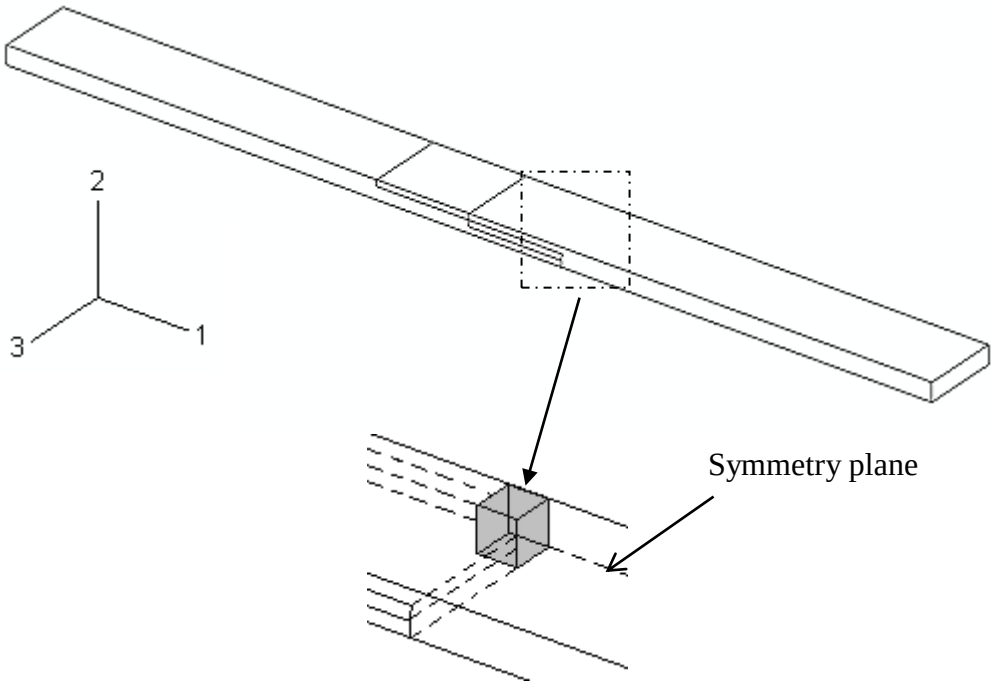

Fig.3.30 *The grey cubic region, from where the 3D submodels have been created*

They have been created with detailed geometries, which include the existence of the protrusions, protrusion distribution density and pattern. The most distant face in the positive 1-direction of grey regular tetrahedron with normal in 1-direction is the end of the second step of the joint.

The different pattern submodels are shown in Fig.3.31, the first three models shown in Fig.3.31 (a), (b) and (c) have been selected with the same protrusion distribution density as the specimens, and half the distribution density with square array for (d).

The arrangements, (a) and (d) in Fig.3.31 are arranged with square array. And arrangement (c) in Fig.3.31 is arranged as the neighbouring protrusion columns (protrusions in 1-direction) shifted in the axial direction for 0.68 mm away from each other; and (d) in Fig.3.31 is arranged as (c) turns 90 degrees clockwise in the (1,3) plane. The (b) and (c) in Fig.3.31 are near hexagonal or hexagonal like arrays, and (c) is similar to the actual Comeld ^{TM} arrangement.

Protrusions on these submodels are perpendicular to the metal surface, and the cross section has the same geometric parameters as the 2D perpendicular model. For the first three submodels, the size of the model is the same, and due to the half distribution density, the last submodel (Fig.3.31 (d)) has a different size (large enough to contain 9 square array protrusions). The hexagonal arrangement submodel, Fig.3.31 (b), is not an exact regular hexagonal array due to the spatial arrangement difficulties. Mathematically, it is impossible to fit 16 protrusions hexagonally within a square area with the size of the submodel.

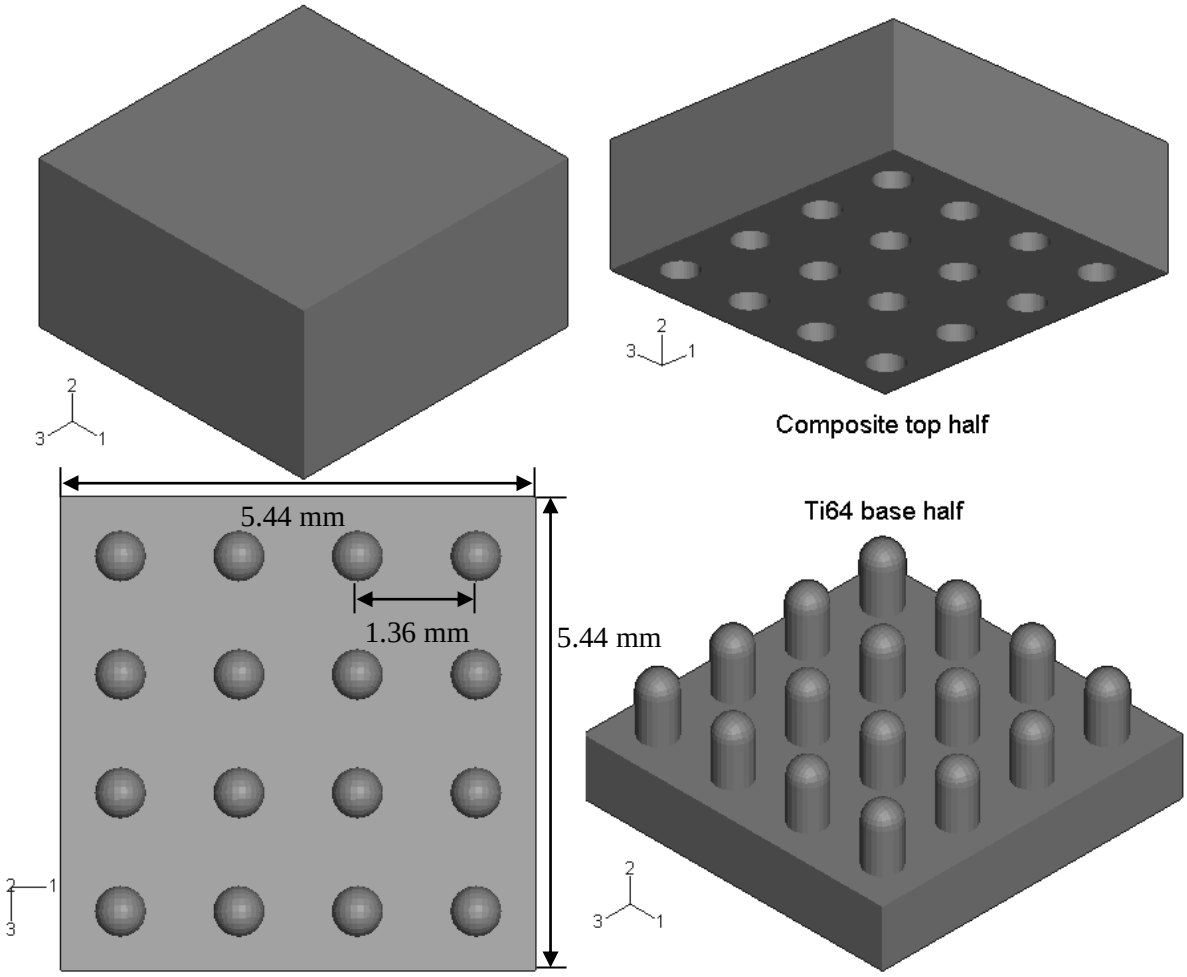

(a) Square array spatial arrangement, with the measured distribution density

Fig.3.31 *3D submodels with different protrusion distribution pattern, arranging with (a) square array, (b) hexagonal array, (c) same as specimen, and (d) half distribution density and square array.*

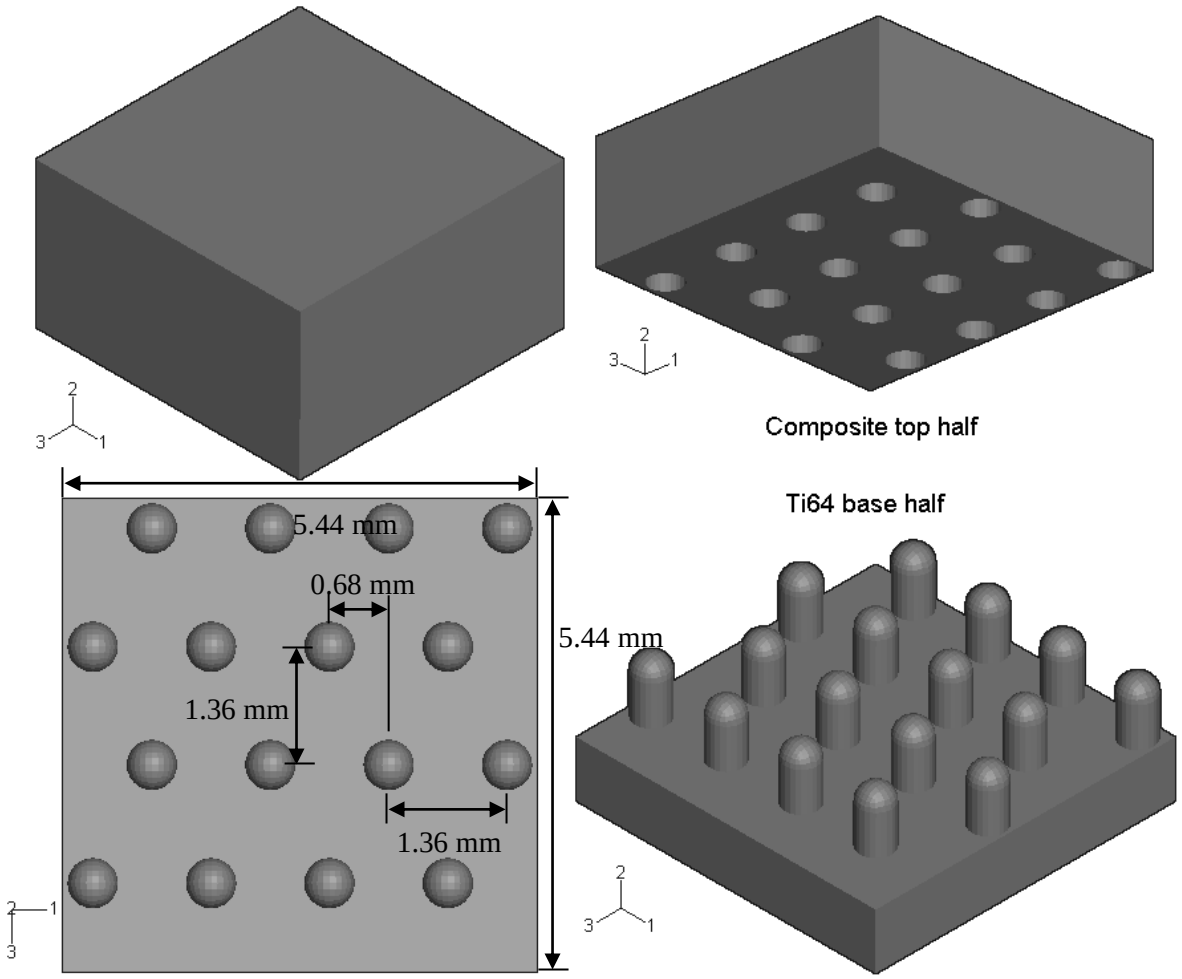

Fig.3.31 *Continued. (b) Hexagonal array spatial arrangement (rotated specimen spatial arrangement), with the measured distribution density*

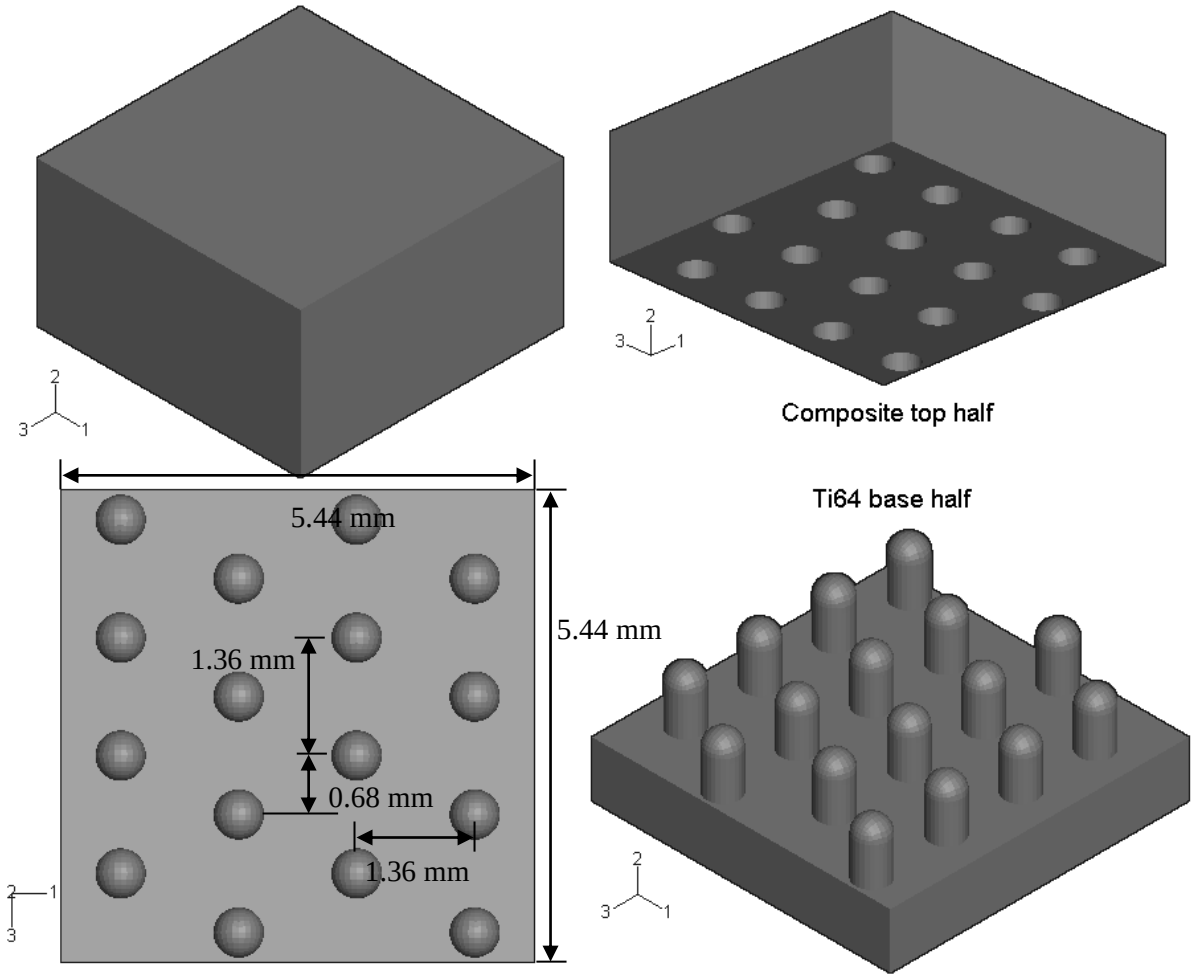

Fig.3.31 *Continued. (c) Specimen spatial arrangement, with the measured distribution density (close to the specimen arrangement)*

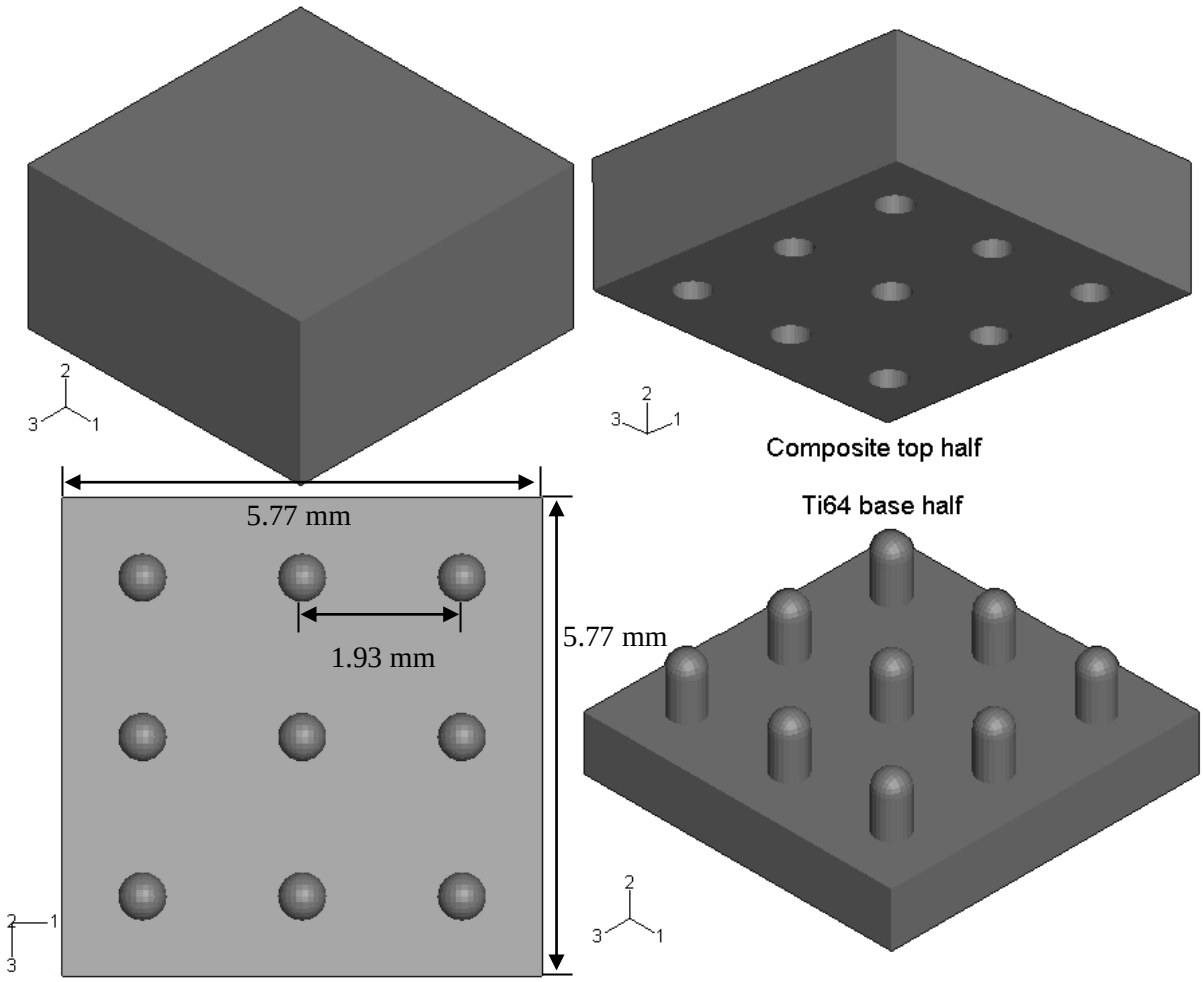

Fig.3.31 *Continued. (d) Square array spatial arrangement, with half the measured distribution density*

The materials used for the 3D global model and submodels are cross ply AS4/8552 prepreg, and Ti64. The composite area in the model has been assigned with homogenised cross-ply $[0/90]_{2S}$ properties calculated based on the classic laminate theory and simulation (see section 3.2.3).

3.4.2 Three-dimensional global model and submodel boundary conditions

Perfect bonding is assumed for the interfaces between different regions. The 3D global model is loaded in tension with displacement on one end face (Fig.3.31 the most distant face in positive 1-direction with normal of 1-direction), with the opposite end face fixed against movement in the tension direction, and two faces (Fig.3.31 the

lowest face with normal in the 2-direction and the most distant face with normal in the negative 3-direction) fixed against movement in the transverse directions respectively due to model symmetry.

The 3D submodel boundary conditions are set up with the global model results, i.e. submodels have been driven by the global model local results, see Fig.3.30. Note that, for the case of the lower distribution density (*d* in Fig.3.31), the protrusion layer properties used for the global model was modified respectively.

3.5 Summary

The modelling methods for 2 and 3-dimensional investigation have been presented in this chapter. The detailed model design and boundary conditions were discussed.

There were two cases considered for the 2-dimensional investigation for the repetitive protrusions in the middle of the joint step and the protrusions on the edge of the joint step. The effects of the height, angle and shape are investigated and presented in Chapter 4.

Submodelling was used to investigate the protrusion spatial arrangements effects, including distribution pattern and distribution spacing. The results are presented in Chapter 5.

A example of the mesh is shown in Fig.3.32. The example of the mesh sensitivity studies was shown in Optimisation of the protrusion geometry in Comeld ™ joints [Tu et al., 2011].

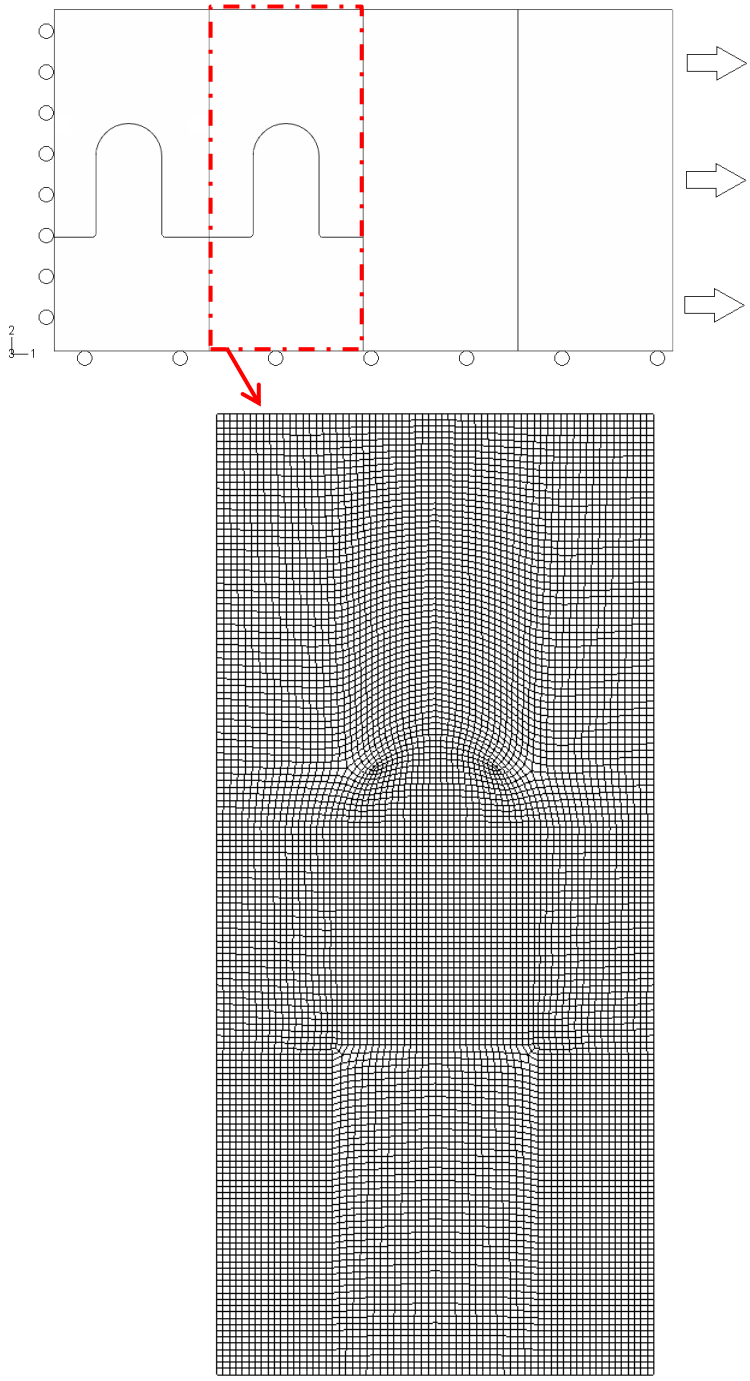

Fig.3.32 *Example mesh of the end protrusion model Strategy A Model 1*

4
GEOMETRIC EFFECTS OF THE PROTRUSIONS WITH TWO DIMENSIONAL MODELS

4.1 Introduction

In this chapter, the results of the two dimensional analyses are presented and discussed in detail. Results are included from the 2D global model and the unit cell model with various geometric parameters. The geometric effects include the height, shape and angle of the protrusion. According to Chapter 3, there are two situations to be considered, i.e. the repetitive case and the protrusion on the edge of the joint step as described in sections 4.2 and 4.3. The height, angle and shape effects are explored for both repetitive protrusions and protrusions on the joint step edge.

Results presented in this chapter were normalised with respect to the applied stress. This chapter describes the stress distributions predicted by the simulations. The significance of those stress distributions to the failure processes is described in Chapter 6.

4.2 Results for the repetitive protrusions

The effects of the geometric parameters including protrusion height, shape and angle are presented in this section. The stress concentration contour results of the whole model are shown in Appendix D. In this work the values of shear stress and concentrations are the absolute values.

4.2.1 Effect of the protrusion height

The height of the protrusion was defined in Chapter 3, Fig.3.4. For the effects of the protrusion height, the cases of 0.50 mm to 1.75 mm with 0.25mm increments were analysed. The stress concentration contour results of the composite region are shown

in figures, Fig.4.1 for the axial stress, Fig.4.2 for the peel stress and Fig.4.3 for the shear stress.

The observed failure of the joint occurs in the composite region on top of the protrusions, see Chapter 6. Therefore, the stress status of the composite region should be examined carefully, especially at the top of the protrusion region.

For axial stress concentration, the contour results are shown in Fig.4.1 and the maximum stress concentrations are listed in Table.4.1.

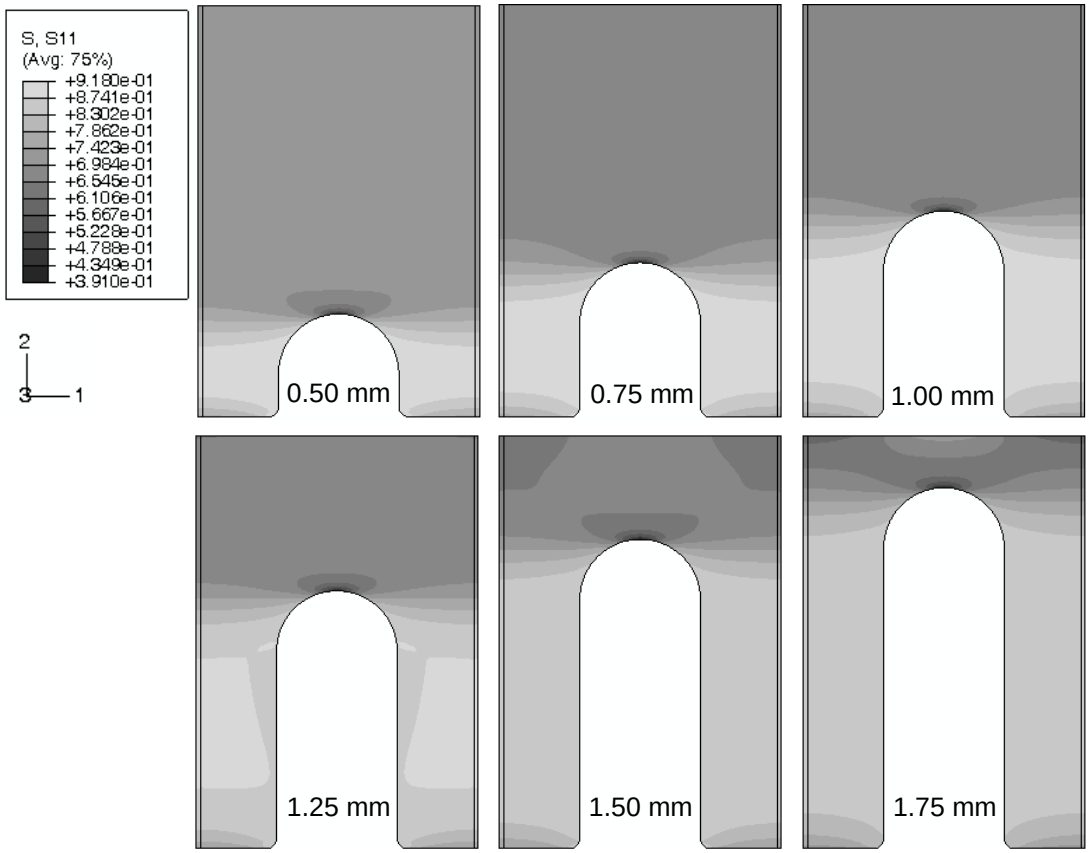

Fig.4.1 *Axial stress concentration contour results in the composite region with different protrusion height*

Stress distributions are symmetrical and mainly concentrated in the regions at both sides of the protrusion. There is not any particular point of stress concentration; the stress concentration spreads with the height of the protrusion. The maximum axial stress concentration lowers with the increase of the protrusion height. This is considered to be caused by the increase of the contact area.

Table.4.1 *Maximum axial stress concentration in the composite region with different protrusion height*

Height [mm]	0.50	0.75	1.00	1.25	1.50	1.75
σ_{11}/σ	9.18e-1	9.08e-1	8.95e-1	8.79e-1	8.64e-1	8.49e-1

For the peel stress concentration, the contour results are shown in Fig.4.2, and the stress distributions are symmetrical; and the maximum concentrations are listed in Table.4.2. The locations of the maximum stress concentration are marked with a circle in Fig.4.2.

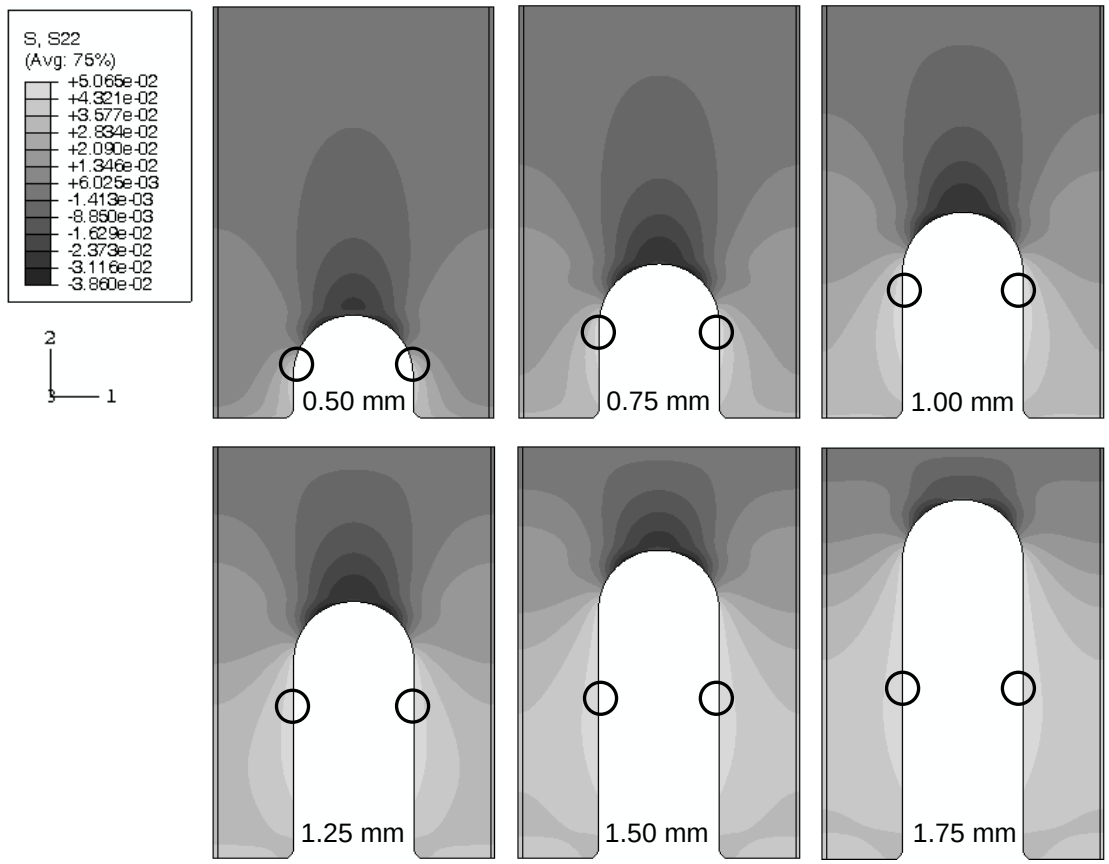

Fig.4.2 *Peel stress concentration contour results in the composite region with different protrusion height*

Table.4.2 *Maximum peel stress concentration in the composite region with different protrusion height*

Height [mm]	0.50	0.75	1.00	1.25	1.50	1.75
σ_{22}/σ	4.64e-2	5.06e-2	5.06e-2	4.98e-2	4.89e-2	4.78e-2

The location for the maximum stress concentration is along the edges of the protrusion, near the top for lower heights; then remaining at around the same height for higher protrusions. The maximum value of stress concentration reaches highest value with 1mm high protrusion. However, the variation is around or less than 3% for the height of 0.75 to 1.75 mm, and much lower for the 0.50 mm protrusion.

For the shear stress concentration, the contour results are shown in Fig.4.3 and the maximum stress concentrations are listed in Table.4.3. The negative value for the shear stress indicates the change of direction. Stress distributions are symmetric and stress concentration occurs at the top of the protrusion for all protrusion heights as marked in Fig.4.3.

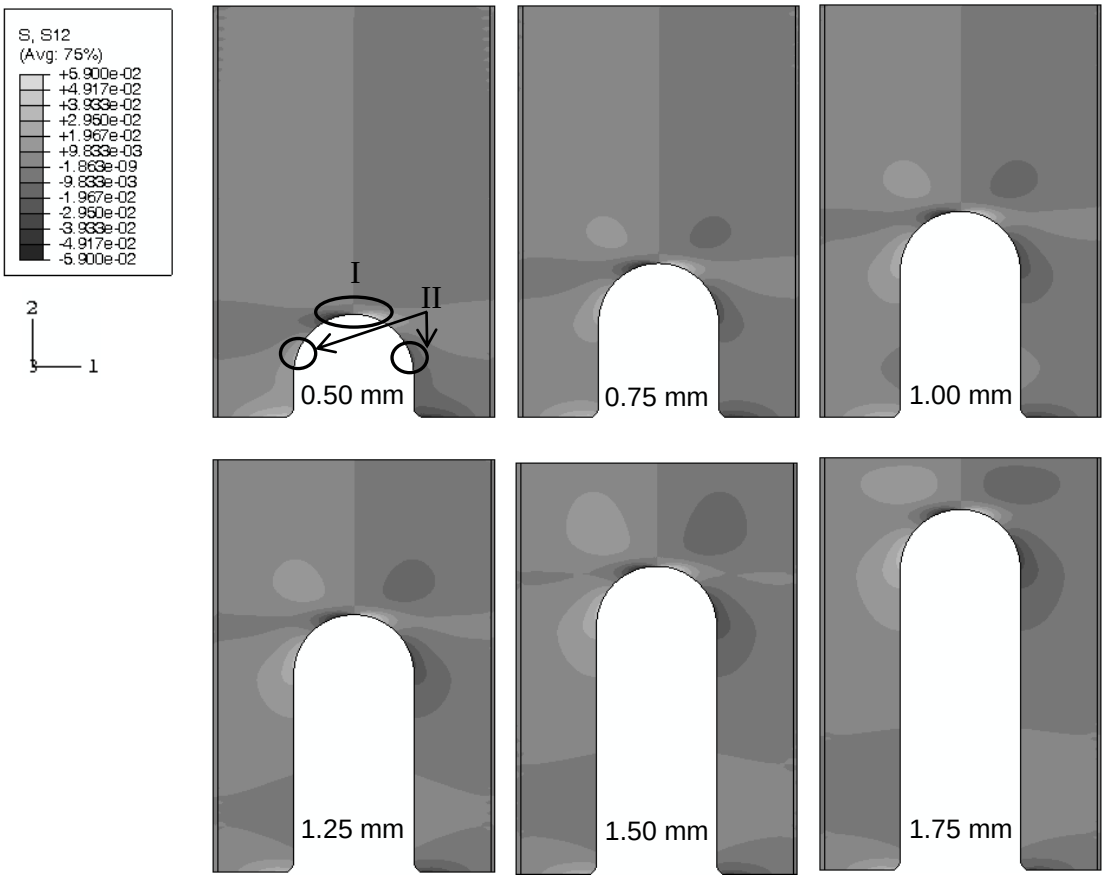

Fig.4.3 *Shear stress concentration contour results in the composite region with different protrusion height*

Table.4.3 *Maximum shear stress concentration in the composite region with different protrusion height*

Height [mm]	0.50	0.75	1.00	1.25	1.50	1.75
σ_{12}/σ Zone I	5.90e-2	5.54e-2	5.37e-2	5.30e-2	5.18e-2	4.96e-2
σ_{12}/σ Zone II	2.45e-2	3.03e-2	3.33e-2	3.44e-2	3.52e-2	3.80e-2

The area for stress distribution along the protrusion side is always smaller than the stress concentration at the tip of the protrusion top and bigger with the protrusion height. The maximum stress concentration decreased with the increase of protrusion height, see Table.4.3. The trend is clear for the protrusion height effects on the maximum shear stress concentration.

4.2.2 Effect of protrusion angle for the parallel shape protrusions

The angle of the protrusion was defined in Chapter 3, Fig.3.4. The protrusion angle effects and the stress concentration contour results for the composite region are shown in Fig.4.4 for axial stress, Fig.4.5 for peel stress and Fig.4.6 for the shear stress.

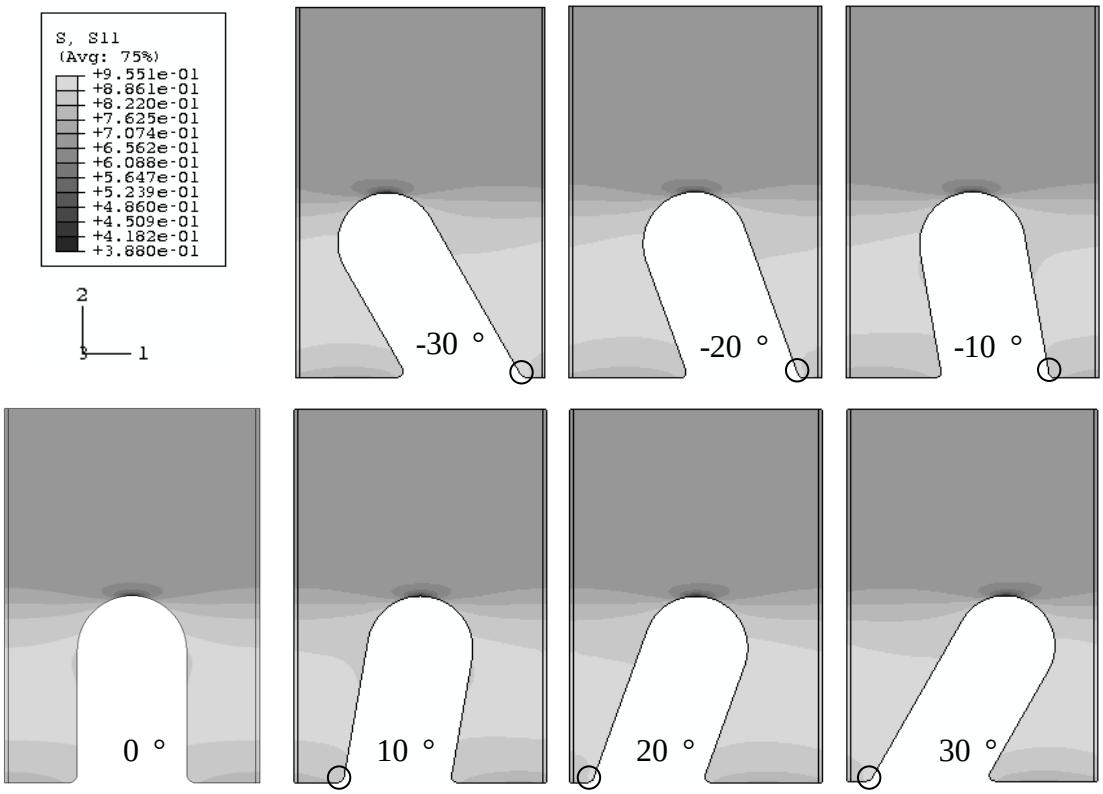

Fig.4.4 *Axial stress concentration contour results in the composite region with different protrusion angle*

For the axial stress in the composite region, see Fig.4.4, stress concentration occurs at the sides of the protrusion. There is not any significant stress concentration at the top of the protrusion region. Maximum stress concentration occurs at the foot of the protrusion. The stress distributions are symmetric for the same absolute protrusion angle. Maximum stress concentration varies slightly for different protrusion angle, see Table.4.4.

Table.4.4 *Maximum axial stress concentration in the composite region with different protrusion angle*

Angle [degrees]	-30	-20	-10	0	10	20	30
σ_{11}/σ	9.55e-1	9.34e-1	9.41e-1	8.95e-1	9.41e-1	9.34e-1	9.55e-1

For the peel stress, the stress concentration contour results are shown in Fig.4.5. Stress distributions are symmetric for the same absolute protrusion angle as well as the maximum stress concentration location. For the perpendicular protrusion, the stress concentration occurs at the sides of the protrusion top with the lowest concentration level, see Table.4.5.

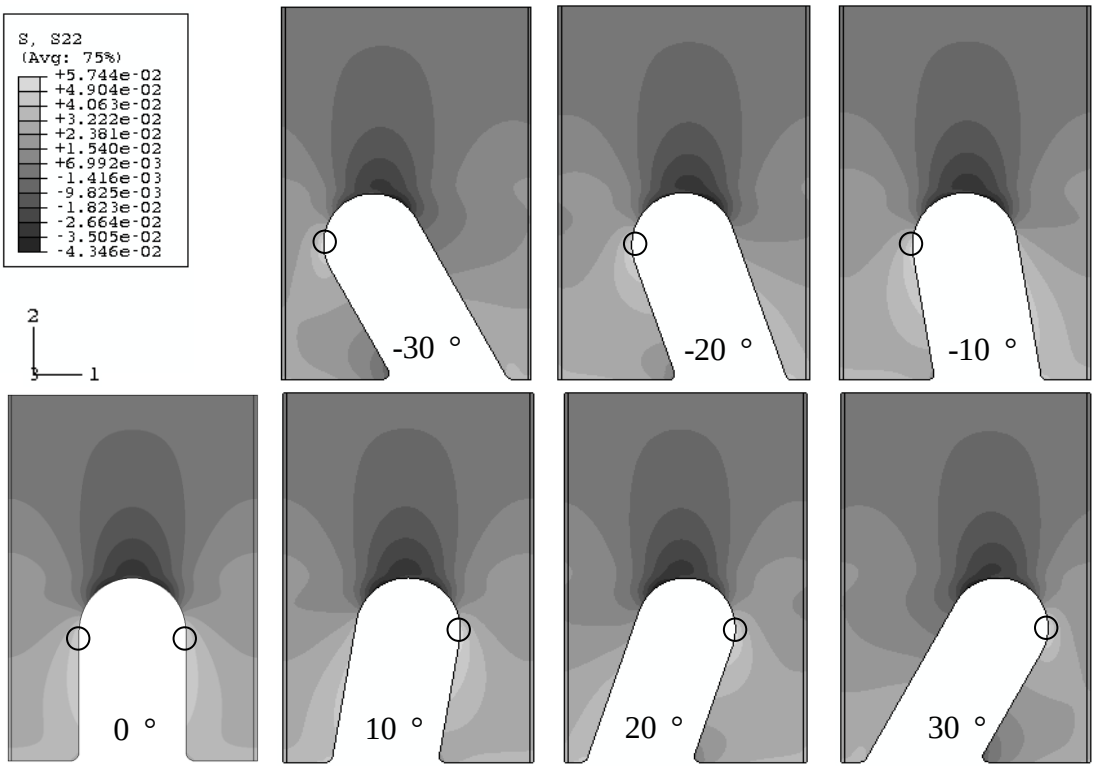

Fig.4.5 *Peel stress concentration contour results in the composite region with different protrusion angle*

Table.4.5 *Maximum peel stress concentration in the composite region with different protrusion angle*

Angle [degrees]	-30	-20	-10	0	10	20	30
σ_{22}/σ	5.70e-2	5.74e-2	5.70e-2	5.06e-2	5.70e-2	5.74e-2	5.70e-2

In Fig.4.6, for the shear stress concentration, negative value indicates the change of shear stress direction. The stress distribution is symmetric for the same absolute protrusion angle with opposite directions. Maximum stress concentrations occur at the foot of the protrusions despite protrusion angle change. The stress concentrations of two zones marked in Fig.4.6 are listed in Table.4.6. The concentration values for

Zone II are minus, indicating the direction change compare with Zone III. The trends for the two zones are both linear and symmetric, and are reversed for the different protrusion angle, see Fig.4.7.

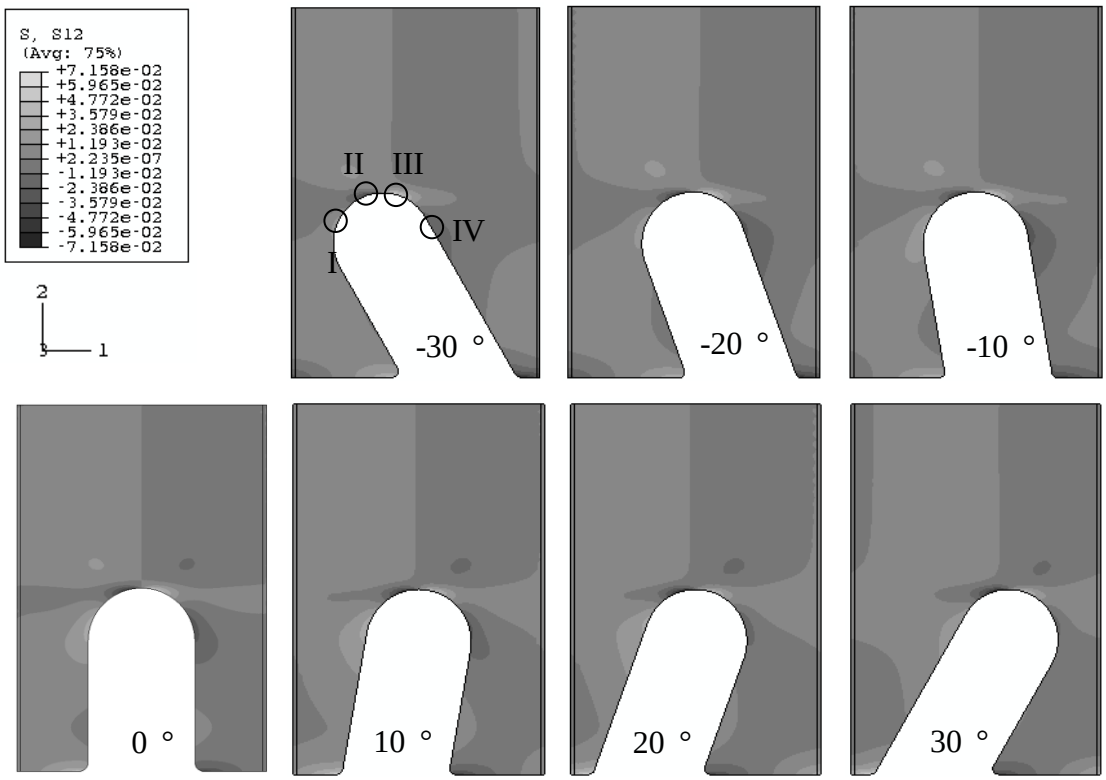

Fig.4.6 *Shear stress concentration contour results in the composite region with different protrusion angle*

Table.4.6 *Maximum shear stress concentration in the composite region with different protrusion angle for zones marked in Fig.4.6*

Angle [degrees]	-30	-20	-10	0	10	20	30
σ_{12}/σ Zone I	1.95e-2	2.48e-2	2.96e-2	3.34e-2	3.51e-2	3.09e-2	2.04e-2
σ_{12}/σ Zone II	4.71e-2	4.84e-2	5.14e-2	5.37e-2	5.76e-2	6.02e-2	6.43e-2
σ_{12}/σ Zone III	6.43e-2	6.02e-2	5.76e-2	5.37e-2	5.14e-2	4.84e-2	4.71e-2
σ_{12}/σ Zone IV	2.04e-2	3.09e-2	3.51e-2	3.33e-2	2.96e-2	2.48e-2	1.95e-2

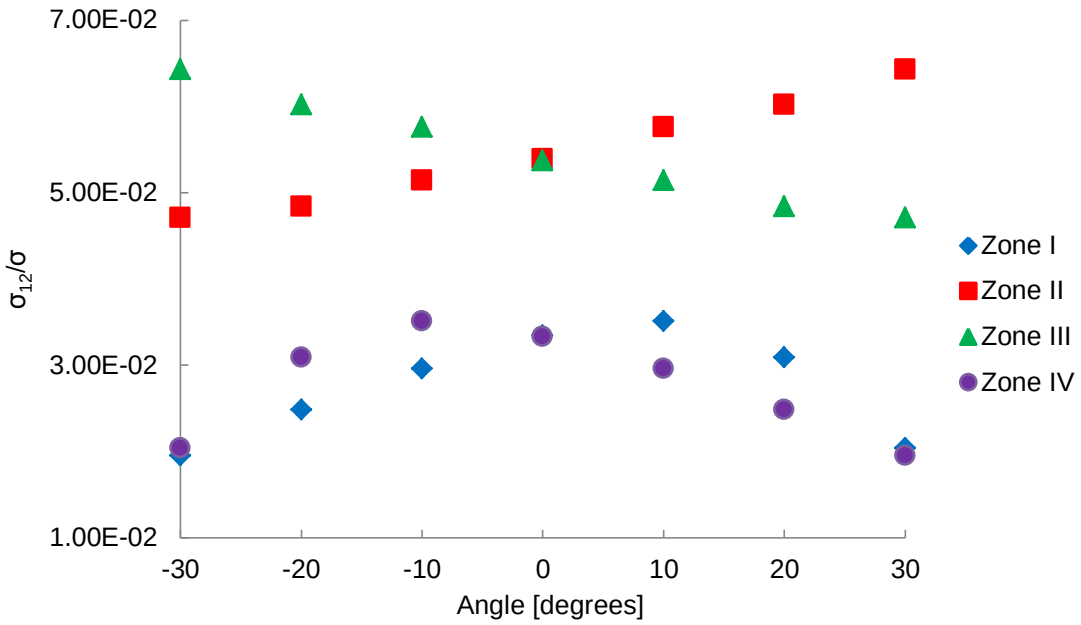

Fig.4.7 *Maximum shear stress concentration with different protrusion angle for marked zones in Fig.4.6*

4.2.3 Effect of protrusion angle for the hill shape protrusions

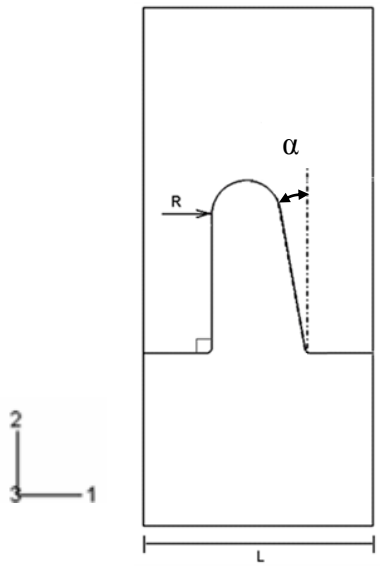

Fig.4.8 *Angle definition for hill shape protrusion (angle shown is minus angle)*

The angle of the hill protrusion is defined in Fig.4.8. The protrusion shapes and angles investigated are based on the same spatial volume fraction and height (1mm), except for the height analysis. For the effects of the protrusion angle, the stress

concentration contour results of the composite region are shown in figures, Fig.4.9 for the axial stress, Fig.4.10 for the peel stress and Fig.4.11 for the shear stress.

For the axial stress concentration, results are very similar to the case of the parallel stress, see Fig.4.8 and Table.4.7. There is not obvious stress concentration around the top of the protrusion, and the maximum stress concentration occurs at the protrusion foot. The stress distributions are symmetric for the relative positive and negative protrusion angles.

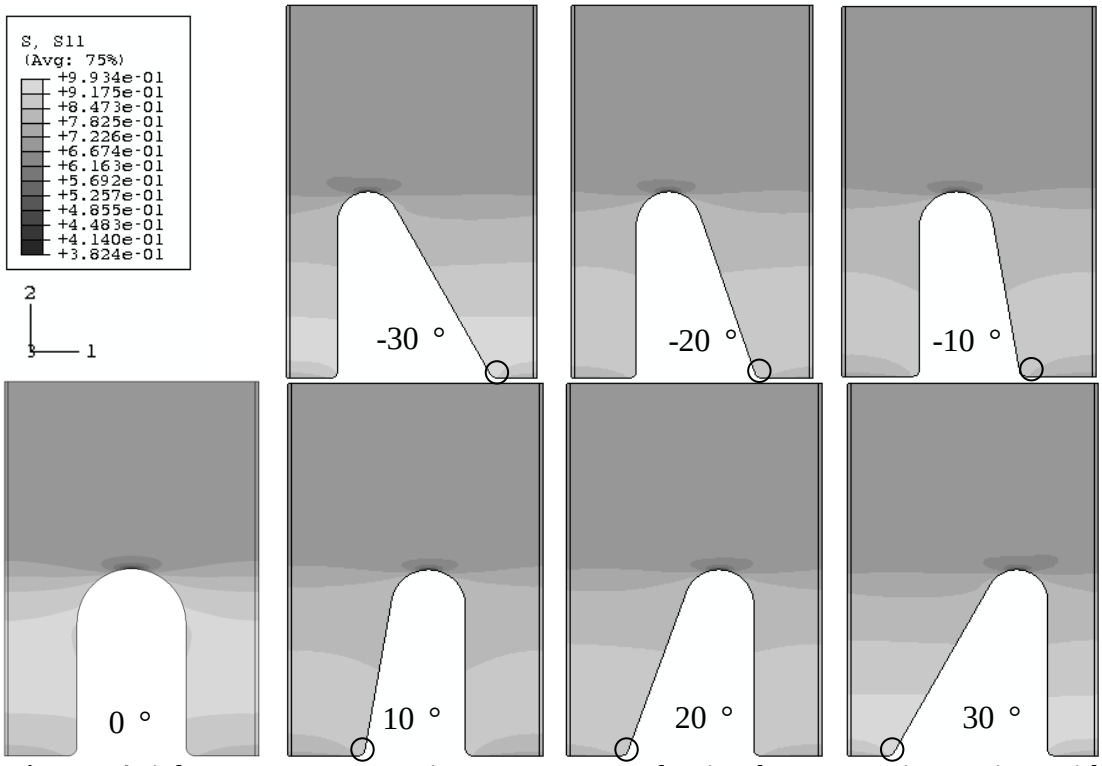

Fig.4.9 *Axial stress concentration contour results in the composite region with different protrusion angle*

Table.4.7 *Maximum axial stress concentration in the composite region with different protrusion angle*

Angle [degrees]	-30	-20	-10	0	10	20	30
σ_{11}/σ	9.93e-1	9.60e-1	9.29e-1	8.95e-1	9.29e-1	9.60e-1	9.93e-1

For the peel stress, the stress concentration contour results are shown in Fig.4.10. Stress distributions are similar to the parallel case. On top of the protrusion region, there is not any obvious peel stress concentration. The maximum stress concentration occurs on the vertical side of the protrusion. The stress concentration level is lower than the case of the parallel protrusions, see Table.4.8.

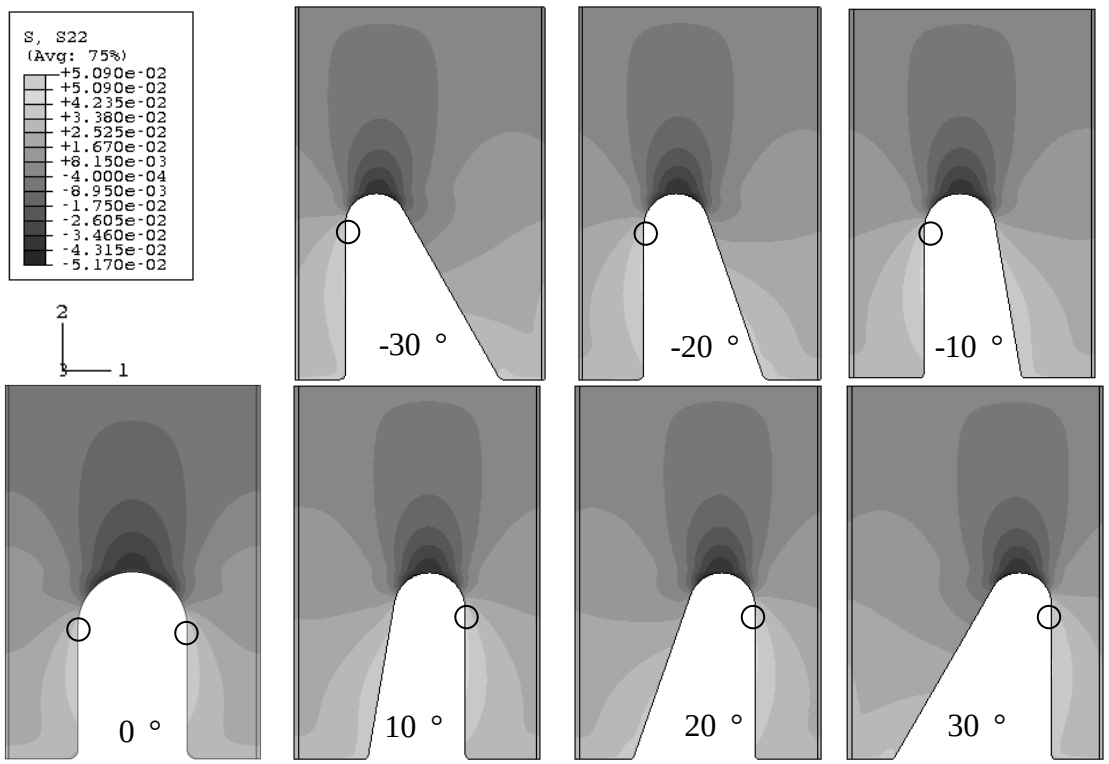

Fig.4.10 *Peel stress concentration contour results in the composite region with different protrusion angle*

Table.4.8 *Maximum peel stress concentration in the composite region with different protrusion angle*

Angle [degrees]	-30	-20	-10	0	10	20	30
σ_{22}/σ	4.45e-2	4.58e-2	4.64e-2	5.06e-2	4.64e-2	4.58e-2	4.45e-2

In Fig.4.11, for the shear stress concentration, the negative value indicates the change of shear stress direction. Similarly to the parallel case, the stress distribution is symmetric for the same absolute protrusion angle with opposite directions. The stress concentrations of two zones marked in Fig.4.11 are listed in Table.4.9. The stress concentration direction for Zone I is the opposite direction for Zone II. The trends for

the two zones are both symmetric and reversed for the different protrusion angle, see Fig.4.12. However the trends are not linear, twenty degree protrusions shows maximum shear stress concentrations at the top of the protrusion.

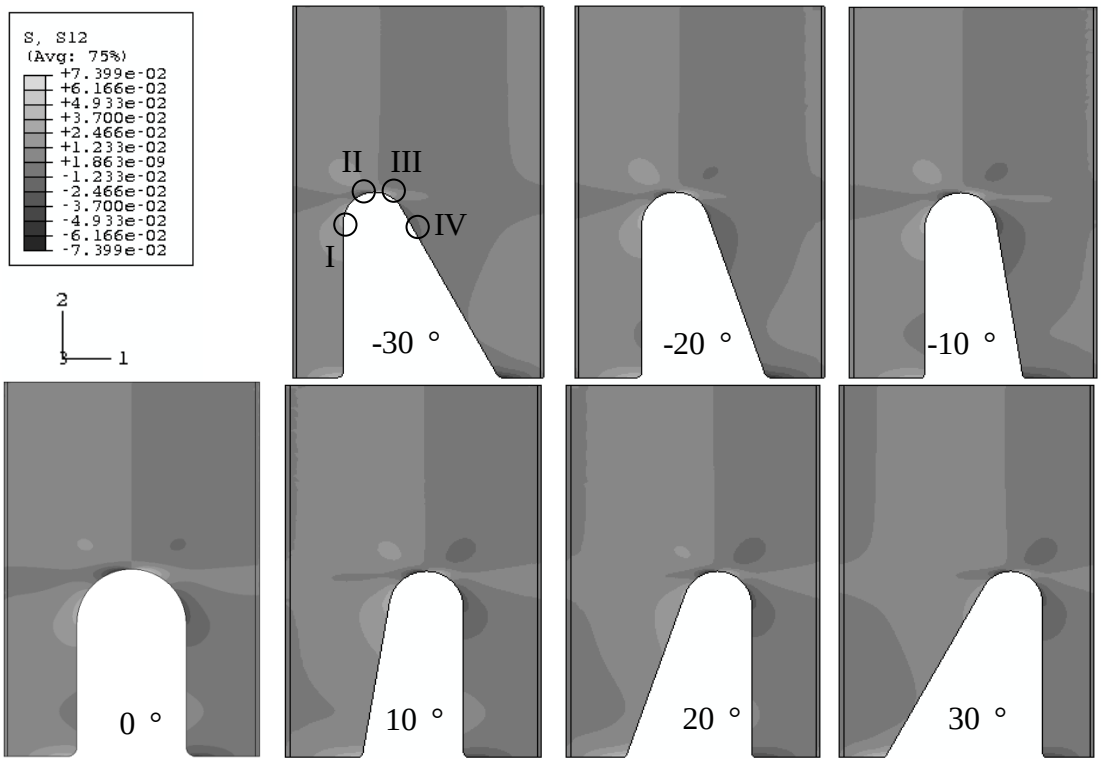

Fig.4.11 *Shear stress concentration contour results in the composite region with different protrusion angle*

Table.4.9 *Maximum shear stress concentration in the composite region with different protrusion angle for Zone I and II*

Angle [degrees]	-30	-20	-10	0	10	20	30
σ_{12}/σ Zone I	3.59e-2	3.59e-2	3.64e-2	3.34e-2	3.79e-2	3.23e-2	2.12e-2
σ_{12}/σ Zone II	4.80e-2	4.92e-2	5.13e-2	5.37e-2	5.58e-2	5.82e-2	5.66e-2
σ_{12}/σ Zone III	5.65e-2	5.82e-2	5.58e-2	5.37e-2	5.13e-2	4.92e-2	4.80e-2
σ_{12}/σ Zone IV	2.12e-2	3.23e-2	3.79e-2	3.33e-2	3.64e-2	3.59e-2	3.59e-2

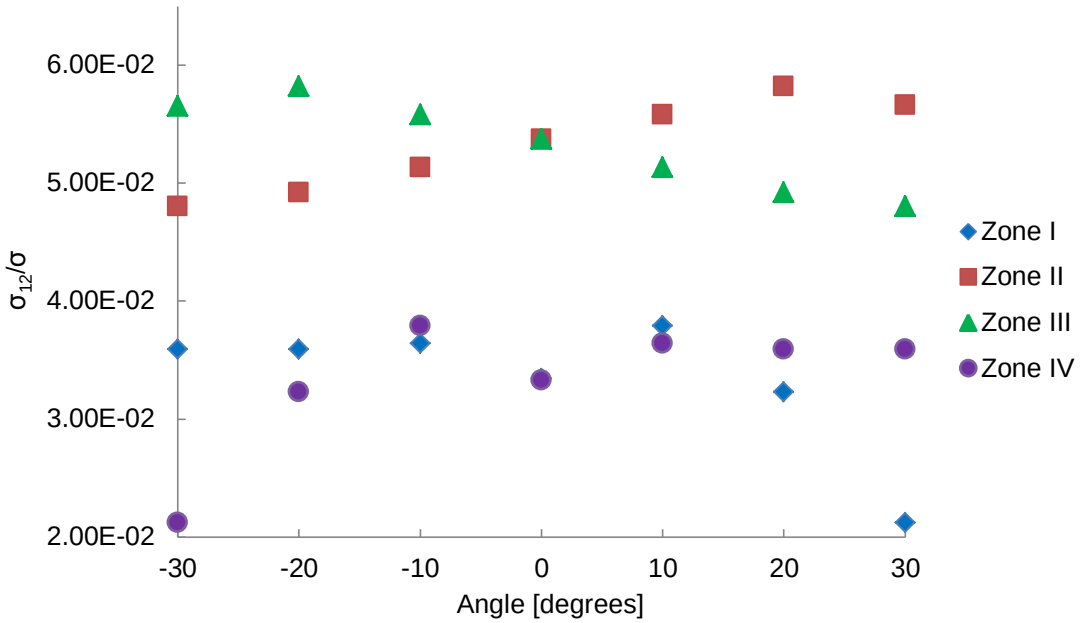

Fig.4.12 *Maximum shear stress concentration with different protrusion angle for marked zones in Fig.4.11*

4.2.4 Effect of protrusion shape for the repetitive protrusions

For the repetitive case, there is not significant axial stress concentration at the top of the protrusion for the composite region. The stress concentrations of peel and shear stresses are compared for the different shape.

The values for the maximum stress concentration at around the top of the protrusion region are listed in Table.4.10 for peel stress and Table.4.11 for shear stress, also see Fig.4.13 and Fig.4.14. The effect of the shape is clear.

For the peel stress, in Fig.4.13, the maximum stress concentration occurs at similar positions with lower values for the hill shape protrusions; the maximum peel stress concentrations are not sensitive to the protrusion angle change for different shapes; and values are lower with the hill shape; the location of which changes from the left side of the protrusion to the right side when the protrusion angle changes from minus to plus.

Table.4.10 *Maximum peel stress concentration in the composite region with different protrusion angle and shape*

Angle [degrees]	-30	-20	-10	0	10	20	30
σ_{22}/σ - parallel	5.70e-2	5.74e-2	5.70e-2	5.06e-2	5.70e-2	5.74e-2	5.70e-2
σ_{22}/σ - hill	4.45e-2	4.58e-2	4.64e-2	5.06e-2	4.64e-2	4.58e-2	4.45e-2

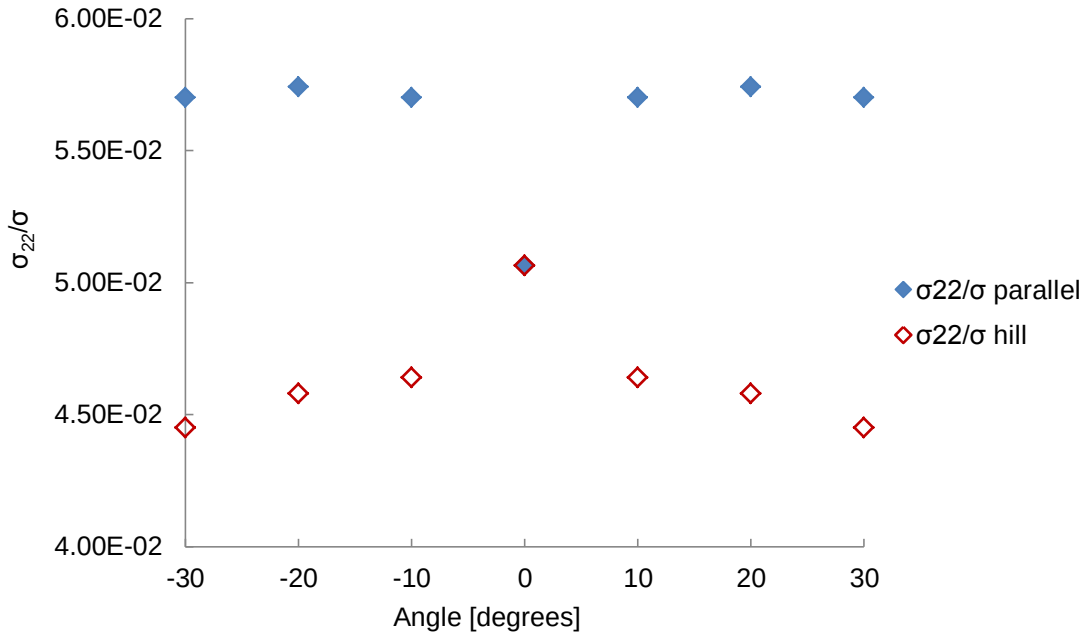

Fig.4.13 *Maximum peel stress concentration with different protrusion angle and shape*

For the shear stress, in Fig.4.14, on top of the protrusions, the trends and values are similar for different shape protrusions in Zone II and III (zones are from Fig.4.7 and 4.12), where hill shape plus and minus 30 degrees protrusion shows lower stress concentration for Zone II and III respectively. In Zone I and IV, the stress concentrations are smaller than other zones for both shapes. For hill shape protrusion, in Zone I, the stress concentration reduces with protrusion angle, and increases in Zone IV with protrusion angle. The parallel shape protrusion shows lower stress concentration towards metal or composite ends of the joint comparing with the perpendicular case. In general, the shape of the diagram for the same shape of protrusion appears to be symmetric with protrusion angle. This indicates that angled protrusions in the middle of the joint step increase stress concentration slightly.

Table.4.11 *Maximum shear stress concentration in the composite region with different protrusion angle and shape*

Angle [degrees]	-30	-20	-10	0	10	20	30
σ_{12}/σ Zone I - parallel	4.71e-2	4.84e-2	5.14e-2	5.37e-2	5.76e-2	6.02e-2	6.43e-2
σ_{12}/σ Zone II - parallel	6.43e-2	6.02e-2	5.76e-2	5.37e-2	5.14e-2	4.84e-2	4.71e-2
σ_{12}/σ Zone I - hill	4.80e-2	4.92e-2	5.13e-2	5.37e-2	5.58e-2	5.82e-2	5.66e-2
σ_{12}/σ Zone II - hill	5.65e-2	5.82e-2	5.58e-2	5.37e-2	5.13e-2	4.92e-2	4.80e-2

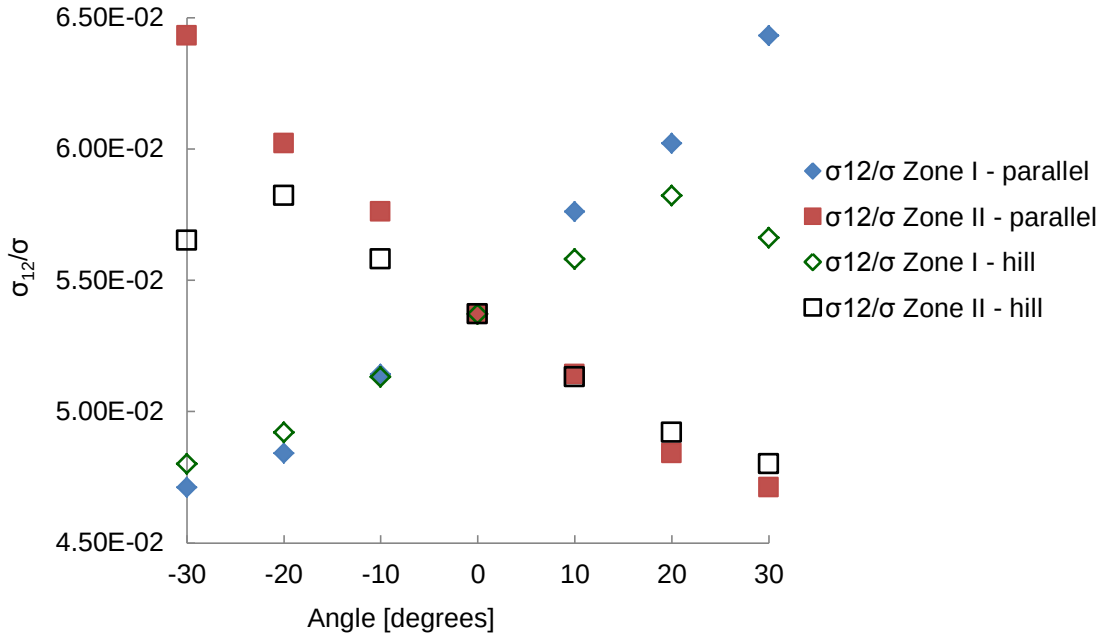

Fig.4.14 *Maximum shear stress concentration with different protrusion angle and shape, the marked zones in Fig.4.6 and Fig.4.11.*

4.3 Results for the protrusions on the joint step edge

The effects of the geometric parameters including protrusion height, shape and angle are presented in this section for the protrusions on the joint step edge. The model design can be found in Chapter 3, section 3.3.3.

4.3.1 Effect of the protrusion height

For the effects of the protrusion height, the cases of 0.50mm to 1.75mm with 0.25mm increments were analysed. The stress concentration contour results of the composite regions are shown in Fig.4.15 for axial stress, Fig.4.17 for peel stress and Fig.4.19 for shear stress.

For the axial stress, there are two zones marked for comparison due to the locations of the maximum stress concentration. The maximum stress concentrations for the two zones are listed in Table.4.12 and shown in Fig.4.16. For Zone I stress concentration increases with protrusion height. For Zone II stress concentration decreases and then increases with protrusion height. The levels of stress concentrations for the two zones tend to similar value with increasing protrusion height.

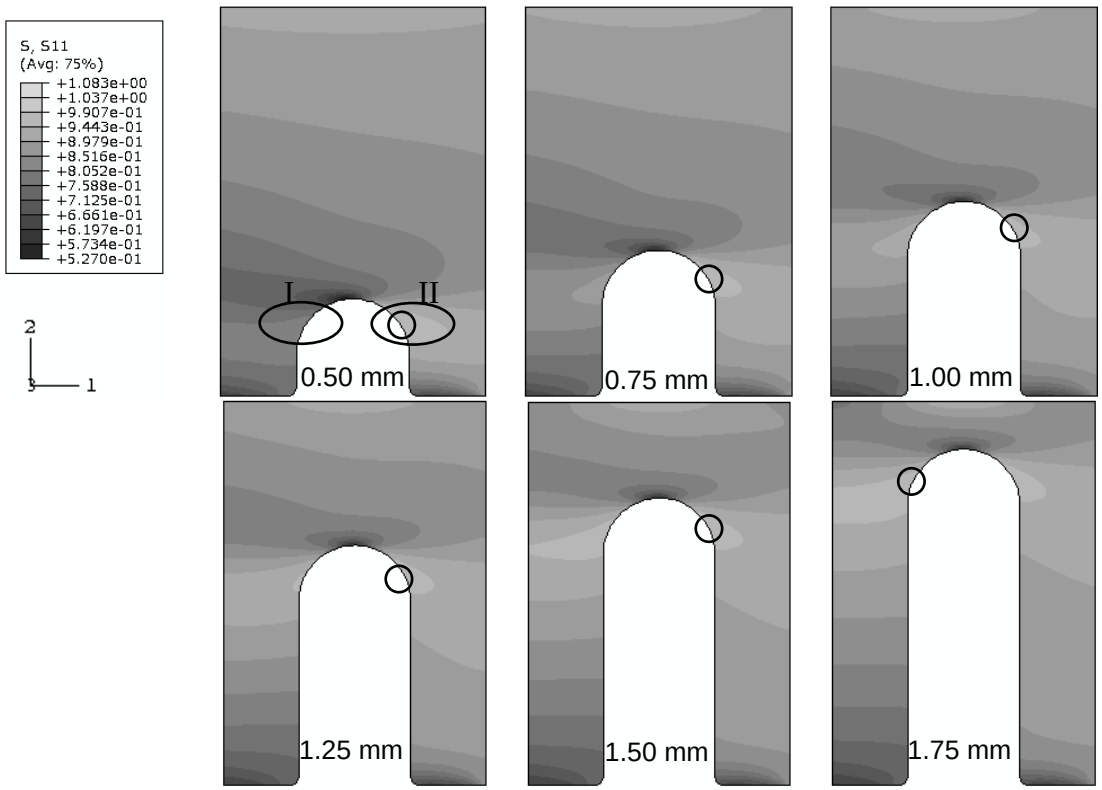

Fig.4.15 *Axial stress concentration contour results in the composite region with different protrusion height*

Table.4.12 *Maximum axial stress concentration in the composite region with different protrusion height for Zone I and II*

Height [mm]	0.50	0.75	1.00	1.25	1.50	1.75
σ_{11}/σ Zone I	9.00e-1	9.67e-1	1.01e0	1.04e0	1.06e0	1.07e0
σ_{11}/σ Zone II	1.08e0	1.06e0	1.06e0	1.06e0	1.06e0	1.06e0

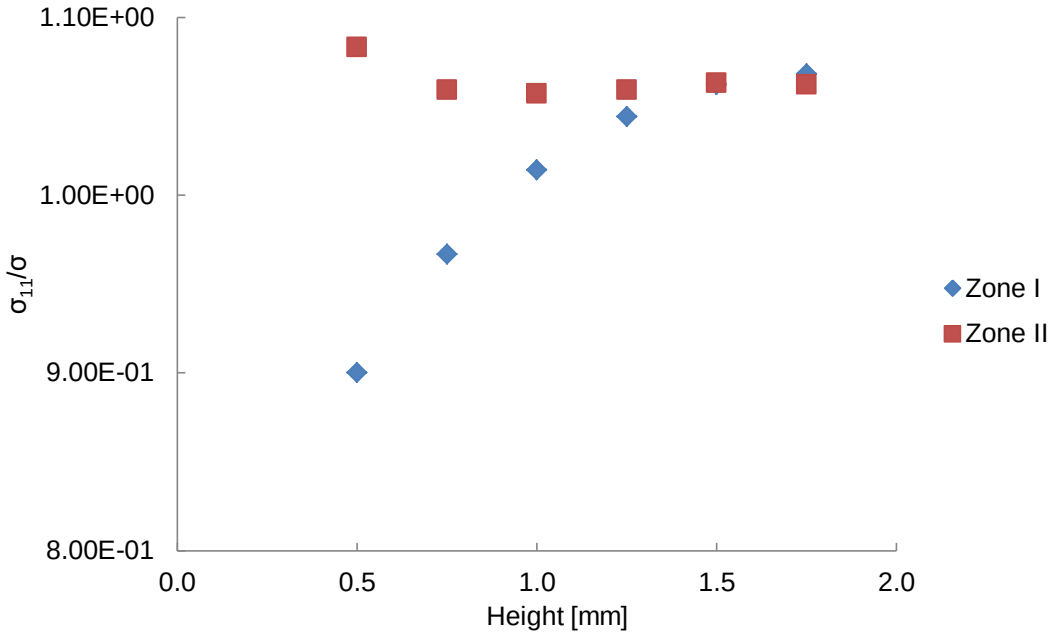

Fig.4.16 *Axial stress concentration for zones marked in Fig.4.15, in the composite region with different protrusion height*

For the peel stress concentration, the contour results are shown in Fig.4.17 and the maximum concentrations are listed in Table.4.13. The locations of the maximum stress concentration are marked with circle in Fig.4.17. Unlike the repetitive case, the maximum stress concentration occurs at the left foot of the protrusions despite the height change. The position of the axial stress concentrations of Zone II stays at near the top of the protrusion despite the protrusion height. For Zone I, stress concentrations increases and then decreases with higher protrusions; for Zone II, stress concentrations increases very slightly with higher protrusions, see Table.4.13.

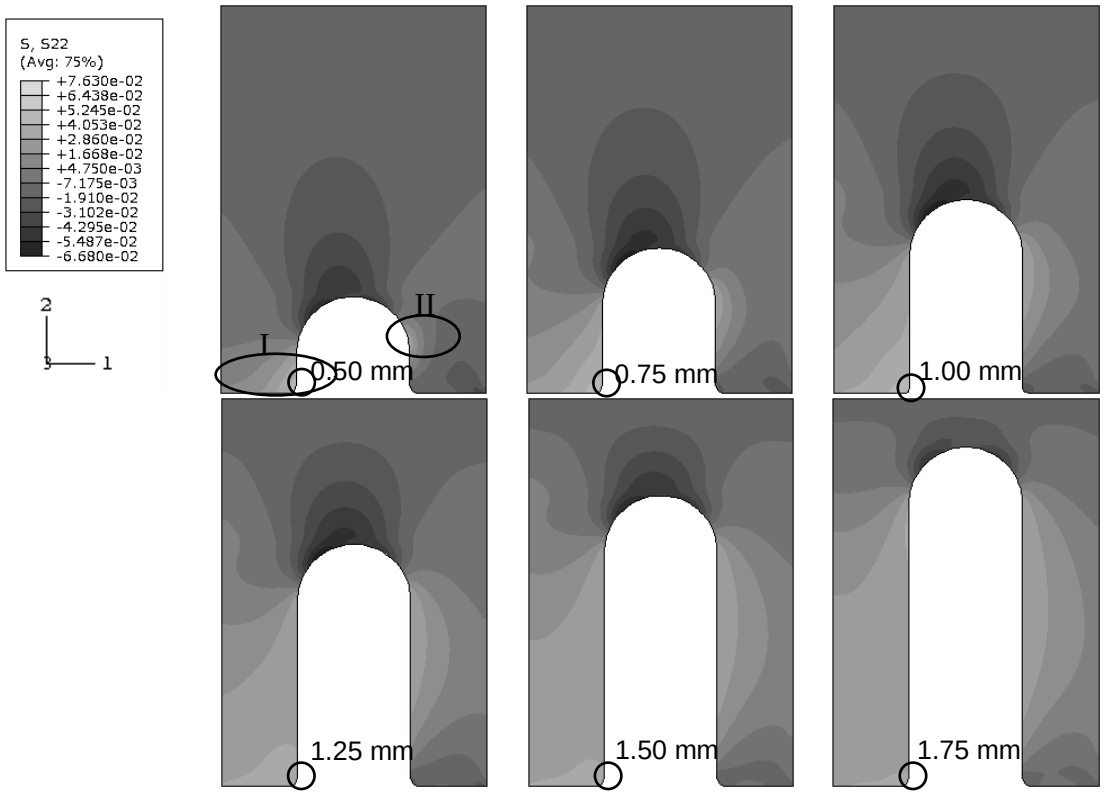

Fig.4.17 *Peel stress concentration contour results in the composite region with different protrusion height*

Table.4.13 *Maximum peel stress concentration with different protrusion height for Zone I and II*

Height [mm]	0.50	0.75	1.00	1.25	1.50	1.75
σ_{22}/σ Zone I	7.05e-2	7.16e-2	7.63e-2	6.34e-2	5.90e-2	5.51e-2
σ_{22}/σ Zone II	4.90e-2	5.27e-2	5.30e-2	5.28e-2	5.23e-2	5.16e-2

For the shear stress concentration, the contour results are shown in Fig.4.18 and the maximum stress concentrations are listed in Table.4.14. The negative value for the shear stress indicates the change of direction. Stress distributions changed dramatically due to the height of the protrusion change. Maximum stress concentration occurs at the top of the protrusion for 0.5mm height protrusion, and at the composite-metal interface for all other protrusion heights as marked with circles in Fig.4.18. There are six zones selected to further examine the stress concentration, see Table.4.14.

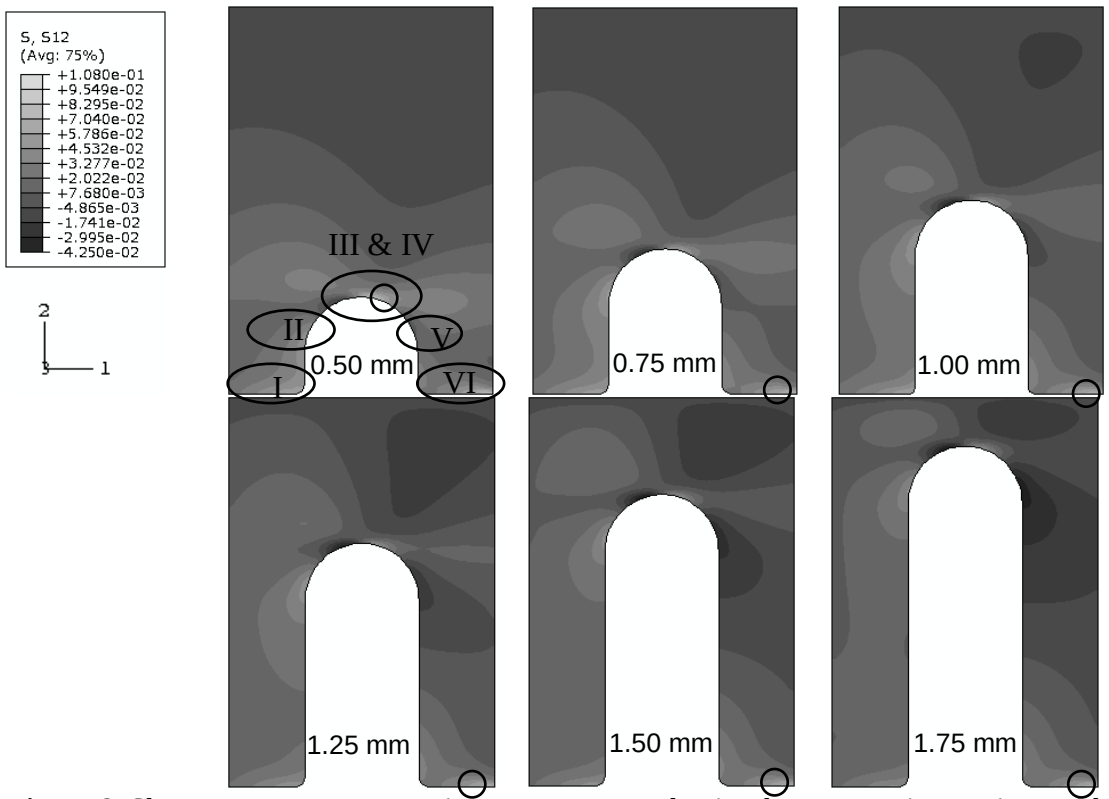

Fig.4.18 *Shear stress concentration contour results in the composite region with different protrusion height*

Table.4.14 *Maximum shear stress concentration in the composite region with different protrusion height for the marked zones*

Height [mm]	0.5	0.75	1.0	1.25	1.5	1.75
σ_{12}/σ Zone I	8.77e-2	8.07e-2	8.23e-2	6.88e-2	6.57e-2	6.15e-2
σ_{12}/σ Zone II	7.02e-2	7.44e-2	7.28e-2	6.82e-2	6.35e-2	6.11e-2
σ_{12}/σ Zone III	7.66e-3	2.02e-2	3.07e-2	3.60e-2	4.10e-2	4.25e-2
σ_{12}/σ Zone IV	1.08e-1	8.12e-2	7.04e-2	6.43e-2	6.33e-2	5.86e-2
σ_{12}/σ Zone V	1.52e-2	3.33e-3	7.95e-3	1.85e-2	2.88e-2	4.03e-2
σ_{12}/σ Zone VI	1.06e-1	1.00e-1	9.87e-2	9.61e-2	9.47e-2	9.33e-2

For Zone I, II, IV, and VI, generally, the stress concentration reduces for higher protrusions. For Zone III and V, generally, the stress concentration increases. The trends of the height for the different zones are shown in Fig.4.19.

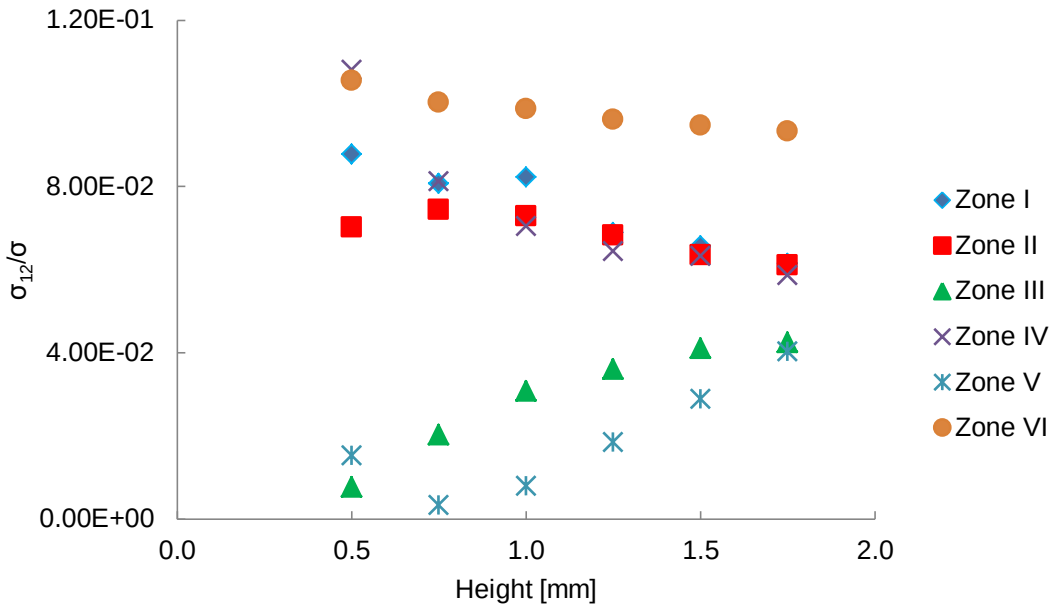

Fig.4.19 *Maximum shear stress concentration at marked zones in the composite region with different protrusion height*

In summary, the higher stress concentrations generally reduce with increasing protrusion height.

4.3.2 Effect of protrusion angle for the parallel shape protrusions

For the effects of the protrusion angle, the cases of -30 to 30 degrees with 10 degrees increments were analysed, where the minus angle stands for the protrusion leaning towards the metal end of the joint and vice versa.; and the stress concentration contour results of the composite region are shown in figures, Fig.4.20 for the axial stress, Fig.4.21 for the peel stress and Fig.4.23 for the shear stress.

For axial stress concentration, the stress distribution is shown in Fig.4.20 and the values of stress concentration are listed in Table.4.15. Stress distributions changes slightly due to the protrusion angle change. The value of the maximum stress concentration hardly changes for both zones.

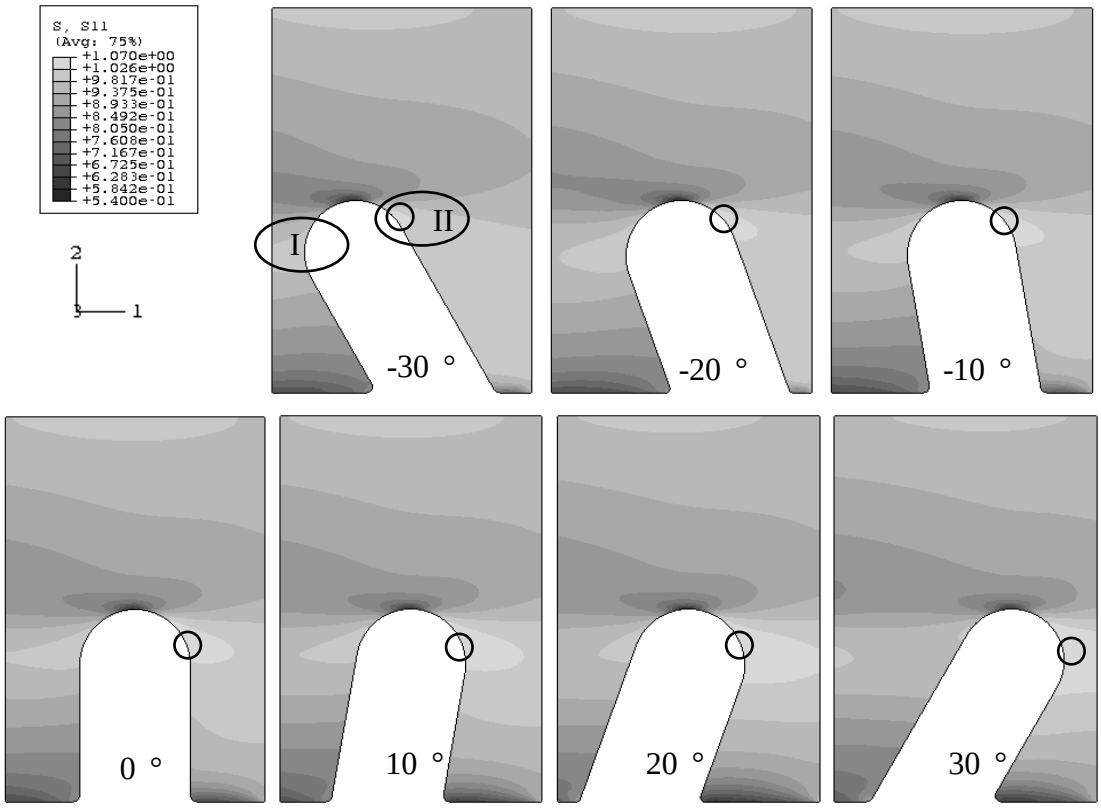

Fig.4.20 *Axial stress concentration contour results in the composite region with different protrusion angle*

Table.4.15 *Maximum axial stress concentration in the composite region with different protrusion angle*

Angle [degrees]	-30	-20	-10	0	10	20	30
σ_{11}/σ Zone I	9.95e-1	1.01e0	1.01e0	1.01e0	1.01e0	1.01e0	9.92e-1
σ_{11}/σ Zone II	1.06e0	1.06e0	1.06e0	1.06e0	1.05e0	1.06e0	1.07e0

For peel stress concentration, the stress distribution is shown in Fig.4.21 and the values of stress concentration are listed in Table.4.16. And the comparison of the maximum peel stress concentration for the marked zones is shown in Fig.4.22.

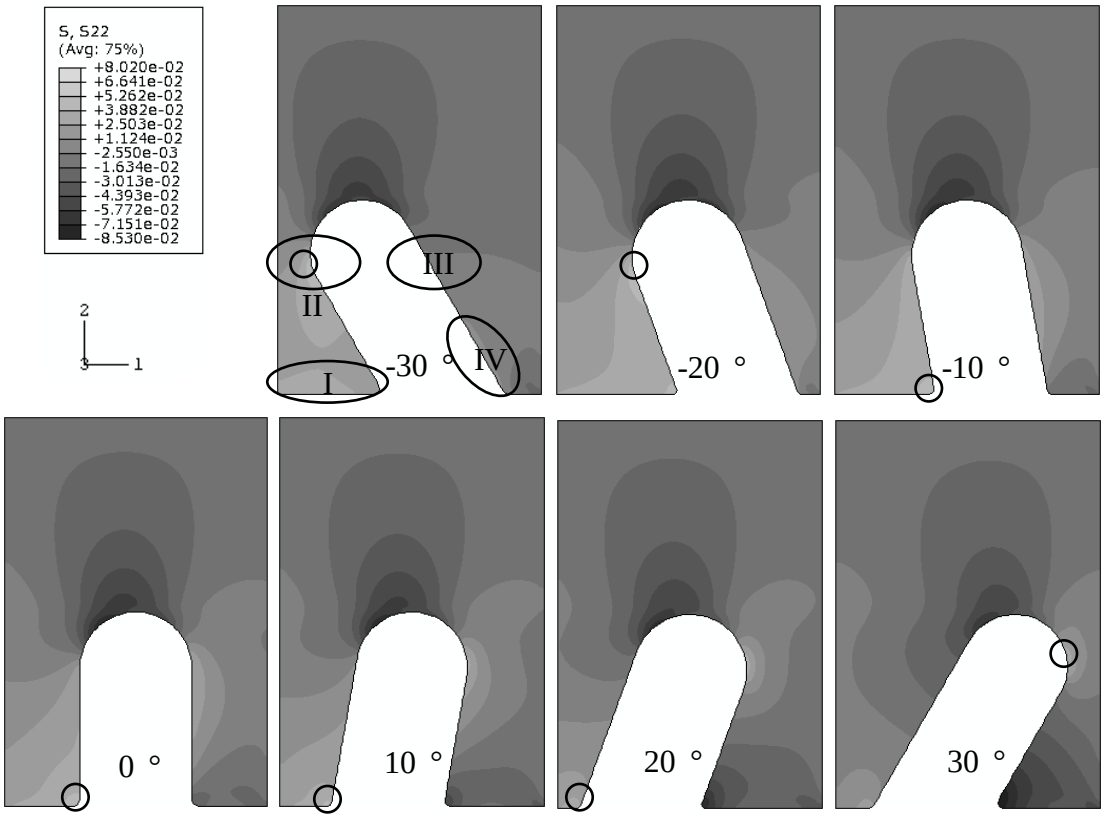

Fig.4.21 *Peel stress concentration contour results in the composite region with different protrusion angle*

Table.4.16 *Maximum peel stress concentration in the composite region with different protrusion angle for the marked zones*

Angle [degrees]	-30	-20	-10	0	10	20	30
σ_{22}/σ Zone I	5.96e-2	6.92e-2	7.32e-2	7.63e-2	6.89e-2	6.61e-2	4.55e-2
σ_{22}/σ Zone II	7.85e-2	8.02e-2	6.78e-2	-	-	-	-
σ_{22}/σ Zone III	2.66e-2	3.83e-2	4.67e-2	5.30e-2	5.73e-2	6.16e-2	6.14e-2
σ_{22}/σ Zone IV	2.76e-2	3.74e-2	3.36e-2	-	-	-	-

For Zone I, stress concentration increases and reaches maximum at perpendicular protrusion angle, and decreases with the protrusion angle to 30 degrees. For Zone II, the stress concentrations occurred only for the minus angle protrusions, and the concentration region moved away for the perpendicular protrusion and the positive

protrusion angles. For Zone III, the situation is almost exactly opposite to Zone II, stress concentration increases with the protrusion angle increase, from around 2.7e-2 to more than 6.0e-2. For Zone IV, the stress concentration decreases from minus angles to positive angles; for the positive angles the stress concentration changes direction from peel to compression.

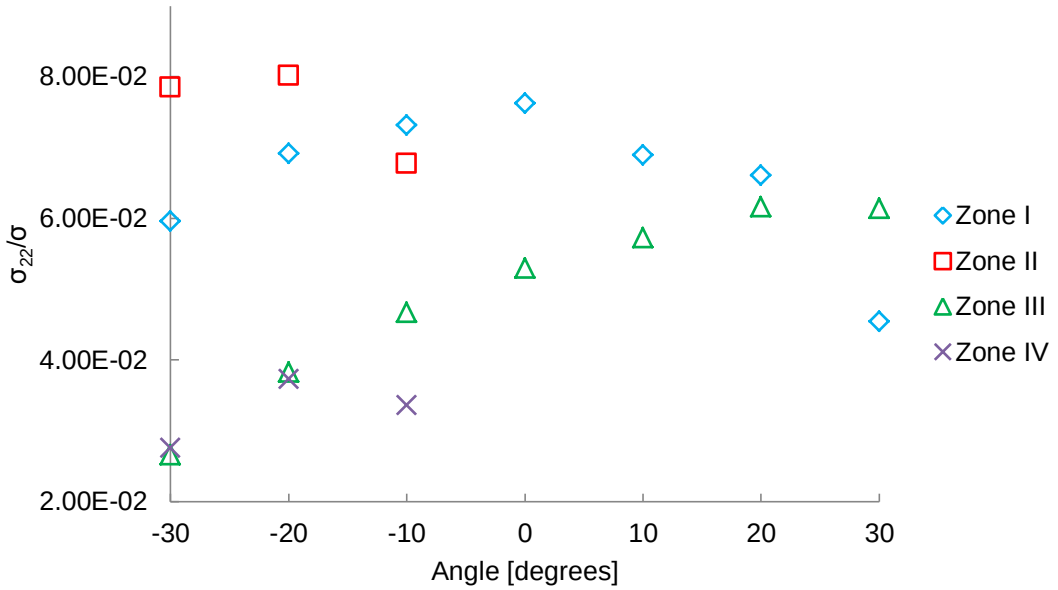

Fig.4.22 *Maximum peel stress concentration with different protrusion angle for marked zones in Fig.4.21*

For shear stress concentration, the stress distribution is shown in Fig.4.23 and the values of stress concentration are listed in Table.4.17. And the comparison of the maximum shear stress concentration for the marked zones is shown in Fig.4.24.

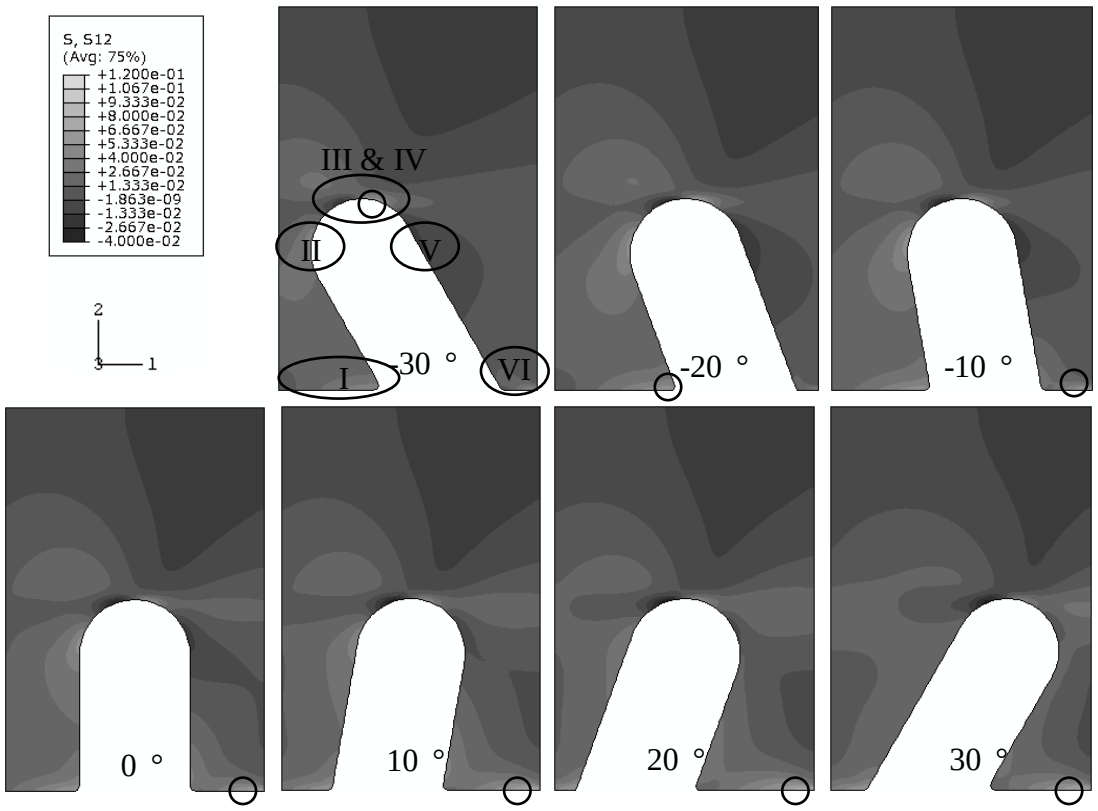

Fig.4.23 *Shear stress concentration contour results in the composite region with different protrusion angle*

Table.4.17 *Maximum shear stress concentration in the composite region with different protrusion angle*

Angle [degrees]	-30	-20	-10	0	10	20	30
σ_{12}/σ Zone I	6.65e-2	8.92e-2	8.57e-2	8.23e-2	8.25e-2	8.80e-2	8.86e-2
σ_{12}/σ Zone II	6.54e-2	7.54e-2	7.54e-2	7.28e-2	6.67e-2	5.42e-2	3.76e-2
σ_{12}/σ Zone III	1.57e-2	2.49e-2	2.67e-2	3.07e-2	3.57e-2	3.91e-2	3.51e-2
σ_{12}/σ Zone IV	7.69e-2	8.49e-2	7.46e-2	7.04e-2	6.54e-2	7.05e-2	6.25e-2
σ_{12}/σ Zone V	4.93e-3	1.50e-2	1.43e-2	7.95e-3	8.70e-4	5.32e-3	1.37e-2
σ_{12}/σ Zone VI	7.34e-2	6.42e-2	9.04e-2	9.87e-2	1.09e-1	1.11e-1	1.05e-1

For Zone I, the maximum stress concentration is the lowest for the minus 30 degree protrusion angle. For Zone II, from minus to positive protrusion angles, the stress concentration increases until minus 10 degrees and then decreases. For Zone III at the

top of the protrusion, the stress concentration increases from minus protrusion angles to 20 degree protrusion angle, and then decreases. For Zone IV, the stress concentration increases until minus 20 degree protrusion, and then hardly changes. For Zone V, the stress concentrations are generally small compare to other zones, the concentration increases until minus 20 degree and decreases until 10 degree and decreases then increases again. For Zone VI, the stress concentration decreases until minus 20 degree and increases until 20 degree, and then decreases slightly to 30 degree.

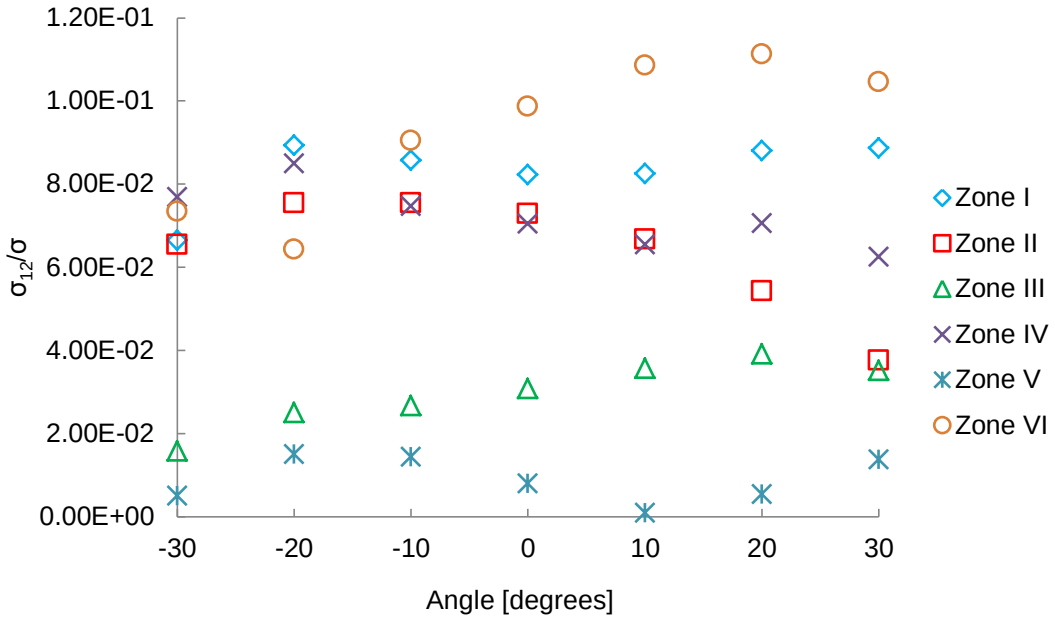

Fig.4.24 *Maximum shear stress concentration with different protrusion angle for marked zones in Fig.4.23*

4.3.3 Effect of protrusion angle for the hill shape protrusions

For the effects of the protrusion angle, the cases of -30 to 30 degrees with 10 degrees increments were analysed, where the minus angle stands for the protrusion leaning towards the metal end of the joint and vice versa. The stress concentration contour results of the composite region are shown in figures, Fig.4.25 for the axial stress, Fig.4.26 for the peel stress and Fig.4.28 for the shear stress.

For the axial stress concentration, the locations of the maximum stress concentration for different protrusion angles are similar. There is less than 5% variation in the maximum stress concentrations for different protrusion angles, see Table.4.18.

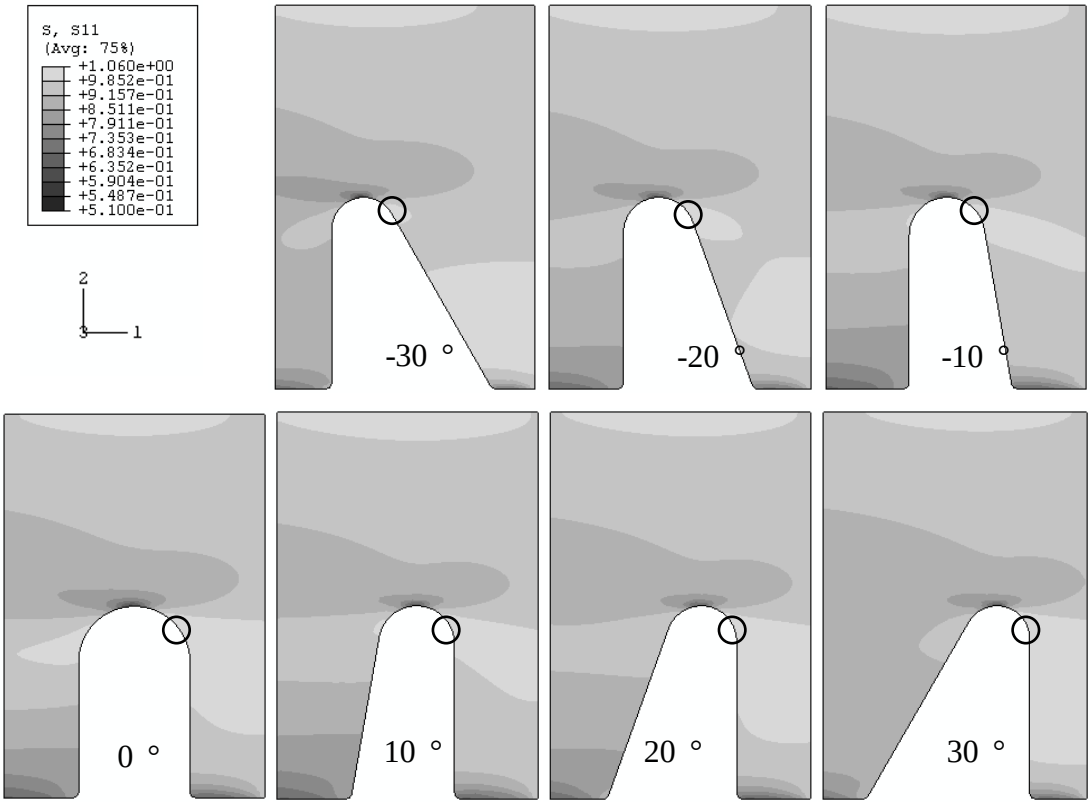

Fig.4.25 *Axial stress concentration contour results in the composite region with different protrusion angle*

Table.4.18 *Maximum axial stress concentration in the composite region with different protrusion angle*

Angle [degrees]	-30	-20	-10	0	10	20	30
σ_{11}/σ	1.02e0	1.03e0	1.03e0	1.06e0	1.03e0	1.03e0	1.04e0

For the peel stress concentration, in Fig.4.26, there are two zones marked for stress concentration comparisons. Apart from the 30 degree protrusion, the maximum stress concentrations occur at the left foot of the protrusion, see the marked circles in Fig.4.26. The maximum stress concentrations are listed in Table.4.19. The stress concentration for Zone I is reduced with protrusion angle change from minus to

positive; and the stress concentration for Zone II increased with protrusion angle change from minus to positive. The trends are clearly shown in Fig.4.27.

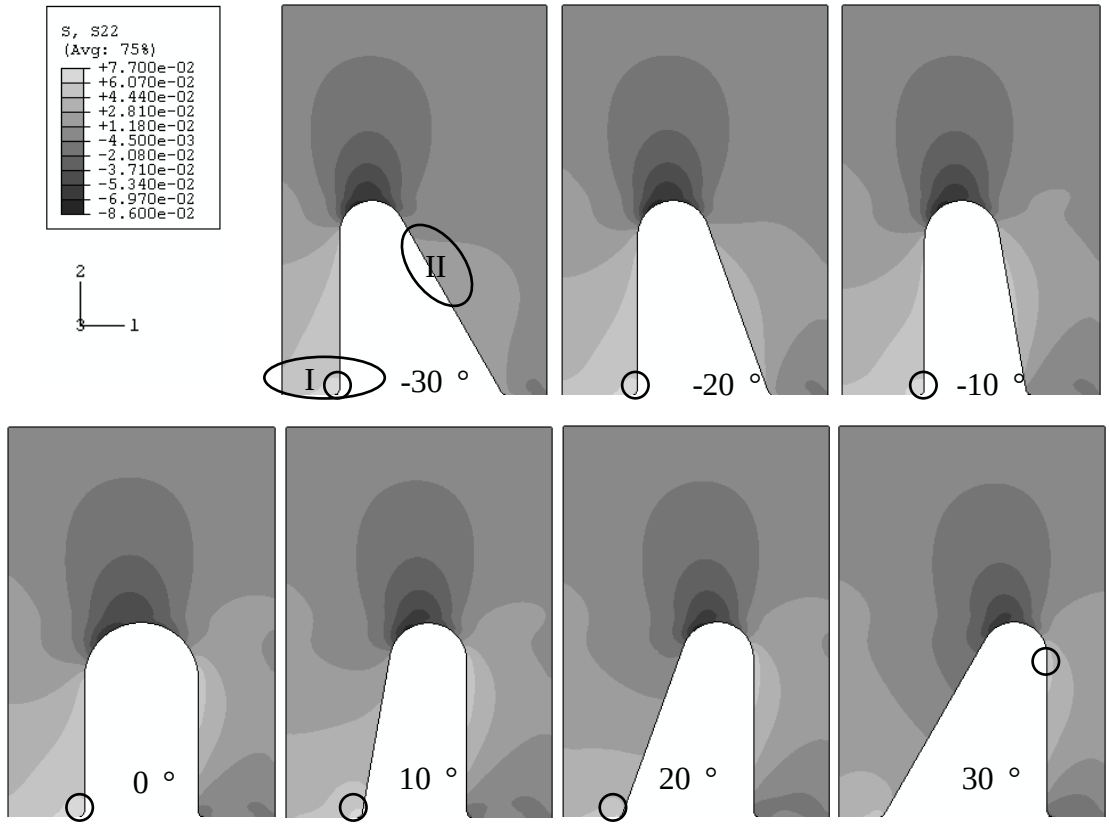

Fig.4.26 *Peel stress concentration contour results in the composite region with different protrusion angle*

Table.4.19 *Maximum peel stress concentration in the composite region with different protrusion angle*

Angle [degrees]	-30	-20	-10	0	10	20	30
σ_{22}/σ Zone I	7.38e-2	7.09e-2	7.24e-2	7.63e-2	7.02e-2	6.40e-2	5.27e-2
σ_{22}/σ Zone II	2.52e-2	3.88e-2	4.81e-2	5.30e-2	5.28e-2	5.16e-2	5.64e-2

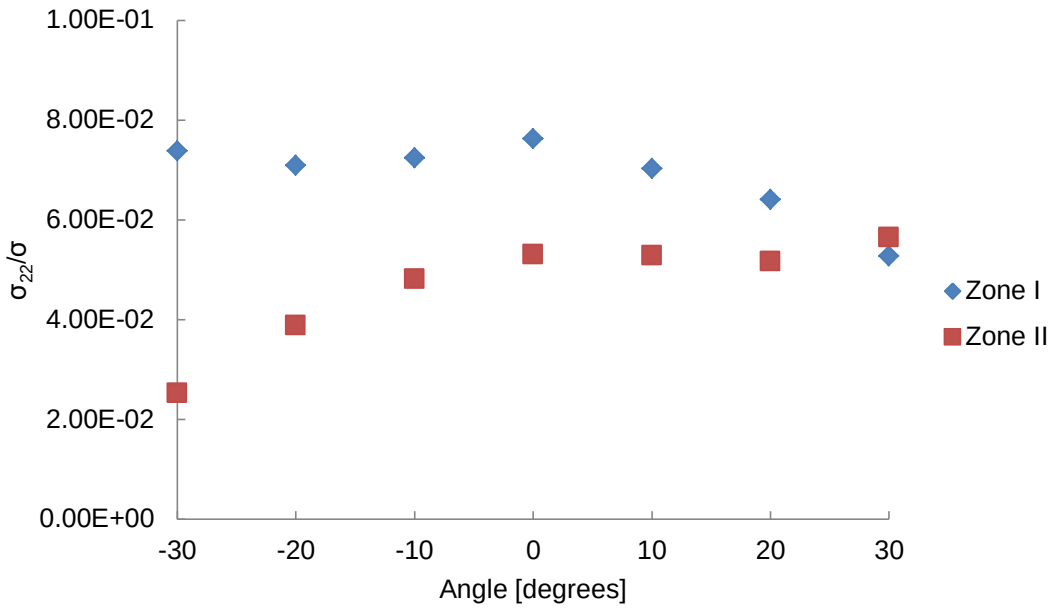

Fig.4.27 *Maximum peel stress concentration with different protrusion angle for marked zones in Fig.4.26*

For the shear stress concentration, the contour results are shown in Fig.4.28. Apart from the 30 degree protrusion, the maximum stress concentrations occur at the right bottom corner for the composite region, see the circles in Fig.4.28. The maximum stress concentrations for six zones are listed in Table.4.20 (absolute values). The effect of the protrusion angle for different zones is shown in Fig.4.29. For Zone V and VI, the stress concentration stays at the same level comparing with other zones. For Zone I, the stress concentrations are at a similar level for the minus protrusion angles, and increases with the positive protrusion angle. For Zone II, the stress concentration decreases with the protrusion angle increase. For Zone III and IV, the stress concentrations stay at similar levels, much lower than that of Zone I or Zone VI.

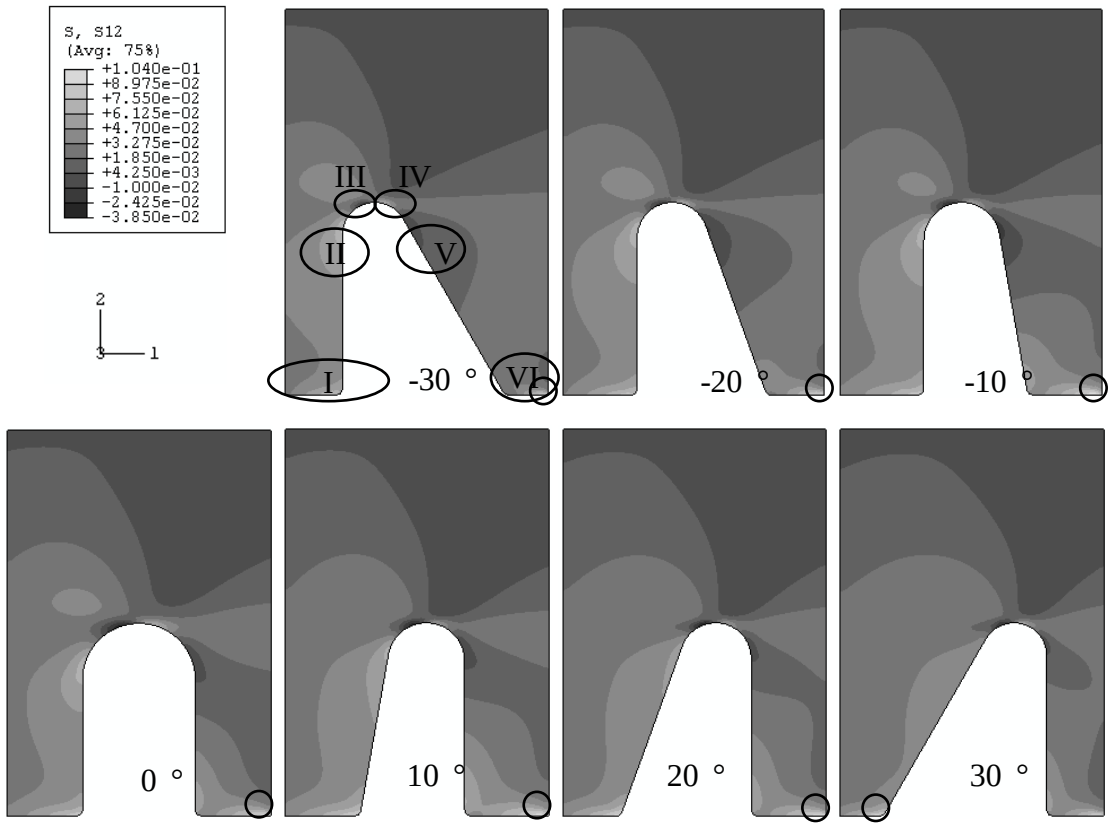

Fig.4.28 *Shear stress concentration contour results in the composite region with different protrusion angle*

Table.4.20 *Maximum shear stress concentration in the composite region with different protrusion angle*

Angle [degrees]	-30	-20	-10	0	10	20	30
σ_{12}/σ Zone I	7.81e-2	8.78e-2	8.39e-2	8.23e-2	8.86e-2	9.83e-2	1.02e-1
σ_{12}/σ Zone II	8.36e-2	7.71e-2	7.70e-2	7.28e-2	6.71e-2	5.39e-2	4.05e-2
σ_{12}/σ Zone III	3.27e-2	1.97e-2	2.72e-2	3.07e-2	3.35e-2	3.84e-2	2.70e-2
σ_{12}/σ Zone IV	6.74e-2	6.72e-2	5.84e-2	7.04e-2	5.24e-2	5.10e-2	7.95e-2
σ_{12}/σ Zone V	5.24e-3	1.23e-2	1.67e-2	7.95e-3	1.02e-2	5.88e-3	7.49e-3
σ_{12}/σ Zone VI	8.86e-2	9.60e-2	1.03e-1	9.87e-2	1.04e-1	1.02e-1	9.54e-2

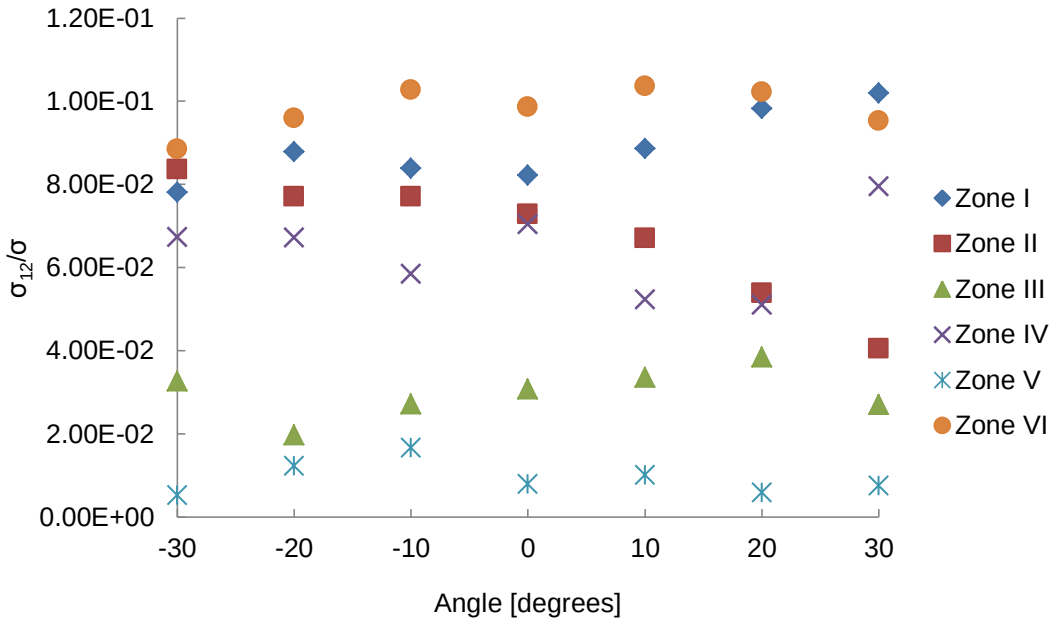

Fig.4.29 *Maximum shear stress concentration with different protrusion angle for marked zones in Fig.4.28*

4.3.4 Effect of protrusion shape for the end protrusions

For the end protrusion case, the stress concentrations of axial, peel and shear stresses are compared for the different shape. Axial stress concentration locations are similar for different shapes and the trends are similar for different protrusion shape. However, the stress concentration is lower with angled hill shape protrusions, around 5% lower. The values of the maximum axial stress concentration are listed in Table.4.21 and

Fig.4.30. The trend is not monotonic, minus 30 degree protrusion shows the lowest maximum stress concentration, especially for the hill shape.

Table.4.21 *Maximum axial stress concentration in the composite region with different protrusion angle and shape*

Angle [degrees]	-30	-20	-10	0	10	20	30
σ_{11}/σ Zone II - parallel	1.06e0	1.06e0	1.06e0	1.06e0	1.05e0	1.06e0	1.07e0
σ_{11}/σ - hill	1.02e0	1.03e0	1.03e0	1.06e0	1.03e0	1.03e0	1.04e0

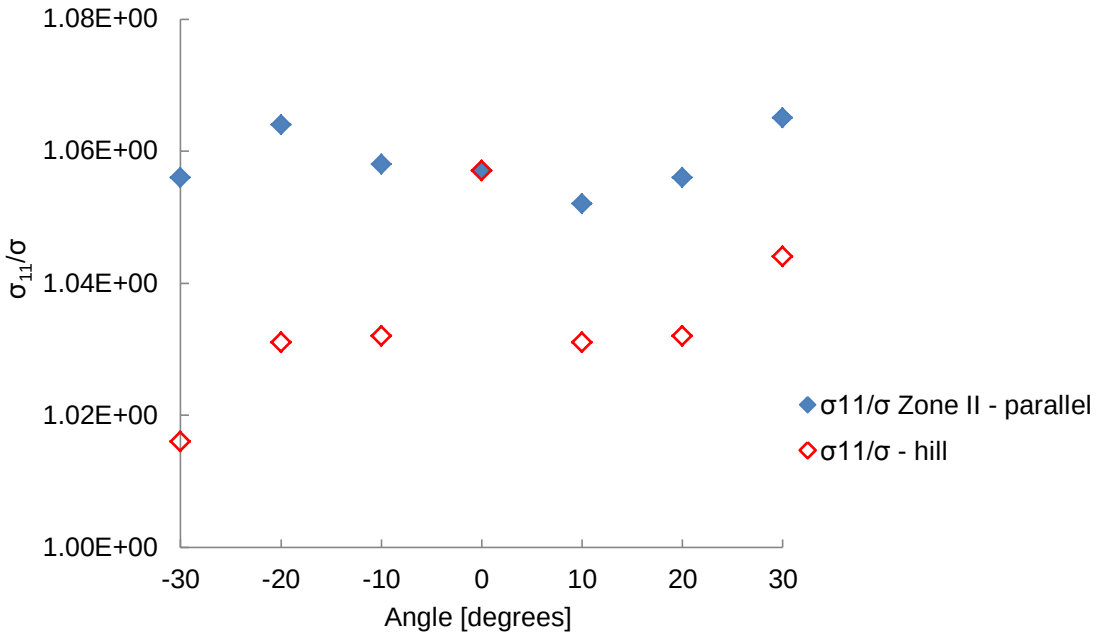

Fig.4.30 *Maximum axial stress concentration with different protrusion angle and shape*

The values for the maximum stress concentration at around the top of the protrusion region are listed in Table.4.22 for peel stress and Table.4.23 for shear stress (absolute values), also see Fig.4.31 and Fig.4.32. For the parallel shape protrusion, the zones are marked in Fig.4.21 and Fig.4.23; for the hill shape protrusion in Fig.4.26 and Fig.4.28. The effect of the shape is not significant. For the peel stress, in Fig.4.31, for the two zones, maximum stress concentrations are similar for most of the protrusion angles.

Table.4.22 *Maximum peel stress concentration in the composite region with different protrusion angle and shape*

Angle [degrees]	-30	-20	-10	0	10	20	30
σ_{22}/σ Zone I - parallel	5.96e-2	6.92e-2	7.32e-2	7.63e-2	6.89e-2	6.61e-2	4.55e-2
σ_{22}/σ Zone III - parallel	2.66e-2	3.83e-2	4.67e-2	5.30e-2	5.73e-2	6.16e-2	6.14e-2
σ_{22}/σ Zone I - hill	7.38e-2	7.09e-2	7.24e-2	7.63e-2	7.02e-2	6.40e-2	5.27e-2
σ_{22}/σ Zone II - hill	2.52e-2	3.88e-2	4.81e-2	5.30e-2	5.28e-2	5.16e-2	5.64e-2

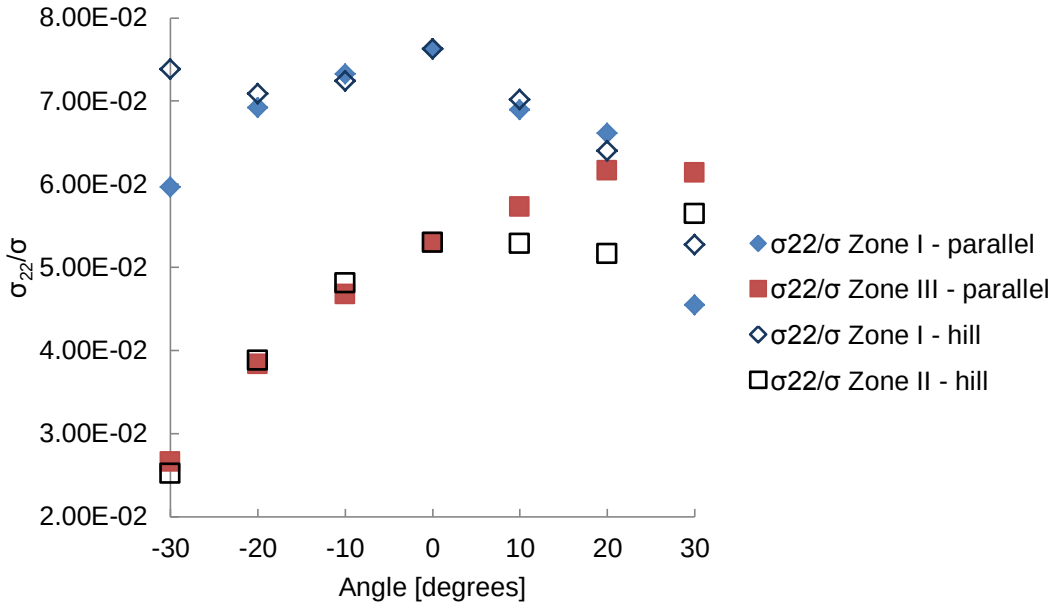

Fig.4.31 *Maximum peel stress concentration with different protrusion angle and shape*

The peel stresses of zones from Chapter 4, Fig.4.21 Zone III for the parallel shape and Fig.4.26 Zone II for the hill shape are compared. For peel stress concentration, there are similar trends with different shapes for protrusion angle change. Generally when the protrusion angle is -30 degrees, the stress concentration is low.

The shear stresses of zones from top of the protrusions are compared, see Zones II to V in Fig.4.24 and Fig.4.29. In Fig.4.32, the values and trends of stress concentration are similar for different shapes in Zone II and V; with the angle change stress concentration decreases in Zone II and oscillating in Zone V. The stress concentration is fairly small in Zone V. For Zone III, the values and trends are also similar for

different shape protrusions; the stress concentration reaches minimum for parallel shape protrusion at -30 degrees. The stress concentration values for Zone III are generally small compared to other zones. For Zone IV, the trends are similar for different shape protrusions, where the stress concentration decreases for the positive angle with some exceptions. The hill shape 30 degrees protrusion shows an increase in the stress concentration. For the shear stress at the bottom of the composite region, in Fig.4.32, for Zone I, stress concentrations are higher for the hill shape with the protrusion towards the composite end of the joint; for Zone VI, the stress concentrations are significantly higher for the hill shape protrusions in the minus angle cases (13 to 20%) and lower for the positive angle cases (less than 10%).

Table.4.23 *Maximum shear stress concentration in the composite region with different protrusion angle and shape*

Angle [degrees]	-30	-20	-10	0	10	20	30
σ_{12}/σ Zone I - parallel	6.65e-2	8.92e-2	8.57e-2	8.23e-2	8.25e-2	8.80e-2	8.86e-2
σ_{12}/σ Zone II - parallel	6.54e-2	7.54e-2	7.54e-2	7.28e-2	6.67e-2	5.42e-2	3.76e-2
σ_{12}/σ Zone III - parallel	1.57e-2	2.49e-2	2.67e-2	3.07e-2	3.57e-2	3.91e-2	3.51e-2
σ_{12}/σ Zone IV - parallel	7.69e-2	8.49e-2	7.46e-2	7.04e-2	6.54e-2	7.05e-2	6.25e-2
σ_{12}/σ Zone V - parallel	4.93e-3	1.50e-2	1.43e-2	7.95e-3	8.70e-4	5.32e-3	1.37e-2
σ_{12}/σ Zone VI - parallel	7.34e-2	6.42e-2	9.04e-2	9.87e-2	1.09e-1	1.11e-1	1.05e-1
σ_{12}/σ Zone I - hill	7.81e-2	8.78e-2	8.39e-2	8.23e-2	8.86e-2	9.83e-2	1.02e-1
σ_{12}/σ Zone II - hill	8.36e-2	7.71e-2	7.70e-2	7.28e-2	6.71e-2	5.39e-2	4.05e-2
σ_{12}/σ Zone III - hill	3.27e-2	1.97e-2	2.72e-2	3.07e-2	3.35e-2	3.84e-2	2.70e-2
σ_{12}/σ Zone IV - hill	6.74e-2	6.72e-2	5.84e-2	7.04e-2	5.24e-2	5.10e-2	7.95e-2
σ_{12}/σ Zone V - hill	5.24e-3	1.23e-2	1.67e-2	7.95e-3	1.02e-2	5.88e-3	7.49e-3
σ_{12}/σ Zone VI - hill	8.86e-2	9.60e-2	1.03e-1	9.87e-2	1.04e-1	1.02e-1	9.54e-2

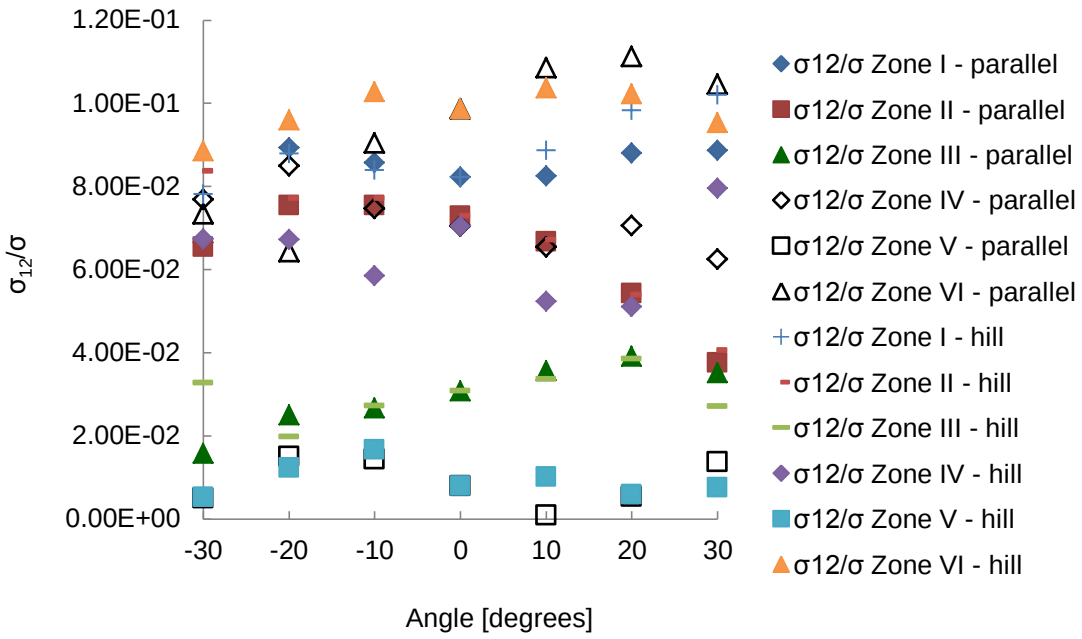

Fig.4.32 *Maximum shear stress concentration with different protrusion angle and shape*

4.4 Summary

Results for the effect of protrusion height, angle and shape are presented in this chapter for two different scenarios. For the repetitive case, the protrusions were assumed to be constrained with repetitive boundary conditions. With increasing height, the stress concentration within the composite region reduces. The stress spreads more into the composite region with the protrusion height with lower concentration level. For the protrusion angle change, the stress distribution is symmetric for the relative positive and negative protrusion angles despite the protrusion shape. The effect of the protrusion shape change leads to significant reduction in peel and shear stress, the level of stress concentration changed for all the stress components.

For the protrusions on the step edge, increasing height reduces the stress concentration. For the peel stress, the shape change did not have obvious effect on either the stress concentration at around top of the protrusion region or the maximum stress concentration. For shear stress concentration, the shape effects are complicated and less obvious due to the shape change comparing with the repetitive protrusion

case. The stress concentration is generally smaller for the minus 30 degrees protrusion angle for both shapes.

For both the repetitive and the end protrusion cases, shear and peel stress concentrations are fairly small. The importance of the shape angle and different zones in respect of the failure processes is discussed in Chapter 6. Further discussions can be found in Chapter 7.

5
FE MODELLING THE PROTRUSION DISTRIBUTION EFFECTS WITH THREE DIMENSIONAL MODELS

5.1 Introduction

In this chapter, the results of the three dimensional analyses are presented from the 3D global model and the submodel with various spatial arrangements along with some protrusion distribution density effects. The models description can be found in Chapter 3 section 3.4, and the composite materials characterisation can be found in Chapter 3, section 3.2.2. The loading applied for the 3D global model was 116 MPa stress [Smith, 2005], and the loading for the submodels was based on the global model result as described in section 2.5.5. This chapter describes the stress distributions predicted by the submodel method. The significance of those stress distributions to the failure processes is described in Chapter 6.

5.2 Modelling the whole joint with three-dimensional global models

The 3D global model was described in Chapter 3 with the homogenised composite region and homogenised protrusion/composites region (obtained by 3D layered composite model analysis, see Chapter 3, section 3.2). Tensile loading was carried out for the whole joint.

The strain data has been taken from the middle of both halves of the model (the titanium half and composite half, see Fig.6.1), which coincide with the strain gauge location in the tensile experiments (discussed later in Chapter 6).

The 3D tensile simulation results and comparisons with 2D models are shown in Fig.5.1, where CPE and CPS stand for plane strain and plane stress elements.

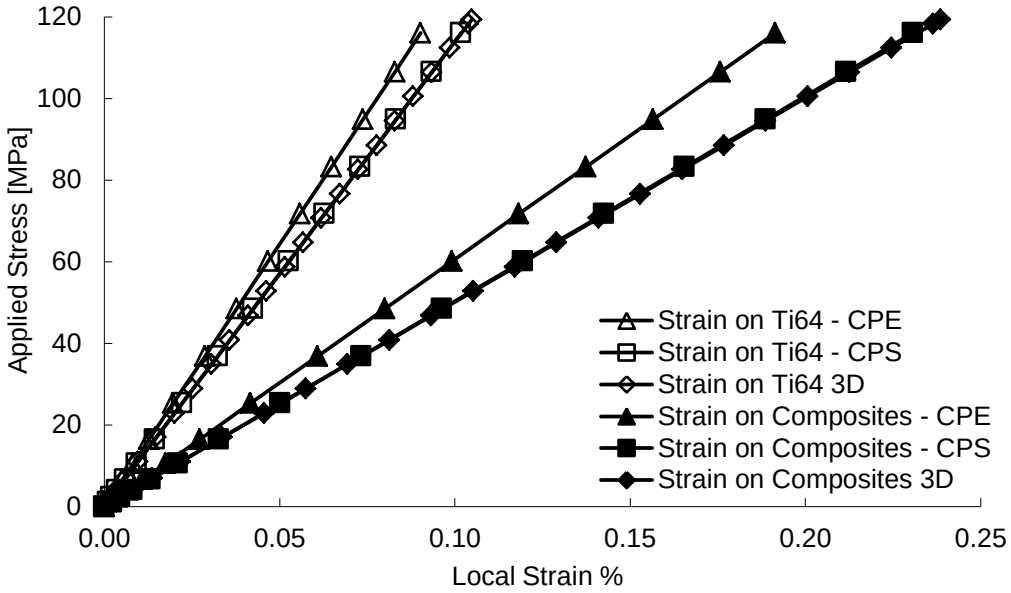

Fig.5.1 *The global models results under tensile loading.*

The global models results are linear elastic. Compared to the 2D global model with homogenised properties, the 2D plane strain global model results as expected are stiffer; the 3D global model results agrees very well with the 2D global model with plane stress elements.

5.3 Three-dimensional submodel tensile simulation results

The 3D submodels include the detailed protrusion geometries and the submodels position within the joint is shown in Fig.3.30 and 3.31, section 3.4.1 Chapter 3. In this section the results are divided in two parts, titanium results and composite results. The diagram of the 3D submodel is shown in Fig.5.2, where the important planes are marked. All results are presented as indicated in Fig.5.2.

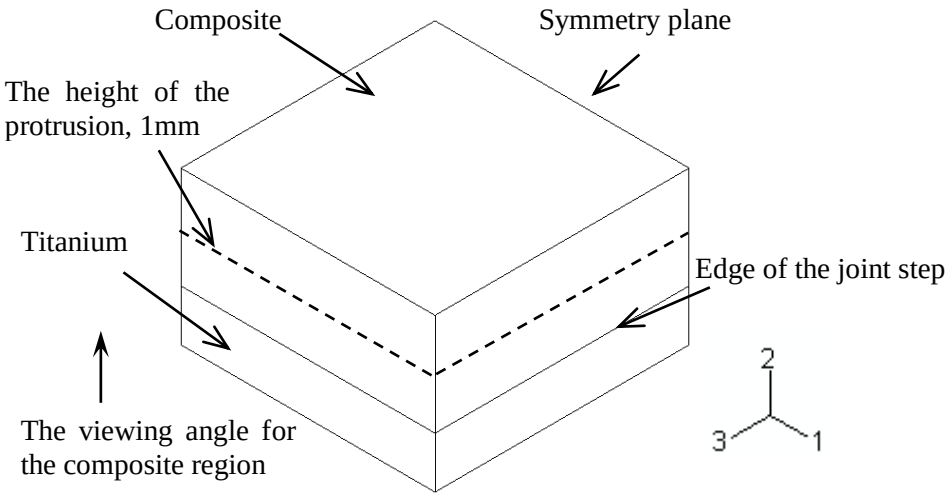

Fig.5.2 *Diagram of the 3D submodel*

5.3.1 Submodel results for the titanium region

Stress contour results for titanium part are shown in Fig.5.3 for the Von Mises stress, (a) square array, (b) rotated measured, (c) measured, and (d) half of the measured density and square array. And the locations for the maximum stress are also shown.

The change of spatial arrangement produces different stress distributions, and variations in the stress components and Von Mises stress. From Fig.5.3 (b), the rotated measured arrangement submodel has higher maximum stresses at the protrusions foot on the edge. This may be caused by these two protrusions located very close to the edge which is driven by the global model. The maximum stress values of stress components and Von Mises are listed in Table.5.1, and also the positions are marked in Fig.5.3 with circles.

Table.5.1 *The maximum Von Mises stress values against protrusion distribution*

	Square array	Rotated measured	Measured	Square array, half distribution density
Von Mises [MPa]	222.4	242.5	223.7	216.7

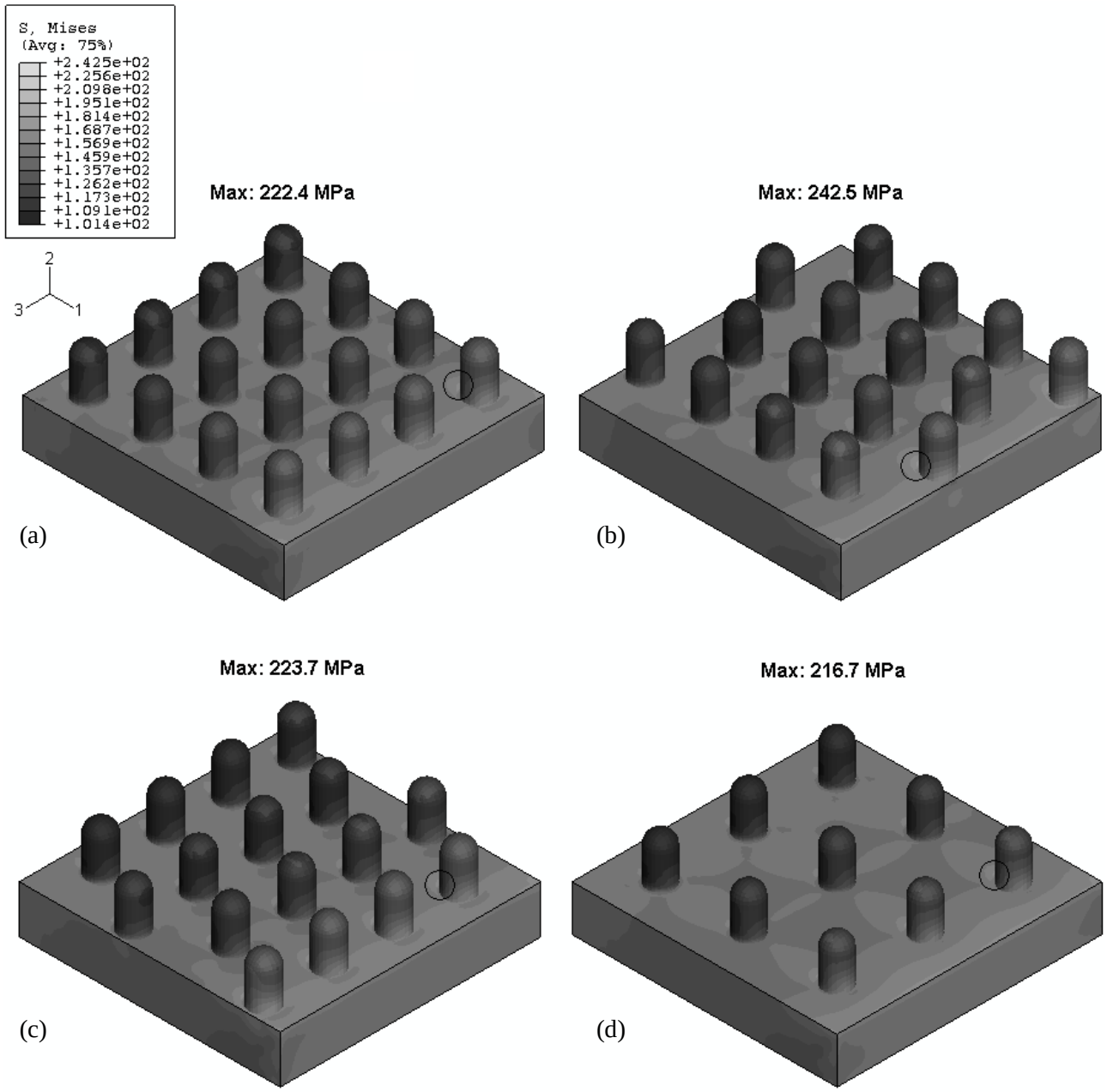

Fig.5.3 *Von Mises results of four different submodels, (a) square array, (b) rotated measured, (c) measured, and (d) half of the measured density and square array*

For Von Mises stress, Fig.5.3, the maximum stress value hardly changes even for the lower protrusion distribution density for different spatial arrangement. There is less than 3% variation in the maximum stresses, despite the protrusion distribution density.

5.3.2 Submodel results for composite region

Stress contour results for the composite part are shown in Fig.5.4, Fig.5.5 and Fig.5.6. Four submodels results are shown for comparison with stress components contours, axial, peel and shear stress respectively in Fig.5.4, Fig.5.5 and Fig.5.6. The region shown includes the composite only above the joint step surface, viewed from the interface and the viewing angle is shown in Fig.5.2. The symmetry plane is the bottom edge of the region shown in the figures. The dimensions are shown in Chapter 3, Fig.3.31. The stress contour results are shown with the unit of MPa.

The change of spatial arrangement resulted in different stress distributions and variation of all the stress components. The maximum stress values for stress components axial stress, peel stress and shear stress are listed in Table.5.2.

Table.5.2 *The maximum stress values of stress components against protrusion distribution*

	Square array	Rotated measured	Measured	Square array, half distribution density
Axial stress [MPa]	141.3	143.0	140.4	139.8
Peel stress [MPa]	12.6	13.6	12.1	12.3
Shear stress [MPa]	16.3	18.1	16.4	15.3

For the axial stress, Fig.5.4, the maximum stress does not vary much for all submodels; high stress concentration occurs on the edge of the joint step for all the arrangements. Other stress concentrations occur at around the foot of the protrusions. The distance between the protrusions in axial direction affects the stress interaction. The further apart the protrusions being in 1-direction, the less stress interaction can be observed. The distance between protrusions in 1-direction (marked in Fig.5.4) is 1.36 mm for (a) and (b), 2.72 mm for (c), and 1.93 mm for (d).

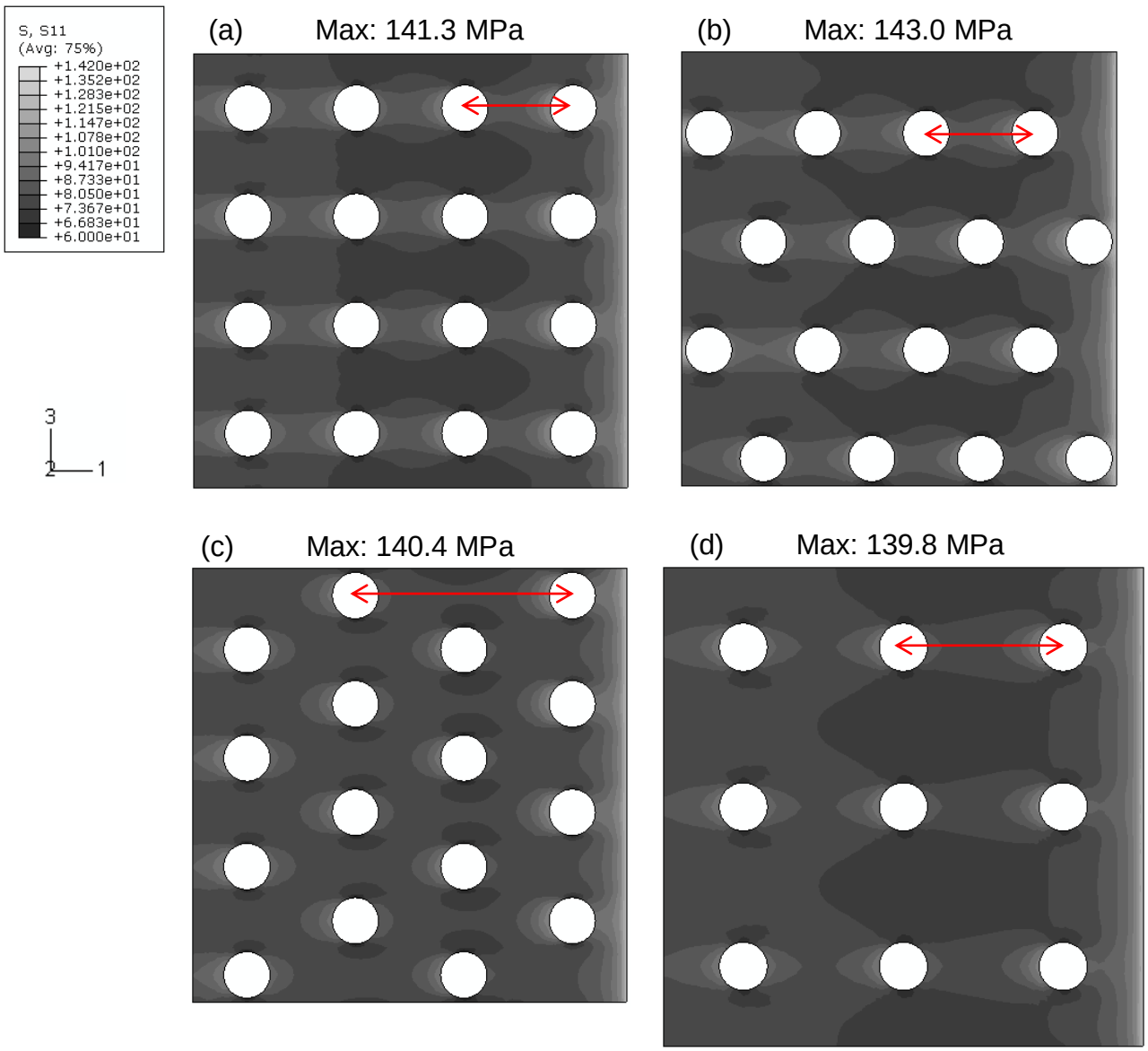

Fig.5.4 *Axial stress results of four different submodels, (a) square array, (b) rotated measured, (c) measured, and (d) half of the measured density and square array*

In Fig.5.5, there is roughly up to 10.6% in average maximum peel stress variation between different spatial arrangement submodels; however, for the half protrusion distribution density submodel, (d) in Fig.5.5, the peel stress is roughly 2.4% lower; (c) in Fig.5.5 shows the lowest stress concentration, 4% lower than (a). Stress concentration mainly occurs at the foot of protrusions despite the spatial arrangements. Once more, the further apart the protrusions being in 1-direction, the less stress concentrations, i.e. (c) in Fig.5.5. For the same distance in 1-direction case, (a) and (b) in Fig.5.5, it is obvious that there is some influence on the stress

distribution and concentration due to the position of the neighbouring protrusions in the other direction (also see Fig.5.4).

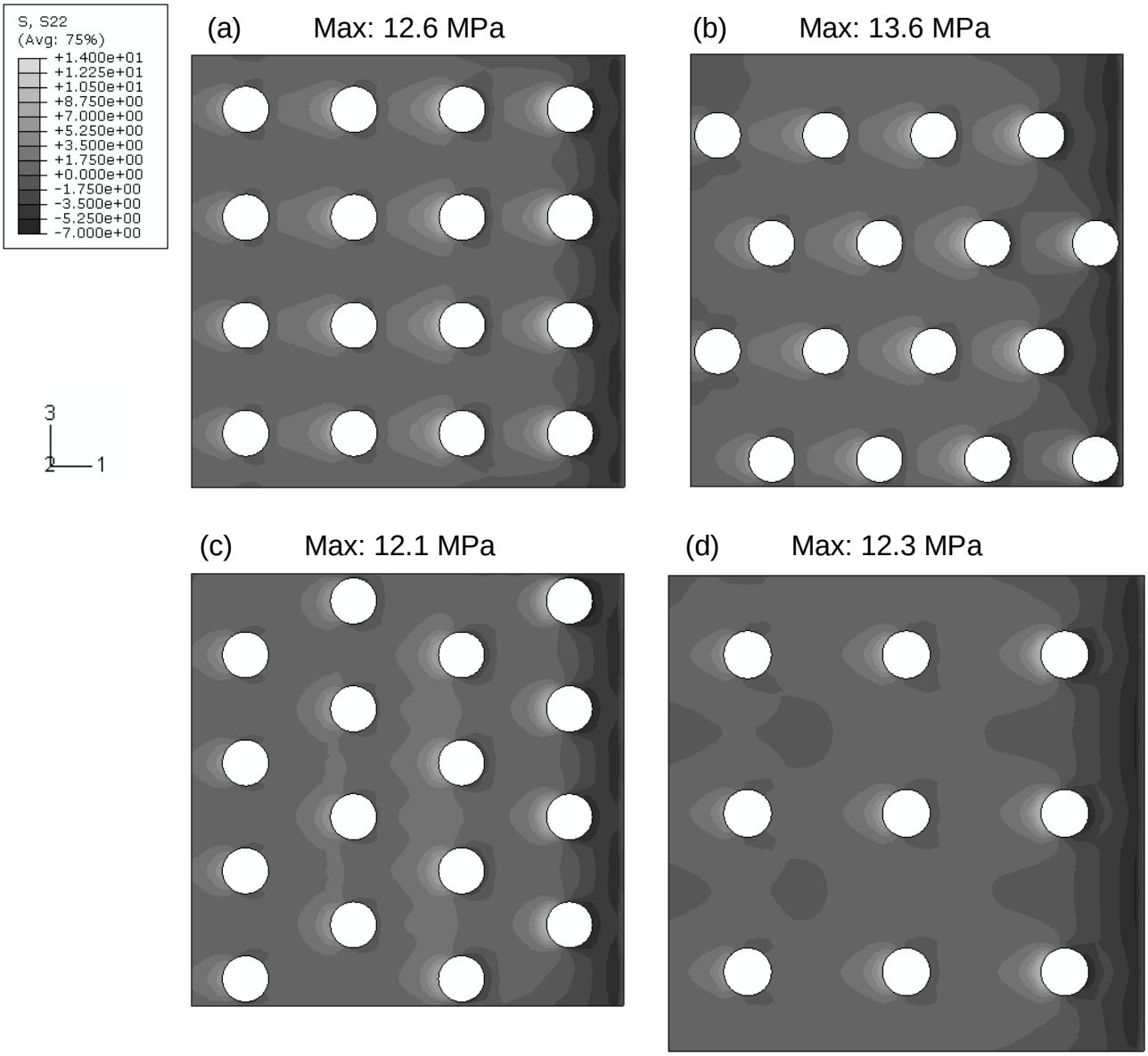

Fig.5.5 *Peel stress results of four different submodels, (a) square array, (b) rotated measured, (c) measured, and (d) half of the measured density and square array*

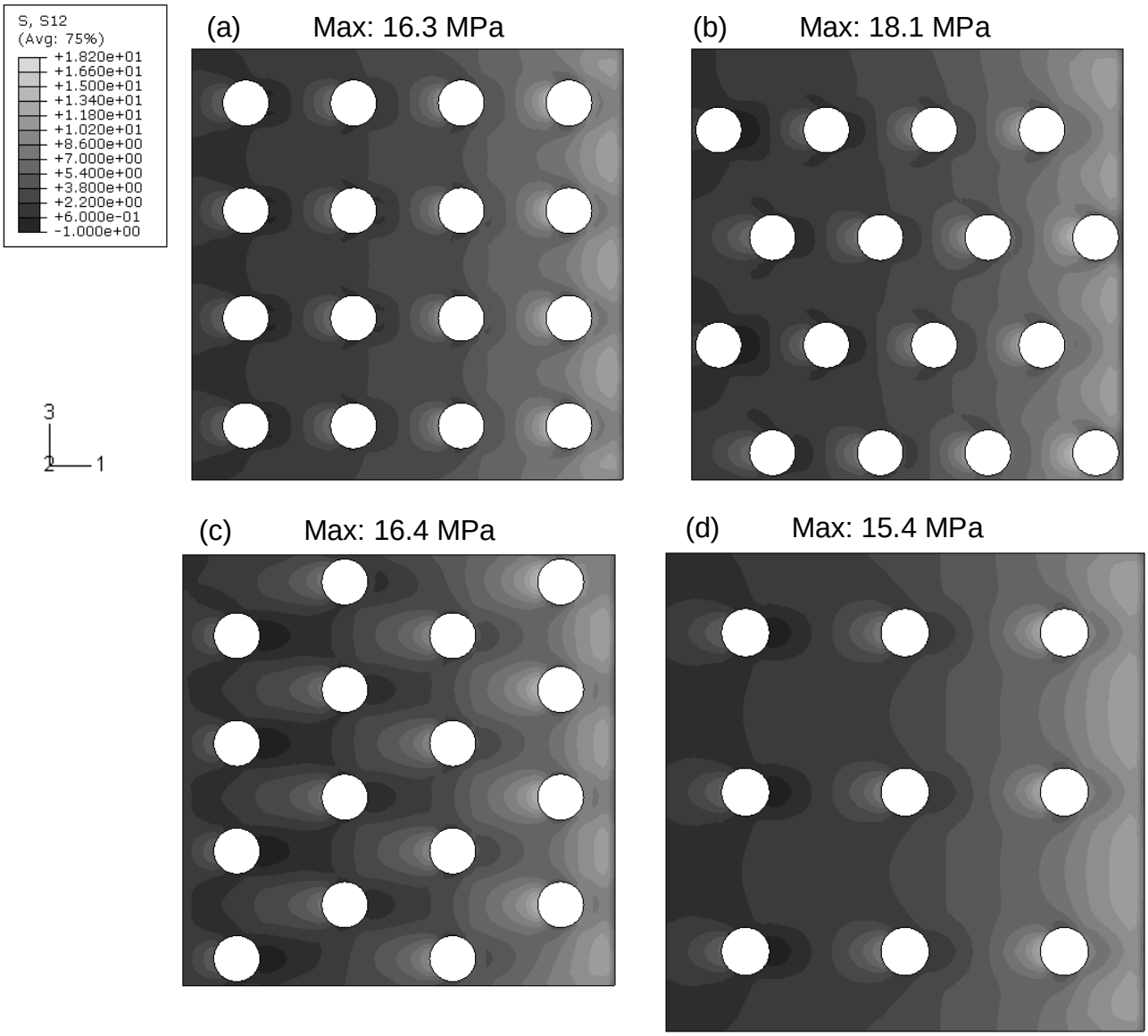

Fig.5.6 *Shear stress results of four different submodels, (a) square array, (b) rotated measured, (c) measured, and (d) half distribution density and square array*

For shear stress component in Fig.5.6, there is some difference of the maximum stress between different spatial arrangement submodels (a), (b) and (c), for the same protrusion distribution density, 9% in average; and there is roughly 6% variation due to the distribution density for the same spatial arrangement, (a) and (d) in the figure. High stress concentration occurs at the joint step edge as well as the foot of the protrusions; and the stress distributions were affected by the position of the neighbouring protrusions. Considering shear and peel stress being the initiation

stresses for composites inter-laminar failure, the axial stress results comparison for the composite part becomes less important.

However, the above results are taken from the interface of the joining surface of the composite. To investigate the composite around the top of the protrusions, the inside of the composite region around the top of the protrusions can be viewed by cutting part of the composite away, see Fig.5.7 and 5.8.

The dotted line in Fig.5.7 represents the cutting plane (0.7mm away from the titanium joint step) for viewing the inside of the composite region around the top of the protrusion. The viewing angle is also shown in the figure. The protrusions of the submodels are 1mm high and the cutting view plane can be seen in cross section in Fig.5.8.

Maximum values of stress components for the different protrusion distribution are listed in Table.5.3. The contour results are shown in Fig.5.9 to Fig.5.11, where the locations for the maximum stress are marked with circles.

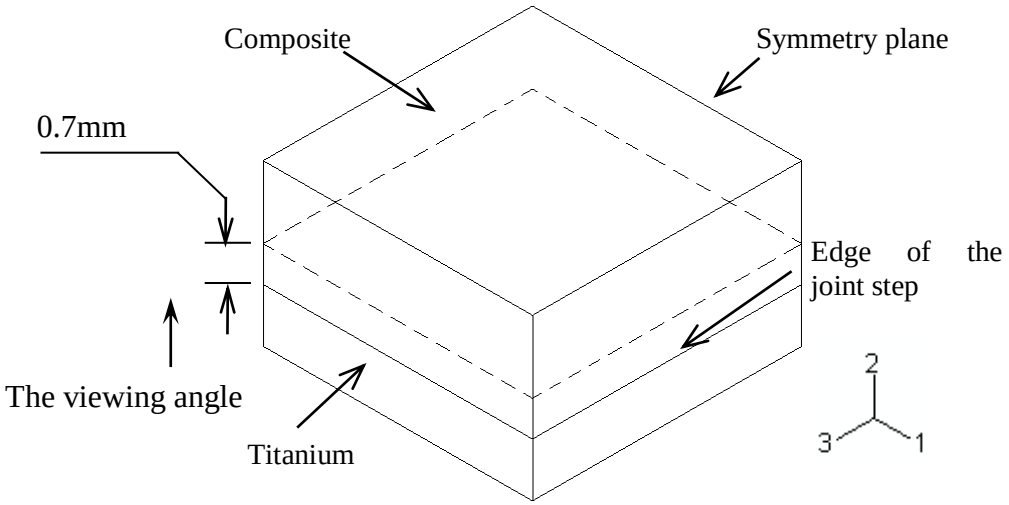

Fig.5.7 *Diagram of the 3D submodel with the dotted line indicating the contour results from where the inside of the composite part can be viewed*

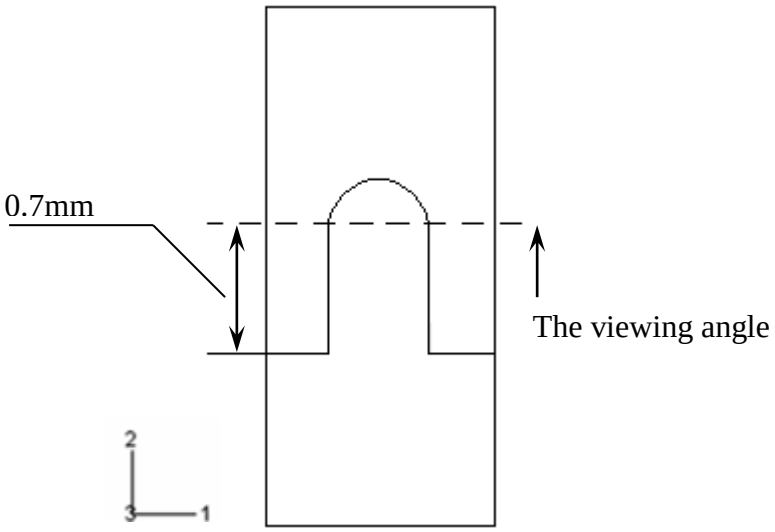

Fig.5.8 *Diagram of the position for around the protrusion top region of the cutting plane as the dotted line, 0.7mm away from the joint step surface*

Table.5.3 *The maximum stress values of stress components against protrusion distribution at around top of the protrusion regions*

	Square array	Rotated measured	Measured	Square array, half distribution density
Axial stress [MPa]	132.4	134.1	130.6	128.7
Peel stress [MPa]	8.2	8.6	7.3	7.0
Shear stress [MPa]	16.3	15.6	13.8	14.9

In Fig.5.9, the maximum stress does not vary much for the same distribution density submodels; the difference for square array submodels with half protrusion distribution density, (d), is roughly 3%. Obvious bands of stress concentration were formed in Fig.5.9 (a), (b) and (d). Comparing (c) with others, with the longest distance between protrusions in 1-direction, only oval shaped stress concentration regions are formed around the protrusions.

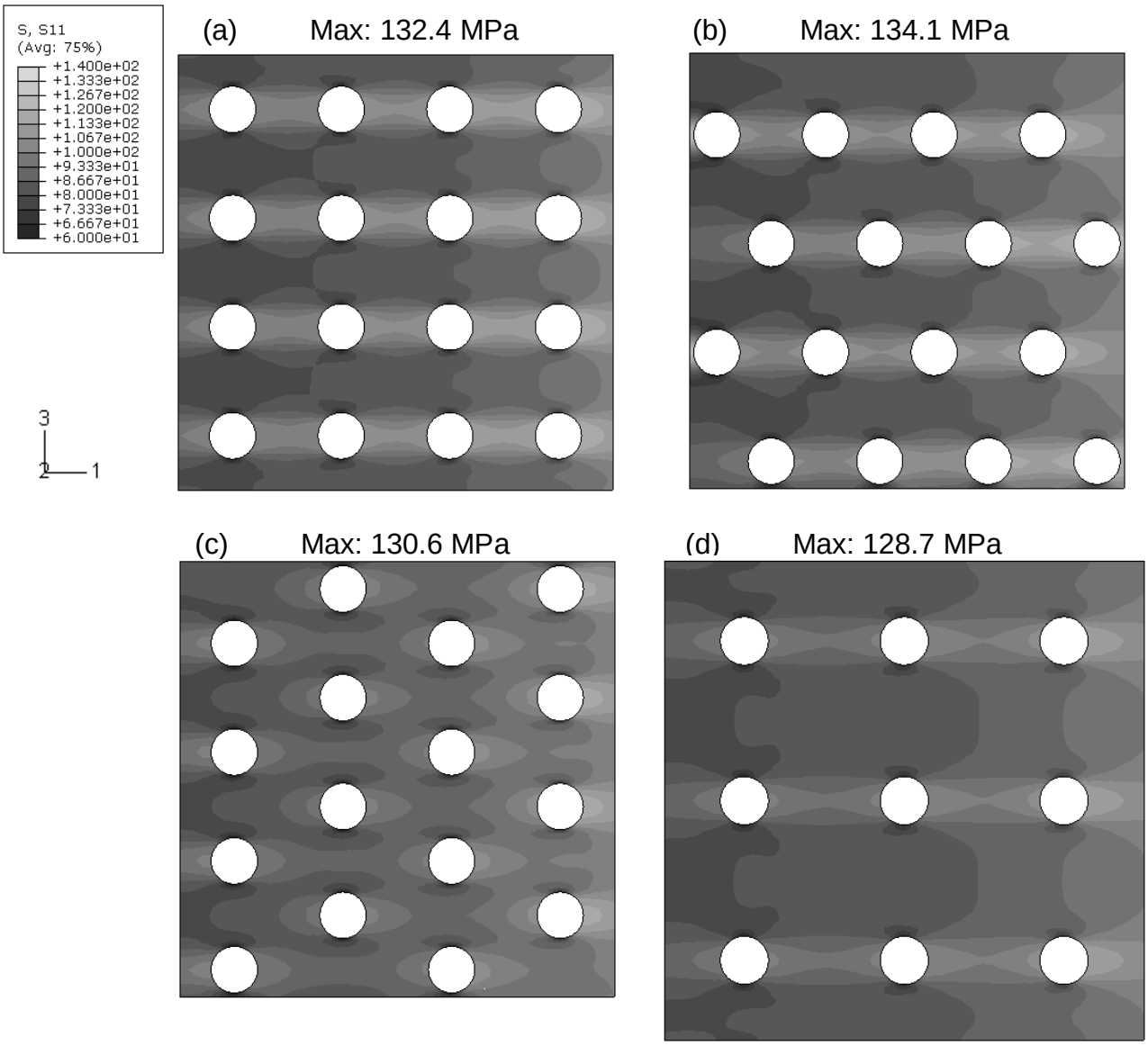

Fig.5.9 *Axial stress results of four different submodels, (a) square array, (b) rotated measured, (c) measured, and (d) half distribution density and square array*

In Fig.5.10, the maximum peel stress value for the rotated measured distribution model, (b), is the highest, a fraction higher than the square model with the same distribution density, (a), more than 18% higher than the measured distribution model, (c), and more than 21% higher compare to the half density square array model, (d). Stress concentration mainly occurs around the protrusions. The influence on the stress distribution due to the protrusion interaction is complicated. Once more, the distance between the protrusions in 1-direction is the longest for (c).

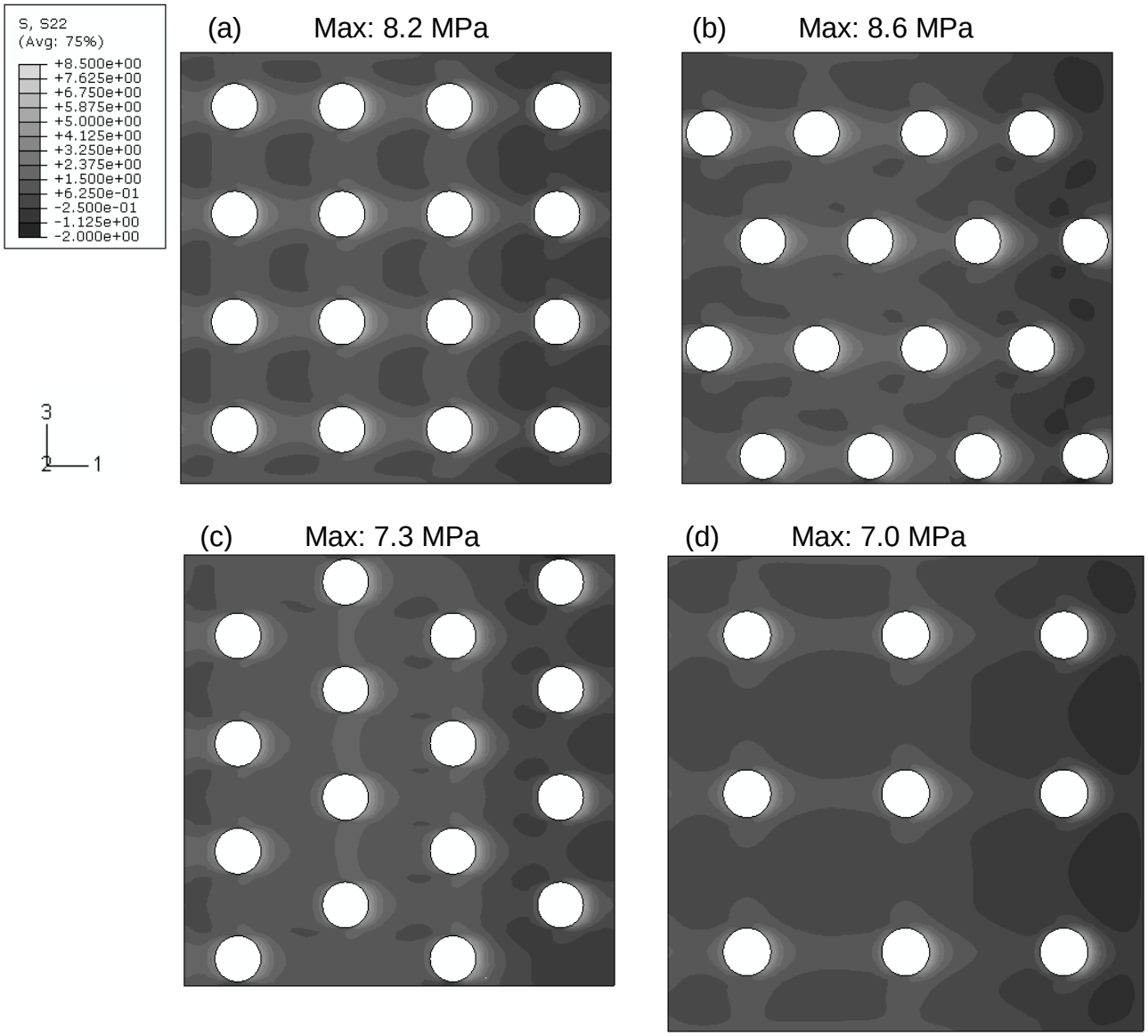

Fig.5.10 *Peel stress results of four different submodels, (a) square array, (b) rotated measured, (c) measured, and (d) half distribution density and square array*

For stress component shear stress in Fig.5.11, the maximum stress of the rotated measured array model is more than 10% higher than the measured distribution model, (c), roughly 3.4% higher than the square array model, (b), and roughly 8.5% higher than the square array with half distribution density model, (d). Stress concentration mainly occurs around the protrusions in the axial direction (1-direction) and around the transverse direction (3-direction) of each protrusion. Higher stress occurs at the left side of the first row of protrusions, and reduces towards the metal end of the joint (left or minus 1-direction).

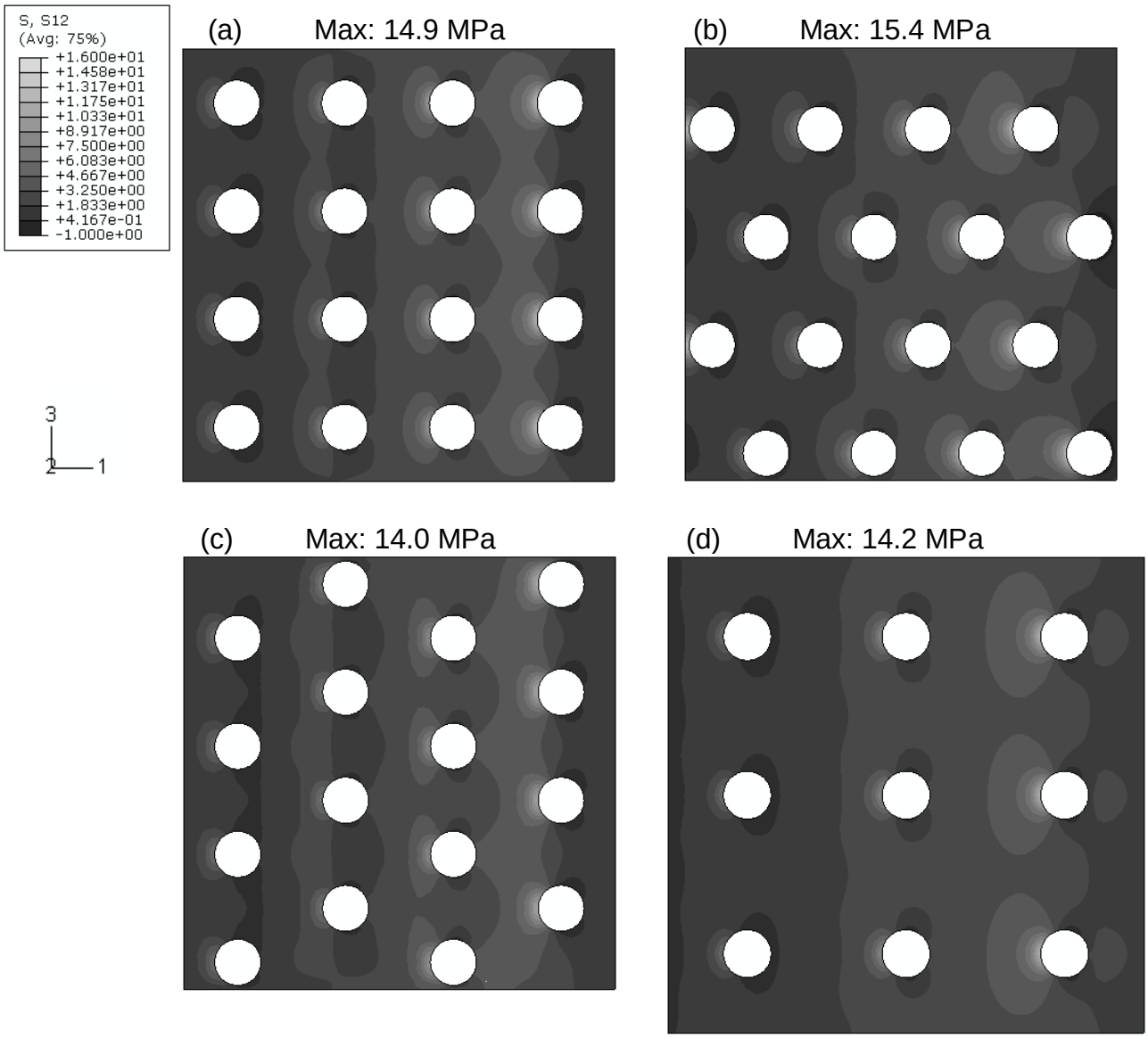

Fig.5.11 *Shear stress results of four different submodels, (a) square array, (b) rotated measured, (c) measured, and (d) half distribution density and square array*

These results suggest that to reduce the maximum stress around the top of the protrusion region within the composite the measured distribution model has advantage over other distribution methods with the same distribution density. These effects are further investigated using cross section of the protrusion layers in the next section.

5.4 Three-dimensional analyses – spatial arrangements

It has been shown in Chapter 4 that there are stress concentrations (axial and shear) around the top of the protrusion region. As also discussed in Chapter 6, the typical failure of the tensile specimens is shown in Fig.5.12. There are failures occurred along the top of the protrusion region just above the tip of the protrusions. This can also be seen in figures in Chapter 6, Fig.6.14 and Fig.6.15.

Therefore, the top of the protrusion region within the composites should be examined carefully. Thus, with the effect of different spatial arrangements, discussions in this section focus on the stresses along the top of the protrusion region.

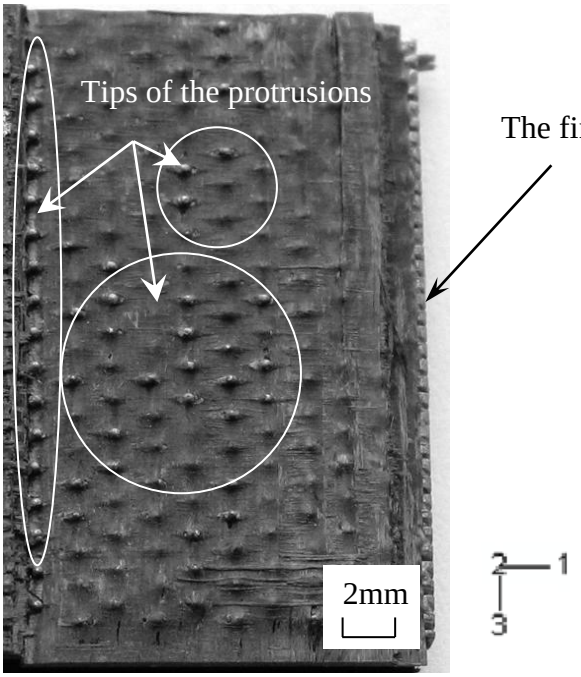

Fig.5.12 *Typical fracture surface of the tensile specimens*

To investigate the composite part in detail, cut was made in the (2, 3) plane and is described as row. Further cuts were made in the (1, 2) plane and are described as columns, see Fig.5.13; the first and second column of protrusions were analysed separately. These cuts were made as cross sections according to the row or columns of protrusions from the model boundary in 1-direction or the symmetry plane. The maximum values for the stress components are listed in Table.5.4 for the first and second column of protrusions.

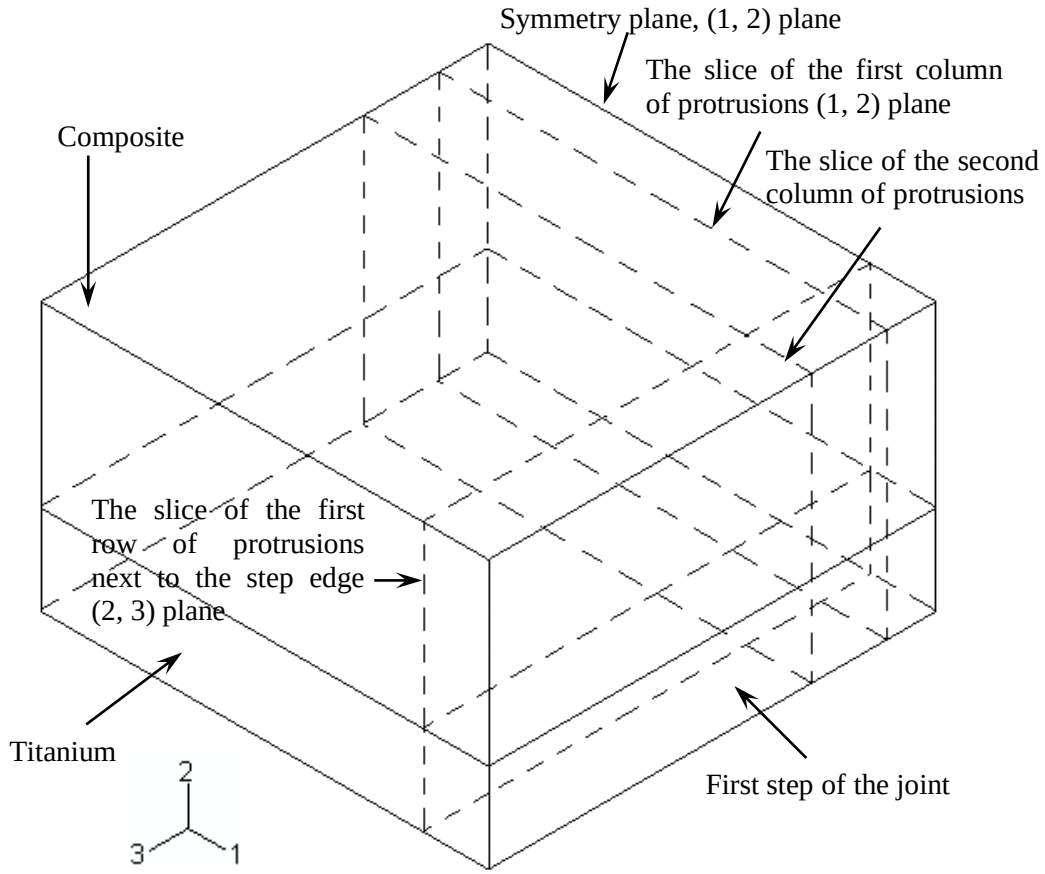

Fig.5.13 *Diagram of the 3D submodel with the positions of the symmetry plane, the first row of protrusions from the step edge, and the first and second column of protrusions*

Table.5.4 *The maximum stress values of stress components against protrusion distribution of the composite part for the first and second column (the result from top of the protrusion region is in italic)*

		Square array	Rotated measured array	Measured array	Square array, half distribution density
The first column	Axial stress [MPa]	141.3	143.0	139.2	139.8
		132.4	*134.1*	*117.6*	*128.7*
	Peel stress [MPa]	12.6	13.2	10.7	12.3
		8.2	*8.6*	*7.3*	*7.0*
	Shear stress [MPa]	16.3	18.1	14.4	15.3
		16.3	*15.6*	*11.8*	*14.9*
The second column	Axial stress [MPa]	141.1	140.4	140.4	139.5
		132.8	*129.7*	*130.6*	*128.7*
	Peel stress [MPa]	12.6	13.6	12.1	12.2
		8.1	*8.2*	*6.9*	*6.9*
	Shear stress [MPa]	16.0	15.0	16.4	15.4
		16.0	*14.9*	*13.8*	*14.9*

Considering the whole composite region, the measured array showed the lowest stress value for stress components peel stress and shear stress for the first column of protrusions. For the stress components axial stress and peel stress in the second column of protrusions, the measured array had the lowest values but it had the highest stress value for stress component shear stress.

With almost all different spatial arrangements, the maximum values of stress components are lower for the top of the protrusion region (italic figures in Table.5.4). For the same protrusion distribution density, the measured protrusion density model showed the lowest maximum values for the stress components around the top of the protrusion region for both columns of the protrusions.

Comparing the first and second column of protrusions, the square array shows similar maximum stress values for all stress components around the top of the protrusion region. For the square array, the lower protrusion distribution density models show lower stress values for all the stress components for both columns and the maximum stress occurs at similar locations.

The contour results of the cross sections for the first and second column of protrusions next to the symmetry plane along 1-direction are shown for all three stress components in Fig.5.14 to Fig.5.19, where maximum stress positions are marked with circles (and arrows for the maximum stress at around top of the protrusion region).

5.4.1 Axial stress results for the first and second columns of protrusions

Figures Fig.5.14 and Fig.5.15 are for the stress components axial stress results of the first and second column of protrusions. Stress concentrations around the top of protrusions region are marked with arrows. The locations of the maximum stress concentration are marked with circles

Comparing the axial stress of the first and second columns of protrusions, for the square array submodels, both stress distribution and the maximum stress are similar for the whole composite region and the top of the protrusion region. Variation occurs only due to the distance between protrusions in 1-direction, i.e. the spatial distribution density. For the rotated measured array submodel, the values of the maximum stress are similar for both columns. In Fig.5.14 and Fig.5.15, for all other arrangements, the maximum stress positions are similar. The maximum stress values from within the whole composite region and top of the protrusion region are similar. For the measured protrusion array, the maximum stress values for the whole composite area occurred at similar positions and stress distributions around the top of the protrusion region.

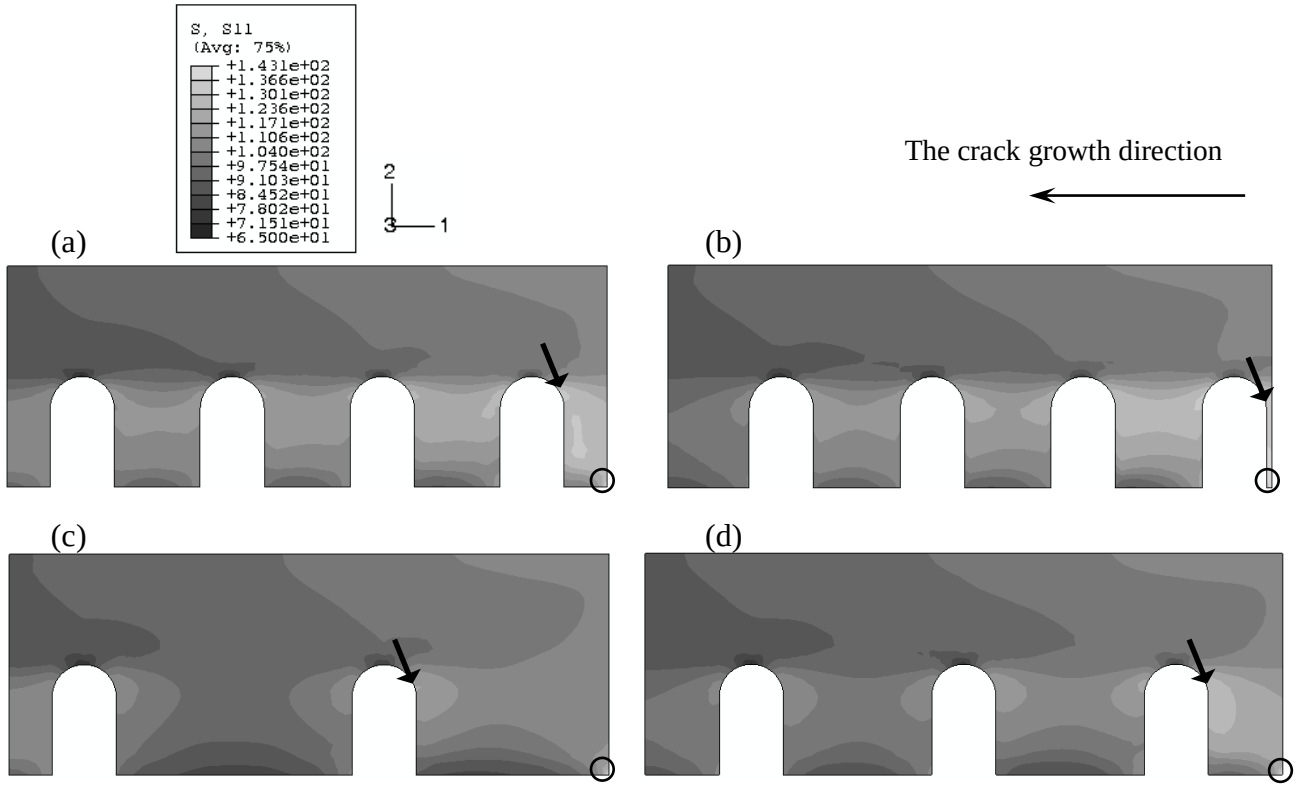

Fig.5.14 *Axial stress results of four different submodels for the first column of protrusions (a) square array, (b) rotated measured, (c) measured, and (d) half distribution density and square array*

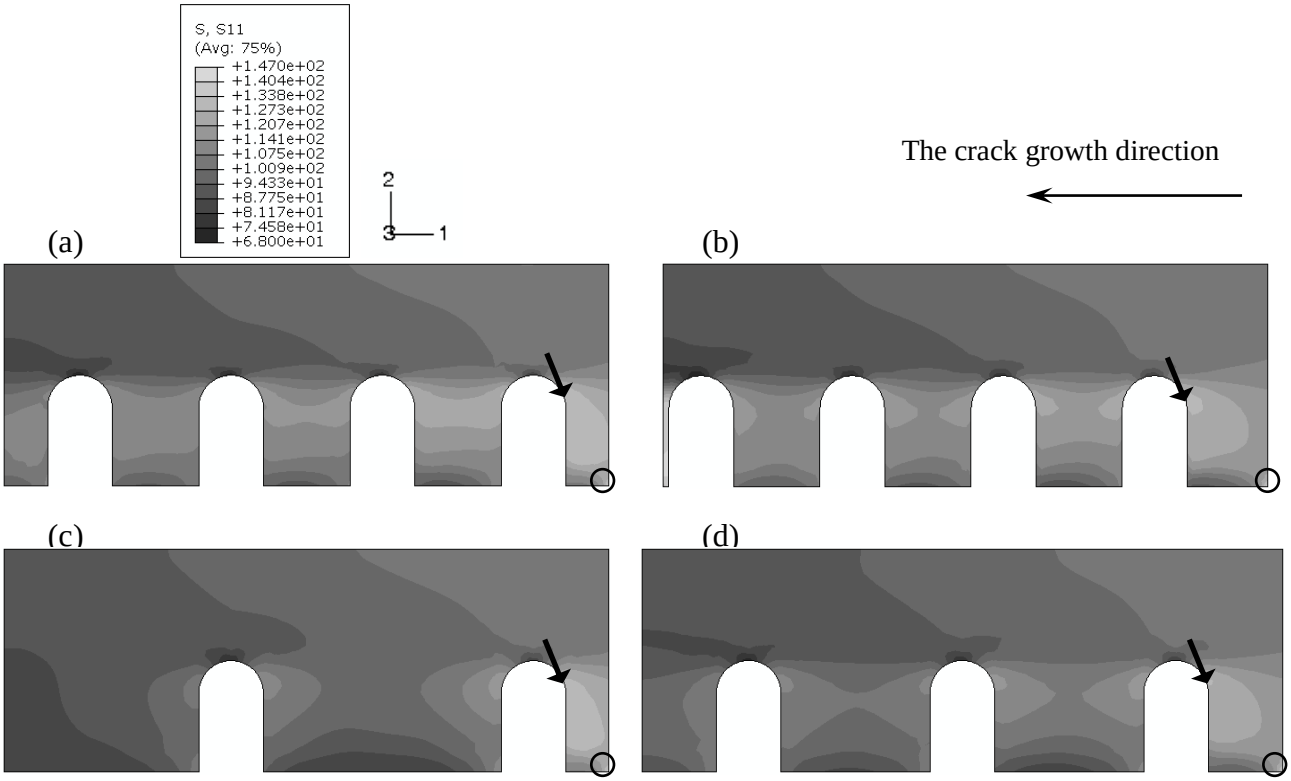

Fig.5.15 *Axial stress results of four different submodels for the second column of protrusions, (a) square array, (b) rotated measured, (c) measured, and (d) half distribution density and square array*

Highest level of axial stress is reached around the top of protrusions for the first protrusion from the composite end, the lightest grey band in Fig.5.14 and Fig.5.15. Then the stress reduced towards the metal end. The measured pattern of the protrusions show differences in stress distribution due to the space before the first protrusion and between two protrusions in the column, which allow the stress to spread before it reached the next protrusion. All other pattern submodels have stress at a relatively high level in between the first and second protrusions. The stress distribution is similar for the second column of protrusions.

5.4.2 Peel stress results for the first and second columns of protrusions

Figures Fig.5.16 and 5.17 show peel stress results of the first and second columns. Stress concentrations around the top of protrusions region are marked with arrows. The locations of the maximum stress concentration are marked with circles.

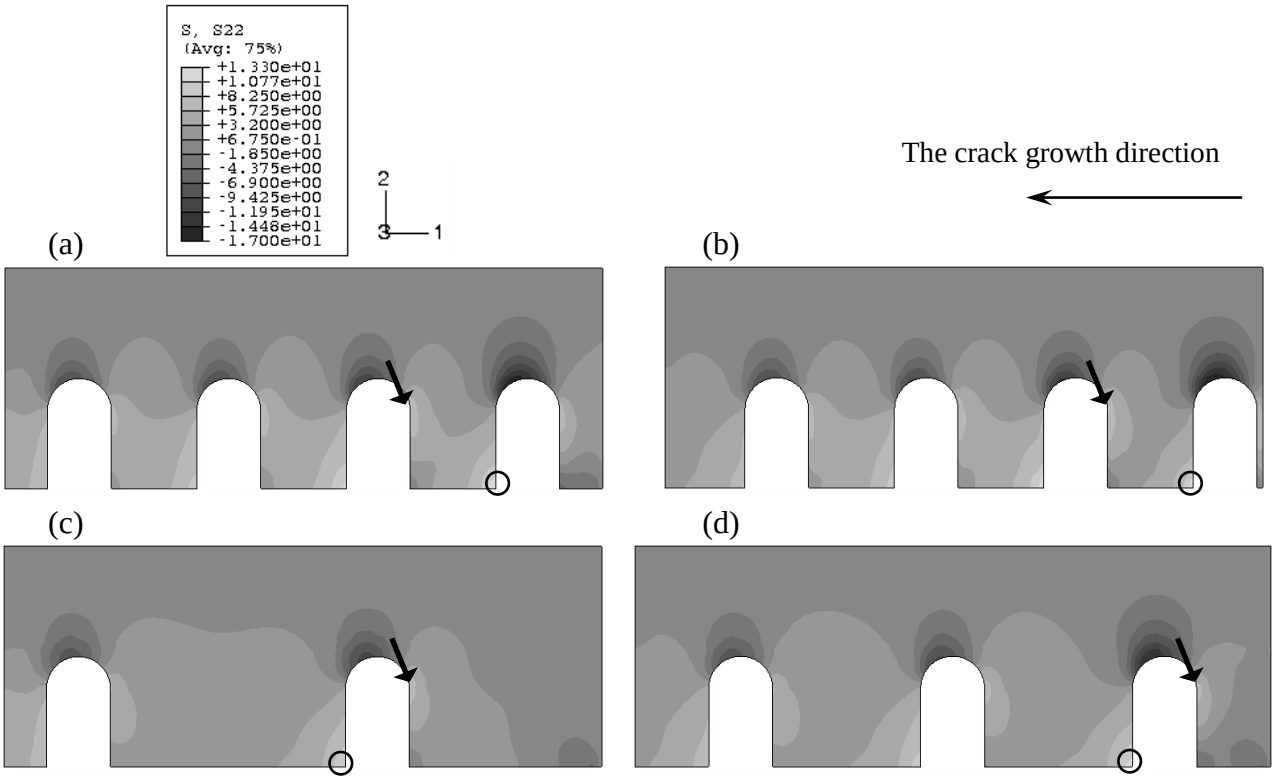

Fig.5.16 *Peel stress results of four different submodels for the first column of protrusions (a) square array, (b) rotated measured, (c) measured, and (d) half distribution density and square array*

Fig.5.16 shows the locations of the maximum stress for the first column of protrusions for the whole composite region, the locations are similar for the second column of protrusions. Comparing peel stress of the first and second column of protrusions, (a) and (b) in both figures show higher maximum stress for both the whole region and the top of protrusions region. For the square array submodels (a) and (d), the stress concentration around the top of the protrusion region occurs at the first protrusion from the joint step for the first column and the second protrusion for the second column. Maximum stress concentrations are identical for the two columns in both cases. The differences between square and the half density square arrays, (a) and (d), for both columns are roughly 2.5% for the whole region and 15% for around the top of the protrusion region.

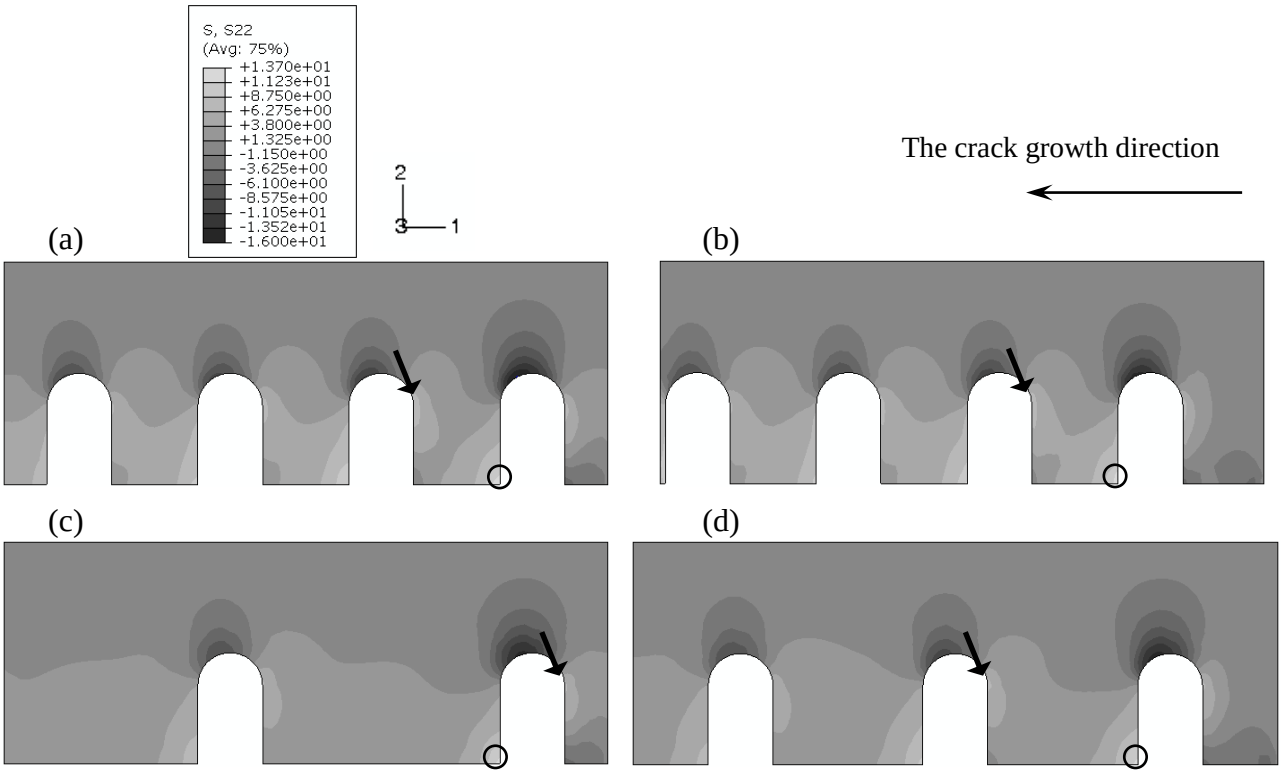

Fig.5.17 *Peel stress results of top of the protrusion for four different submodels for the first column of protrusions, (a) square array, (b) rotated measured, (c) measured, and (d) half distribution density and square array*

For the rotated measured array submodel, the values of the maximum stress are similar; however, the locations are different especially for the second column of protrusions, see (b) in Fig.5.16 and 5.17. The stress concentration reached 8.6 MPa for the first column and 8.2 MPa for the second column within the top of the protrusion region; and similar positions compared with the other submodels.

For the measured protrusion array, the stress response for the whole composite area occurred at similar positions compared with other submodels as well as around the top of the protrusion region for both rows of protrusions. The stress values are the lowest for the same protrusion distribution densities, i.e. (a) and (b), for the whole composite region and around the top of the protrusion region.

For the stress distribution of peel stress, it reached a high level around the top of protrusions between the first two protrusions from the joint step. Then the stress kept

at a similar level between the protrusions around top of the protrusions region towards the metal end of the joint. The measured array submodel, (c), shows differences in stress distribution due to the space between two protrusions, which allow the deformation between the protrusions as stress distributes around the next protrusion (lower average stress).

5.4.3 Shear stress results for the first and second columns of protrusions

Figures Fig.5.18 and Fig.5.19 are for the stress components shear stress of the first and second column of protrusions, the locations of the maximum stress concentration for the whole region and for around the top of protrusions region are marked with circles and arrows respectively.

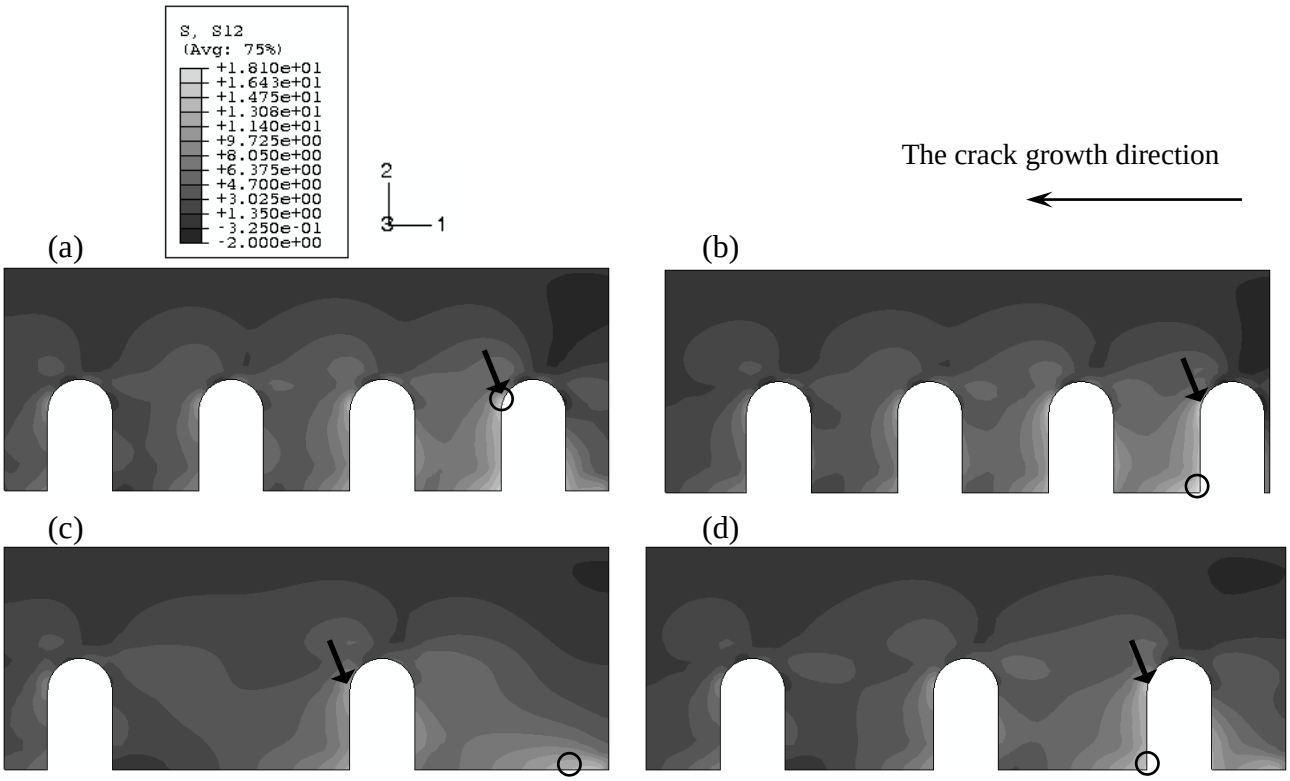

Fig.5.18 *Shear stress results of four different submodels for the first column of protrusions, (a) square array, (b) rotated measured, (c) measured, and (d) half distribution density and square array*

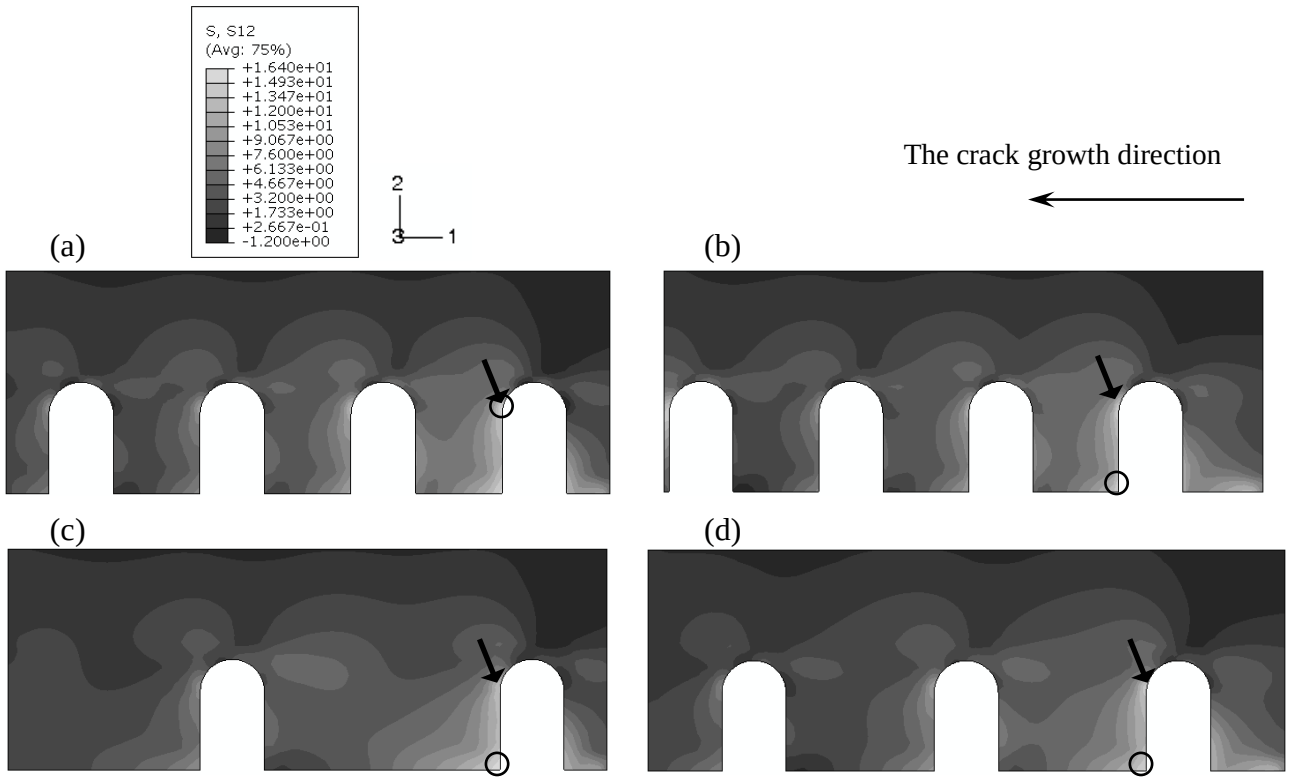

Fig.5.19 *Shear stress results of four different submodels for the second column of protrusions, (a) square array, (b) rotated measured, (c) measured, and (d) half distribution density and square array*

Shear stress concentrates at the joint surface near the step and then reaches a high level around the top of protrusions as well as between the first two protrusions from the joint step edge in Fig.5.18 and Fig.5.19. The shear stress reduces towards the metal end of the joint. The measured array of protrusions shows differences in stress distribution due to the space between two protrusions, which allow the stress to spread before it reached the next protrusion (lower average stress). The stress distribution is similar for the second column of protrusions.

Comparing the shear stress of the first and second column of protrusions for the square array submodels, (a) and (d), the stress responses are similar for the top of the protrusion region. However, for the whole region, the positions of the maximum stress are different. In (a) of Fig.5.18 and Fig.5.19, the maximum stress positions are at around the top of the protrusions, but it is at the foot of the protrusions for all other protrusion spatial arrangement models.

For the rotated measured array submodel, (b) in the figures, the values of the maximum stress are different, where the highest value of stress occurred at the first column for all different arrangement submodels; however, the positions are similar for the first and second column of protrusions.

For the measured protrusion array, the stress response for the whole composite region occurred at different positions, see (c) in Fig.5.18 and Fig.5.19, comparing with other submodels for the first column of protrusions. This position difference indicates that leaving enough space between the step edge and the first protrusion may reduce the maximum stress concentration as well as the stress concentration around top of the protrusion region. The stress values are the lowest for all protrusion distribution densities at around the top of the protrusion region.

5.4.4 Transverse stresses – through the width of the joint

Under tensile loading, Poisson's contraction in through-the-width direction (3-direction) combined with stiffness mismatch of the composites and titanium alloy, causes transverse stresses in this direction to be induced.

Fig.5.20 shows the transverse stress in the composite region for the first column of protrusions of the square array. The transverse stress concentrated around the protrusions in the (1, 2) plane, maximum stress concentration was marked in the figure. The maximum transverse stress is roughly 24 MPa. This is relatively low comparing with the axial direction stress (1-direction).

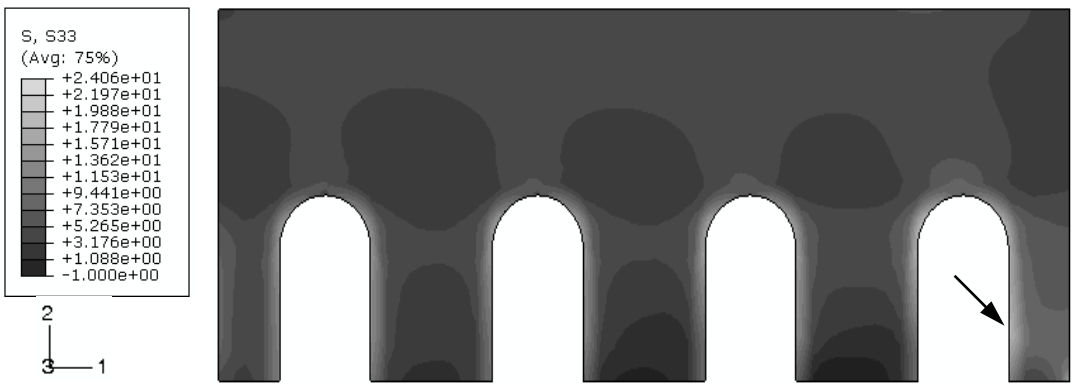

Fig.5.20 *Transverse stress for the first column of protrusions of the square array*

The transverse shear stresses in the same region are smaller than 10 MPa, which is smaller than the shear stress in (1, 2) plane.

Therefore, these transverse stresses are not considered to be the primary cause for the initiation and propagation of failure.

5.4.5 Stress distribution for the columns of protrusions

As shown from Fig.5.14 to Fig.5.20, the stress distribution in 1-direction was shown for all different spatial arrangements with axial peel and shear stresses. For these different stresses, the protrusion on the joint step edge shows higher stress concentrations around the top of the protrusion. The stress distribution in all cases reduced along towards the metal end of the joint. The indication is clear for the distance between protrusions in 1-direction or the number of protrusions in the (1, 2) plane. For the first several protrusions from the step edge, more distance between the protrusions in 1-direction or fewer numbers of protrusions allow stresses reduction for axial and shear stress cases, where for the peel stress the level of stress concentration between protrusions varies slightly.

Note that comparing the first and second columns' results in terms of the maximum stresses, the square array protrusions show similar results, the rotated measured array protrusions show slight reduction of the maximum stresses for the second protrusion column, the measured array of protrusions show slight increase in the shear and peel stresses for the second column.

To further understand the influence of the protrusion in terms of stress distribution in 3-direction, protrusion row will be investigated for the next section. The contour results of the first row of protrusions from the first step edge (see Fig.5.13 for the definition of the first row of protrusions) are shown in Fig.5.21 to Fig.5.23.

5.4.6 Stress distribution for the first row of protrusions

In Fig.5.21 to Fig.5.23, it shows the stress distribution for stress components axial, peel and shear stress for the first row of protrusions from the joint step edge in the (2, 3) plane. The definition of the row can be found in Fig.5.13.

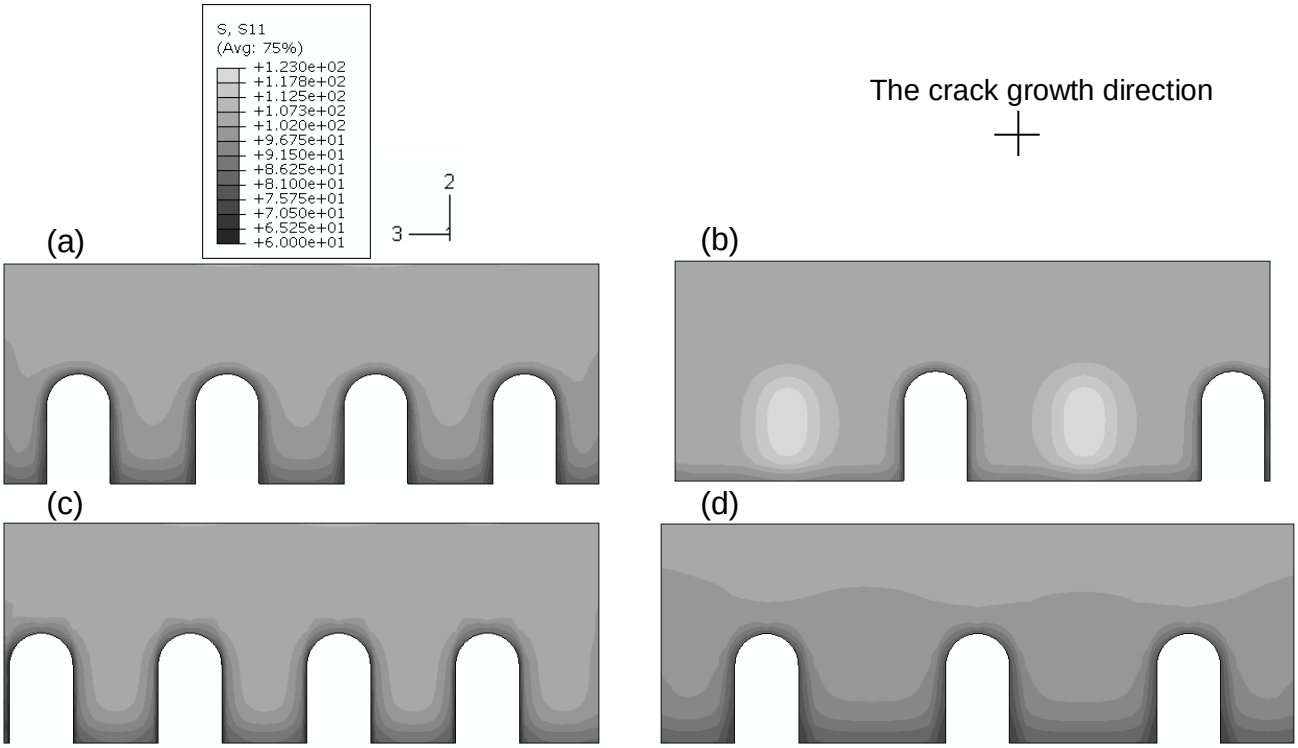

Fig.5.21 *Axial stress results of the first row protrusions from the joint step edge for four different submodels, (a) square array, (b) rotated measured, (c) measured, and (d) half distribution density and square array*

In Fig.5.21, the most marked stress concentrations occur in the rotated measured array, (b). Stress concentration cannot be found around the top of the protrusion. In (b), the stress concentrations occur in between the protrusions. This is caused by the position of the next row of protrusions. Comparing square array with different densities, (a) and (d), the distance between protrusions allows lower stress concentration in these regions.

In Fig.5.22, at both side of the protrusion, there is some peel stress concentration. And similarly to axial stress, comparing square array with different densities, (a) and

(d), the stress concentration in the regions between the protrusions is lower for the half density square array, (d). Also for the rotated measured array, (b), there are regions of stress concentrations caused by the position of the next row of protrusions.

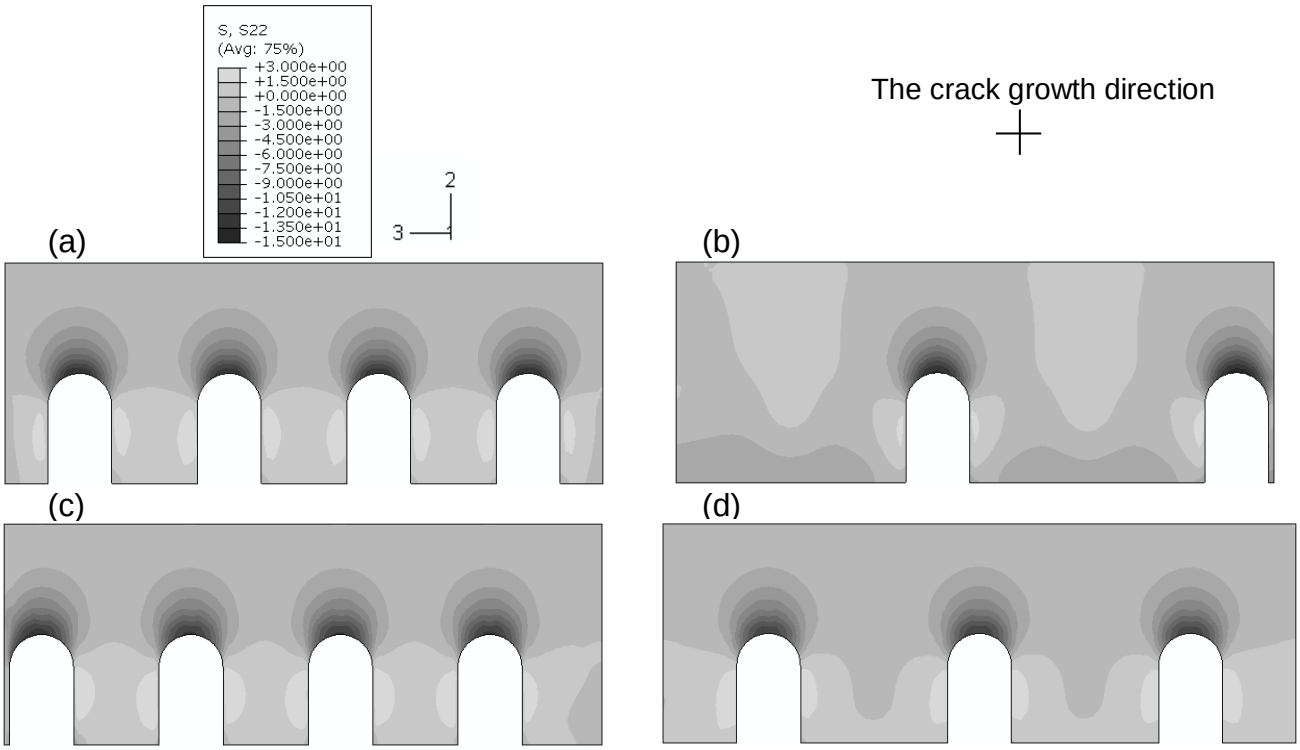

Fig.5.22 *Peel stress results of the first row protrusions from the joint step edge for four different submodels, (a) square array, (b) rotated measured, (c) measured, and (d) half distribution density and square array*

In Fig.5.23, there is not any obvious shear stress concentration around the top of the protrusion. Comparing square array with different densities, (a) and (d), the stress concentration in the regions between the protrusions is similar and just the regions are larger for (d). And similarly to the previous cases, for the rotated measured array, (b), there are regions of stress concentrations caused by the position of the next row of protrusions. However, the regions for higher stress concentration is small, indicating the influence of the next row of protrusions is limited.

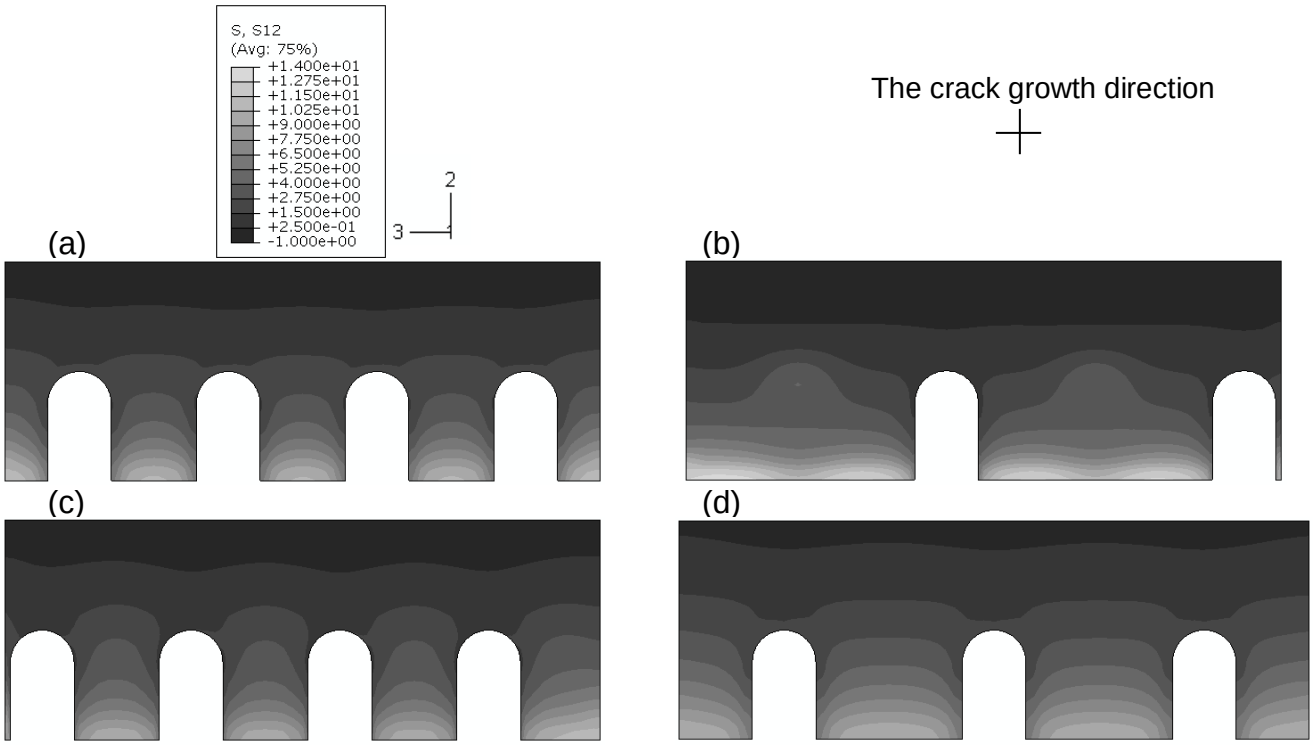

Fig.5.23 *Shear stress results of the first row protrusions from the joint step edge for four different submodels, (a) square array, (b) rotated measured, (c) measured, and (d) half distribution density and square array*

Overall, for square array with different densities, (a) and (d) in all the figures, it shows that in the regions between the protrusions, stress distributions are similar, while the hexagonal arrays (b) and (c) in the figure shows otherwise.

Although the square and measured arrays, (a) and (c) are similar in terms of spatial arrangement, the stress between protrusions in the measured array, (c), is generally slightly higher than that in the square array, (a). The stress between the protrusions also built up in the measured array, (b), for all stresses. These stress concentrations are considered to arise from the existence of the protrusions in the next row towards the metal end of the joint axial direction, or away from the joint step edge.

Under the global tensile loading (1-direction) condition, all stress components distribute in a similar manner. There are no consistent trends for the axial, peel and shear ((1, 2) plane) stresses. This is expected also to be true for the second and other

rows of protrusions from the joint step edge, where lower stress concentrations are expected as shown by the results of the columns of protrusions.

5.5 Summary

Three dimensional submodels for different spatial arrangements were analysed. Detailed results from the composite region bottom surface and the stress profiles around the top of the protrusions were examined. The protrusions around the end of the joint step were compared. The first and second columns of protrusions from the symmetry plane, (1, 2) plane, and the first row of protrusions from the joint step, (2, 3) plane were compared to examine the spatial arrangement effects. The key factor is considered to be the space between the protrusions in the global loading direction.

The importance of the stress concentration location has not been addressed. In the next chapter, Chapter 6, the failure processes will be presented and described, showing the importance of the stress concentration locations. These locations of stress concentration will be taken into account in Chapter 7 with detailed discussions regarding the comparisons between the 2 and 3-dimensional analyses.

6
EXPERIMENTAL INVESTIGATIONS

6.1 Introduction

This chapter focuses on the global response of the joint under tension, which should allow for validation of the two and three-dimensional global models' analyses, and further to support the results of the repetitive unit cell models and three-dimensional sub-models.

This chapter is divided into two stages, with the first part concentrating on joint manufacture, while the second part is the tensile experiments.

6.2 Joint preparation

The joint studied in this project is designed for high performance applications, therefore, titanium alloy and cross-ply of carbon fibre prepreg have been used. For laminate preparation using the carbon prepreg, an autoclave has been employed for the manufacture process.

6.2.1 Cross-ply composites

The cross-ply composite used in this project is made of carbon prepreg with epoxy resin, HexPly®AS4/8552from Hexcel. According to the data sheet of the HexPly® products, this prepreg material contains typically 57 % carbon fibre by volume. When used in the joining system, cross-plies have been employed to cope with the tensile loads and these are 50% longitudinal, i.e. 0 degree, plies with 50% plies in the transverse direction holding the composite part of the joint on to the metal surface as the keying mechanism. The stacking sequence for the entire adherend cross-ply composite is $[0/90]_{12S}$, where the ply thickness is roughly 0.125 mm. The mechanical properties of the prepreg unidirectional ply are listed below in Table.6.1 (also see

Table.3.2 in Chapter 3 as materials data used from literature for finite element analyses).

Table.6.1 *Tensile properties of AS4/8552 prepreg from datasheet**

	Modulus [GPa]	Strength [MPa]	Failure strain [%]
0 °AS4/8552	141 (135) **	2207 (2137) **	1.55
90 °AS4/8552	10	81	N/A

* - data for room temperature ** - data from US version Hexcel data sheet

6.2.2 Titanium alloy joint part

The titanium alloy used for the joining system in this project is Ti-6Al-4V, Ti64. Typical elastic properties are 114 GPa for modulus and 0.336 for Poisson's ratio. Roughly, the whole joint is 25mm in width, 6mm in thickness, 15mm long for the joint steps, and 250 mm in length (150 mm gauge length). The diagram of the joint is shown in Fig.6.1, on which first and second step are marked as well as the positions for the strain gauges.

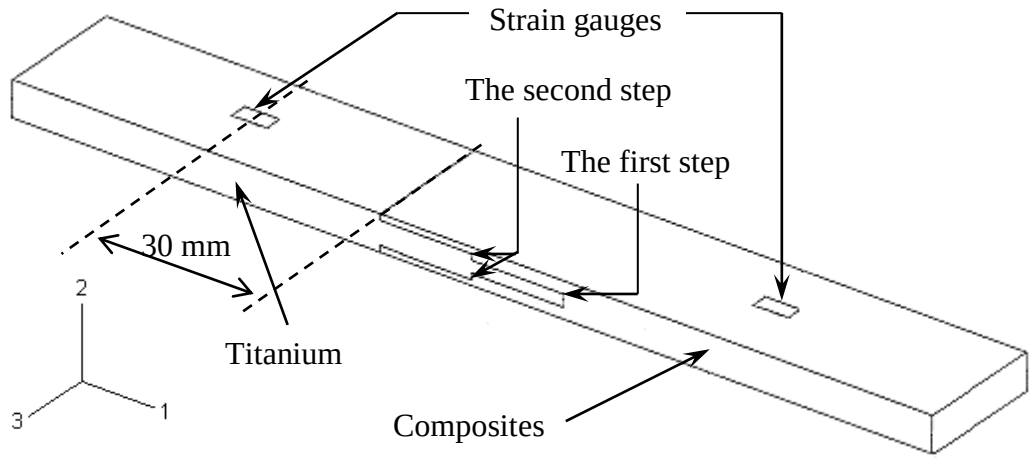

Fig.6.1 *Diagram of the joint*

The preparation of the surface patterns have been done by TWI applying Surfi-Sculpt™ technology, which employs electron beam operation on the titanium joint surface. The prepared titanium part of the joint is shown in Fig.6.2 and Fig.6.3. Fig.6.2 shows one side of the double-step with patterns of protrusions, marked on the picture with black strips. Fig.6.3 shows the side view of the joint steps including the

shape of the protrusions, which are similar to the protrusion in the hill shape 2D unit cell models.

The protrusion distribution density is obtained by the number of protrusions on the Comeld [TM] joint titanium joint steps divided by the area of the joint step.

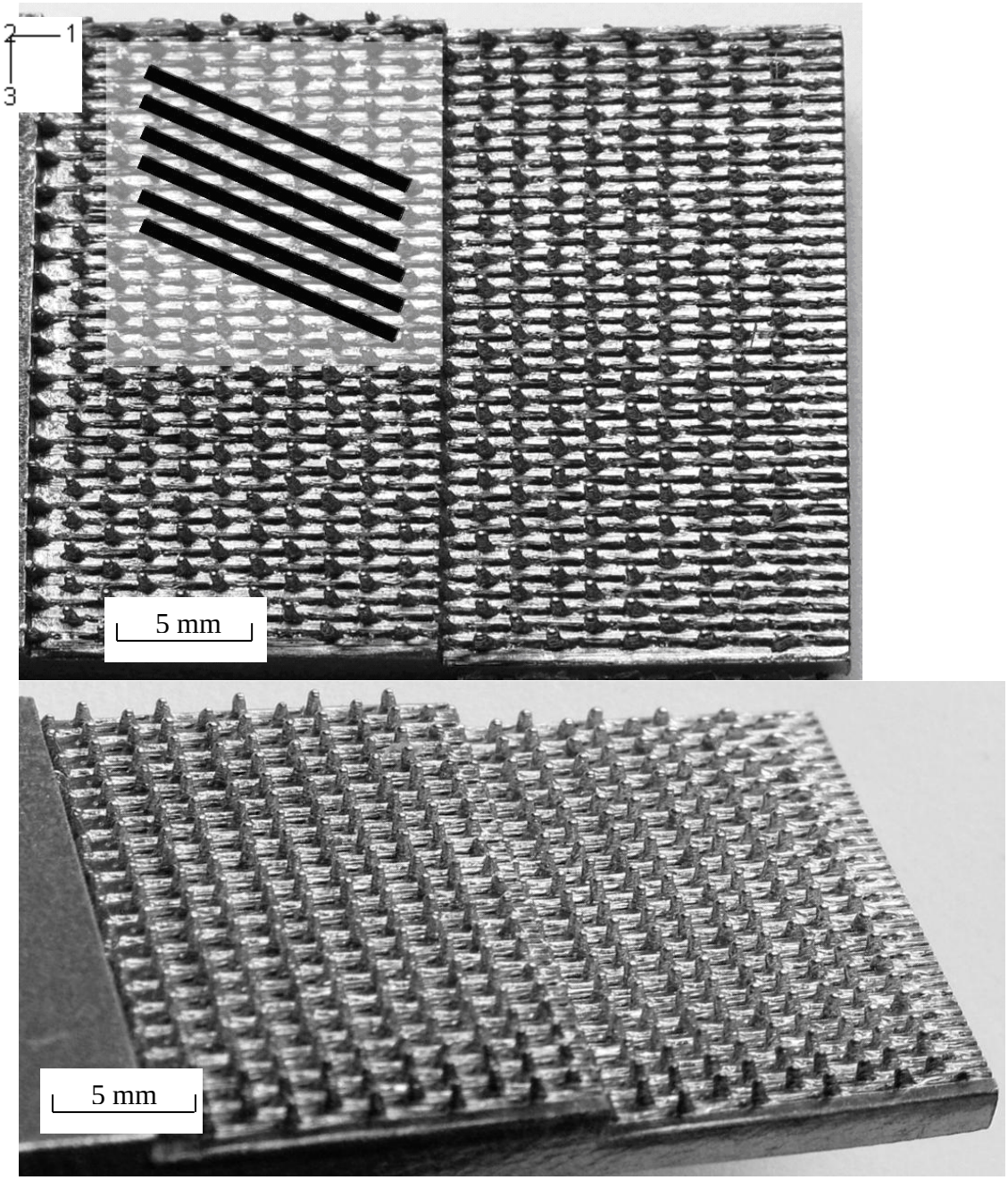

Fig.6.2 *Titanium double-step with protrusions*

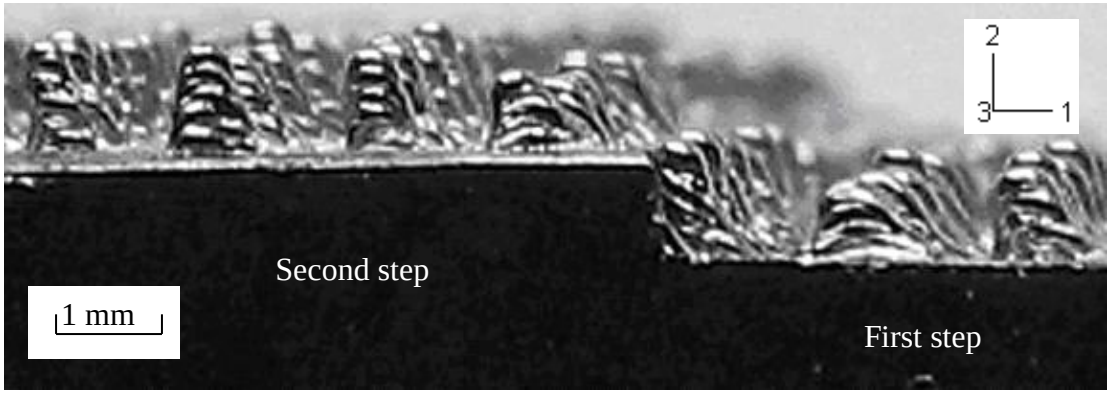

Fig.6.3 *Titanium double-step with protrusions, side view, half thickness*

6.2.3 Manufacture

Before the lay-up process, the titanium joint needs some surface treatments to remove contaminations and etching for better bonding with epoxy resin. The surface treatments include grit blasting the surface with Al_2O_3 powder (120-200 mesh) to remove oil or grease contamination; wash in the detergent solution for 10 minutes at about 75 ℃; wash with cold distilled water and dry in oven for 5 to 10 minutes at a temperature less than 95 ℃; etch for 5 to 10 minutes at room temperature; wash with cold distilled water and dry in oven for 10 to 15 minutes at about 75 ℃. The lay-up process was carried out immediately after the surface treatment process.

The detergent solution consists of METFIN AK 16, non-silicate immersion cleaner; tetrasodium pyrophosphate; sodium hydroxide; sodium metasilicate; and distilled water. The etchant consists of chromium trioxide; sodium fluoride; concentrated sulphuric acid; and distilled water.

The composite part consists of carbon prepreg which requires hand lay-up and autoclave consolidation. The carbon prepregs have to be hand lay-up on to the processed metal surface to form the joint.

One polished steel plate measuring 450×450 mm were used as the platform for hand lay-up. Six titanium specimens were arranged with polycarbonate spacers between them and taped together. The required amount of pre-cut sheets of prepreg is 8 plies for each of the two steps and to the end of the stage (see Fig.6.4) with length varying

of 105mm (section C and D), 120mm (section B and E) and 135mm (section A and F) as cross-ply with stacking sequence of $[0/90]_4$. The laminates for each step have been laid up for six specimens all together (Fig.6.4section A to F). The laminate section B was laid up first and then section A on to the 6 titanium specimens. Then the entire laid up together part was turned upside down for laying up sections D to F one after another.

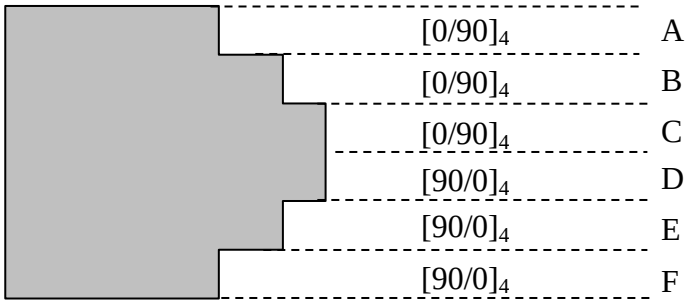

Fig.6.4 *Prepreg laminate lay-up schematic graph*

During all the lay-up process a heavy plastic tube was used to consolidate the laminate and push them on to the protrusions of the joint surface. During the lay-up process, it is impossible to force all the protrusions to penetrate the prepreg thickness, however, it was not considered as a problem as during the cure process, with the vacuum expelling entrapped air, the drop in viscosity of the resin and the high pressures used may allow the prepreg to move further down onto the protrusions. Once the lay-up process was completed, it was bagged up ready to go into the autoclave and was left over night, under vacuum consolidating. The prepared specimens were then put into autoclave at 20 psi pressure and 180 ℃ for 2 hours.

Typical Comeld ™ specimens are shown in Fig.6.5 (a), and the resin rich area is shown in Fig.6.5 (b).In Fig.6.5, the "1" marked regions are obvious resin rich area, which have been caused by the cross-ply prepreg not being compressed down onto the step surfaces; the marked regions "2" shows the difference of the resin rich phenomenon whether the protrusion is present, which is the further evidence for the explanation of regions marked "1". However, for the prepreg plies, the resin pockets can be caused by the resin bleeding on the side of the joint due to the plies pushed

down moving sideways during compaction processes. There could be some evidence of 90 ° fibre tows perpendicular to the plane between the protrusions (see Fig.6.5).

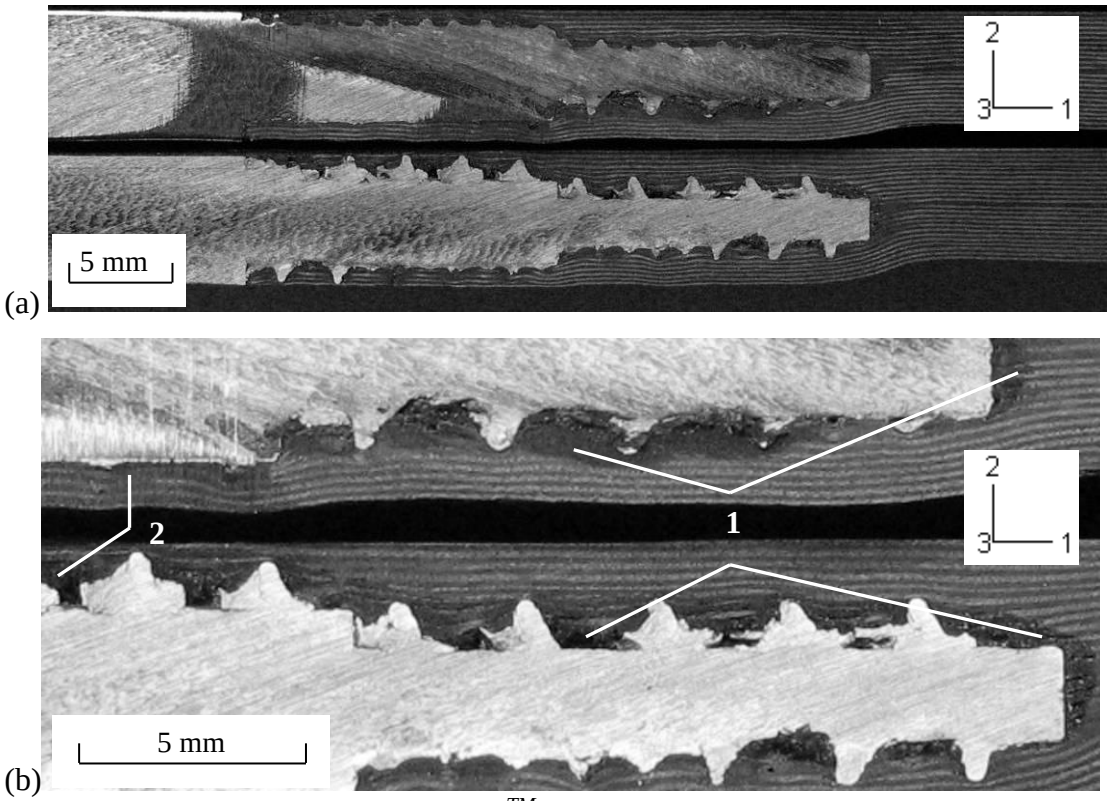

Fig.6.5 *Side views of typical Comeld ™ specimens, (a) with ruler in mm, (b) resin rich area marked "1"*

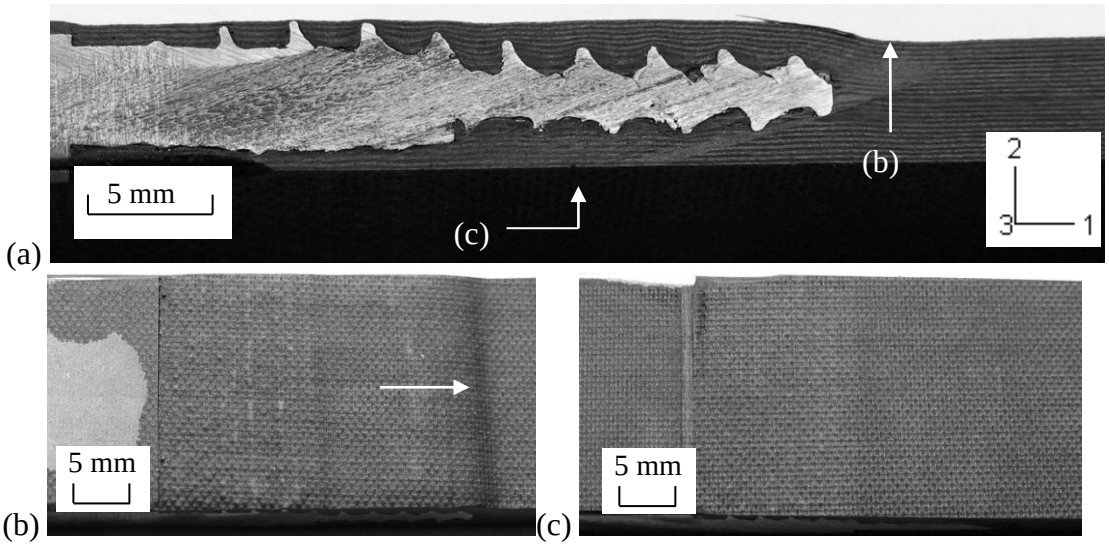

Fig.6.6 *Both surfaces of the specimens, (a) side view of the joint top and bottom surfaces; (b) top view of the joint curved top surface and (c) bottom flat surfaces*

It can be noticed that the Comeld ™ specimens have only the bottom (during autoclave) surface flat, in contrast the bagging side of the joint is curved a little where the same explanation for the resin rich area can be employed. The surfaces of the joint are shown in Fig.6.6. The curvature can also be caused by the differences in coefficients of thermal expansion of the joint components.

The manufacture of these joints is complex and not always consistent. In some joints, the resin rich region near the protrusion foot is caused by the complexity of the manufacturing. A particular problem is at the ends of layers C and D (see Fig.6.4). Every effort was made to consolidate the joints. Despite these difficulties in manufacture, it is notable that failure did not initiate at these regions in any tests, see Fig.6.14. Manufacturing defects/flaws are key to joint behaviour; resin rich and depleted zones can be expected to influence load transfer behaviour and subsequently failure location and joint strength.

6.2.4 Specimen preparation

After the prepregs were fully post-cured, some resin bleeding was observed around the double-step region, see Fig.6.7; approximately 20 mm at the end of the composite edges were cut off using a water-cooled diamond saw ensuring the length of the specimens of 200mm and maintaining the double-step in the middle of the joint.

The bled resin on the side of the specimens was carefully removed using a file ensuring no damage to the titanium part of the specimens and then the titanium surfaces were cleaned using Acetone. The length of 25mm was measured and marked from both ends of the specimens for clamping; the central positions from the marks (on titanium and composite) to the middle of the specimens were marked for the strain gauge to be mounted. Before mounting the strain gauges, the specimens' dimensions were measured. The strain gauges positions are shown in Fig.6.1.

After the two strain gauges were mounted on each specimen, the preparation for the tensile test was completed. The mounted strain gauges can be seen in Fig.6.8.

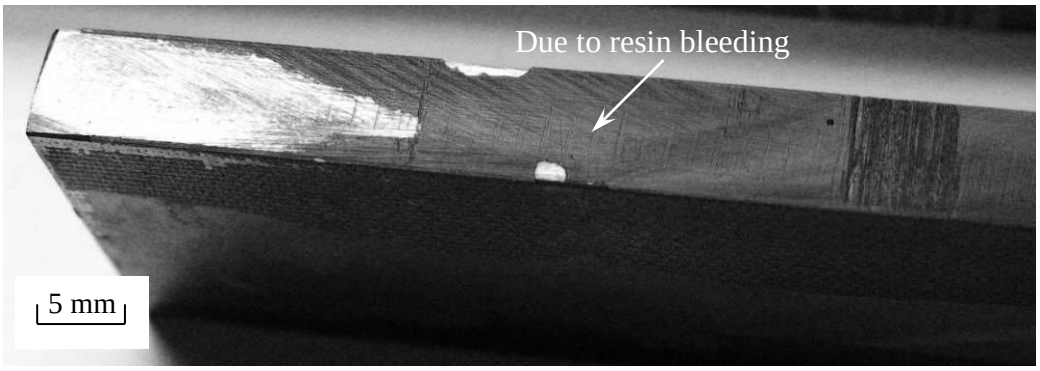

Fig.6.7 *Titanium part of the joint with resin bled, the shiny part is the titanium*

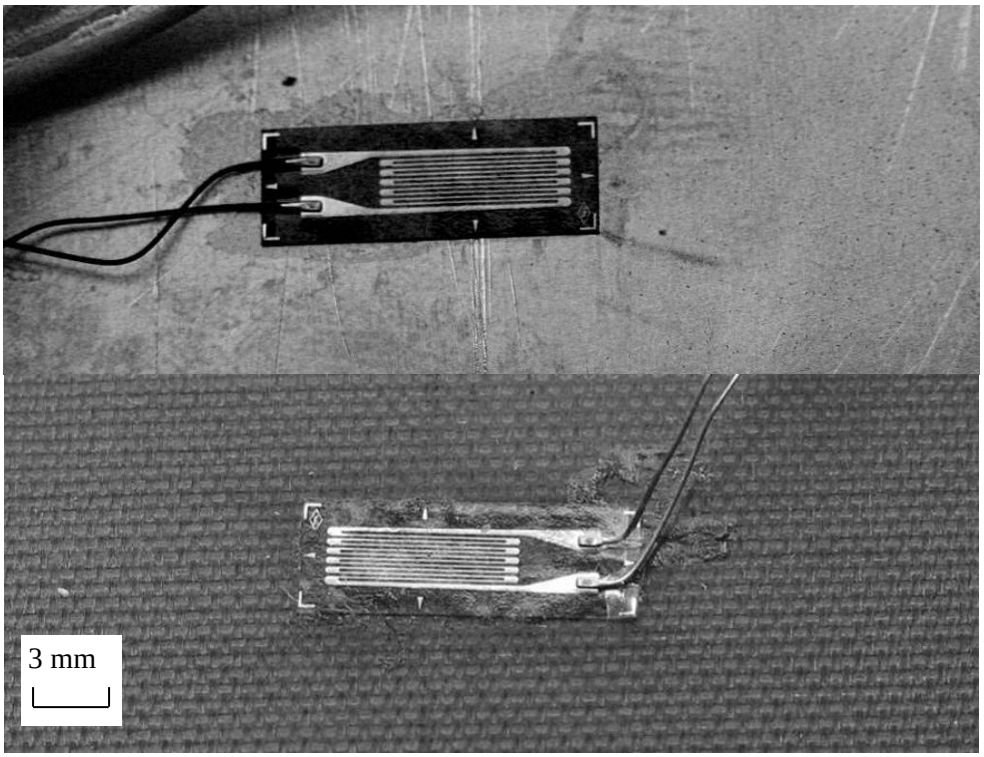

Fig.6.8 *The strain gauges mounted on the joint*

6.3 Experimental results

Tensile experiments have been conducted. Date was acquired from the Instron machine for the force and displacement. And the local strain data was acquired from strain gauges. Tensile experiments' results are presented and comparing with 2D and 3D global models simulation.

6.3.1 Tensile experiments results to failure

Typical performance of the joints under tensile load is presented. The final failure occurred as composite delamination and fibre breakage, see Fig.6.9, which shows that the final failure is caused by fibre breakage. However, the failure initiation is more complex. Tensile performance of load against displacement is shown in Fig.6.10 (data obtained directly from the Instron machine; the stress was calculated using the nominal cross-section area). There were five specimens tested in tension, however the strain gauge for specimen A5 was broken and thus strain data was not acquired for that specimen.

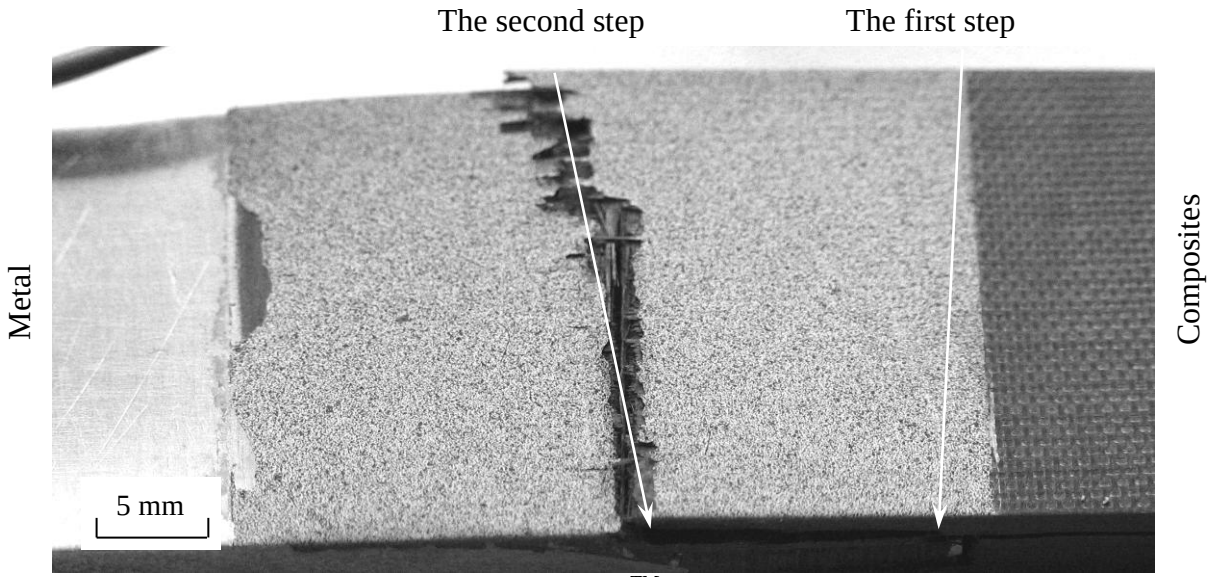

Fig.6.9 *Typical tensile failure of the Comeld™ joints*

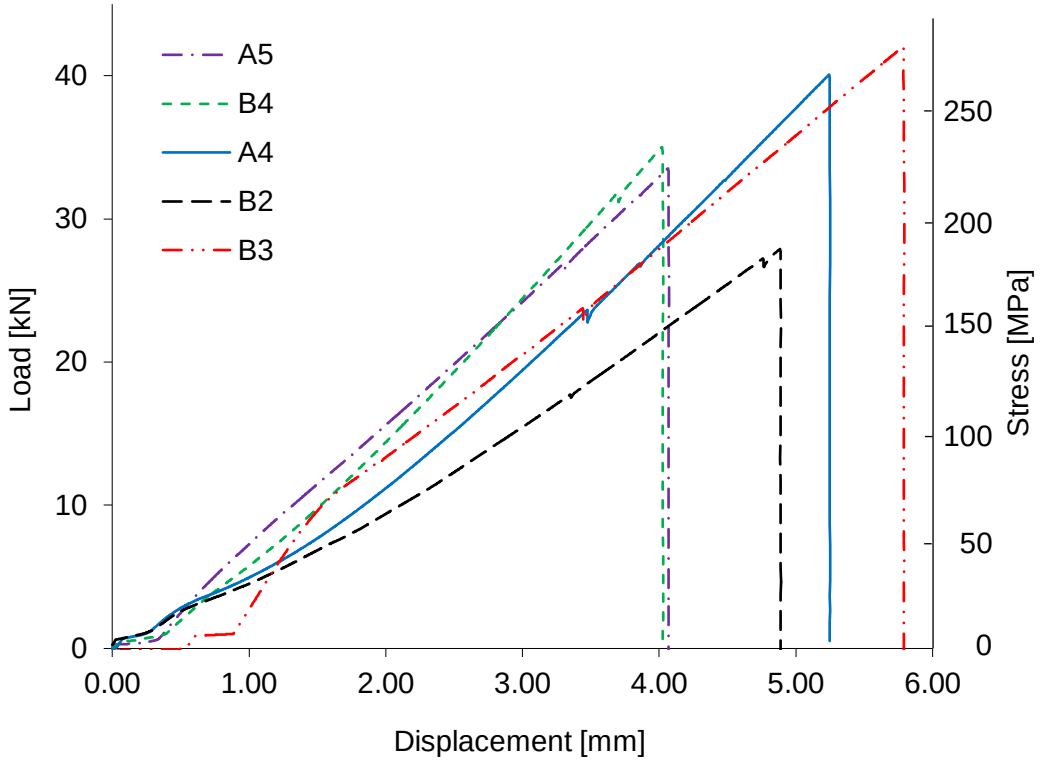

Fig.6.10 *Typical tensile performance, load against displacement*

Fig.6.10 shows at the beginning of the tests, there might be some slipping in the grips. Then the load displacement relation keeps almost linear before and after a slight drop in stiffness. Some kinks can be identified in the middle of the tensile test or close to the final failure, which is considered to be the crack initiation and propagation (or delamination) process. This also can be seen in the stress strain behaviour in Fig.6.11. There are some scattering in the ultimate load upon failure, from around 28 to 42 kN. The average ultimate load is 35.8 kN. This is considered caused by the manufacturing processes. During autoclave, the top surface of the specimens formed curvature near the position of the first joint step; while carrying out the tensile experiments, due to these curvatures, one side of the specimen may carry substantially more load than the other, resulting in the scattering of the failure load and reduction of the composite part stiffness from the strain gauge.

In Fig.6.11, the local strains from the metal and composites part are shown as strain1 and strain2 for all the samples. Strain1 of all the samples apart from A4 are shown (the strain1 data for A4 is not reasonable indicating faulty strain gauge), and are similar; strain2 of samples A4, B2, and B3 show similar initial linear response, and

significant non-linearity above around 120 MPa. The strength of the joints of samples except B2 is more than 200 MPa.

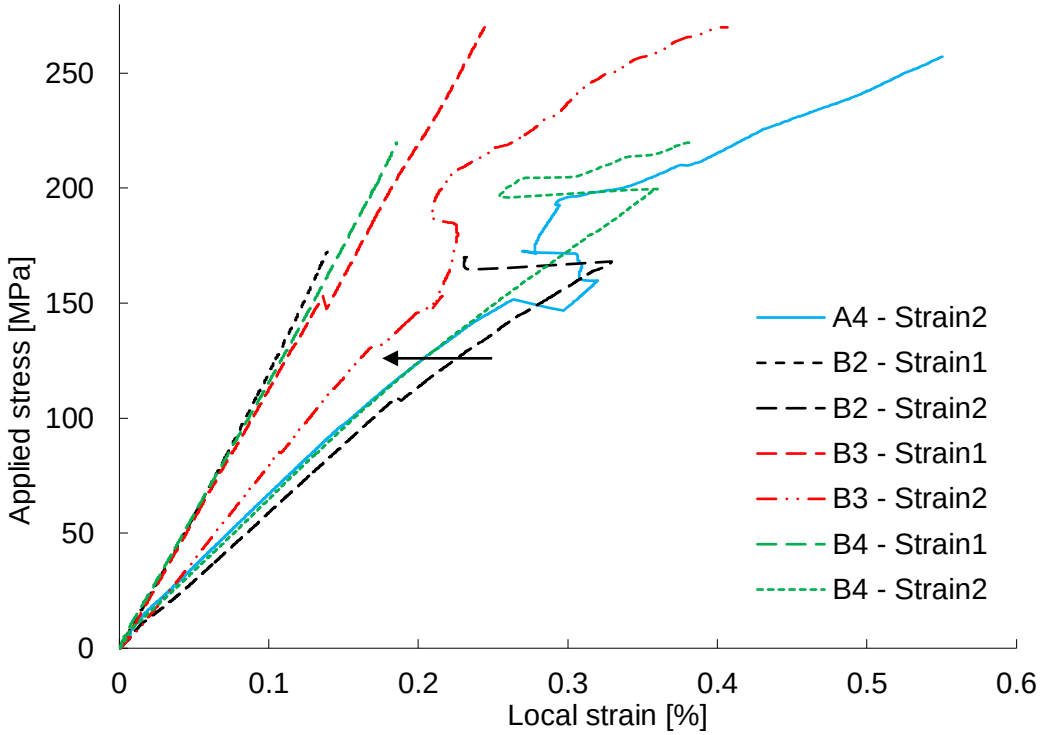

Fig.6.11 *Typical tensile performance, stress against strain from the strain gauges*

During tests, distinct cracking noise was heard indicting localised failure events. These appeared to occur after the slight stiffness drop on the load-displacement diagram, see Fig.6.10.

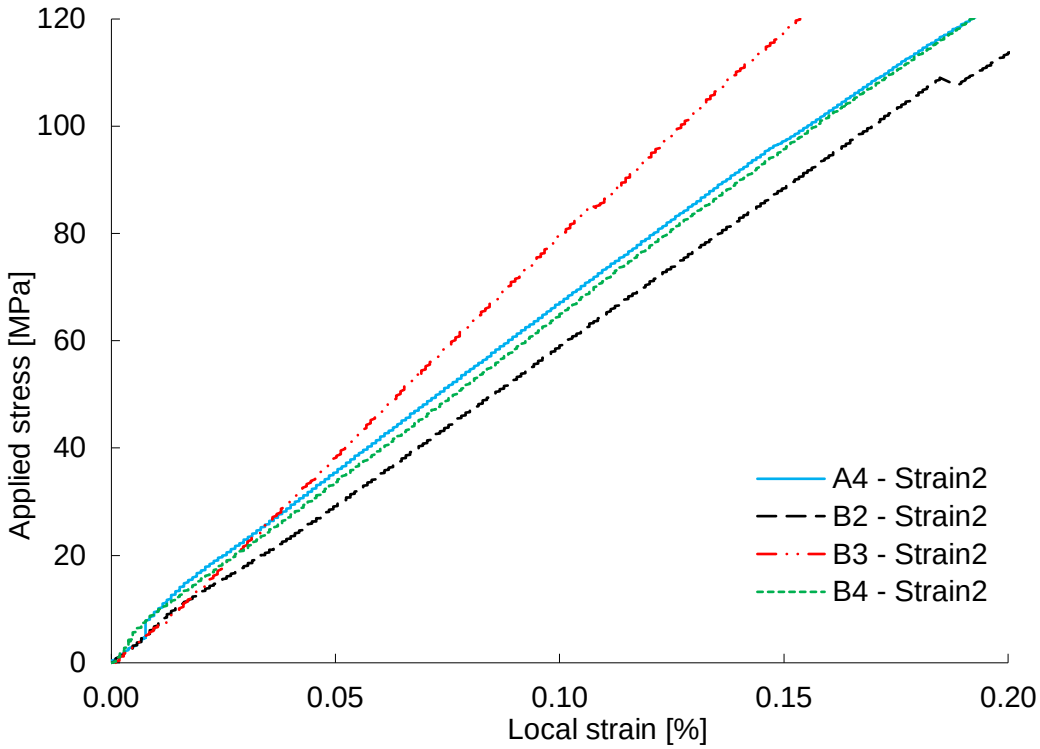

Fig.6.12 *Stress against strain from the strain gauges on the composite part of the joint with first failure identified*

For the composite part of the joint, the first failure can be identified for samples B2 and B3 in Fig.6.12. Otherwise, in the linear region, the estimated stiffness of the composites is ranging from 55.3 to 77.8 kN/mm with an average value of 61.8 kN/mm. The stiffness data was calculated by the applied stress and local strain data.

The stress-strain relation of strain on composite part of the joint in Fig.6.11 shows non-monotonic trend towards failure. This may be caused by the local delamination process and the effect of the uneven surface finish of the joint near the first step. This occurs prior to failure. The explanation is that the delamination occurred on top of the protrusions on the first step for both sides, and then stopped at the edge of the second step on the top surface of the joint (the flat surface from the moulding), at the connecting position of the first step to the second step, while delamination could continue on the other side of the step, (c) in Fig.6.6.

Tensile test was also carried out with digital correlation technique with up to 10kN applied load, ARAMIS 3D (with two cameras) from GOM. The specimen was tested

within the elastic limit. The position of the area captured by the technique and the contour results are shown in Fig.6.13. Minus values indicate the direction change of the shear angle.

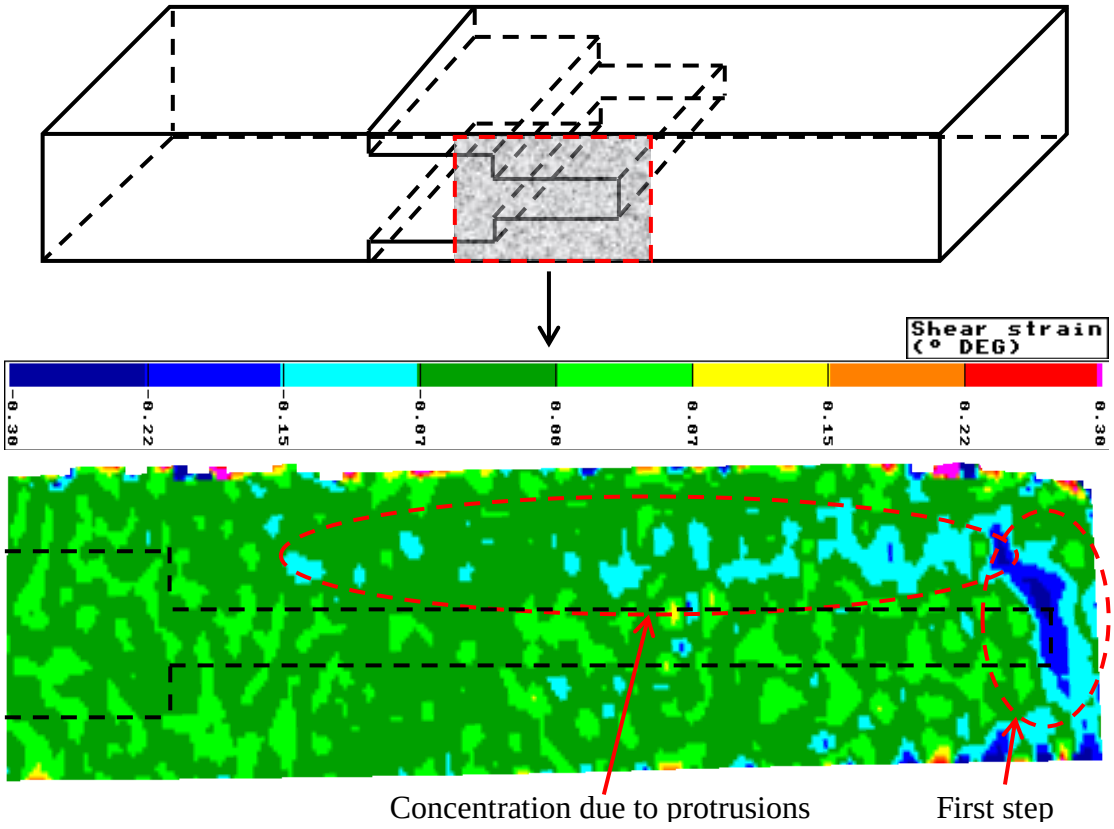

Fig.6.13 *Shear strain obtained by digital correlation method on the side of the joint.*

Shown in the figure, the shear strain angle mapping of the first step region shows obvious concentration at the first step (marked in the figure); this concentration is also obvious with strain mapping in other directions (not shown). The length of the step marked in the figure is 15 mm. There are signs of the protrusions on the first step (marked in the figure); although protrusions exist on both sides of the step, they are only visible on the top half. This is believed to arise from factors including manufacture of the protrusions and loading conditions. The specimen may not perfectly align with the tensile direction; the protrusions are created by the electron beam processes for a large area and then specimens are cut to size. Therefore when preparing the joint, there are chances that the protrusions were not on the side of the joint, i.e. after autoclave, the protrusions do not appear on the side of the joint all the

time. This misalignment may change the effective spatial arrangement slightly. During tensile loading, there might be misalignment with the clamps, and therefore, the specimen may rotate and twist slightly during tensile loading. However, these misalignments should not cause such big deflections in stiffness and strength shown previously.

The failure of the joint occurred away from the composite-metal interface which is on the double-step surfaces, see Fig.6.14, where (a) and (b) showing different region of failure in detail.

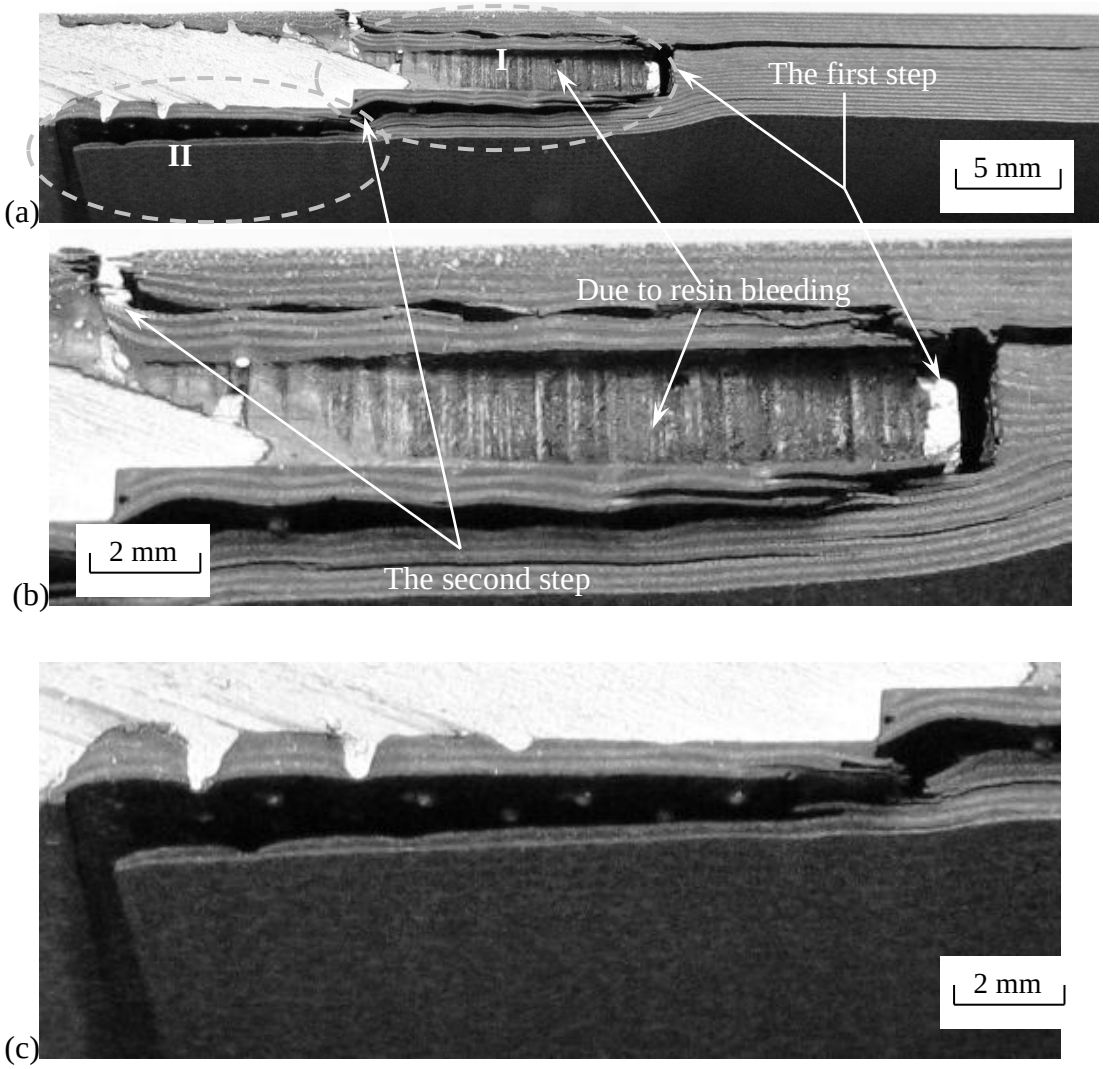

Fig.6.14 *Typical failure condition of the tensile specimens, (a); (b) failure in the region I of the first step; (c) region II, the failure of the second step*

The manner of failure is clear. With increasing applied load, initial failure appears near the first joint step with a snap sound and propagates towards the composite end; with increasing applied load, cracks initiate on the top of the protrusions and propagates along the top of the protrusions in the first step until the second step, see region I in Fig.6.14 (b); with a sudden snap noise crack initiates and propagates along the top of protrusions on the second step, see region II in Fig.6.14 (c) (this occurred for B2 in Fig.6.10); and then with the separation of the joint step and the composites final failure occurs with fibre breakage, in the case. Therefore, the explanation of the lower strength for sample B2 comparing with other samples was obtained.

Typical fracture surfaces on the first step are shown in Fig.6.15, where (a) and (b), (c) and (d) are mirror failure surfaces. As explained in Fig.6.14, the fracture surfaces show that the delamination occurred on top of the protrusion region, not within the height of the protrusion, see (a) and (c) in Fig.6.15. Surfaces in (a) and (c) in Fig.6.15 are two sides of the first step after failure, on which the protrusions are contained in the prepreg cross-ply composite and signs of delamination and fibre breakage are obvious which also can be seen in Fig.6.16.

A few tips of the protrusions can be seen on both sides and more on the flat side of the specimen, see Fig.6.15 (a), which left small black dots on the composite fracture surfaces in Fig.6.15 (b) and (d); it has been explained that during the lay-up process it is impossible to force all the protrusions to penetrate the prepreg thickness, which can explain that not all the protrusions can be seen on the fracture surface. This can be caused by the moulding process (the base is flat metal and top vacuum bagging is not sufficient to make the top surface of the joint flat). The other possibility is that the protrusions are not exactly the same height.

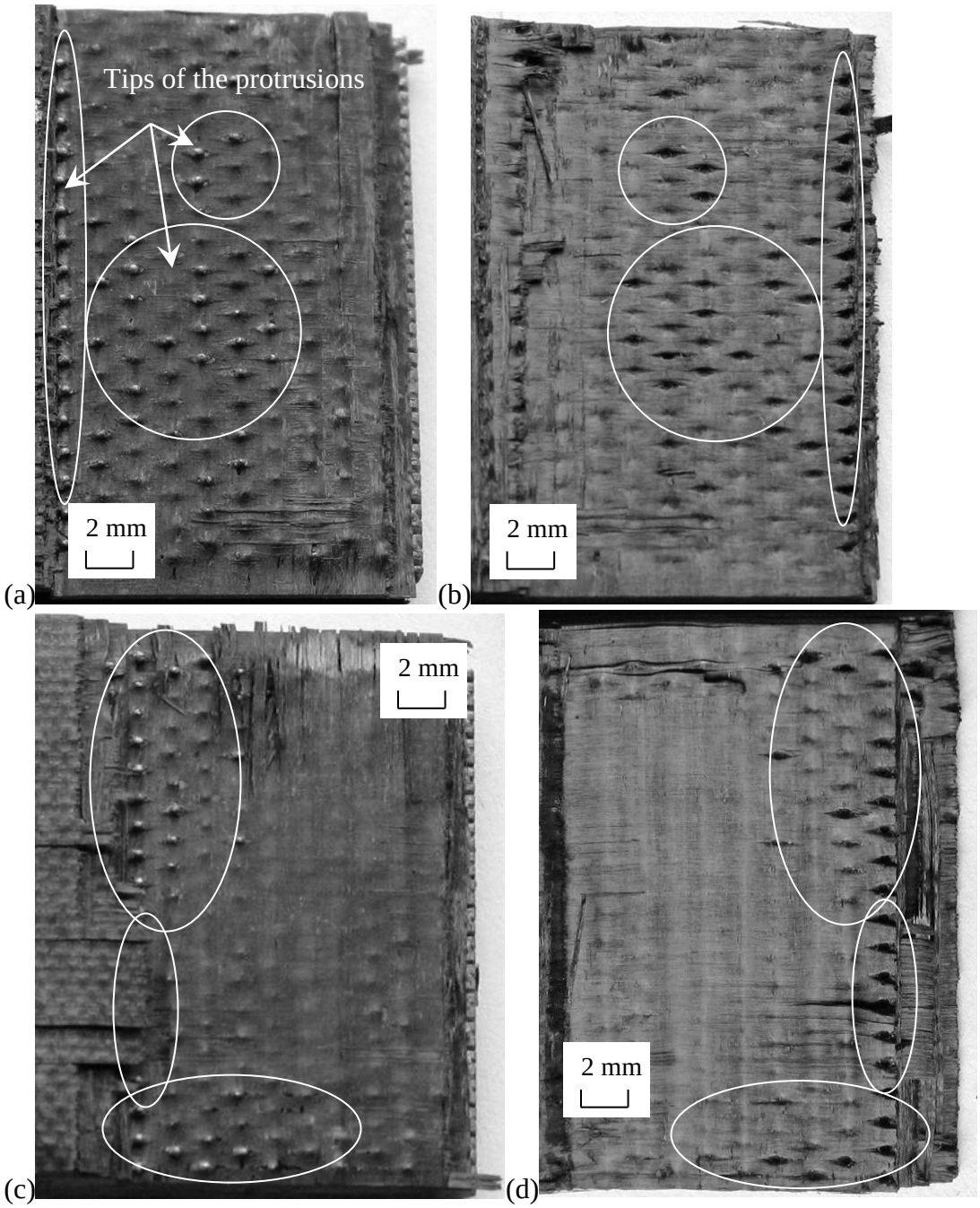

Fig.6.15 *Typical fracture surfaces of the failed joint, (a) fracture surface on top of the protrusions; (b) fracture composite surface corresponding to (a); (c) the other fracture surface on top of the protrusions; (d) fracture composite surface corresponding to (c)*

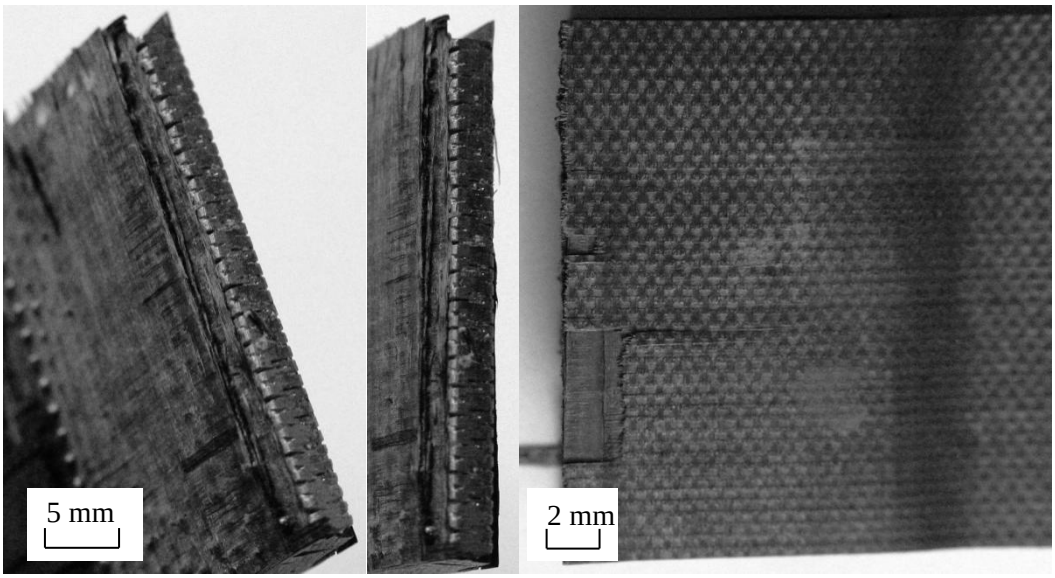

Fig.6.16 *Failure of the joint at the end of the titanium double-step*

6.3.2 Comparison of modelling and experimental results

Apart from extremely localised plastic deformation around the foot of the protrusions within the titanium, the modelling results shown are elastic (elastic-plastic materials properties were used for titanium). The typical elastic results from the experiments are shown in Fig.6.17, which shows that the performance is similar for different specimens for the linear part of the tests.

The comparisons of the stress-strain results with homogenised composite 2D global models and the experiments are shown in Fig.6.18 including the effects of element types. The elastic-plastic properties were used for the titanium; however, only local plastic deformation occurred at around the foot of the protrusions, which can be ignored for the overall stress analysis.

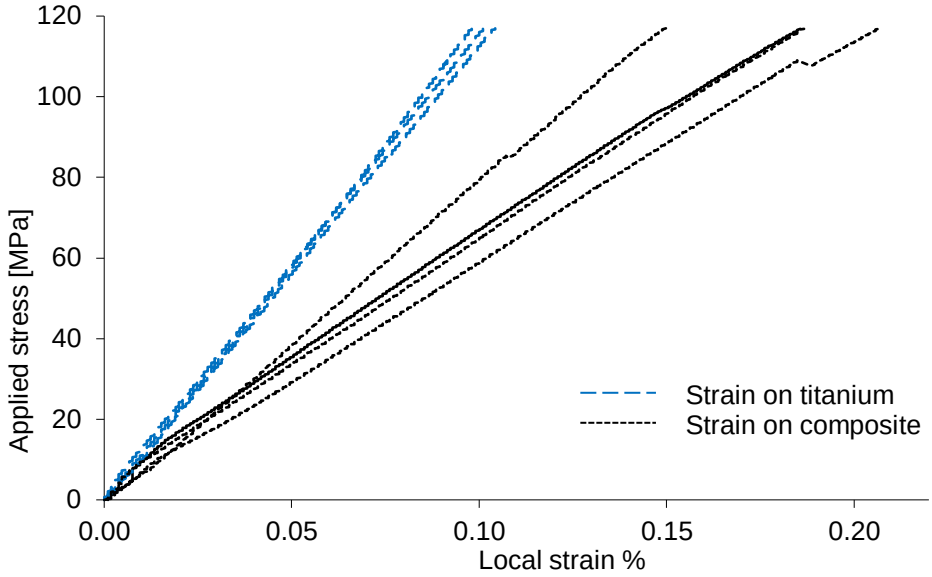

Fig.6.17 *The elastic stress-strain results of the tensile experiments from strain gauges*

In Fig.6.18, for the strain data on titanium, the plane stress element model performed similar as the experiments turned out while the plane strain element model had a little stiffer behaviour; for the strain data on the composite, the plane strain element model performed similar as the experiments and a little stiffer than the plane stress element model as expected.

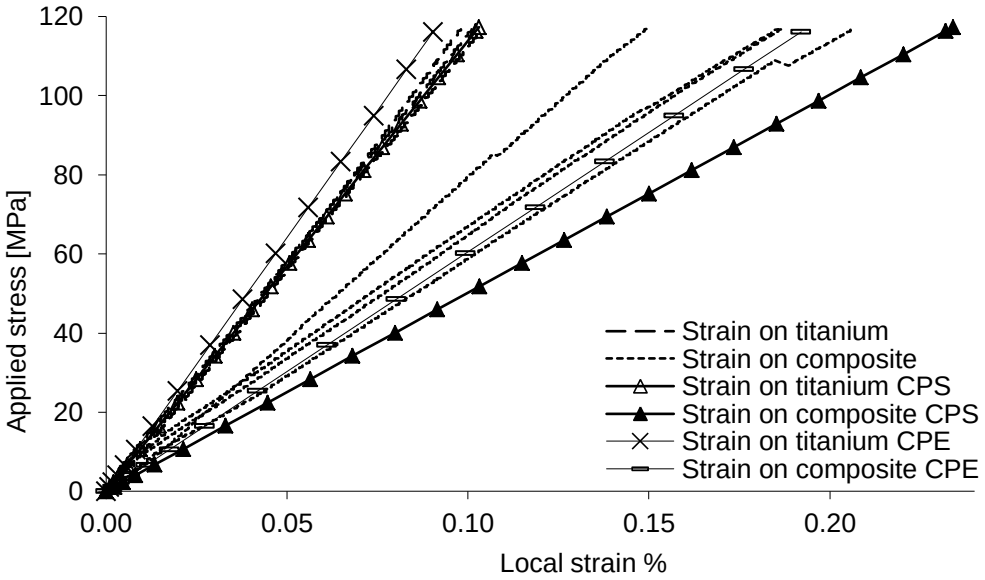

Fig.6.18 *The elastic stress-strain results comparison of the tensile experiments and simulation of 2D global model with homogenised composite region for different element types*

The stress-strain results comparison of 3D global models and the experiments are shown in Fig.6.19.

As shown in Fig.6.19, for the strain data on titanium the 3D global model results match the experiments well while the strain data on composite is stiffer for the experiments than the simulation.

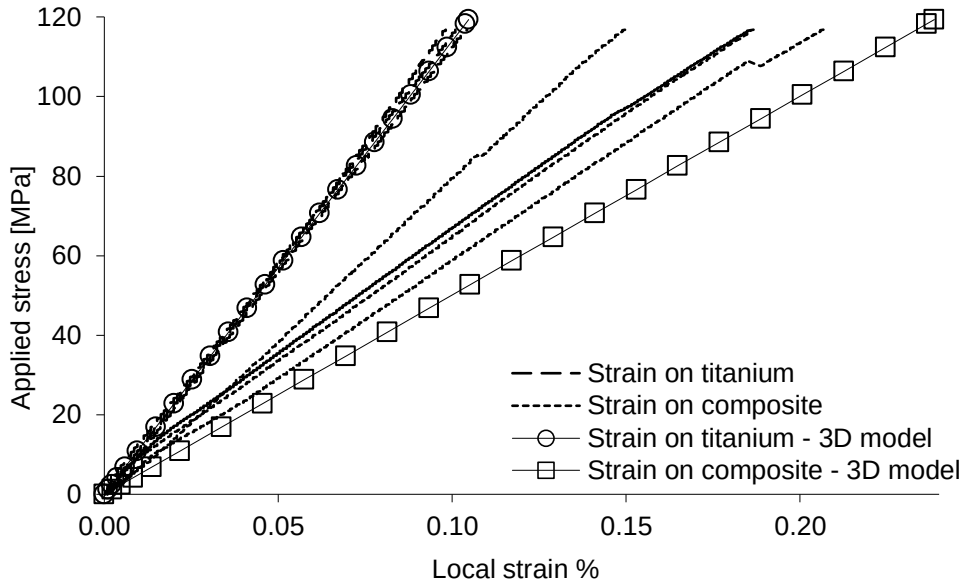

Fig.6.19 *The elastic stress-strainresults comparison of the tensile experiments and simulation of 3D global model with homogenised composite region for stress element*

The different results for the composite region can be caused by the different material properties used from literature, see Table.3.2 and Table.6.1. The Young's modulus from the literature is significantly smaller than the manufacturer's data sheet. Scatter could be caused by the manufacturing issues summarised in section 6.4.

6.4 Summary

The results have shown that the failure is initiated at the end of the double-step area in the composite part of the joint. Some delamination from the butt end in the direction towards the end of the composite part may occur. Cracks then initiate around the top of the protrusions on the first step and propagate along the protrusions

until the end of the first step. In some cases, cracks also initiate and propagate along the second step. Final failure occurs at the steps with fibre breakage.

For the manufacturing processes, there are issues need to be taken into account. Firstly, the curvature at the joint step may cause the axial fibres, especially on the joint surface, to deflect away from the desired direction; this may lead to some stiffness reduction. Secondly the resin rich regions at the joint step end may cause initial delamination within the composite; however, as shown in Chapter 7, this initial failure is not predicted to cause significant changes to the overall stress distribution. Thirdly, the prepreg can not always be pushed down completely leaving resin rich regions at the bottom of the protrusions; such resin-rich regions are not expected to contribute to the failure process since, as described above, failure is not observed in this region. Fourthly, there are slight misalignments of the protrusions which change the spatial arrangement of the protrusions; the simulations assume perfect spatial arrangement. Further, the height of the protrusions is not constant due to the creation processes of the protrusions through electron beam melting, etc. These manufacturing issues may cause some variability in the mechanical performance of the joining system.

The 2D and 3D global models simulations agree well with the local strain especially on the titanium. On the composite, the experimental values of strain show more scatter, as expected from the manufacturing problems described above. Further, the material properties used for the composite were gained from the literature, and are not in agreement with the manufacture's data. The modelling approach used for the global model analyses implies that the 2D unit cell modelling approach and 3D sub-modelling approach can be used as guidelines for the optimisation of these joints.

7
DISCUSSION

7.1 Introduction

In this chapter, after observing the failure processes (see Chapter 6), discussion of the importance of stress concentrations for the two and three dimensional analysis are presented. The effect of the geometric parameters are included along with considerations of the location importance for the two dimensional analysis. The protrusion distribution are included for the three dimensional analysis accounting for the stress concentrations location. Results of the two and three dimensional analysis for the protrusions on the step edge are compared and discussed. Considerations of the step joint design are also discussed.

Through private communication with Dr Faye Smith from TWI, the advantage of the joining system can be seen in Fig.7.1, for tensile experiments. Typical comparison of the control and Comeld ™ joints is shown with load and displacement data. The advantage of the joining system is clear. The displacement is much larger at failure for the Comeld ™ joint. Discontinuities in the load-displacement curve can also be identified for the Comeld ™ joint. This advantage can be explained. The protrusions change the stress distribution and concentration in the whole joint and delay the initial crack from propagation along the joint step or the bond line. Note that, both surfaces of the specimens manufactured by Dr Faye Smith were flat, i.e. the fibres were not deflected from the loading direction.

Compared to the experimental results obtained in Chapter 6, the difference is clear. The differences include a clear plastic zone during loading. This difference is considered to be caused by the manufacturing processes, in particular, the surfaces flatness and axial fibre orientation. Both surfaces of the specimens tested in Fig.7.1 were flat with a higher volume fraction of fibres. A flat panel was also put on top of

the specimens during autoclave to achieve the flat top surface finish. These differences are key for the different mechanical performances.

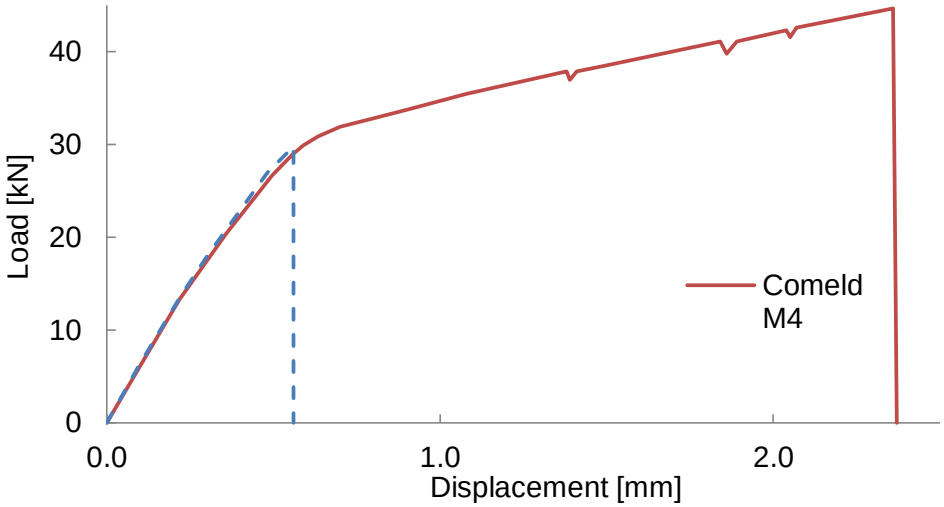

Fig.7.1 *Comparison of mechanical behaviour of Comeld ™ and control joints [Smith, 2005]*

7.2 Global control model

A two dimensional global control model was analysed to examine the local stress concentration difference brought by the protrusions. This control model shares the same dimensions and step design.

7.2.1 Global control model geometry and boundary conditions

The control model was analysed with the same geometry, load and boundary conditions as the global model of the Comeld ™ joints with detailed protrusions. There are no protrusions on the joint steps. The schematic diagram for the control model is shown in Fig.7.2.

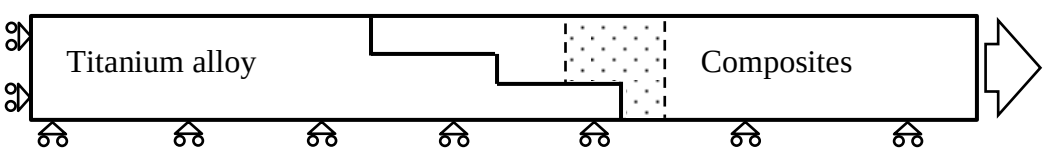

Fig.7.2 *Schematic diagram of the control model*

7.2.2 Comparisons of the global model with detailed protrusions and global control model

The region for comparison is marked in Fig.7.2. The comparisons of the axial, peel and shear stress concentrations are shown in Fig.7.3. Compared with the control model, the stress concentration is lifted away from the step surface to the top of the protrusion region.

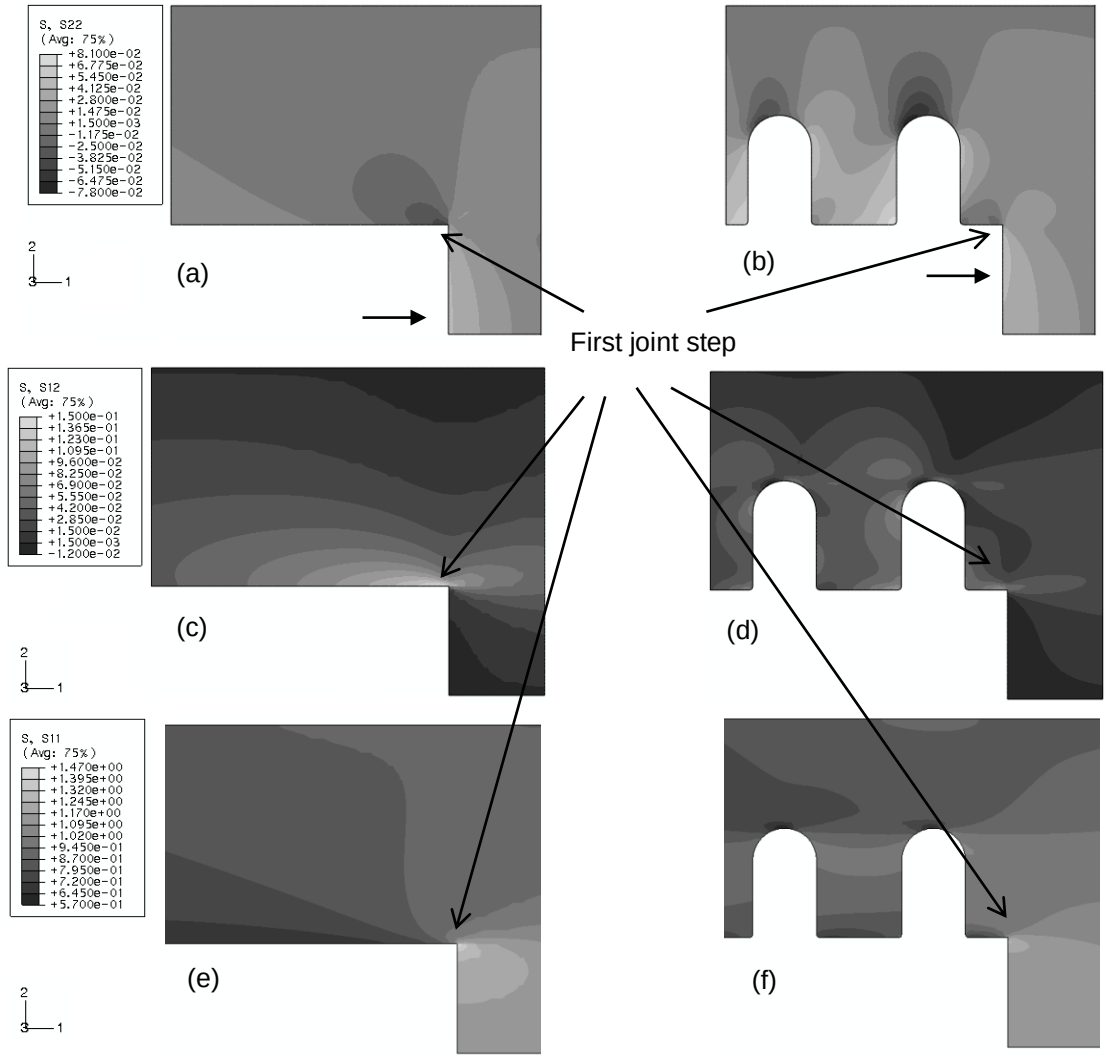

Fig.7.3 *Stress concentrations of the composite regions for control model (a) peel stress, (c) shear stress, (e) axial stress; and for the Comeld ™ joint (b) peel, (d) the shear stress, and (f) the axial stress*

For the peel stress, the stress concentrations around the step joint are very similar. The point of concentration is closer to the first step for the Comeld ™ joint, see the horizontal arrows shown in Fig.7.3 (a) and (b). However, the maximum stress concentration occurs at the left foot of the first protrusion, towards the metal end of the joint.

The shear stress concentration comparison of the global control model and Comeld ™ model is clear. There is almost 40% reduction in stress concentration around the first step. Comparing the control model maximum stress concentration (at the joint step) to that around the top of the first protrusion, there is even more reduction. The protrusions make it unlikely for the crack to propagate along the foot of the protrusions. Effectively, the shear stress concentration has been introduced into the composite by the protrusions.

For the axial stress, the stress concentration is similar for both cases, which is at the first step corner. There is roughly 12% reduction in stress concentration for the joint with protrusions. And again, the stress was distributed more in to the composite regions around the protrusions.

The effects of the Comeld ™ joint compared to conventional adhesive joint are clear. In general, the protrusions distribute stresses further away from the joint bondline into the composite region. This potentially utilises the fibre reinforced composites more effectively.

7.3 Experimental observations

The main purpose of the experimental work is to understand the failure process and accordingly understand the importance of the stress concentration for the finite element analysis. Therefore, the effect of the geometric parameters can be better understood, and this is also true for the protrusion distribution.

7.3.1 Failure processes

The failure processes can generally be described as follows. During the tensile test, with increasing applied load,

1. Initial failure appears near the joint step with a snap noise

2. Crack appears with a cracking noise and propagates along the top of the protrusions on the first step; it stops near the second step

3. Crack appears and propagates near the top of the protrusions on the second step; in some cases, crack does not appear for the second step before final failure occurs

4. Final failure occurs with a loud noise, as complete separation of the joint (in some cases, the crack does not appear for the second step).

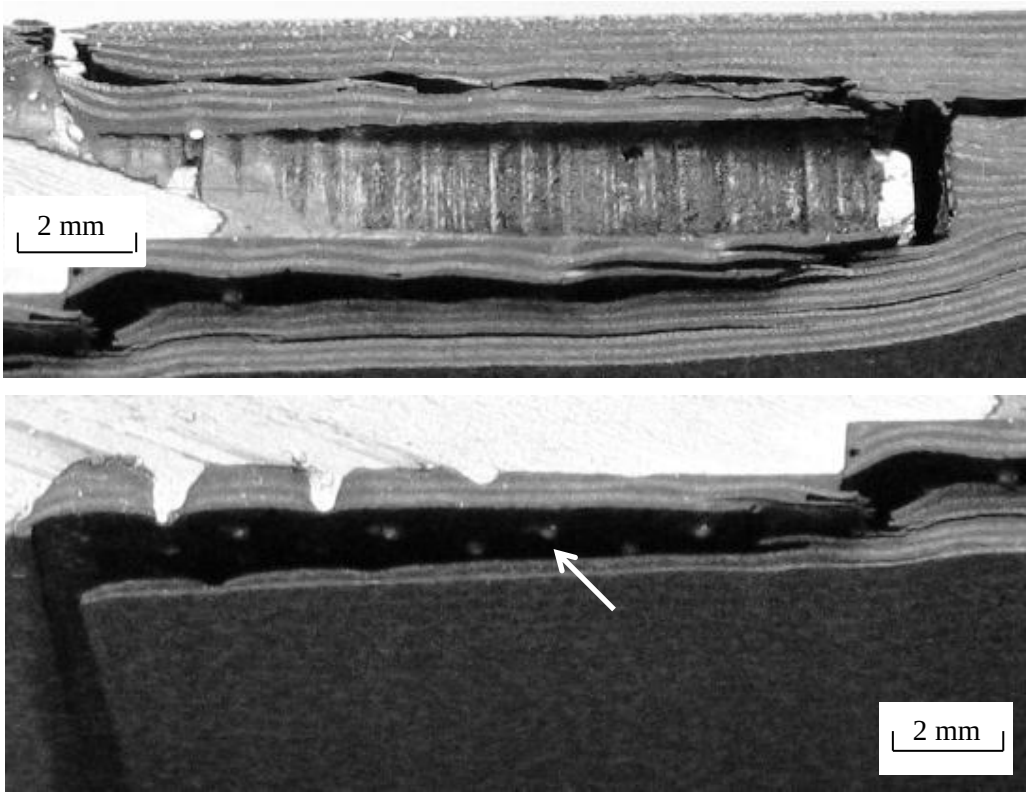

Fig.7.4 *The side view of the failed sample (arrow indicates the tip of protrusion)*

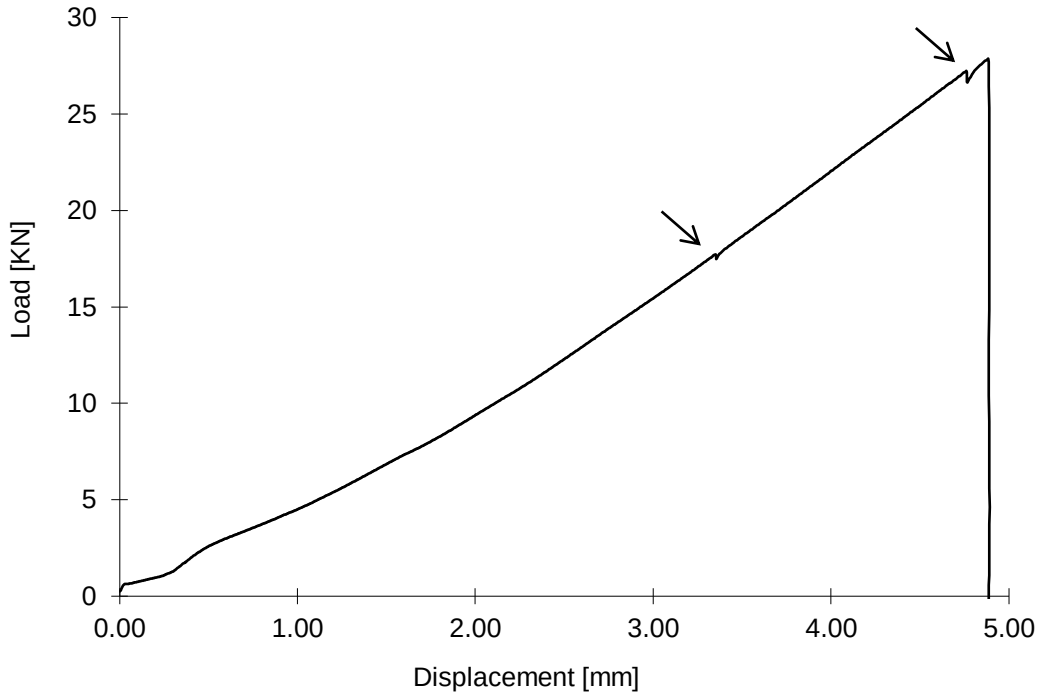

Fig.7.5 *Load displacement diagram for typical Comeld™ samples*

Fig.7.4 shows the side view of the failed sample. As the tips of the protrusions can be seen on the failure surfaces, the failure is confirmed to occur around the top of the protrusion region. This is also shown in Fig.6.15 in Chapter 6. The initiation of the cracks can also be identified with the load extension diagram, see Fig.7.5, where the arrows indicate the probable initiation and propagation of cracks.

7.3.2 Importance of different stress concentration locations

From the descriptions of the failure processes and the final failure of the joint, it can be identified that the top of the protrusion region and the first step joint surface just ahead of the first protrusion are important.

For the finite element analysis in two dimensions, the repetitive model represents the protrusions in the middle of the joint step. Therefore, the stress concentrations around the top of the protrusion regions are important. For the protrusions next to the step edge, the stress concentration at the region just ahead of the first protrusion is also important before the crack growth along the step occurs. Inevitably the final failure

will be the fibre breakage of the regions without the protrusions. However, the stress status has changed after the crack initiation.

For the three dimensional analysis, protrusions near the step edge were analysed, therefore, the stress concentrations around the top of the protrusions are important.

According to the importance of the stress concentration locations, two and three dimensional analysis will be discussed in the following sections to investigate effects of geometric and spatial arrangement parameters.

7.4 Global model with crack

Since manufacturing faults sometimes cause a resin rich region at the end of the joint step (see Fig.6.5). Premature failure could occur around the end of the joint. The effect of such failure on the overall stress distribution has been investigated. A small crack was created in the global model with protrusions to examine the effect on stress distributions.

7.4.1 Global model with protrusions and crack

The crack is marked in Fig.7.6. The load and boundary conditions were kept the same for the global model. The length of the small crack is four times the unit cell model width. Hard contact [ABAQUS, 2005] between the crack surfaces was defined. This is to ensure that there is not any mesh penetration.

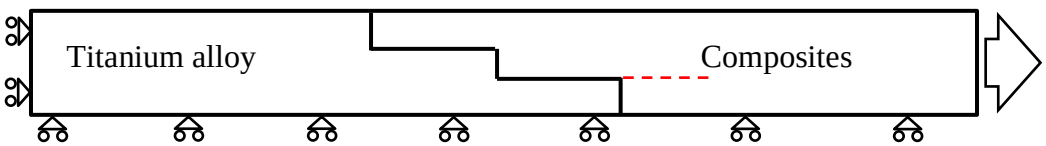

Fig.7.6 *Schematic diagram of the global model with the initial crack*

7.4.2 Comparisons of stress status of the protrusion on the joint step

The comparisons of the protrusion at the joint step of global models with or without the crack are shown in Fig.7.7, 7.8, and 7.9.

The axial stress distributions are similar as shown in Fig.7.7. The maximum stress concentration is enlarged by the crack for axial stress near the joint step. The stress concentrations around the top of the protrusion region are hardly influenced. The stress concentrations are listed in Table.7.1.

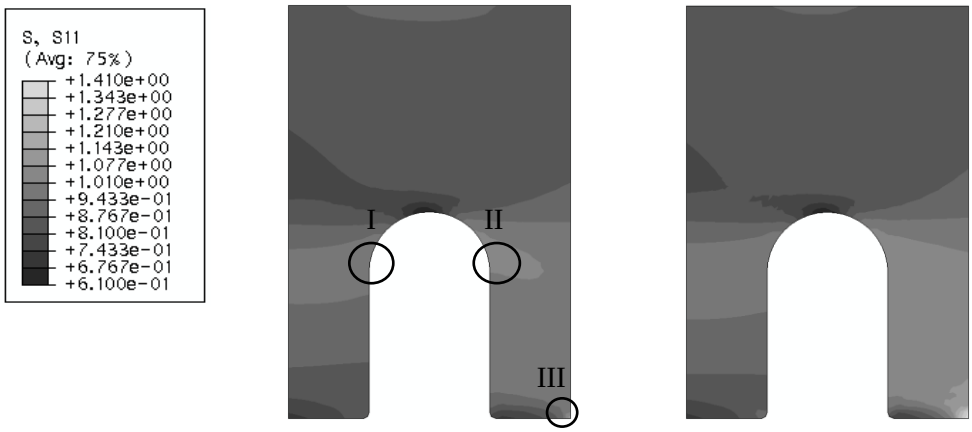

(a) normal (b) cracked

Fig.7.7 *Comparisons for the axial stress of the protrusion on the joint step*

Table.7.1 *Comparisons of axial stress concentrations for selected regions*

	Normal	Cracked
Zone I	9.84e-1	9.99e-1
Zone II	1.03e-0	1.04e-0
Zone III	1.13e-0	1.41e-0

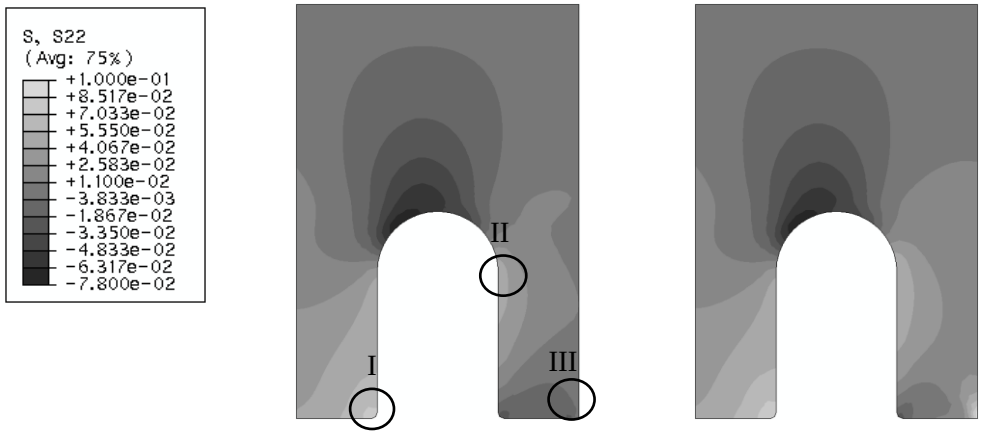

Fig.7.8 *Comparisons for the peel stress of the protrusion on the joint step*

Table.7.2 *Comparisons of peel stress concentrations for selected regions*

	Normal	Cracked
Zone I	8.02e-2	8.63e-2
Zone II	4.79e-2	5.29e-2
Zone III	8.77e-4	9.52e-2

The peel stress distributions are similar and are shown in Fig.7.8. The stress concentrations are increased by the crack for all three marked regions, especially for III, which is near the joint step. In regions I and II, the increases are not substantial. The stress concentrations are listed in Table.7.2.

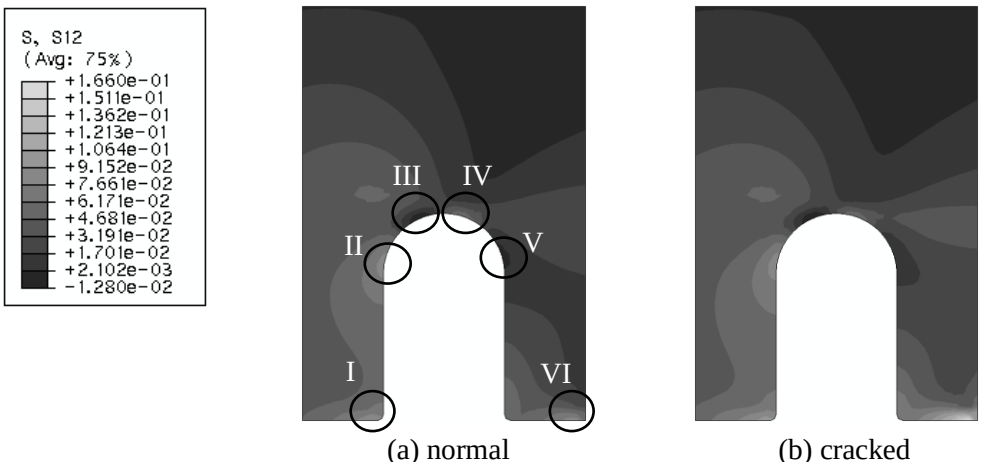

Fig.7.9 *Comparisons for the shear stress of the protrusion on the joint step*

Table.7.3 *Comparisons of shear stress concentrations for selected regions*

	Normal	Cracked
Zone I	8.74e-2	9.69e-2
Zone II	8.42e-2	8.60e-2
Zone III	1.08e-2	1.28e-2
Zone IV	6.03e-2	5.98e-2
Zone V	2.41e-3	5.63e-3
Zone VI	8.61e-2	1.66e-1

The shear stress distributions are similar as shown in Fig.7.9. The stress concentrations are listed in Table.7.3. The stress concentrations are similar for regions II, III and IV. In regions I and VI, the stress concentration increased significantly. Especially for VI, it is almost doubled, which is near the joint step. In region V, the shear stress changes direction compared to the normal global model, however, the values are relatively small. Note that the minus values indicate direction change for the shear stress.

To summarise, stress distributions around the top of the protrusion are not significantly affected by the small crack. Stress concentrations near the joint step are increased by the existence of the crack. Therefore, the crack in the composite next to the joint step is not significant for the investigation at the stress concentrations around the top of the protrusion region at this stage.

7.5 Two dimensional analysis

For the two-dimensional analysis, the stress concentrations results are presented with discussions according to the importance of the local stress concentration. The effect of geometric parameters will be further analysed. Height, shape, and angle effect will be discussed to identify the optimised parameters under global tensile loading.

7.5.1 Importance of the local stress concentration

Stress concentration contours of peel and shear stresses are shown in Fig.7.10 to demonstrate the important regions for protrusions on the joint step edge.

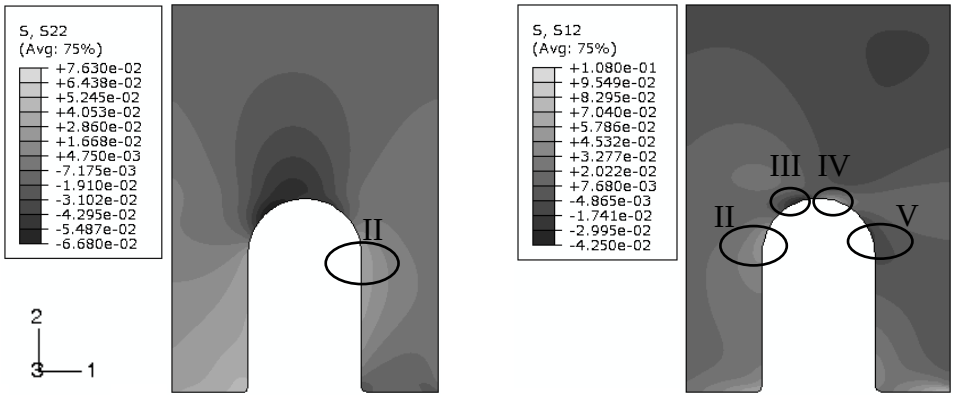

Fig.7.10 *Stress concentration zones for peel and shear stress around the protrusion at the step edge*

The important zones are marked in Fig.7.10. For the 1mm perpendicular protrusion, the right straight boundary of the protrusion just next to the top is marked for the peel stress. On the left of the region, there is not any obvious stress concentration (minus values in this case is compression). Four zones around the top of the protrusion region are marked for the shear stress.

For the repetitive protrusions (representing protrusions in the middle of the joint step), the important zones are marked in Fig.7.11 for different stress components. The region around top of the protrusions is the only concern, as failure occurs away from the foot of the protrusions.

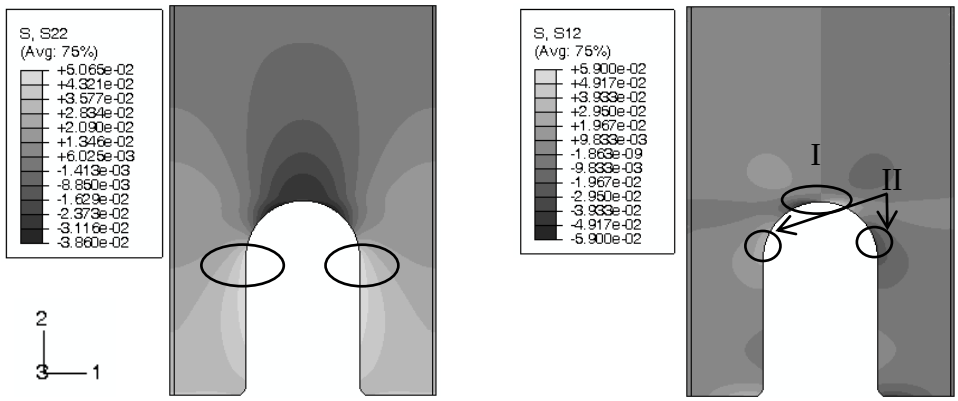

Fig.7.11 *Stress concentration zones for axial, peel and shear stress around the protrusion with repetitive boundary conditions*

The cracks around the top of the protrusion regions initiate and propagate very quickly. Fibre breakage is not present at the crack initiation and propagation, therefore axial stress concentrations are not important at this stage. The delamination is caused by shear stress assisted by peel stress. At the final failure of the joint, fibre breakage and interface failure can be found at the first step near the step corners and sometimes also at the second step. This due to the increased loading after the cracks propagated along the top of the protrusions.

As discussed in Chapter 4, the height effect was investigated with square array spatial arrangement assumption for the measured protrusion distribution density, and for the perpendicular protrusions only, where the shape effect has not been included. For different shape of the protrusions, the volume was kept the same for the unit cell models, see Chapter 3 for the definition of the protrusion height and angle. The shape and angle effects are explored for the 1mm height protrusion. However, it is considered that the height effect for the measured protrusion distribution density and perpendicular protrusions can be extended to different protrusion distribution densities.

7.5.2 Optimisation of the end protrusion

As shown in Chapter 4, Fig.4.21 and 4.26, for both parallel and hill shapes, the peel stress concentration around the top right of the protrusion moved down as the protrusion turns towards the metal end of the joint; since the protrusion angle makes the change more gradual in material stiffness for the minus protrusion angle. And in addition, for the hill shape, at the left side of the protrusion, distinct peel stress concentration stays in Zone I.

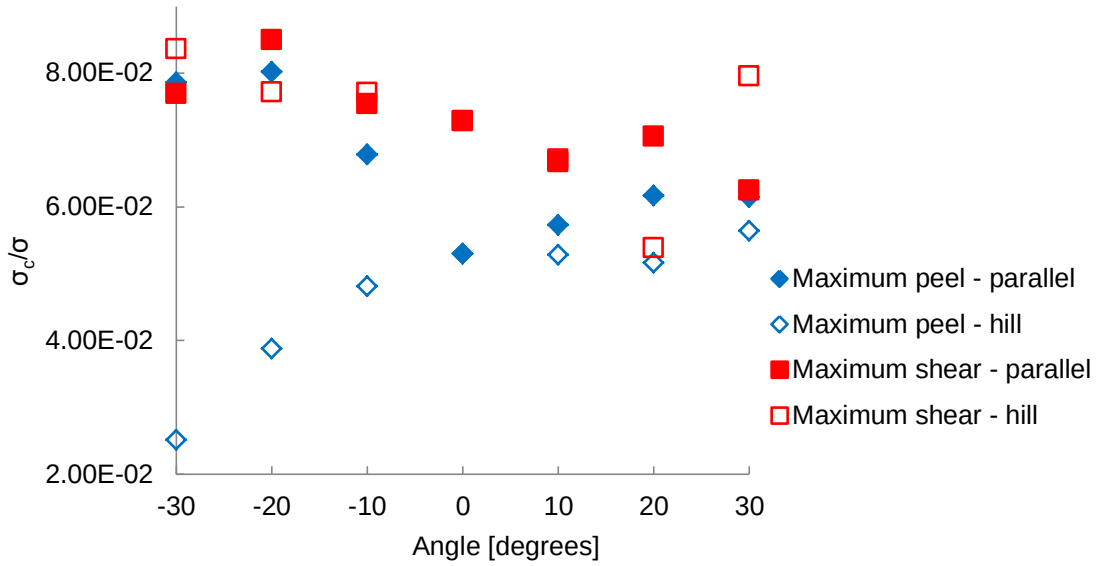

Fig.7.12 *The maximum stress concentrations of peel and shear stress around the top of the end protrusion – shape and angle effect*

The maximum stress concentrations for the whole region around the top of the protrusion are compared in Fig.7.12. In the case of peel stress concentrations, the angle effect is clear: stress concentration reduces with protrusion angle towards the metal end of the joint for the hill shape protrusions. Hill shape shows slight lower stress concentration for the protrusion angle towards the composite end of the joint. Minus angle hill shape protrusions significantly reduces the peel stress concentration around the top of the protrusion region.

For shear stress, the trend is not clear. The only obvious stress distribution change is due to the protrusion angle and geometric difference. Otherwise, the stress distributions are similar for different protrusion shapes, see Fig.4.23 and 4.28. The maximum stress concentration results from the around the top of the protrusion are not monotonic since values are extracted from different zones at different angles (see Table.4.20). For the 30 degree protrusions, hill shape protrusions show higher values of maximum stress concentration. For the 20 degree protrusions, hill shape protrusions show lower values of maximum stress concentrations. For all other angles, hill shape protrusions show similar maximum stress concentrations with parallel shape. The plus 20 degree hill shape protrusion shows the lowest shear stress concentration.

The maximum stress concentrations around the top of the protrusion region for different protrusion height are shown in Fig.7.13. For all regions around the top of the protrusions, trends for the height effect are clear. Generally higher protrusions show lower maximum shear stress concentration and the peel stress concentration only varies slightly.

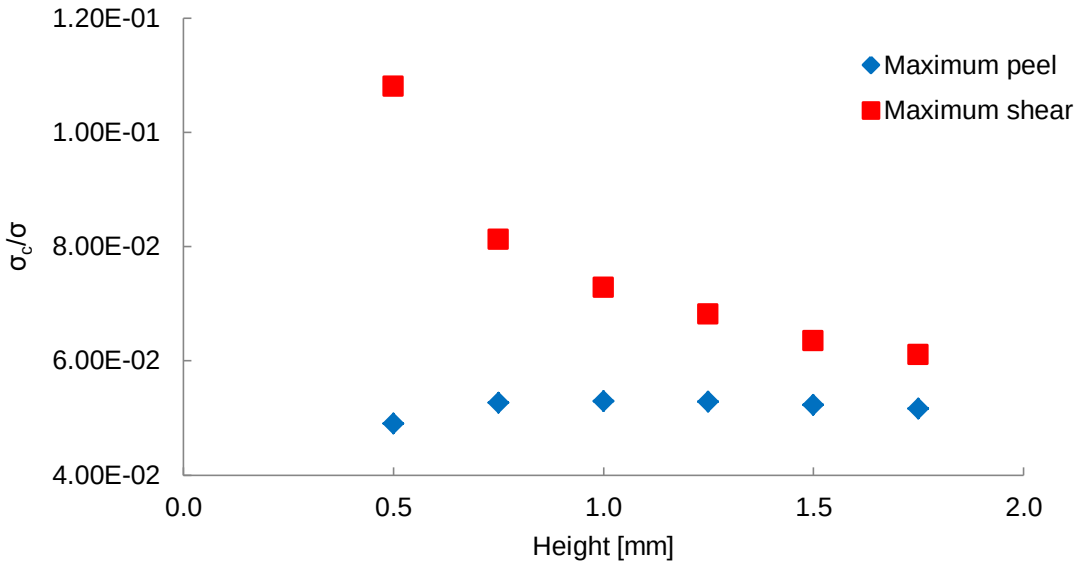

Fig.7.13 *The maximum stress concentrations of peel and shear stress around the top of the end protrusion – height effect*

To summarise, the stress concentration around the top of the protrusion region at the joint step, maximum values stress concentrations from this region have been examined carefully. Plus 20 degree hill shape protrusion shows lowest shear stress concentration. However, the stress concentration increases dramatically for protrusion angle of plus 30 degrees, where stress interactions between the protrusion and the joint step occur. The peel stress is greatly reduced for minus protrusion angles for the hill-shaped protrusions. Minus 20 degree hill-shaped protrusion is considered to be the best to minimise peel stress whereas the shear stress only increase slightly. With protrusion height, the stress distributes more into the composite region and lower stress concentration was found.

7.5.3 Optimisation of the repetitive protrusion

The repetitive protrusions are examined to explore the propagation of the cracks along the tops of the protrusions. Peel and shear stresses from the top of the protrusion region are compared to optimise the angle, shape and the height of the protrusion.

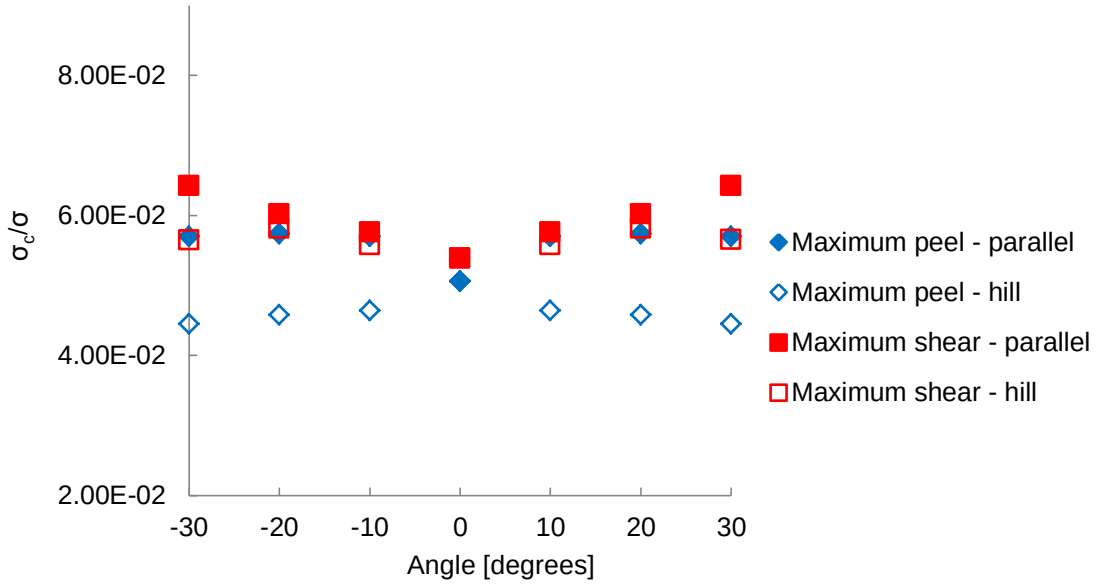

Fig.7.14 *The maximum stress concentrations of peel and shear stress around the top of the repetitive protrusion – shape and angle effect*

The comparisons for the maximum values of peel and shear stress concentrations for the shape and angle are shown in Fig.7.14. These stress concentrations are from the top of the protrusion region. Due to symmetry, the values show symmetric behaviours for the protrusion angle. Peel stress concentrations are not sensitive to the protrusion angle change for different shapes; and values are lower with the hill shape. Shear stress concentrations increased slightly with angled protrusions compared to the perpendicular case. For reduced peel stress concentration, plus or minus 10 degree hill shape protrusions can be selected.

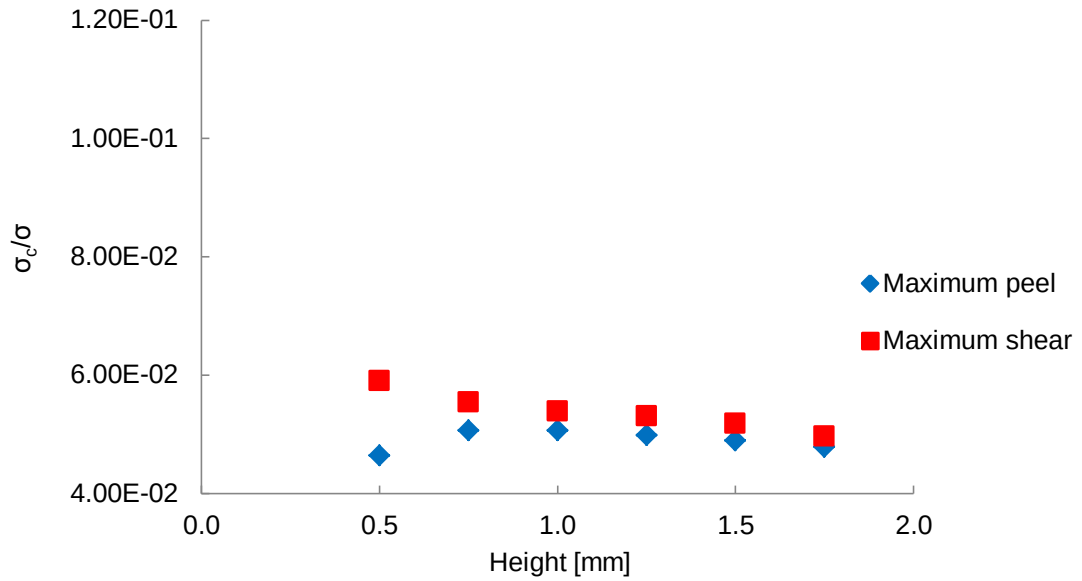

Fig.7.15 *The maximum stress concentrations of peel and shear stress around the top of the repetitive protrusion – height effect*

Maximum stress concentrations for the peel and shear stresses from the top of the protrusion region are shown in Fig.7.15 for the height effect. The peel stress concentrations vary slightly with protrusion height. The low value of peel stress around the top of the 0.5 mm protrusion arises from the near circular shape of this protrusion.

For the maximum shear stress concentration of the top of the protrusion region, the trend is clear that with protrusion height, stress concentration reduces. Shear stress concentration is generally larger than the peel stress concentration.

To summarise, the angle effects of repetitive protrusions are smaller than those for the end protrusion. Angled protrusions lead to lower peel stress and only a small increase in shear stress. The height effects of repetitive protrusions are also smaller. And again, with protrusion height, the stress distributes more into the composite region and lower stress concentration was found.

7.6 Three-dimensional analysis

For the three-dimensional analysis, spatial arrangements were included. The effect of the spatial arrangements will be compared.

7.6.1 Importance of protrusion distribution

The importance of stress components and local stresses are the same as the two-dimensional analysis. Therefore, peel and shear stresses were selected for the discussion; the axial stress would contribute to the final failure when the stress states are changed due to delamination of the composites. The local stress concentrations are from around top of the protrusion regions marked in Fig.7.10 for peel and shear stresses.

7.6.2 Importance of the spatial arrangements

For the local peel stress, the stresses around the top of the protrusion on the joint step are compared for different spatial arrangements. The maximum values of peel stress around the top of the protrusion on the joint step edge from the first and second column is shown in Fig.7.16.

The effect of the spatial arrangements is clear. For the half density square array arrangement, the local peel stress is the lowest. The maximum local peel stress is from the rotated measured array, and the other arrangements are showing similar values. The effect of spatial arrangements is similar for the second column. The square array arrangement shows similar values between first and second column of protrusions, where others are reduced. The indication for the protrusion distribution is clear, the measured array shows lower local peel stresses, and reducing the protrusion distribution can reduce the local peel stresses.

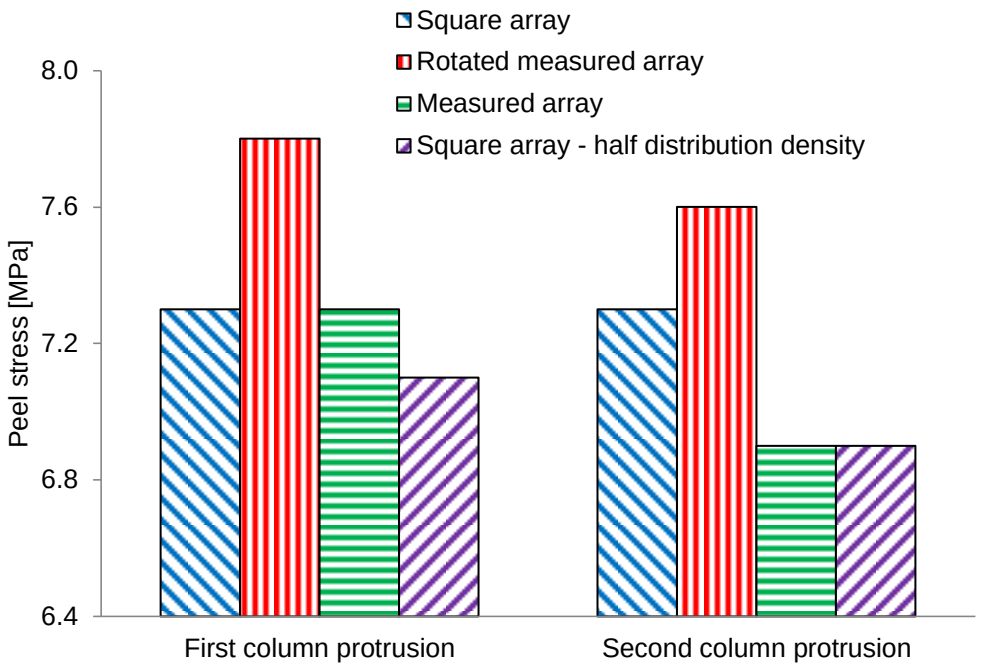

Fig.7.16 *Maximum peel stress for the protrusion on the edge of the joint from the first and second column; the marked zones are shown in Fig.7.10*

For the local shear stress, the first protrusion on the joint step was compared for different spatial arrangements. The maximum values of shear stress around the top of the protrusion on the joint step edge from the first and second column are shown in Fig.7.17 and 7.18. The values shown in the case of shear stress.

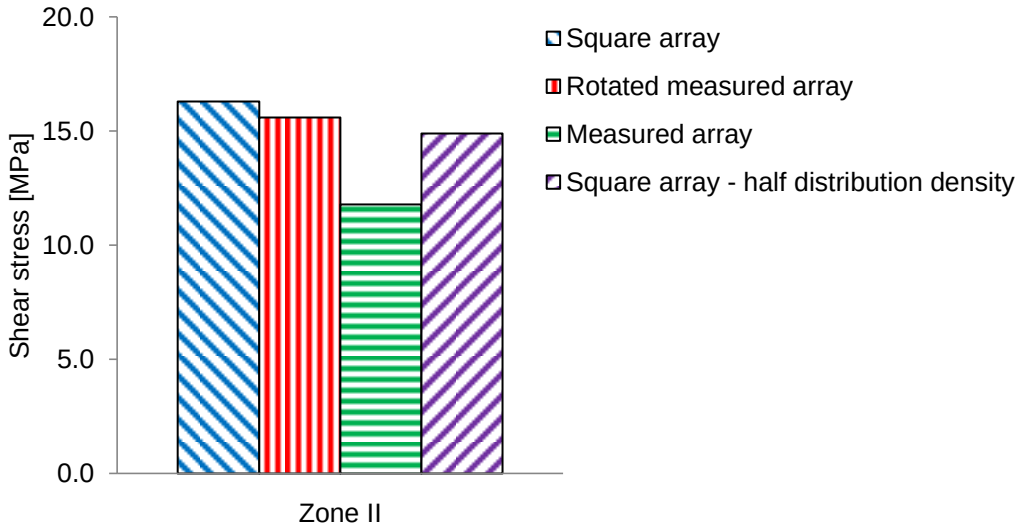

Fig.7.17 *Maximum shear stress for the protrusion on the edge of the joint of the first column, the marked zones are shown in Fig.7.10*

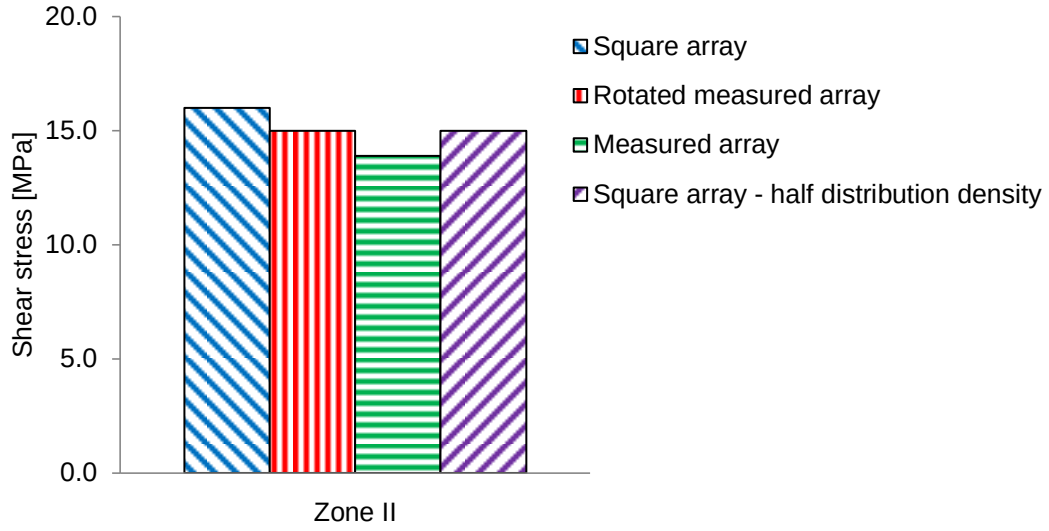

Fig.7.18 *Maximum shear stress for the protrusion on the edge of the joint of the second column, the marked zones are shown in Fig.7.10*

With local shear stresses, marked zones at around the side of top of the protrusions are important. Zone II shows higher values comparing with the other zones in both cases. The measured array shows a little increased shear stress compared to the first column protrusion, and other arrangements stress hardly changes.

With tensile load applied globally, square array protrusions responses are similar within the row (comparing first and second column protrusions), especially for the maximum stress concentration locations. For the hexagonal like arrangements, due to the shifted location from the neighbouring protrusion rows, the induced stress concentration shifts with the protrusions.

Generally, local shear stress is small for Zone III and V and intermediate for Zone IV, which is near the tip of the protrusion.

7.6.3 Protrusion spacing

To summarise, the measured array and square array with reduced density of protrusions lower the peel stress concentrations. Measured array of protrusions shows lower shear stress concentrations around the top of the protrusion region. The

indication is clear that the distance between the protrusions in the loading direction determines the level of stress concentrations around the top of the protrusion region.

As shown in Fig.7.19, it is clear that axial and shear stress reduces with increasing distance in the axial direction; peel stress reduces and then increases slightly, indicating further increase for too high spacing. Stresses are extracted from the first column of protrusions around the top of the protrusion region.

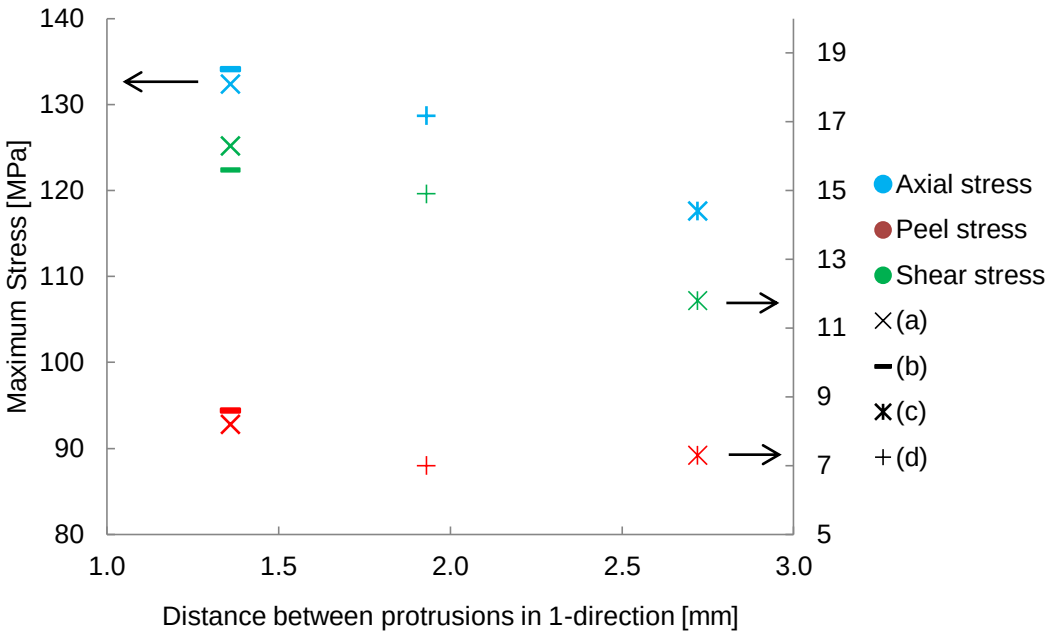

Fig.7.19 *Effect of distance between protrusions in 1-direction for the stress around the top of the protrusions*

Local maximum stresses in arrangements (a) and (b) (see Fig.3.31 for arrangement definition) are very similar despite the change in arrangement in the through-the-width direction. (b) and (c) are the same near hexagonal arrangement, but the separation in the axial direction is larger in (c) resulting in lower local stresses. (a) and (c) have the same protrusion distribution density, but the hexagonal arrangement of (c) causes significant reduction in axial and shear stresses, and some reduction in peel stress. The reduced protrusion distribution density arrangement of (d) causes smaller stress reduction compared to arrangement (c) showing the importance of the 1-direction distance.

These observations show that the hexagonal arrangement tends to cause lower local stresses, provided that protrusions are arranged with maximum separation in the direction of applied load. Reducing the protrusion distribution density from the measured density used is beneficial, but half the density may be too much for hexagonal arrangement of protrusions as this may cause increase in peel stress.

7.7 Comparisons for two and three dimensional analyses

In the two dimensional analysis, two conditions have been considered, where in the three dimensional analysis, submodels from the joint step edge have been considered. The comparable figures are the protrusions on the joint step edge. The assumption for the two dimensional analysis are many, one of which is to assume square array spatial arrangement. Therefore, comparisons can be made between the two and three-dimensional analyses. The edge protrusion model of the two-dimensional analysis and the protrusions from two columns in the square array three-dimensional analysis were compared. Axial, peel, and shear stress contours are compared in Fig.7.20, 7.21 and 7.22 respectively. The first and second columns are defined in Chapter 5, see Fig.5.13. The first column is next to the symmetry plane.

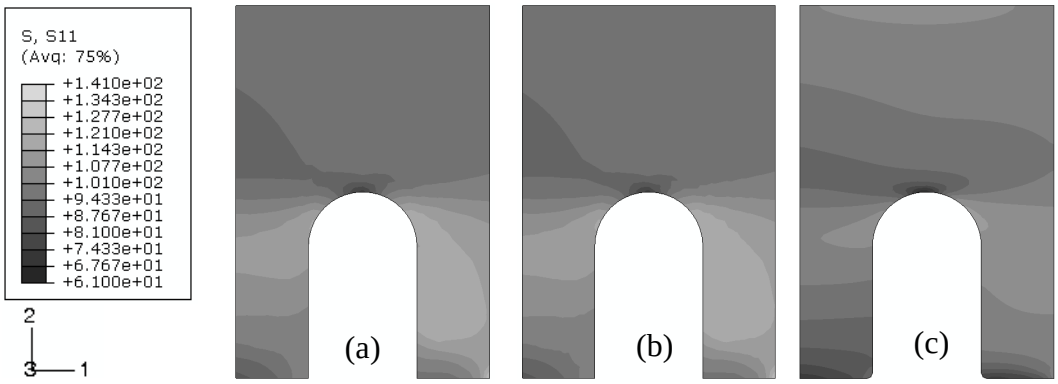

Fig.7.20 *Axial stress comparisons between cross-sections of (a) 3D square array first column, (b) 3D square array second column, and (c) 2D protrusion at the step edge*

The comparisons in Fig.7.20 to 7.22 are from different applied loads. For two-dimensional analysis, stress concentrations were the main focus (unit pressure load was applied), whereas 116 MPa was applied for the three-dimensional analysis.

However, the scales have been manipulated so that the contours can be directly compared.

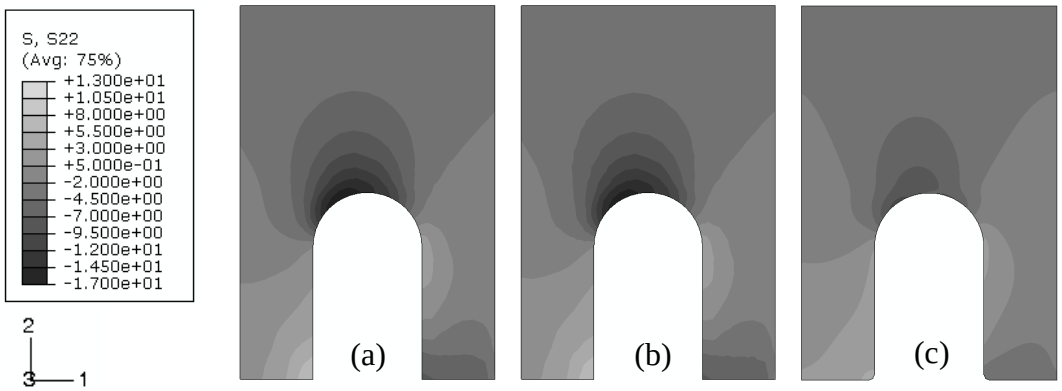

Fig.7.21 *Peel stress comparisons between cross-sections of (a) 3D square array first column, (b) 3D square array second column, and (c) 2D protrusion at the step edge*

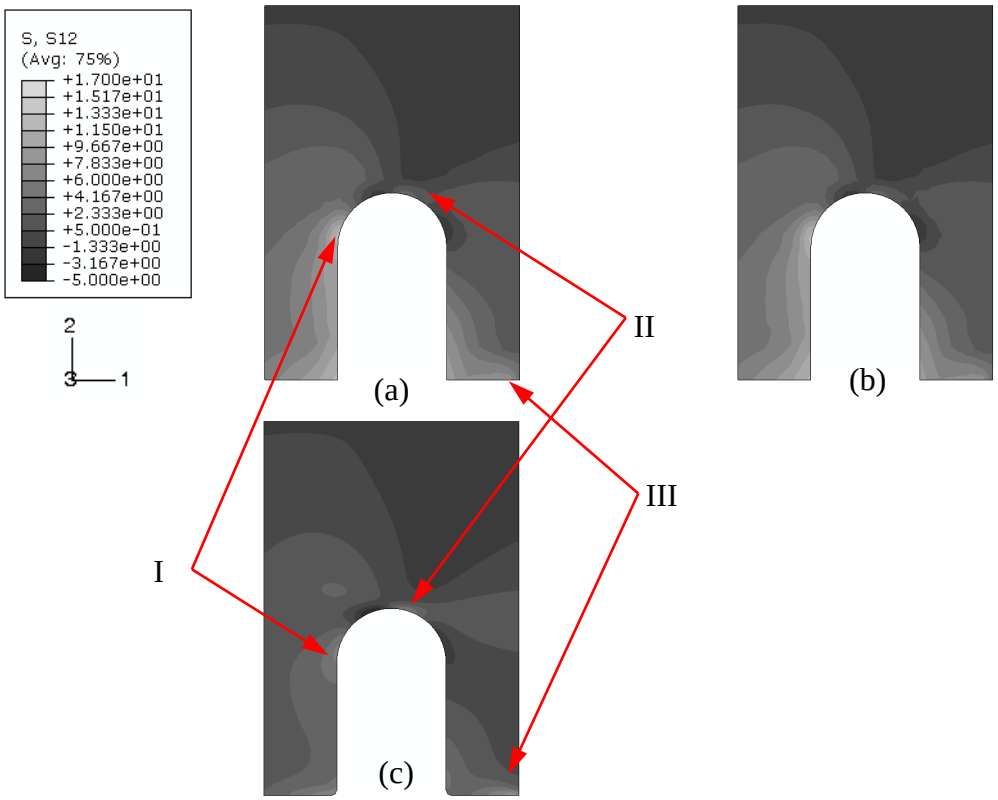

Fig.7.22 *Shear stress comparisons between cross-sections of (a) 3D square array first column, (b) 3D square array second column, and (c) 2D protrusion at the step edge*

Clearly, the stress distributions are similar for all the stress components in the figures. Especially for the peel and shear stresses, stress concentrations occur at nearly the

same locations. For axial stress in Fig.7.20, the recalculated stress range is similar to those of three-dimensional analysis, and the maximum value of axial stress for the two-dimensional model is slightly lower.

However, for peel stress in Fig.7.21, the maximum stress concentrations are smaller compared with the three-dimensional analysis, 8.9 MPa comparing with 12.9 MPa, as well as for the top of the protrusion region, 6.1 MPa comparing with 7.5 MPa. Generally, the peel stress concentrations are lower for the two-dimensional analysis.

For the shear stress, the stress concentration is different for the two-dimensional analysis. For marked stress concentration locations in Fig.7.22, region I, the value of stress concentration is significantly higher for the three-dimensional analysis, 16.3 MPa comparing with 8.4 MPa; region II, the value of stress concentration is higher for the two dimensional analysis, 8.2 MPa comparing with 5.5 MPa; region III, the values of stress concentration are similar with small variation, 11.4 MPa for three-dimensional model comparing with 11.2 MPa for two-dimensional model.

For the two dimensional analysis, one of the assumptions is the two-dimensional model represents the cross section of the protrusion, and plane strain elements were used. Therefore, in the cases of peel and shear stresses, interactions between the neighbouring protrusions in the through-width direction were not taken into account. This may explain that there is less peel and shear stress in the two dimensional analysis results.

7.8 Other techniques

Improvements in through-thickness strength of composites can be achieved by the insertion of metal or fibrous composite pins through the thickness; these are described as z-pins [Mouritz, 2007]. However, reduction for the in-plane mechanical properties of z-pinned composite laminates has been observed; such reduction may be due to combined effects of fibre volume fraction change, resin-rich pockets around the z-fibres causing stress concentrations and misalignment of the laminate longitudinal fibres (in-plane and out-of-plane), caused by the insertion of z-fibres [Lenzi et al.,

2007; Grassi et al., 2002]. Similarly, the existence of the protrusions may have the same trend reducing the in-plane mechanical properties for the composite part of the joint, as the protrusions are much larger than the fibre tow dimension.

The Comeld ™ joining system is designed to improve metal-composites joints using through-thickness inserts from the metal step into the composite laminate. Comparing Comeld ™ joint and z-pin reinforcement, the essential difference is that in Comeld ™ joints, the protrusions are created from, and connected to, the metal joint surface, but z-pins are individual pins. The effects of z-pins on delamination behaviour have been studied using miniature experiments which showed that bridging of delamination cracks may suppress the growth of the crack [Cartié et al., 2004]. Improvement in joint behaviour using through-thickness z-pins in the adherends has been shown to significantly improve joint performance [Mouritz, 2007]. The effect of z-fibre insertion depth has been studied using finite element analysis [Grassi et al., 2003]: through-thickness z-pinned laminates were predicted to perform significantly better than those of smaller insertion depth laminates. The analysis of Comeld ™ joints regarding the protrusion height effect indicated that higher protrusions reduce the danger of delamination progress along the top of the protrusions, which suggests a similar trend to that found for z-pinned laminates.

Rugg and his co-workers [Rugg et al., 1998] studied the effect of angled through-thickness metallic rods the delamination of reinforced carbon fibre epoxy single lap joints. Although the angle effect has not been fully investigated, some trends could be recognised. They found that the so called orientation R of the inserted metallic rods, which was oriented against the loaded end of the adherend of the lap joint, and the angle was approximately 39 º, contributed more effectively. Similar results were found in the miniature experiments [Cartié et al., 2004] which showed that angled inserts opposing the shear were most effective in restricting delamination growth.

Reduction for the in-plane mechanical properties of the z-pinned composite laminates was also observed, and these may be due to combined effects of fibre volume fraction change, resin-rich pockets around the z-fibres causing stress concentrations and misalignment of the laminate longitude fibres (in-plane and out-of-plane), caused by

the insertion of z-fibres [Lenzi et al., 2007; Grassi et al., 2002; Mouritz, 2007]. Similarly, the existence of the protrusions may have the same trend reducing the in-plane mechanical properties for the composite part of the joint.

Although the size of the protrusions is not studied, finer protrusions may be preferred as reported that the significant degradation of mechanical properties such as modulus and strength can be avoided by using finer z-fibres [Chang et al., 2006]. For compression strength, it was suggested that increasing pin density was more detrimental to in-plane compression strength, in other words, for the same density, finer z-fibre insertion offers higher compression strength, for the same diameter, smaller volume density z-fibre insertion offers higher compression strength, and the effect of density is greater than that of the diameter [O'Brien et al., 2006].

It is hopeful that these techniques may reveal some inspirational indications for the future research of the Comeld ^{TM} joining system.

7.9 Summary

The advantage of the Comeld ^{TM} joint over conventional control joint is clear. The importance of the stress concentration location was discussed. According to this, the effects of height, shape and angle of the protrusions were further assessed. Protrusion height of 1.75mm shows lower stress concentrations. If it is desired to investigate the height together with the shape and angle effects, there are many more parameters to be considered. These include the width of the unit cell model. This is difficult to achieve for the plus and minus angle protrusion models with increasing height. The models will be less tractable for greater protrusion angles. This could be solved with a different spatial arrangement that leaves more distance between the protrusions in the axial direction. The discussion on the height of the protrusions only investigated the situation for the height of the protrusion smaller than the joint thickness. The height can be designed to reach or exceed the height of the composite thickness, which may result in the protrusions acting as crack stoppers which can toughen the composite part of the joint and lead to higher joint strength. In this way, the failure of the joint may no longer take place at the interface.

However, the material forming the protrusions is taken from the joint step. The higher the protrusions (if maintaining the protrusion radius), the more material needs to be taken from the joint step to create the protrusions and the amount of material taken could be significant. This may weaken the metal joint step severely. Therefore, to maintain performance, thicker joint steps may be desired, and this will result in a heavier joint. This may be a very important issue for high performance industries, which sometimes require the best performance over weight ratio.

The crack initiation and propagation processes are found to occur from a combination of peel and shear stress concentrations. The improved performance of Comeld ™ joints has been demonstrated both experimentally in work carried out in parallel to this research (see Fig.7.1) and from comparative finite element analyses.

The optimisation of the end protrusion is obtained from the consideration of the reduction of peel stress for protrusions with hill shape angled towards the metal end of the joint. The peel strength, at around 80 MPa (see Table.3.2, Chapter 3), is the lowest strength, so reduction in this stress concentration should improve joint performance. The shear strength is around 128 MPa (see Table 3.2, Chapter 3), almost 60% higher than the peel strength, and the stress concentrations of shear stress is similar to peel stress for the positive angle, hill-shaped protrusions. Therefore, the negative protrusion angles should improve joint performance, since the peel stress concentration is reduced although there is a slight increase in shear stress concentration.

The repetitive protrusion has smaller reductions in peel stress concentrations for angled protrusions and a slight increase in shear stress concentration. Angled protrusions should improve joint performance. As the crack propagates, it will lose the repetitiveness, so negative protrusion angles should improve the performance of the joint. This improvement for angled through-thickness insertions is also found in some other enhancement techniques [Rugg et al., 1998; Carti é et al., 2004].

This research has shown that the optimised density of protrusions is lower than that originally proposed and used in the experimental work. The optimisation of the array

is more complex; the prediction indicate that the protrusions should be arranged well-spaced in the loading direction which is most easily obtained using a hexagonal arrangement.

8
CONCLUSIONS AND FUTURE WORK

A summary of the basic conclusions of this work is given here.

Chapter 3 describes the methods used for the two and three dimensional analyses. Chapter 4 reveals the effects on the stress response of two different protrusion shapes along with different protrusion angle and different protrusion height. Significant differences were found between parallel and hill shape two dimensional unit cell models with protrusions with negative angles or greater height corresponding to lower values of stress concentrations under global tensile loading.

Chapter 5 reveals the effects of the protrusion distribution pattern. Stress responses were investigated. The key factor to reduce the maximum stress concentration around the protrusion tip is the distance between the protrusions in the axial direction. This arises from the interaction between the protrusions leading to stress concentration around the top of the protrusions.

Chapter 6 presented limited experimental work in an attempt to understand the failure processes and the possible influence of the manufacturing processes. The findings indicate the importance of the local stress concentrations. The two and three dimensional finite element analyses for the globally tensile loaded joining system were also compared to the experimental work in the elastic region and reasonable agreement was found.

The results of the two and three dimensional analyses were further investigated in Chapter 7. The locations and values of the stress concentrations were considered. The effects on the parameters, such as protrusion shape, height, orientation, and distribution patterns were further discussed. Based on the stress concentration results of the shear and peel stresses before failure occurs, the minus 20 degree hill-shaped protrusion is considered to be the most appropriate angle and shape for protrusions

both on the joint step and in the middle of the step. In this work, three distribution patterns and two distribution densities have been investigated. The hexagonal distributions considered were the array used for the experimental work, and the same array rotated through 90 degrees such that the distance between the protrusions aligned in the loading direction was halved. Further analyses were carried out for a square array. Both hexagonal and square arrays were analysed at the protrusion density used for the experimental work and half that density. On this basis, the preferred arrangement, giving lower peak stress concentrations, is a hexagonal array oriented so that the distance between the protrusions aligned in the loading direction was maximised, and a lower protrusion distribution density than used in the experimental work. Two and three dimensional analyses were compared. Similar stress distributions were found, although the two-dimensional analysis results in generally lower maximum values of stress concentration for the peel and shear stresses. This was caused by the limitation of the two-dimensional analysis which cannot take into account interactions between neighbouring protrusions in the width direction. In addition, the design and manufacture issues were raised for further research.

This work can be considered the very beginning of a new era of joining technology. Therefore, more needs to be done to gain better understanding of the joining system. First of all, the manufacturing limitations must be studied carefully to frame the simulation work (these include the curvature at the joint step, the resin rich region, the fact that the prepreg cannot always be pushed down completely, slight misalignment of the protrusions, height of the protrusion not being exactly the same, etc.). Secondly, as the scatter in the experimental work is large, most probably arising from the manufacturing limitations, further experimental studies are necessary. In addition, fatigue and environment studies are desired to further develop and optimise this joining system. Thirdly, further study of the effects of the geometry of the protrusions, including the protrusion radius and different spatial distribution patterns and densities, may be required. Fourthly, work must be done to investigate the failure mechanisms for the joining system before it can be utilised in the wide range of industries that require bonding of composites and metal, including the automobile and

aeroplane industries. The development of a suitable failure criterion is important. Last but not least, it was assumed that the titanium alloy properties are homogeneous, however a metallurgical investigation is needed to check this assumption since the electron beam process melts the metal.

REFERENCES

ABAQUS, Analysis User's Manual, 10.2.1, 2005

ABAQUS, Analysis User's Manual, 13.1.1, 2005

ABAQUS, Analysis User's Manual, 18.2.1, 2005

R.D. Adams, J. Comyn, W.C. Wake, Structural adhesive joints in engineering, Chapman & Hall, Second edition 1997

R.D. Adams, J. Comyn, Joining using adhesives, Assembly Automation, Volume 20 - Number 2, 109-117, 2000

T.L. Anderson, Fracture Mechanics – Fundamentals and Applications, 3rd ed., Taylor & Francis, 2005

Z.H. Barber, ed., Introduction to Materials Modelling, Maney, 2005

P. Bastid, TWI Ltd., private communication, 2005

B.R.K. Blackman, H. Hadavinia, A.J. Kinloch, J.G. Williams, The use of a cohesive zone model to study the fracture of fibre composites and adhesively-bonded joints, International Journal of Fracture 119: 25-46, 2003

J. Bonhomme, A. Argüelles, J. Viña, I. Viña, Fractography and failure mechanisms in static mode I and mode II delamination testing of unidirectional carbon reinforced composites, Polymer Testing 28 612–617, 2009

J. Busfield, PhD thesis, The prediction of the mechanical performance of

elastomeric components using finite element analysis, 2000

J. Byström, N. Jekabsons, J. Varna, An evaluation of different models for prediction of elastic properties of woven composites, Compoistes: Part B 31, 7-20, 2000

P.P. Camanho, C.G. Dávila, Mixed-mode decohesion finite elements for the simulation of delamination in composite materials, NASA/TM-2002-211737, 2002

Denis D.R. Cartié, B.N. Cox, N.A. Fleck, Mechanisms of crack bridging by composite and metallic rods, Composites Part A 35, 1325-1336, 2004

Denis D.R. Cartié, G. Dell'Anno, E. Poulin, I.K. Partridge, 3D reinforcement of stiffener-to-skin T-joints by z-pinning and tufting, Engineering Fracture Mechanics 73, 2532–2540, 2006[a]

Denis D.R. Cartié, M. Troulis, I.K. Partridge, Delamination of z-pinned carbon fibre reinforced laminates, Composites Science and Technology 66, 855–861, 2006[b]

P. Chang, A.P. Mouritz, B.N. Cox, Properties and failure mechanisms of z-pinned laminates in monotonic and cyclic tension, Composites: Part A 37, 1501–1513, 2006

B. Chen, D.A. Dillard, The effect of the T-stress on crack path selection in adhesively bonded joints, International Journal of Adhesion & Adhesives 21, 357-368, 2001

B. Chen, D.A. Dillard, J.G. Dillard, R.L. Clark, JR., Crack path selection in adhesively bonded joints: roles of external loads and specimen geometry, International Journal of Fracture 114: 167-190, 2002

J. Comyn, Adhesion Science, The Royal Society of Chemistry, 1997

R. Cook, Concepts and Applications of Finite Element Analysis, 4th Edition, WILEY, 2002

I.M. Daniel, Ori Ishai, Engineering Mechanics of Composite Materials, Oxford University Press, 1994

C.G. Dávila, P.P. Camanho, M.F. de Moura, Mixed-Mode Decohesion Elements for Analyses of Progressive Delamination, Paper AIAA-01-1486, 42nd AIAA/ASME/ASCE/AHS/ASC Structures, Structural Dynamics and Materials Conference, April 16-19, 2001

D. A. Dillard, Fundamentals of stress transfer in bonded systems, Adhesion Science and Engineering - I, Elsevier Science B.V., First edition, 2002

M.J. Fagan, Finite Element Analysis - Theory and Practice, Longman Group, Harlow, 1992

D.N. Fenner, Engineering Stress Analysis, John Wiley, Chichester, 1987

R.L. Foye, D.J. Baker, in Proceedings of 11th Annual AIAA Conference on Structures, Structural Dynamics, and Materials, AIAA, Denver CO, April, 1970

M. Grassi, X. Zhang, M. Meo, Prediction of stiffness and stresses in z-fibre reinforced composite laminates, Composites Part A: Applied Science and Manufacturing, 33(12), 1653–1664, 2002

M. Grassi, X. Zhang, Finite element analyses of mode I interlaminar delamination in z-fibre reinforced composite laminates, Composites Science and Technology 63, 1815–1832, 2003

F.J. Guild, K.D. Potter, J. Heinrich, R.D. Adams, M.R. Wisnom, Understanding and control of adhesive crack propagation in bonded joints between carbon fibre

composite adherends II. Finite element analysis, International Journal of Adhesion & Adhesives 21, 445-453, 2001

H. Hadavinia, A.J. Kinloch, M.S.G. Little, A.C. Taylor, The prediction of crack growth in bonded joints under cyclic-fatigue loading I. Experimental studies, International Journal of Adhesion & Adhesives 23, 449–461, 2003

H. Hadavinia, A.J. Kinloch, M.S.G. Little, A.C. Taylor, The prediction of crack growth in bonded joints under cyclic-fatigue loading II. Analytical and finite element studies, International Journal of Adhesion & Adhesives 23, 463–471, 2003

L.J. Hart-Smith, in the 4th Conference on fibrous composites in structural design, San Diego, CA, Plenum, New York, 1978

L.J. Hart-Smith, Further developments in the design and analysis of adhesive-bonded structural joints, Joining of composite materials, ASTM, STP 749, K.T. Kedward, Ed., pp. 3-31, ASTM 1981

L.J. Hart-Smith, Joining Fibre-Reinforced Plastics, ed. F. l. Matthews, chap. 6, 1986

H. He, Y.C. Roth, N. Himmel, Elastic constants estimation of stitched NCF CFRP laminates based on a finite element unit-cell model, Composites Science and Technology, 67, 1081-1095, 2007

D. Hull, An introduction to composite materials, Cambridge University Press, 1981

D. Hunston, R. Dehl, The role of polymer toughness in matrix dominated composite fracture, paper EM87-335, Society of Manufacturing Engineers, Deerborn, MI, 1987

B.M. İçten, R. Karakuzu, M.E. Toygar, Failure analysis of woven Kevlar fiber reinforced epoxy composites pinned joints, Composite Structures v 73, n 4, p 443-450, 2006

R. Karakuzu, T. Gülem, B.M. İçten, Failure analysis of woven laminated glass–vinyl ester composites with pin-loaded hole, Composite Structures 72, 27–32, 2006

E.JC Kellar, BGI Dance: Workpiece structure modification. International Patent Publication Number WO 2004028731 A1

E.JC Kellar, F. Smith, A new approach to damage control for composite to metal joints, www.twi.co.uk, 2004

B.H. Le Page, F.J. Guild, S.L. Ogin, P.A. Smith, Finite element simulation of woven fabric composites, Composites: Part A 35, 861–872, 2004

F. Lenzi, A. Riccio, A. Clarke, R. Creemers, Coupon tests on z-pinned and unpinned composite samples for damage resistant applications, Volume 247 Issue 1, 230 - 237, 2007

G. Liu, Meshfree methods, moving beyond finite element methods, CRC press, 2003

D.M. McGowan, D.R. Ambur, Damage characteristics and residual strength of composite sandwich panels impacted with and without compression loading, AIAA Paper No.98-1783, 1998

A.R. Melro, P.P. Cmanho, S.T. Pinho, Generation of random distribution of fibres in long-fibre reinforced composites, Composites Science and Technology 68, 2092-

2102, 2008

J.F. Meyer, International encyclopedia of composites, ed. S. M. Lee, VCH, New York, vol. 2, 1990

Y. Meziere, L. Michel, D. Carronnier, Mixed-mode delamination failure criteria in carbon fibre/composite under quasi-static and cyclic loading, ESIS Publication 27, Elsevier, 2000

A.P. Mouritz, Review of z-pinned composite laminates, Composites: Part A 38, 2383–2397, 2007

T.K. O'Brien, Interlaminar fracture of composites, USAAVSCOM Technical Report TR-84-B-2, 1984

T.K. O'Brien, R. Krueger, Influence of compression and shear on the strength of composite laminates with Z-pinned reinforcement, Applied Composite Materials, v 13, n 3, p 173-189, 2006

N.J. Pagano, R.B. Pipes, The influence of stacking sequence on laminate strength, J. Composite Materials, Vol. 5, 1971

N.J. Pagano, G.A. Schoeppner, Delamination of polymer matrix composites: problems and assessment, Comprehensive Composite Materials, Elsevier, 2000

I.K. Partridge, Denis D.R. Carti é, Delamination resistant laminates by z-Fiber® pinning: Part I manufacture and fracture performance, Composites: Part A 36, 55–64, 2005

S.T. Pinho, P. Robinson, L. Iannucci, Fracture toughness of the tensile and compressive fibre failure modes in laminated composites, Composites Science and

Technology 66, 2069–2079, 2006

S.T. Pinho, L. Iannucci, P. Robinson, Physically-based failure models and criteria for laminated fibre-reinforced composites with emphasis on fibre kinking: Part I: Development, Composites: Part A 37, 63-73, 2006

S.T. Pinho, L. Iannucci, P. Robinson, Physically-based failure models and criteria for laminated fibre-reinforced composites with emphasis on fibre kinking: Part II: FE implementation, Composites: Part A 37, 766-777, 2006

S.T. Pinho, L. Iannucci, P. Robinson, Formulation and implementation of decohesion elements in an explicit finite element code, Composites Part A 37, 778-789, 2006

K.D. Potter, F.J. Guild, H.J. Harvey, M.R. Wisnom, R.D. Adams, Understanding and control of adhesive crack propagation in bonded joints between carbon fibre composite adherends I. Experimental, International Journal of Adhesion & Adhesives 21, 435-443, 2001

J.R. Rice, A path independent integral and the approximate analysis of strain concentration by notches and cracks, J. Applied Mechanics, Vol. 35, 1968

K.L. Rugg, B.N. Cox, K.E. Ward, G.O. Sherrick, Damage mechanisms for angled through-thickness rod reinforcement in carbon-epoxy laminates, Composites Part A 29A, 1603-1613, 1998

K.L. Rugg, B.N. Cox, R. Massabò, Mixed mode delamination of polymer composite laminates reinforced through the thickness by z-fibers, Composites: Part A 33, 177-190, 2002

A.J. Russell, K.N. Street, The effect of matrix toughness on delamination: static and fatigue fracture under Mode II shear loading of graphite fiber composites,

Toughened composites, ASTM STP 937, American Society for Testing and Materials, Philadelphia, 1987

R.A. Schapery, B.D. Davidson, Applied Mechanics Review, 43(5), Part 2, 1990

D.K. Shaffer, H.M. Clearfield, J.S. Ahearn, Treatise on adhesives, ed. J. D. Minford, Marcel Dekker, New York, 1991

L.F.M. da Silva, R.D. Adams, Techniques to reduce the peel stresses in adhesive joints with composites, International Journal of Adhesion & Adhesives 27, 227-235, 2007

F. Smith, Comeld ^{TM}, TWI Knowledge Summary, 2004

F. Smith, Comeld ^{TM} – An innovation in composite to metal joining, presented at Composites Processing 2004, CPA, Bromsgrove, UK, 2004

F. Smith, TWI, private communication, 2005

C.A. Steeves, N.A. Fleck, In-plane properties of composite laminates with through-thickness pin reinforcement, International Journal of Solids and Structures, 43, 3197-3212, 2006

V.K. Stokes, Joining methods for plastics and plastic composites. An overview, Polymer Engineering and Science, 29(19), 1989

A. Taliercio, Generalized plane strain finite element model for the analysis of elastoplastic composites, International Journal of Solids and Structures 42 (2005) 2361–2379, 2005

J.J. Tierney, J.W. Gillespie JR., P.-E. Bourban, Joining of composites,

Comprehensive Composites Materials, Elsevier, vol.2, 2.31, 2000

W. Tu, P. Wen, F.J. Guild, Optimisation of the protrusion geometry in Comeld ™ joints, Composites Science and Technology, Vol 71, Issue 6, p868-p876, 2011

C.E.S. Ueng, K. Zhang, Strength prediction of a mechanically fastened joint in laminated composites, AAIA J., 23(11), 1985

S. Ucsnik, M. Scheererb, S. Zarembac, D.H. Pahr, Experimental investigation of a novel hybrid metal–composite joining technologynext term, Composites Part A: Applied Science and Manufacturing, Vol 41, Issue 3, Pages 369-374, 2010

J.D. Venables, Adhesion and durability of metal-polymer Bonds, J. Material Science, 19, 1984

J.R. Vinson, Mechanical fastening of polymer composites, Polymer Engineering and Science., 29(19), 1989

R.F. Wegman, Materials science and process technology series, Noyes Publications, Park Ridge, NJ, 1989

Z. Yang, C.T. Sun, Fracture mode separation for delamination in plate-like composite structures, AIAA/ASME/ASCE/AHS/ASC Structures, Structural Dynamics & Materials Conference, v 4, 1998

A.Y. Zhang, H.Y. Liu, A.P. Mouritz, Y.W. Mai, Experimental study and computer simulation on degradation of z-pin reinforcement under cyclic fatigue, Composites: Part A 39, 406–414, 2008

APPENDIX A

Multi-region mesh free method for Comeld™ joints

Computational Materials Science 48 (2010) 481–489

Contents lists available at ScienceDirect

Computational Materials Science

journal homepage: www.elsevier.com/locate/commatsci

Multi-region mesh free method for Comeld™ joints

W. Tu [a], P.H. Wen [a,*], F.J. Guild [b]

[a] School of Engineering and Materials Science, Queen Mary, University of London, Mile End Road, London E1 4NS, UK
[b] Mechanical Engineering, Imperial College, South Kensington Campus, London SW7 2AZ, UK

ARTICLE INFO

Article history:
Received 24 November 2009
Received in revised form 3 February 2010
Accepted 4 February 2010
Available online 11 March 2010

Keywords:
Comeld™ joints
Mesh free Galerkin method
Radial basis functions
Finite element method
Optimization and design
Material strength

ABSTRACT

Based on the variation principle of the potential energy, the element-free Galerkin method is developed with radial basis function interpolations to solve Comeld™ joints two dimensional stress distributions. The aim of this work is to show the efficiency and accuracy of the meshless method to the multi-region problems comparing with finite element method using ABAQUS. Considering large number of protrusions of joint, a unit cell models with one protrusion has been proposed. Numerical modeling with correct boundary conditions of unit cell has been verified through different numerical algorithms. The accuracy and convergence of mesh free method are demonstrated with several examples.

1. Introduction

With the widespread applications of polymer matrix composites, making individual components is just the first step; assembly and joining separate components made of different materials introduces problems. Conventionally, joining techniques include mechanical fastening and adhesive bonding. The technology for joining metals is quite mature including a number of processes: riveting, bolting, welding, adhesive bonding, brazing and soldering [1]. However, the technology for joining composites or composites to metal is less well understood, but still important. In structures made of or consisting of polymer matrix composites, the components must be joined to retain the structural integrity in the face of both mechanical (static and dynamic) and environmental loads [1].

In general, joining is required when there is need to: (i) produce larger physical size, (ii) create "un-mouldable" geometries, (iii) co-join two dissimilar materials, or (iv) preserve a degree of access [2]. For structural applications [3], the important issues for joint performance regardless of the joining technology used include the strength of the joint under static and dynamic loads, the resistance of the joint to impact loads, the effect of resin ageing, residual stresses, creep, foreign fillers such as particulates, fibres, and bond heating sources, and the influence of environmental factors such as temperature, moisture, and solvents. Each of these issues must be addressed when selecting the proper joint design with as much if not more respect as is the case in material selection for the overall structure [4]. Formation of a whole structure with complex geometry using composite materials would be extremely difficult to mould. For such applications, the connection of dissimilar material components is vital.

1.1. Mechanical fastening

Typical assemblies include threaded and unthreaded fasteners with interlocking design features, and metallic and thermoplastic riveted assemblies [3]. These fastenings can either be permanent or consist of joints that can be opened or closed. Mechanical fastening offers the following advantages [5]: (i) no need of surface preparation, (ii) they are not sensitive to adversely affected by thermal cycling loads or high humidity environments, (iii) they can be disassembled without structural or surface damage, and (iv) they are easy to inspect visually for damage/wear. The unique characteristics of composite structures raise many difficulties associated with mechanical fastening [4] including some of the following disadvantages: (i) cyclic loading, in-plane shear, and transverse pulling forces can lead to high stress concentrations; (ii) cold flow can cause deformation of fasteners or holes and can lead to fastener loosening or pull-out, and joint failure; (iii) fastener tear-out or pull-through can also be observed especially with thin adherend materials; (iv) stress profiles are complex and multiple failure mechanisms are possible; and (v) increased weight, part

* Corresponding author. Tel.: +44 20 7882 5371; fax: +44 20 8983 1007.
E-mail addresses: w.tu@qmul.ac.uk (W. Tu), p.h.wen@qmul.ac.uk (P.H. Wen), f.guild@imperial.ac.uk (F.J. Guild).

0927-0256/$ - see front matter © 2010 Elsevier B.V. All rights reserved.
doi:10.1016/j.commatsci.2010.02.009

count, and costs. Mechanical fasteners can fail in a variety of modes, including tension, shear, bolt, and cleavage-tension failure, as well as from bolt pull-through [1,6,7]. In the case of vibration, mechanically fastened components can show fretting due to small relative movement between the components, while adhesive bonding eliminates and even serve to damp the vibration. Furthermore, the failure mode for any given joints is highly dependent of geometry, and still may vary with the fibre orientation or laminate stacking sequence. For instance, connecting composite components with pinned or bolted joints may reduce costs and desired for its simplicity, however, drilled holes often lead to the reduction of the load carrying capacity due to the stress concentration around the boundary of the holes. Special attention must be given for the design of bolted joints to avoid catastrophic failure. These mechanical fastened joints normally suffer from three failure modes, which are net-tension, shear-out and bearing, reported by İçten et al. [8].

1.2. Adhesive bonding

Adhesive bonding is widely used for joining sheet materials for load-bearing engineering applications, and also for transferring loads in large structures for civil engineering. The development of adhesive bonding has depended heavily on understanding of the chemistry involved [3]. A vast literature of research exists on adhesive bonding of composites, and several key issues have been identified [7,9–11]. These include adhesive selection, surface preparation of the composite adherends, wetting, mechanisms of bonding, durability, and bonding of dissimilar materials. Generally, adhesive bonded joints can carry greater loads than mechanically fastened polymers or composites, due to more uniformly distributed loadings over large areas resulting in lower stresses and fewer stress concentrations. The strength of the adhesive material usually determines the maximum bond stress, and the chemical structure and temperature of the adhesive ultimately determines the mechanical behaviour of the joint during its operating life [4].

According to Comyn [12], there are six theories of adhesion, physical adsorption, chemical bonding, diffusion, electrostatic, mechanical interlocking and weak boundary theories. Epoxides are the most widely used structural adhesives for composite bonding, and they are also used as matrix resins for composite. Epoxide resins can be mixed with a wide range of hardeners to connect dissimilar components. During the application of epoxide adhesives there is no volatile formed on hardening with very low shrinkage, but may cause skin diseases [12].

1.3. Comeld™ joints

Adhesive bonding and mechanical fastening both have advantages and disadvantages, as reported by Smith [13]. Despite disadvantages including weight, bonding strength, stress distribution, surface finish, mechanically fastened joints containing composite materials can be designed to compete with adhesively bonded joints. Mechanically fastened joints can also be disassembled relatively easily in comparison to adhesively bonded joints, which make them attractive for inspection, repair and recycling purposes amongst others. This means that, in industry sectors used to dealing with metals, mechanical fasteners have been commonly used to join composite materials to themselves and other materials. The Comeld™ joining system is designed to enable the improvements for metal-composites joints. This technology use both adhesive and mechanical bonding mechanisms, and careful design of a joining system leads to the advantages of both methods. Comeld™ joints connect metal and composite components with the application of a new surface treatment technique, called Surfi-Sculpt™, on the metal surface. Surfi-Sculpt™ technology has been developed by TWI using an electron beam to create various surface textures through the manipulation of the electron beam. This technique is applicable to a wide range of materials, allows the creation of a range of hole and protrusion patterns, which can be precisely controlled. Comeld™ is the application which uses Surfi-Sculpt™ to create protrusions and cavities on and in the metal onto which the composite is laid and cured, forming the Comeld™ joint. A typical titanium metal surface is shown in Fig. 1. Comeld™ joining system has certain advantages in joining dissimilar components. However, further research is required to investigate the mechanisms of the protrusions. In addition, there are many possible variables which could be adjusted with Surfi-Sculpt™ technology. The variables include the distribution, radius, height and orientation of the protrusions. Therefore, numerical simulations of the Comeld™ joining system are required to gain better understanding of the mechanism of the protrusions, and to optimize the joining system. Although there is a vast amount of research reported in the literature regarding joints with adhesive or mechanical bonding mechanism, very little work has been carried out on stress analysis and optimization of design of the Comeld™ joining system.

1.4. Methods of analysis

As a new development, the costs of the technology of Surfi-Sculpt™ are very high. To study various geometric parameters would be most economically investigated using the finite element analysis and advanced numerical simulation. Boundary element method has been developed to mechanical fastening and adhesive bonding problems by Wen et al. [14–17]. Satisfactory accuracy has been achieved compared with the finite element method. Recently, mesh free approximations have received much interest since Nayroles et al. [18] proposed the diffuse element method. Later, Belytschko et al. [19] and Liu et al. [20] developed the element-free Galerkin method reproducing kernel particle methods. A key feature of these methods is that they do not require a structured grid and are hence called meshless. Recently, Atluri and co-workers presented a family of meshless methods, based on the Local weak Petrov–Galerkin formulation (MLPGs) for arbitrary partial differential equations (see Atluri et al. [21,22] with moving least-square (MLS) approximation. MLPG is reported to provide a rational basis for constructing meshless methods with a greater degree of

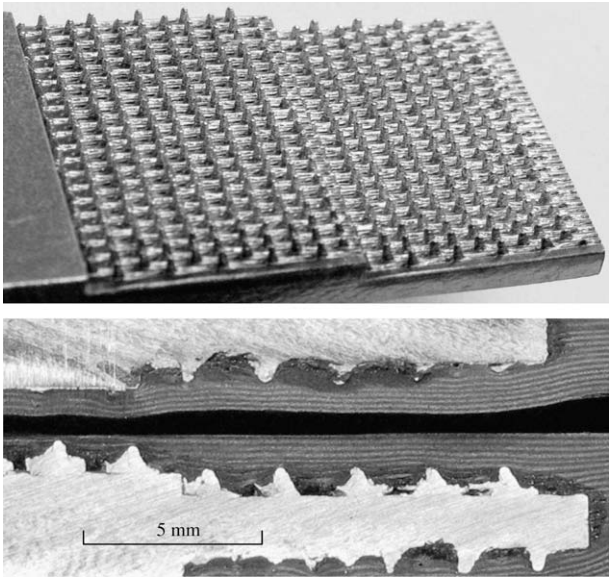

Fig. 1. Titanium double-step with protrusions and side views of typical Comeld™ specimens.

flexibility. Local Boundary Integral Equation (LBIE) with moving least square and polynomial radial basis function (RBF) has been developed by Sladek et al. [23,24] for the boundary value problems in anisotropic non-homogeneous media. Both methods (MLPGs and LBIE) are meshless, as no domain/boundary meshes are required in these two approaches. However, Galerkin-base meshless methods, except that presented by Atluri [22], still include several awkward implementation features such as numerical integrations in the local domain. A comprehensive review of meshless methods (MLPG) can be found in the book by Atluri [22].

The aim of this paper is to develop the mesh free Galerkin method to study the various geometric parameters of the surface treatment technique to optimize the design of the joining system. In this paper, the formulation and numerical implementation of mesh free Galerkin method for the multi-region problems such as Comeld™ joints have been developed. Following a similar approach to the finite element method, the stiffness matrix is derived by the variation principle of potential energy and the element-free Galerkin method is presented with radial basis function (RBF) interpolation. Special points have to be selected on the interface and shared by jointed objects in order to connect joint parts. The accuracy of the proposed method has been demonstrated with comparing the results by the finite element method (ABAQUS). After that, the unit cell models including different height of protrusion, has been analyzed.

2. Variation principle of potential energy

For a linear two dimensional elasticity, equilibrium equations can written as follows

$$\sigma_{ij,j} + f_i = 0 \tag{1}$$

where σ_{ij} denotes the stress tensor, f_i the body force. Consider homogeneous anisotropic and linear elasticity, the relationships between stresses and strains by Hooke's law are given by

$$\sigma_{ij}(\mathbf{x}) = C_{ijkl}(\mathbf{x})\varepsilon_{kl}(\mathbf{x}) = C_{ijkl}(\mathbf{x})u_{k,l}(\mathbf{x}), \tag{2}$$

where $\varepsilon_{kl} = (u_{k,l} + u_{l,k})/2$, and C_{ijkl} denotes the elasticity tensor which is function of coordinate for functionally graded materials and has the following symmetries

$$C_{ijkl} = C_{jikl} = C_{klij}. \tag{3}$$

For a homogeneous isotropic solid, we have

$$C_{ijkl}(\mathbf{x}) = \lambda(\mathbf{x})\delta_{ij}\delta_{kl} + \mu(\mathbf{x})(\delta_{ik}\delta_{jl} + \delta_{il}\delta_{jk}) \tag{4}$$

where λ and μ are the Lame's constants. For the isotropic plane strain state, Hooke's law can also be written, in matrix form, as

$$\boldsymbol{\sigma} = \begin{Bmatrix} \sigma_{11} \\ \sigma_{22} \\ \sigma_{12} \end{Bmatrix} = \mathbf{D}\begin{Bmatrix} \varepsilon_{11} \\ \varepsilon_{22} \\ \varepsilon_{12} \end{Bmatrix} = \mathbf{D}\boldsymbol{\varepsilon} \tag{5}$$

where

$$\mathbf{D} = \frac{E(1-v)}{(1+v)(1-2v)}\begin{bmatrix} 1 & \frac{v}{1-v} & 0 \\ \frac{v}{1-v} & 1 & 0 \\ 0 & 0 & \frac{1-2v}{2(1-v)} \end{bmatrix} \tag{6}$$

in which, E is the Young's modulus and v the Poisson's ratio. For orthotropic materials, we have

$$\mathbf{D} = \begin{bmatrix} D_{1111} & D_{1122} & 0 \\ D_{1122} & D_{2222} & 0 \\ 0 & 0 & D_{1212} \end{bmatrix} \tag{7}$$

Considering the domain Ω enclosed by boundary Γ, we have total potential energy by

$$\Pi = U - W \tag{8}$$

where the initial elastic strain energy

$$U = \frac{1}{2}\int_\Omega \boldsymbol{\sigma}^T(\mathbf{y})\boldsymbol{\varepsilon}(\mathbf{y})d\Omega(\mathbf{y}) = \frac{1}{2}\int_\Omega \boldsymbol{\varepsilon}^T(\mathbf{y})\mathbf{D}\boldsymbol{\varepsilon}(\mathbf{y})d\Omega(\mathbf{y}) \tag{9}$$

and the external energy, the sum of contributions from known interior and external forces, is

$$W = \int_\Omega \mathbf{u}^T(\mathbf{y})\mathbf{b}(\mathbf{y})d\Omega(\mathbf{y}) + \int_\Gamma \mathbf{u}^T(\mathbf{y})\mathbf{t}(\mathbf{y})d\Gamma(\mathbf{y}) \tag{10}$$

where $\mathbf{b} = \{b_1, b_2\}^T$ is the vector of body force, vector of traction $\mathbf{t} = \{t_1, t_2\}^T$, in which $t_i = \sigma_{ij}n_j$, n_i denotes a unit outward normal vector. With shape functions, the displacements $\mathbf{u}(\mathbf{y})$ at the point $\mathbf{y}$ can be approximated in terms of the nodal values in a local domain (see Fig. 1) as

$$u_i(\mathbf{y}) = \sum_{k=1}^{n(\mathbf{y})} N_k(\mathbf{y}, \mathbf{x}_k)\hat{u}_i^k = \mathbf{N}(\mathbf{y}, \mathbf{x})\hat{\mathbf{u}}_i \tag{11}$$

where

$$\mathbf{N}(\mathbf{y}, \mathbf{x}) = \{N_1(\mathbf{y}, \mathbf{x}_1), N_2(\mathbf{y}, \mathbf{x}_2), \ldots, N_{n(\mathbf{y})}(\mathbf{y}, \mathbf{x}_{n(\mathbf{y})})\} \tag{12}$$

and real nodal values $\hat{\mathbf{u}}_i = \left\{\hat{u}_i^1, \hat{u}_i^2, \ldots, \hat{u}_i^{n(\mathbf{y})}\right\}^T, i = 1, 2$, at point $\mathbf{x}_k = \{x_1^{(k)}, x_2^{(k)}\}$, where $k = 1, 2, \ldots, n(\mathbf{y})$, N_k is the shape function and $n(\mathbf{y})$ represents the number of node in the local supported domain. For the two dimensional elasticity, we can rearrange the above relation in a matrix form as

$$\begin{aligned} &\mathbf{u}(\mathbf{y}) = \{u_1, u_2\}^T = \bar{\mathbf{N}}(\mathbf{y}, \mathbf{x})\hat{\mathbf{u}} \\ &\bar{\mathbf{N}}(\mathbf{y}, \mathbf{x}) = \begin{bmatrix} \mathbf{N} & 0 \\ 0 & \mathbf{N} \end{bmatrix} = \begin{bmatrix} N_1 & 0 & N_2 & 0 & \ldots & N_{n(\mathbf{y})} & 0 \\ 0 & N_1 & 0 & N_2 & \ldots & 0 & N_{n(\mathbf{y})} \end{bmatrix} \end{aligned} \tag{13}$$

where $\hat{\mathbf{u}} = \left\{\hat{u}_1^1, \hat{u}_1^2, \hat{u}_1^2, \hat{u}_2^2 \ldots, \hat{u}_1^{n(\mathbf{y})}, \hat{u}_2^{n(\mathbf{y})}\right\}^T$ is the nodal displacement vector. Therefore, the relationship between strains and displacements is given by

$$\boldsymbol{\varepsilon}(\mathbf{y}) = \begin{bmatrix} \frac{\partial N_1}{\partial y_1} & 0 & \frac{\partial N_2}{\partial y_1} & 0 & \ldots & \frac{\partial N_{n(\mathbf{y})}}{\partial y_1} & 0 \\ 0 & \frac{\partial N_1}{\partial y_2} & 0 & \frac{\partial N_2}{\partial y_2} & \ldots & 0 & \frac{\partial N_{n(\mathbf{y})}}{\partial y_2} \\ \frac{\partial N_1}{\partial y_2} & \frac{\partial N_1}{\partial y_1} & \frac{\partial N_2}{\partial y_2} & \frac{\partial N_2}{\partial y_1} & \ldots & \frac{\partial N_{n(\mathbf{y})}}{\partial y_2} & \frac{\partial N_{n(\mathbf{y})}}{\partial y_1} \end{bmatrix}\hat{\mathbf{u}} = \mathbf{B}(\mathbf{y})\hat{\mathbf{u}} \tag{14}$$

Considering the variation of the total potential energy, with respect to the each nodal displacements, gives

$$\delta\Pi = \delta U - \delta W = 0 \tag{15}$$

Inserting the relations $\mathbf{u} = \boldsymbol{\Phi}\hat{\mathbf{u}}, \boldsymbol{\varepsilon} = \mathbf{B}\hat{\mathbf{u}}$ and $\boldsymbol{\sigma} = \mathbf{D}\boldsymbol{\varepsilon}$ into (15) yields $2 \times N$ a linear algebraic equation system in a matrix form as

$$[\mathbf{K}]_{2N\times 2N}\hat{\mathbf{u}}_{2N} = \mathbf{f}_{2N} \tag{16}$$

where N is the number of node in the domain Ω and on the boundary. The stiffness and mass matrices can be written as

$$\mathbf{K} = \int_\Omega \mathbf{B}^T(\mathbf{x}, \mathbf{y})\mathbf{D}(\mathbf{y})\mathbf{B}(\mathbf{x}, \mathbf{y})d\Omega(\mathbf{y}) \tag{17}$$

for nodes $\mathbf{x} = \mathbf{x}_i$, $i = 1, 2, \ldots, N$, and nodal force vector is defined by

$$\mathbf{f} = \int_\Omega \boldsymbol{\Phi}^T(\mathbf{x}, \mathbf{y})\mathbf{b}(\mathbf{y})d\Omega(\mathbf{y}) + \int_{\Gamma_\sigma} \boldsymbol{\Phi}^T(\mathbf{x}, \mathbf{y})\mathbf{t}(\mathbf{y})d\Gamma(\mathbf{y}) \tag{18}$$

where Γ_σ denotes the boundary on which the traction is given. For a concentrated force acting at node i, we may determine the nodal force vector directly by

$$\mathbf{f}_i = \left\{F_1^i, F_2^i\right\}^T \tag{19}$$

3. The approximation scheme

RBFs have been initially used for scattered data fitting and general multi-dimensional data interpolation problems, (see Ref. [25]), and were later applied by Kansa [26] for the analysis of partial differential equations. Consider a spherical support domain Ω_R shown in Fig. 2, which is the neighbourhood of a point $\boldsymbol{\eta}$ (=$\{x, y\}$) and is considered as the domain of definition of the RBF approximation for the trail function at $\boldsymbol{\eta}$ and also called the support domain of the computation point $\boldsymbol{\eta}$. To interpolate the distribution of function u in the support domain Ω_R over a number of randomly distributed nodes ξ [=$\{\xi_1, \xi_2, \ldots, \xi_n\}$, $\xi_i = (x_i, y_i)$, $i = 1, 2, \ldots, n$], the approximation of function u at the point $\boldsymbol{\eta}$ can be expressed by

$$u(\boldsymbol{\eta}) = \sum_{k=1}^{n} R_k(\boldsymbol{\eta}, \xi) a_k + \sum_{j=1}^{t} P_j(\boldsymbol{\eta}) b_j = \mathbf{R}(\boldsymbol{\eta}, \xi)\mathbf{a} + \mathbf{P}(\boldsymbol{\eta})\mathbf{b} \tag{20}$$

along with the constraints

$$\sum_{j=1}^{n} P_k(\xi_j) a_j = 0, \quad 1 \le k \le t \tag{21}$$

where $\{P_k\}_{k=1}^{t}$ is a basis for P_{m-1}, the set of d-variate polynomials of degree less than or equal to $m-1$, and

$$t = \binom{m+d-1}{d} \tag{22}$$

is the dimension of P_{m-1}. $\mathbf{R}(\boldsymbol{\eta}, \xi) = \{R_1(\boldsymbol{\eta}, \xi), R_2(\boldsymbol{\eta}, \xi), \ldots, R_n(\boldsymbol{\eta}, \xi)\}$ is the set of radial basis functions centred around the point $\boldsymbol{\eta}$, and $\mathbf{a} = \{a_1, a_2, \ldots, a_n\}^T$ are the unknown coefficients to be determined. The radial basis function is selected in this paper to be multi-quadrics,

$$R_k(\boldsymbol{\eta}, \xi) = \sqrt{c^2 + \alpha_1^2 (x - x_k)^2 + \alpha_2^2 (y - y_k)^2} \tag{23}$$

where c is a free parameter (is chosen to be unit in this paper), and α_i are scale factors [27]. A set of linear equations can be written, in matrix form, as

$$\mathbf{R}_0\mathbf{a} + \mathbf{P}\mathbf{b} = \hat{\mathbf{u}}, \quad \mathbf{P}^T\mathbf{a} = \mathbf{0} \tag{24}$$

where

$$\mathbf{R}_0(\xi) = \begin{bmatrix} R_1(\xi_1) & R_2(\xi_1) & \ldots & R_n(\xi_1) \\ R_1(\xi_2) & R_2(\xi_2) & \ldots & R_n(\xi_2) \\ \cdot & \cdot & \cdots & \cdot \\ \cdot & \cdot & \cdots & \cdot \\ \cdot & \cdot & \cdots & \cdot \\ R_1(\xi_n) & R_2(\xi_n) & \ldots & R_n(\xi_n) \end{bmatrix},$$

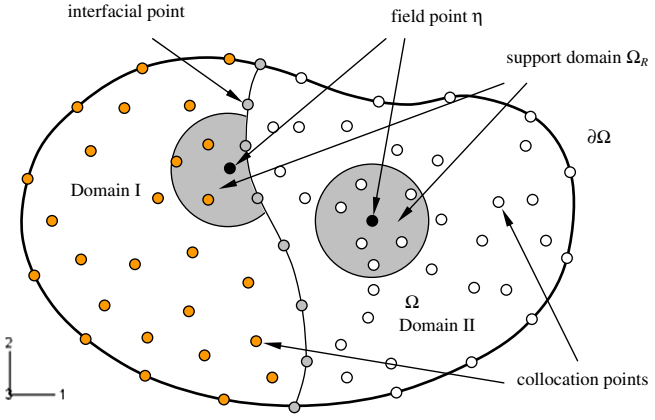

Fig. 2. The support domain Ω_R for the RBF approximation of the trial function, and support area of the weight function around node $\boldsymbol{\eta}$.

$$\mathbf{P}(\xi) = \begin{bmatrix} P_1(\xi_1) & P_2(\xi_1) & \ldots & P_t(\xi_1) \\ P_1(\xi_2) & P_2(\xi_2) & \ldots & P_t(\xi_2) \\ \cdot & \cdot & \cdots & \cdot \\ \cdot & \cdot & \cdots & \cdot \\ \cdot & \cdot & \cdots & \cdot \\ P_1(\xi_n) & P_2(\xi_n) & \ldots & P_t(\xi_n) \end{bmatrix}. \tag{25}$$

and

$$\hat{\mathbf{u}} = \{\hat{u}_1, \hat{u}_2, \ldots, \hat{u}_n\}^T \tag{26}$$

are the nodal values, $u_i = \hat{u}(\xi_i)$. Solving the equations in (24) gives

$$\mathbf{b} = (\mathbf{P}^T\mathbf{R}_0^{-1}\mathbf{P})^{-1}\mathbf{P}^T\mathbf{R}_0^{-1}\hat{\mathbf{u}}, \quad \mathbf{a} = \mathbf{R}_0^{-1}[\mathbf{I} - \mathbf{P}(\mathbf{P}^T\mathbf{R}_0^{-1}\mathbf{P})^{-1}\mathbf{P}^T\mathbf{R}_0^{-1}]\hat{\mathbf{u}} \tag{27}$$

where $\mathbf{I}$ denotes the diagonal unit matrix. Substituting the coefficients $\mathbf{a}$ and $\mathbf{b}$ from (27) into (20), we can obtain the approximation of the field function in terms of the nodal values

$$u(\boldsymbol{\eta}) = \sum_{k=1}^{n} N_k(\boldsymbol{\eta}, \xi)\hat{u}(\xi_k) = \mathbf{N}\hat{\mathbf{u}}, \mathbf{N} = \{N_1, N_2, \ldots, N_n\} \tag{28a}$$

and the first derivative with respect to coordinate i is obtained by

$$u_{,i}(\boldsymbol{\eta}) = \sum_{k=1}^{n} N_{k,i}(\boldsymbol{\eta}, \xi)\hat{u}(\xi_k) = \mathbf{N}_{,i}\hat{\mathbf{u}}, \mathbf{N}_{,i} = \{N_{1,i}, N_{2,i}, \ldots, N_{n,i}\} \tag{28b}$$

Certain number of collocation point should be distributed on the boundary and interface as shown in Fig. 2. For a collocation point which is close to the interface in the domain I, the support domain should not cover the domain II as shown in Fig. 2. Therefore, the collocation points in the support domain are located in the domain I and on the interface only. It is evident that the continuity of displacement and equilibrium condition along the interface are satisfied.

4. Evaluation of stiffness matrix

To determine the stiffness matrix $\mathbf{K}$ in (19), a domain integral in (16) should be carried out over the domain Ω. For convenience of analysis, we assume that the domain Ω can be divided into M rectangular sub-regions (cells) (for an irregular shape of cell, coordinate transformation should be applied). A 2D domain integral over a rectangular of area A is approximated by Gaussian integration formula as

$$\int\int_A f(x_1, x_2)dx_1dx_2 \approx A\sum_{l=1}^{L} w_l f\left(x_1^{(l)}, x_2^{(l)}\right) \tag{29}$$

where w_l denotes the weight of integral, L the number of Gaussian points and $(x_1^{(l)}, x_2^{(l)})$ is the coordinate of Gaussian points. If domain Ω is divided into M sub-domain, then the matrix of stiffness can be written, in a summation, as

$$\begin{aligned} \mathbf{K}(\mathbf{x}) &= \int_{\Omega} \mathbf{B}^T(\mathbf{x}, \mathbf{y})\mathbf{D}(\mathbf{y})\mathbf{B}(\mathbf{x}, \mathbf{y})d\Omega(\mathbf{y}) \\ &= \sum_{m=1}^{M}\sum_{l=1}^{L} A_m w_l \mathbf{B}^T(\mathbf{x}, \mathbf{y}_m^{(l)})\mathbf{D}(\mathbf{y}_m^{(l)})\mathbf{B}(\mathbf{x}, \mathbf{y}_m^{(l)}) = \sum_{m=1}^{M}\sum_{l=1}^{L} \Delta\mathbf{K}_l^m \end{aligned} \tag{30}$$

where the integration points $\mathbf{y}_m^{(l)}\left(y_1^{(ml)}, y_2^{(ml)}\right)$. For instance, if $L = 4$ we have

$$\begin{aligned} &\mathbf{y}_m^{(1,2,3,4)} = \left(y_1^m \pm \sqrt{\frac{1}{3}}h_1, y_2^m \pm \sqrt{\frac{1}{3}}h_2\right), w_{1,2,3,4} = \frac{1}{4}, \\ &A_m = 4h_1h_2 \end{aligned} \tag{31}$$

where $\mathbf{y}_m(y_1^m, y_2^m)$ presents the centre of cell with area A_m (rectangular), h_1 and h_2 are half width and height of the cell respectively. For

each Gaussian point $\mathbf{y}_l$, all elements in the sub-matrix $\Delta\mathbf{K}_l^m$ can be simplified, for isotropic, as

$$\Delta\mathbf{K}_l^m = \frac{A_m E(1-v)}{4(1+v)(1-2v)} \begin{bmatrix} \frac{\partial N_i}{\partial y_1}\frac{\partial N_j}{\partial y_1} + \frac{1-2v}{2(1-v)}\frac{\partial N_i}{\partial y_2}\frac{\partial N_j}{\partial y_2} & \frac{v}{1-v}\frac{\partial N_i}{\partial y_1}\frac{\partial N_j}{\partial y_2} + \frac{1-2v}{2(1-v)}\frac{\partial N_i}{\partial y_2}\frac{\partial N_j}{\partial y_1} \\ \frac{v}{1-v}\frac{\partial N_i}{\partial y_2}\frac{\partial N_j}{\partial y_1} + \frac{1-2v}{2(1-v)}\frac{\partial N_i}{\partial y_1}\frac{\partial N_j}{\partial y_2} & \frac{\partial N_i}{\partial y_2}\frac{\partial N_j}{\partial y_2} + \frac{1-2v}{2(1-v)}\frac{\partial N_i}{\partial y_1}\frac{\partial N_j}{\partial y_1} \end{bmatrix} = \begin{bmatrix} k_{11}^l & k_{12}^l \\ k_{21}^l & k_{22}^l \end{bmatrix}_{ij} \tag{32}$$

where i and j denote the number of nodes in the local support domain centred at $\mathbf{y}_l$, $N_i = N_i(\mathbf{y}_l, \mathbf{x})$, $i, j = 1, 2, \ldots n(\mathbf{y}_l)$. These elements in (35) and (36) should be added to the global system stiffness matrix $\mathbf{K}$, i.e. to the elements $k_{2I-1,2J-1}$, $k_{2I-1,2J}$, $k_{2I,2J-1}$ and $k_{2I,2J}$ respectively, where I and J denote the nodes in the global system for the nodes i and j in the local support domain centred at $\mathbf{y}_l$. For each Gaussian point $\mathbf{y}_l$, the number of node i varies due to the change of support domain centre. The implementation of this method can be carried out according to the following algorithm similar to the MLPGs discussed by Atluri [22]:

1. Choose a finite number of nodes N in the domain Ω, on the boundary $\partial\Omega$ of the given physical domain and on the interface;
2. Select the size and shape of local support domain or the minimum number in the support domain Ω_y
3. Divide domain Ω into segments and choose the shape of integral sub-domain
4. Loop over integral in sub-domain m ($m = 1, 2, \ldots, M$) centred at $\mathbf{y}_m$
   - Loop over Gaussian integration points $\mathbf{y}_l$ for each cell,
     (a) Loop over all nodes in the support domain (i,j);
     (b) Calculate the shape function $N_i(\mathbf{y}, \mathbf{x}_i)$ and first derivative $N_{i,k}(\mathbf{y}, \mathbf{x}_i)$;
     (c) Evaluate the elements $\Delta\mathbf{K}_l^m = [a_{kl}^l]_{ij}$;
     (d) Assemble the system stiffness matrix $\mathbf{K}_{(IJ)}$;
     (e) End the node loop in the local domain,
   - End the Gaussian point loop,
5. End the cell-integral loop,
6. Introduce the displacement boundary condition and modify the system equation;
7. Solve the linear equations for the nodal values;
8. Determine variables (stresses and displacements) in the domain or on the boundary.

5. Two dimensional unit cell and numerical examples

5.1. Geometry and boundary conditions for the unit cell

The 2D modeling investigates the geometric parameters influence on the stress states locally around the individual protrusion along with the effect of the protrusion distribution density change. Considering that there large number protrusions located on the metal surface with certain patterns, a repetitive cell as shown in Fig. 3 can be employed for each pattern. 2D models are based on the repetitive condition and consider only one protrusion. These unit cell models are used to investigate the geometric parameters effects along with the protrusion distribution density. In Fig. 3, R represents the radius of the protrusion and h_p is the height of the protrusion; h_b is the height of the metal base which is 1 mm; L is the width of the protrusion which varies for different protrusion distribution density; b is the distance between the root of the protrusion and left hand side; H represents the unit cell height is taken to 3 mm; the protrusion angle with respect to the perpendicular direction is α. The material applied for the global models are titanium alloy, Ti64, and homogenized cross-ply prepreg composites, AS4/8552 (layered and homogenized). The Ti64 elastic material properties are Young's modulus, $E = 114$ GPa and Poisson ratio $v = 0.336$ and

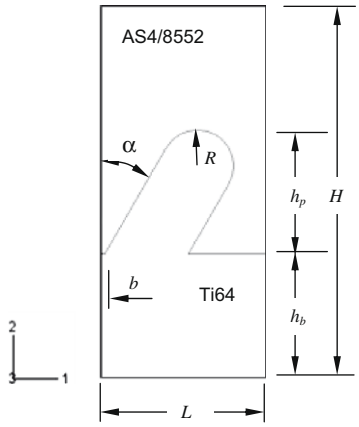

Fig. 3. Geometry of a unit cell model with protrusion.

Table 1
3D Material constants matrix **D** of composite AS4/8552 (unit: GPa).

D_{1111}	D_{2222}	D_{3333}	D_{1122}	D_{1133}	D_{2233}	D_{1212}	D_{1313}	D_{2323}
64.44	11.06	62.76	6.532	26.76	2.457	4.31	5.28	4.31

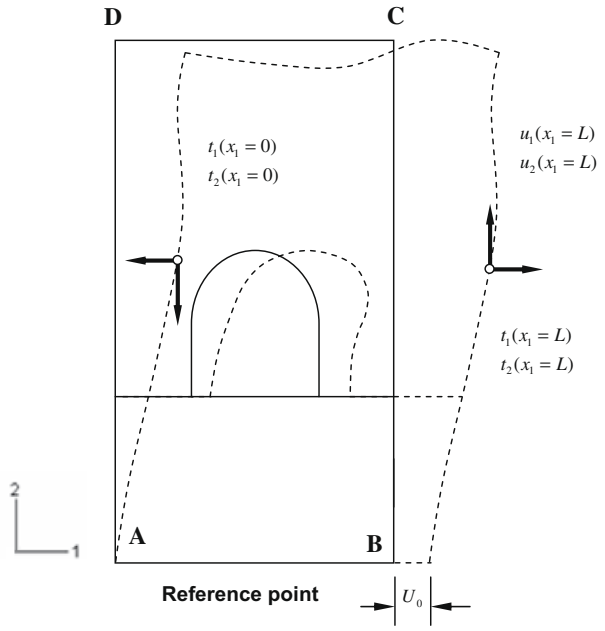

Fig. 4. Deformation and boundary conditions on the unit cell.

Table 2
Geometry factors of protrusion for two cases (unit: mm).

	L	H	h_p	h_b	α	R	b
Case 1	1.361	3.0	1.0	1.0	0°	0.291	0.3895
Case 2	1.361	3.0	1.0	1.0	30°	0.2705	0.18732

the values for the **D** Matrix, see Eq. (7), of the homogenized cross ply material calculated according to the requirements of the software [28] for the 2D unit cell models are shown in Table 1.

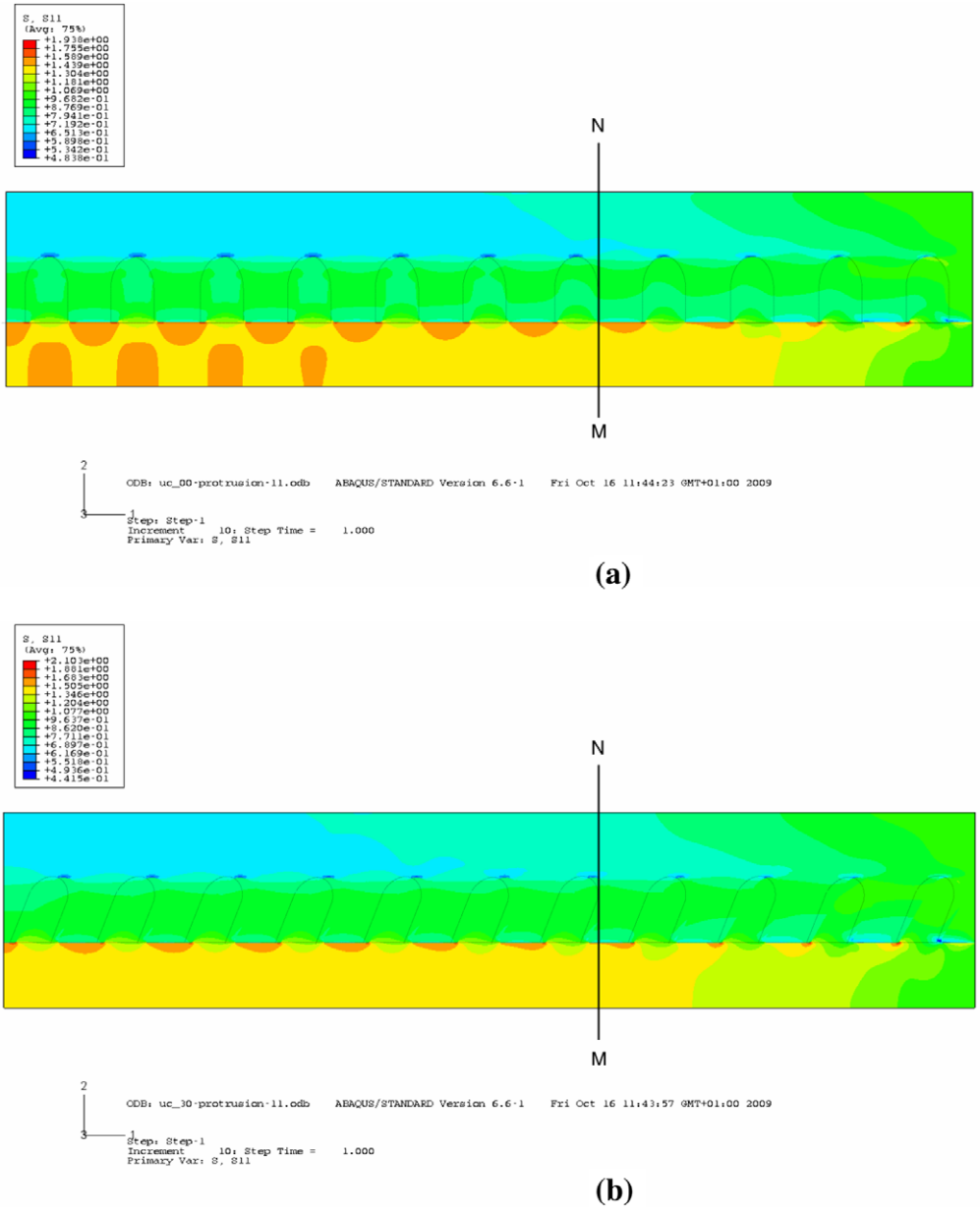

Fig. 5. The contours of stress σ_{11} given by finite element method (ABAQUS) with (a): 0° of protrusion and (b) 30° of protrusion. Unit traction is loaded at the right hand side and the end of left hand side is fixed along direction 1.

By considering the symmetry of structure, the displacement and traction for both sides of the unit cell can be presented, as shown in Fig. 3, as

$$\begin{aligned} u_1(L,x_2) - u_1(0,x_2) &= U_0 \\ u_2(L,x_2) - u_2(0,x_2) &= 0 \end{aligned} \tag{33}$$

and

$$\begin{aligned} t_1(L,x_2) + t_1(0,x_2) &= 0 \\ t_2(L,x_2) + t_2(0,x_2) &= 0 \end{aligned} \tag{34}$$

where U_0 denotes the relative movement between these two sides as shown in Fig. 4, which is constant. The applied 1-direction traction, F_0, is at point B (see Fig. 4) and the applied tractions are distributed along B C by the boundary conditions in Eqs. (33) and (34). The boundary conditions on bottom, A B, are

$$\begin{aligned} u_2(x_1,0) &= 0 \\ t_1(x_1,0) &= 0 \end{aligned} \tag{35}$$

and the top, C D, is free. The constant U_0 should be determined by the equilibrium condition

$$U_0 = F_0 / \int_0^H t_1^*(L,y)dy \tag{36}$$

where F_0 is the applied force at the end and $t_1^*(L,y)$ is the traction distribution for a unit relative movement $U_0 = 1$.

Two different protrusion geometries have been analyzed for perpendicular or angled protrusions. The geometry factors for the two cases are listed in Table 2.

Stress distributions have been extracted along the right-hand edge of the unit cell, B C (see Fig. 4). These results can be compared

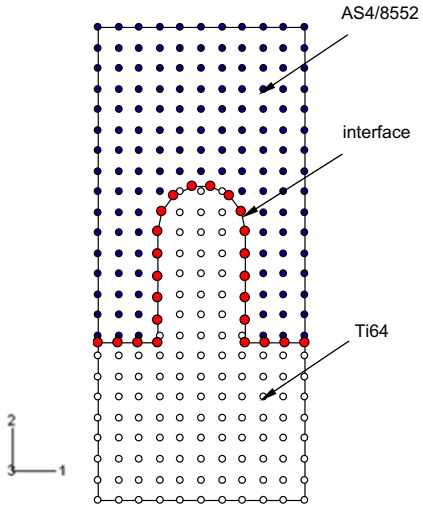

Fig. 6. Distribution of collocation points in domain.

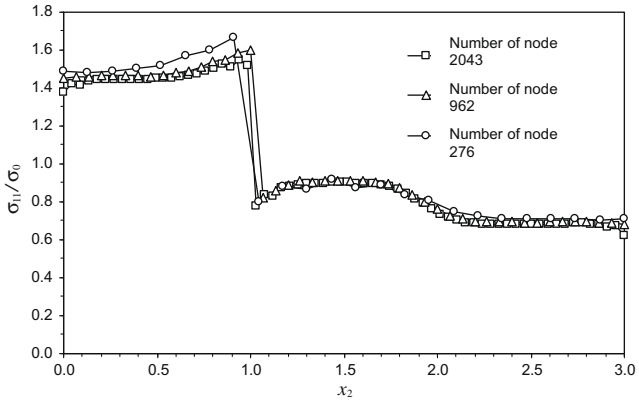

Fig. 7. Sensitivity study for collocation point density of distribution.

with the results from the section from the array of protrusions (see Section 5.2) and the results from the mesh free Galerkin method.

5.2. Geometry and boundary conditions for array of protrusions

An alternate finite element model consisting of an array of 11 protrusions has been analyzed for comparison. The geometry of these models for the two cases of protrusion geometry is shown in Fig. 5. Uniformly distributed traction is applied at the end of right hand side. The end of left hand side is simply supported along 1 direction, the bottom is simply supported along direction 2 and the top is free. Results for comparison with the unit cell models have been extracted from the section A-A as indicated in Fig. 5.

5.3. Mesh free Galerkin method

Collocation points on the interface are selected first. Then collocation points on the boundary and in the domain are uniformly distributed as shown in Fig. 6. The total number of collocation point in the domain is $N_1 \times N_2$, where N_1 and N_2 are numbers of points along the directions of axes 1 and 2, respectively. Fig. 6 shows the distribution of collocation point for Case 1 with 276 nodes ($N_1 = 11$ and $N_2 = 24$). If the gap between two collocation points is less than 0.04 mm, this domain point should be removed. The support domain is selected as a circle of radius d_y centred at field point **y**, which is determined such that the minimum number

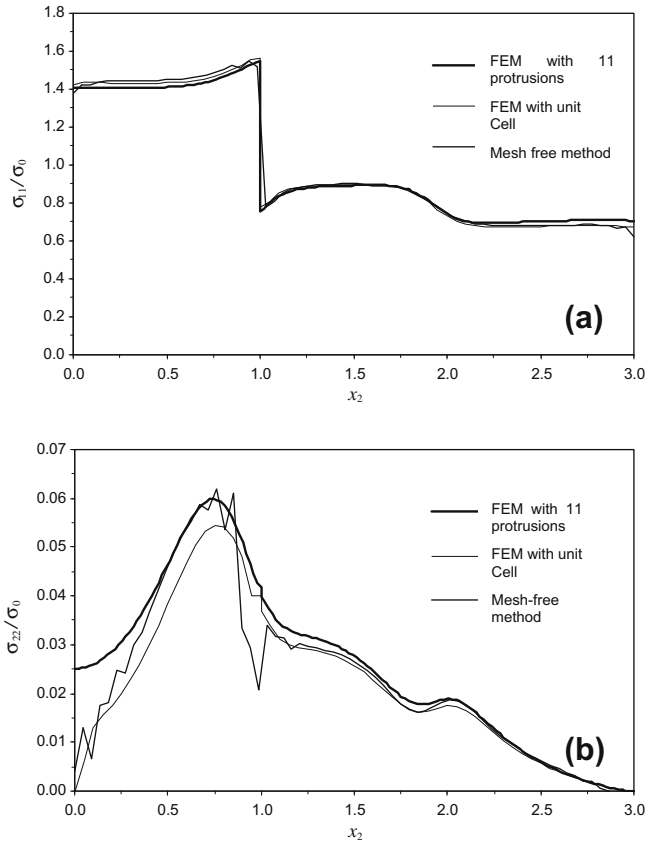

Fig. 8. Distributions of normal stress along the edge of right side: (a) σ_{11}/σ_0; (b) σ_{22}/σ_0, where $\sigma_0 = F_0/H$ (average tensile load over the section).

of nodes in the support domain $n(\mathbf{y}) \geqslant 15$. Free parameters are selected as $c = L/N_1$, $\alpha_1 = \alpha_2 = 1$.

Results have been extracted from the right-hand edge of the unit cell for comparison with the finite element results.

6. Results

6.1. Optimization of mesh free method

Results from the mesh free Galerkin method have been obtained for different collocation point densities. To investigate the collocation point density dependency, we consider three different point densities, i.e. 276, 962 and 2043 collocation points, and the results of normal stress are shown in Fig. 7. These results show that using more collocation points leads to more accurate results.

6.2. Comparison of models

The contours of 1-direction stress, σ_{11}, for the two angles of protrusion, Cases 1 and 2, for the array of protrusions analyzed using the finite element method are shown in Fig. 5. It is clear that the distribution of stress around the protrusions has reached a steady state around section A-A. Fig. 8 compares the stress profiles of normal stress for the two finite element models and the mesh free model, using 2043 collocation points, for Case 1 with the perpendicular protrusion.

Fig. 9 compares the stress profiles of normal stress and shear stress for the two finite element models and the mesh free model using 2055 collocation points, for Case 2 with the angled protrusion.

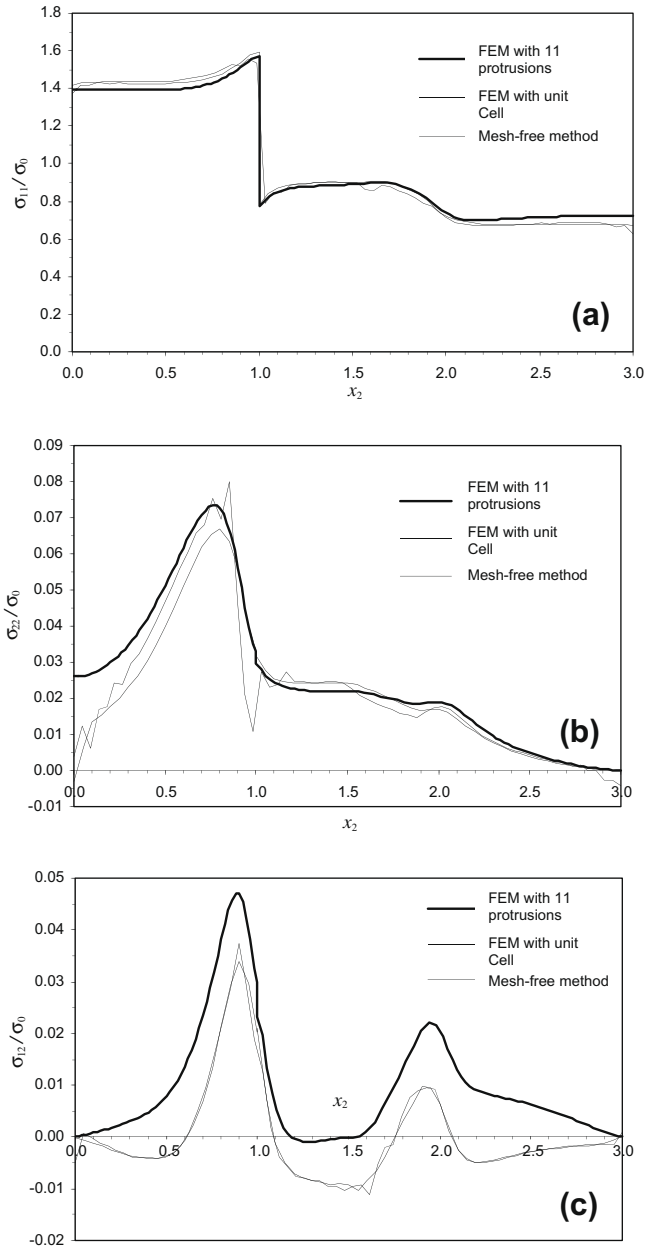

Fig. 9. Stress variations on the edge of right hand side for different modeling: (a) σ_{11}/σ_0; (b) σ_{22}/σ_0 and (c) σ_{12}/σ_0, where σ_0 denotes the average tensile load over the section.

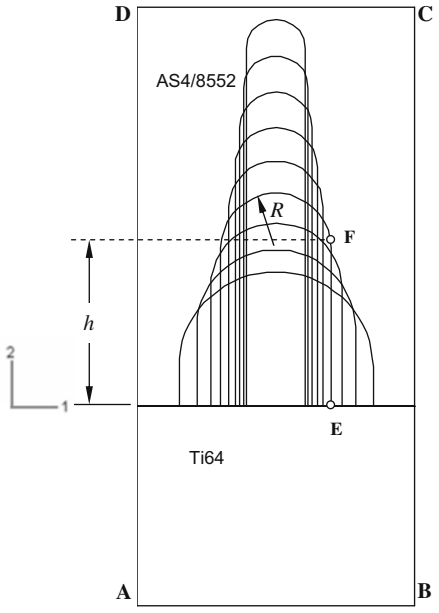

Fig. 10. Dimensions of protrusion for different height, where $h = 0.8$ mm is indicated.

Table 3
Geometry factors of protrusion for two cases.

L (mm)	H (mm)	h_b (mm)	α	V_0 (mm^2)
1.361	3.0	1.0	0°	0.5457

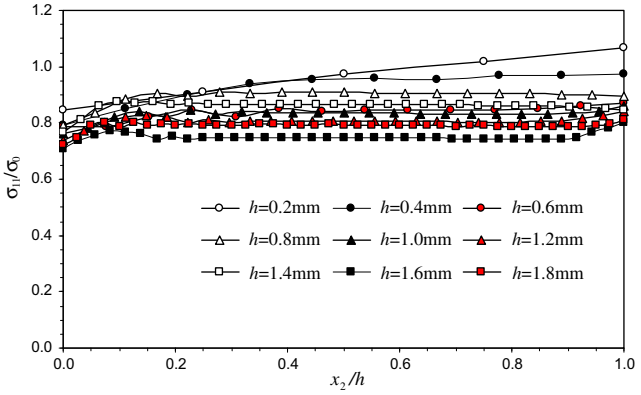

Fig. 11. Distribution of normal stress σ_{11} over interface AB.

These results show satisfactory agreement between the three different models. Particularly the agreement of shear stress is excellent between the mesh free method and FEM for the unit cell modeling. We also observed that the more protrusions are considered in the finite element modeling (here we consider 11 protrusions only), better agreement can be achieved with unit cell modeling. In other words, the agreement in stress profiles from section M N in the array model, and the edge B C in the unit cell model, show that the boundary conditions in described in Eqs. (33) and (34) for unit cell are correct.

6.3. Parametric study of unit cell under tensile load

There are many independent parameters shown in Fig. 3, each dimension parameter can be studied for optimization of joint design. In this example, the effect of height ($h = h_p - R$) selection as shown in Fig. 10 has been investigated. For different height of the protrusions, we assume that the volume of protrusion should be unchanged. Thus, we hold

$$2Rh + \pi R^2/2 = V_0 \tag{37}$$

where V_0 is the volume of protrusion. If the height h is given, the radius of the protrusion can be obtained

$$\begin{aligned} R &= \frac{\sqrt{4h^2 + 2\pi V_0} - 2h}{\pi} \\ h_p &= h + R \\ b &= L/2 - R \end{aligned} \tag{38}$$

The rest of parameters are given in Table 3 and heights of protrusions are selected from 0.2 mm to 1.8 mm.

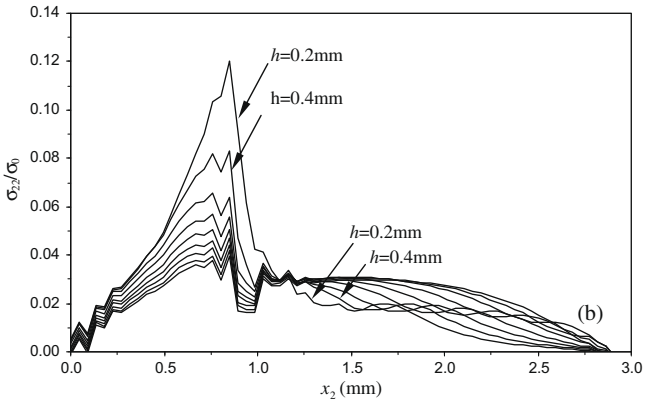

Fig. 12. Normal stress distribution variations along direction 2: (a) stress σ_{11}/σ_0; (b) stress σ_{22}/σ_0 for different heights of protrusion.

The distributions of normal stress σ_{11} on the interface EF are shown in Fig. 11. We can observe that for larger height of protrusion, the maximum stress on interface decreases slightly. When h = 1.6 mm, the average stress seems to be minimum. We may conclude that for certain volume of protrusion with selections of parameters in Table 3, the optimized design of height is about 1.6 mm. Fig. 12 shows the variations of two normal stresses along the edge BC for different height. There is large jump in value of the stress σ_{11} at interface x_2 = 1.0 mm, at the change of material as expected. We also observed that the maximum stress both for σ_{11} and σ_{22} on the interface are found along the interface when h = 0.2 mm. The distribution of stress should be improved for larger height of protrusion.

7. Conclusion

A mesh free method has been extended to multi-region problems and applied to the stress analysis for Comeld™ joints in this paper. For multi-region problems, we need to select collocation points on the interface and the special treatment needs to be considered for the interpolation field point which is close to the interface. Radial basis function interpolation is utilized to derive the shape functions for the field points. A unit cell mode was proposed to deal with large number of protrusions. Numerical solutions by the use of finite element method (ABAQUS) were presented with both 11 protrusions modeling and unit cell modeling. Comparisons have been made between these different numerical techniques. Obviously mesh free method does not need any elements in the domain. The first advantage over finite element method is simplicity and accuracy. Secondly, optimization of geometry parameters for any design can be carried out easily as there is no re-meshing problem. However, mesh free method has a free parameter, which affects the accuracy more or less. How to select this parameter is different topic.

References

[1] J.R. Vinson, Polymer Engineering and Science 29 (19) (1989).
[2] J.F. Meyer, in: S.M. Lee (Ed.), International Encyclopedia of Composites, vol. 2, VCH, New York, 1990.
[3] V.K. Stokes, Polymer Engineering and Science 29 (19) (1989).
[4] J.J. Tierney, J.W. Gillespie JR., P.-E. Bourban, Joining of Composites, Comprehensive Composites Materials, vol. 2, Elsevier, 2000. 2.31.
[5] C.E.S. Ueng, K. Zhang, AAIA Journal 23 (11) (1985).
[6] L.J. Hart-Smith, in: The 4th Conference on Fibrous Composites in Structural Design, San Diego, CA, Plenum, New York, 1978.
[7] L.J. Hart-Smith, in: F.L. Matthews, (Ed.), Joining Fibre-reinforced Plastics, 1986 (Chapter 6).
[8] Bülent Murat İçten, Ramazan Karakuzu, M. Evren Toygar, Composite Structures 73 (4) (2006) 443–450.
[9] R.F. Wegman, Materials Science and Process Technology Series, Noyes Publications, Park Ridge, NJ, 1989.
[10] J.D. Venables, Journal of Material Science 19 (1984).
[11] D.K. Shaffer, H.M. Clearfield, J.S. Ahearn, in: J.D. Minford (Ed.), Treatise on Adhesives, Marcel Dekker, New York, 1991.
[12] J. Comyn, The Royal Society of Chemistry (1997).
[13] F. Smith, TWI Knowledge Summary (2004).
[14] P.H. Wen, M.H. Aliabadi, A. Young, CMES Computer Modeling in Engineering & Sciences 3 (2002) 1–10.
[15] P.H. Wen, M.H. Aliabadi, A. Young, Engineering Fracture Mechanics 69 (2002) 2129–2146.
[16] P.H. Wen, M.H. Aliabadi, A. Young, Journal of Strain Analysis for Engineering Design 37 (2002) 223–237.
[17] P.H. Wen, M.H. Aliabadi, A. Young, International Journal for Numerical Methods in Engineering 58 (2003) 43–61.
[18] B. Nayroles, G. Touzot, P. Villon, Computational Mechanics 10 (1992) 307–318.
[19] T. Belytschko, Y.Y. Lu, L. Gu, International Journal for Numerical Methods in Engineering 37 (1994) 229–256.
[20] W.K. Liu, S. Jun, Y. Zhang, International Journal for Numerical Methods in Engineering 20 (1995) 1081–1106.
[21] S.N. Atluri, T. Zhu, Computer Modeling and Simulation in Engineering 3 (1998) 187–196.
[22] S.N. Atluri, The Meshless Method (MLPG) for Domain and BIE Discretizations, Tech Science Press, Forsyth, GA, USA, 2004.
[23] V. Sladek, J. Sladek, M. Tanaka, Ch. Zhang, Engineering Analysis with Boundary Elements 29 (2005) 829–843.
[24] J. Sladek, V. Sladek, P.H. Wen, M.H. Aliabadi, CMES: Computer Modeling in Engineering & Sciences 13 (2006) 103–117.
[25] R.L. Hardy, Journal of Geophysical Research 76 (1971) 1905–1915.
[26] E. Kansa, Computers & Mathematics with Applications 19 (1990) 149–161.
[27] P.H. Wen, M.H. Aliabadi, Journal of Multiscale Modelling 1 (2) (2009) 303–319.
[28] Section 17.2.1, Abaqus Analysis User's Manual, Abaqus Version 6.7 Documentation, 2007.

APPENDIX B
Boundary conditions for end protrusion

The boundary conditions for the modelling strategy B and C for the end protrusion analyses can be described as following.

The loading on the right side of the model has been achieved by applying pressure. On the left edge of the model repetitive boundary conditions from middle of the step was assumed. By interpolation of the extracted displacements, the correspond nodes on the models of strategy B and C can be identified and therefore, displacement can be assigned according to the node position.

The example of applying repetitive deformation on the left edge for strategy C is shown as following.

```
#
# global delta U1 on the right edge of the protrusion line of 6
from bisect import bisect
nodelist=open(r'e:/phd/comeld-py/nodes-list.inp', 'r')
nodelist_l=open(r'e:/phd/comeld-py/nodes-list-left.inp', 'r')
coord=open(r'e:/phd/comeld-py/node-coord.inp','r')
lcurve=open(r'e:/phd/comeld-py/loading-curve-repetitive-uc30-u1.inp','r')
lcurve_r=open(r'e:/phd/comeld-py/loading-curve-6protrusion-uc30.inp','r')
outputset=open(r'e:/phd/comeld-py/nodeset-list.inp', 'w')
outputset.write('')
outputset.close()
outputset=open(r'e:/phd/comeld-py/nodeset-list.inp', 'a')
outputload=open(r'e:/phd/comeld-py/u1-load-left-uc30.inp','w')
outputload.write('')
outputload.close()
outputload=open(r'e:/phd/comeld-py/u1-load-left-uc30.inp','a')
# nodes list for the protrusion line 6 left and right edge
A=['']
A1=['']
B=['']
B1=['']
#
A3=['']
A4=['']
B3=['']
B4=['']
```

```
# nodes coords
C=['']
D=['']
# global delta loading curve left side
L1=['']
M1=['']
L2=['']
M2=['']
L3=['']
L4=['']
M3=['']
M4=['']
L=['']
M=['']
# global delta loading curve right side
U1=['']
W1=['']
U2=['']
W2=['']
U3=['']
W3=['']
U4=['']
W4=['']
U=['']
W=['']
# loading for line protrusion left and right
E=['']
F=['']
F1=['']
#########################
grades=['']
gradesr=['']
noderead=['']
while noderead[0]!='*':
   noderead=nodelist_l.readline()
   a=noderead.split(',')
#    a.remove('')
   for n in range(0, len(a)):
#       inta=int(a[n])
       A1.append(a[n])
A1.remove('*\n')
A1.remove('')
for n in range(0,len(A1)):
   a1=int(A1[n])
   A.append(a1)
A.remove('')
noderead=['']
while noderead[0]!='*':
   noderead=coord.readline()
```

```
    temp=noderead.split(',')
    if temp[0]!='*\n':
        c=int(temp[0])
        d=float(temp[-1])
        C.append(c)
        D.append(d)
C.remove('')
D.remove('')
for n in range(0, len(A)):
    an=str(A[n])
    for m in range(0, len(C)):
        cm=str(C[m])
        if an==cm:
            dm=3.0-float(D[m])
            if dm<=0.00001:
                dm=0.0
                B.append(dm)
            elif dm>2.99999:
                dm=3.0
                B.append(dm)
            else:
                B.append(dm)
B.remove('')
for n in range(0, len(B)):
    b1n=3.0-B[n]
    B1.append(b1n)
B1.remove('')
def findbotnode(data):
    for n in range(0,len(data)):
        if data[n]==3.0:
            return n
def findtopnode(data):
    for n in range(0,len(data)):
        if data[n]==0.0:
            return n
bn=findbotnode(B)
bt=findtopnode(B)
#
noderead=['']
while noderead[0]!='*':
    noderead=nodelist.readline()
    a=noderead.split(',')
    for n in range(0, len(a)):
        A4.append(a[n])
A4.remove('*\n')
A4.remove('')
for n in range(0,len(A4)):
    a4=int(A4[n])
    A3.append(a4)
```

```
A3.remove('')
for n in range(0, len(A3)):
   an=str(A3[n])
   for m in range(0, len(C)):
      cm=str(C[m])
      if an==cm:
         dm=3.0-float(D[m])
         if dm<=0.00001:
            dm=0.0
            B3.append(dm)
         elif dm>2.99999:
            dm=3.0
            B3.append(dm)
         else:
            B3.append(dm)
B3.remove('')
for n in range(0, len(B3)):
   b4n=3.0-B3[n]
   B4.append(b4n)
B4.remove('')
b3n=findbotnode(B3)
b3t=findtopnode(B3)
#
#
#
#
#print 'bn=',bn
noderead=['']
while noderead[0]!='*':
   noderead=lcurve.readline()
   temp=noderead.split(',')
   if temp[0]!='*\n':
      l=float(temp[0])
      m=float(temp[-1])
      L1.append(l)
      M1.append(m)
L1.remove('')
M1.remove('')
for n in range(0,len(L1)-1):
   l2n=(L1[n]+L1[n+1])/2.0
   L2.append(l2n)
for n in range(0,len(M1)-1):
   m2n=(M1[n]+M1[n+1])/2.0
   M2.append(m2n)
L2.remove('')
M2.remove('')
for n in range(0,len(L1)):
   if n < len(L2):
      l1n=L1[n]
```

```
        l2n=L2[n]
        L3.append(l1n)
        L3.append(l2n)
    else:
        l1n=L1[n]
        L3.append(l1n)
for n in range(0,len(M1)):
    if n < len(M2):
        m1n=M1[n]
        m2n=M2[n]
        M3.append(m1n)
        M3.append(m2n)
    else:
        m1n=M1[n]
        M3.append(m1n)
L3.remove('')
M3.remove('')
for n in range(0,len(L3)-1):
    l4n=(L3[n]+L3[n+1])/2.0
    L4.append(l4n)
for n in range(0,len(M3)-1):
    m4n=(M3[n]+M3[n+1])/2.0
    M4.append(m4n)
L4.remove('')
M4.remove('')
for n in range(0,len(L3)):
    if n < len(L4):
        l3n=L3[n]
        l4n=L4[n]
        L.append(l3n)
        L.append(l4n)
    else:
        l3n=L3[n]
        L.append(l3n)
for n in range(0,len(M3)):
    if n < len(M4):
        m3n=M3[n]
        m4n=M4[n]
        M.append(m3n)
        M.append(m4n)
    else:
        m3n=M3[n]
        M.append(m3n)
L.remove('')
M.remove('')
##
##
noderead=['']
while noderead[0]!='*':
```

```
    noderead=lcurve_r.readline()
    temp=noderead.split(',')
    if temp[0]!='*\n':
        u=float(temp[0])
        w=float(temp[-1])
        U1.append(u)
        W1.append(w)
U1.remove('')
W1.remove('')
for n in range(0,len(U1)-1):
    u2n=(U1[n]+U1[n+1])/2.0
    U2.append(u2n)
for n in range(0,len(W1)-1):
    w2n=(W1[n]+W1[n+1])/2.0
    W2.append(w2n)
U2.remove('')
W2.remove('')
for n in range(0,len(U1)):
    if n < len(U2):
        u1n=U1[n]
        u2n=U2[n]
        U3.append(u1n)
        U3.append(u2n)
    else:
        u1n=U1[n]
        U3.append(u1n)
for n in range(0,len(W1)):
    if n < len(W2):
        w1n=W1[n]
        w2n=W2[n]
        W3.append(w1n)
        W3.append(w2n)
    else:
        w1n=W1[n]
        W3.append(w1n)
U3.remove('')
W3.remove('')
for n in range(0,len(U3)-1):
    u4n=(U3[n]+U3[n+1])/2.0
    U4.append(u4n)
for n in range(0,len(W3)-1):
    w4n=(W3[n]+W3[n+1])/2.0
    W4.append(w4n)
U4.remove('')
W4.remove('')
for n in range(0,len(U3)):
    if n < len(U4):
        u3n=U3[n]
        u4n=U4[n]
```

```
            U.append(u3n)
            U.append(u4n)
        else:
            u3n=U3[n]
            U.append(u3n)
    for n in range(0,len(W3)):
        if n < len(W4):
            w3n=W3[n]
            w4n=W4[n]
            W.append(w3n)
            W.append(w4n)
        else:
            w3n=W3[n]
            W.append(w3n)
    U.remove('')
    W.remove('')
    ##
    ##
    for n in range(0,len(L)):
        grades.append(n)
    grades.remove('')
    #E.append()
    def grade(total):
        return grades[bisect(L, total)]
    for n in range(0,len(U)):
        gradesr.append(n)
    gradesr.remove('')
    def grader(total):
        return gradesr[bisect(U, total)]
    for n in range(0, len(B)):
        if n==bn:
            E.append(M[-1])
        elif n==bt:
            E.append(M[0])
        else:
            x=grade(B[n])
            y=(M[x-1]+M[x])/2.0
            E.append(y)
    E.remove('')
    for n in range(0, len(B3)):
        if n==b3n:
            F.append(W[-1])
        elif n==b3t:
            F.append(W[0])
        else:
            x=grader(B3[n])
            y=(W[x-1]+W[x])/2.0
            F.append(y)
    F.remove('')
```

```
for n in range(0, len(B3)):
    if n==b3n:
        F1.append(M[-1])
    elif n==b3t:
        F1.append(M[0])
    else:
        x=grade(B3[n])
        y=(M[x-1]+M[x])/2.0
        F1.append(y)
F1.remove('')
#
for q in range(0,len(A)):
    outputset.write('\n*Nset, nset=td-l-')
    outputset.write(str(q))
    outputset.write(', instance=uc_2d_30-line-protrusion-1\n')
    s=str(A[q])
    outputset.write(s)
for q in range(0,len(A3)):
    outputset.write('\n*Nset, nset=td-')
    outputset.write(str(q))
    outputset.write(', instance=uc_2d_30-line-protrusion-1\n')
    s=str(A3[q])
    outputset.write(s)
for q in range(0,len(A)):
    outputload.write('\n*Boundary\ntd-l-')
    outputload.write(str(q))
    outputload.write(', 1, ,')
    t=str(E[q])
    outputload.write(t)
for q in range(0,len(A)):
    outputload.write('\n*Boundary\ntd-')
    outputload.write(str(q))
    outputload.write(', 1, ,')
    right=F[q]+F1[q]
    t=str(right)
    outputload.write(t)
#
#
outputset.close()
outputload.close()
nodelist.close()
nodelist_l.close()
coord.close()
lcurve.close()
lcurve_r.close()
```

The example of processed input file is shown as following.

```
*Heading
…
*Part, name=uc_2d_30-line-protrusion
*End Part
…
*Assembly, name=Assembly
**
*Instance, name=uc_2d_30-line-protrusion-1, part=uc_2d_30-line-protrusion
*Node
…
*End Instance
**
*Nset
….
*Nset, nset=td-0, instance=uc_2d_30-line-protrusion-1
37
*Nset, nset=td-1, instance=uc_2d_30-line-protrusion-1
38
…
*Nset, nset=td-150, instance=uc_2d_30-line-protrusion-1
1949
*End Assembly
**
** MATERIALS
…
*Step, name=Step-1
*Static
0.1, 1., 1e-05, 0.1
**
** BOUNDARY CONDITIONS
**
** Name: BC-1 Type: Displacement/Rotation
***Boundary
**fixed_1-3, 1, 1
**
*Boundary
td-0, 1, ,1.53838875e-07
…
*Boundary
td-150, 1, ,2.10175875e-07
…
*Dsload
load, P, -1.0
…
*End Step
```

APPENDIX C
Model strategies for end protrusion

Appendix C.1 Contour results for perpendicular protrusions models

The stress concentration contour results are shown in Fig.C.1 to Fig.C.4 for the whole end protrusion in various strategies. The locations of the maximum stresses are marked with circle on each of the contour results. The maximum concentrations are listed in Table.C.1 to Table.C.4. For peel and shear stresses, minus concentrations indicate change in stress direction.

Comparisons of the end protrusion with composites

Fig.C.1 shows the concentration of the von Mises stress concentration contour results for various models. These comparisons are made to assess the modelling strategy. The maximum stress concentrations shown here occurred in the titanium alloy, shown in Table.C.1, therefore the concentrations are not important for the joint failure in this work. With the same scale the stress distributions are similar to the global model. The maximum stresses occurred at the foot of the protrusion within the titanium region, except Strategy B, Fig.C.1 (d). The maximum concentrations for Strategy A Model 1 and Strategy C are close to the global model end protrusion with 2.6% higher and 2.3% lower concentrations; maximum concentration for other strategies are much higher than the global model. In Fig.C.1 (d) for Strategy B, for the same location of the global model maximum stress concentration, the von Mises stress concentration is 1.585, which is 10.4% more than the global model. These results indicate that the different strategies are worth investigating further.

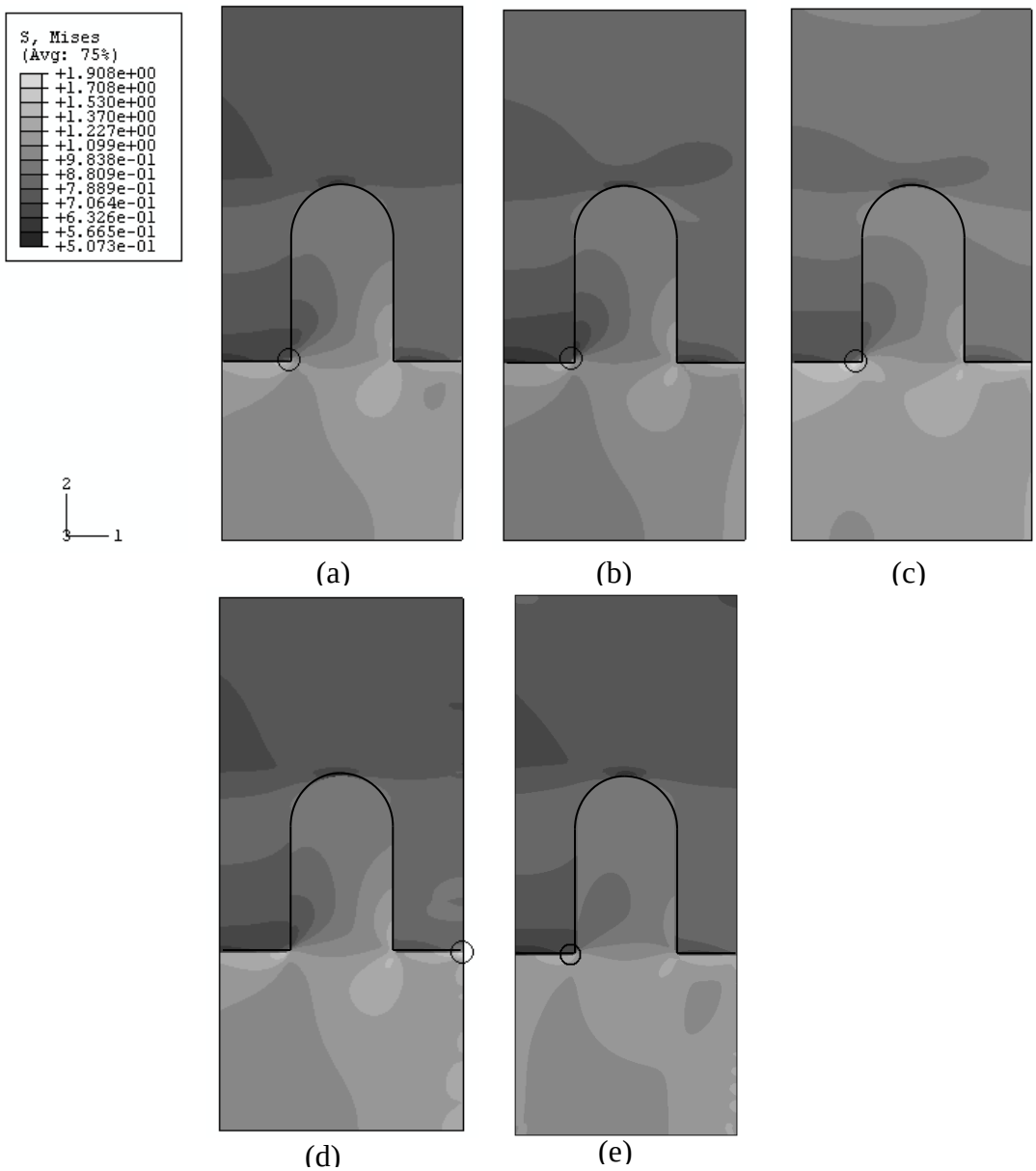

Fig.C.1 *Von Mises stress concentration contour results of the end protrusion for the global model with detailed geometries (a); Strategy A Model 1 (b); Strategy A Model 2 (c); Strategy B (d); Strategy C (e)*

Table.C.1 *Maximum concentration of Von Mises stresses for various models*

Global Model	Strategy A Model 1	Strategy A Model 2	Strategy B	Strategy C
1.436	1.474	1.890	1.908	1.403
% compare to the global model	+2.6%	+31.6%	+32.9%	-2.3%

Contour results of stress components are shown in Fig.C.2 for axial stress, Fig.C.3 for peel stress, and Fig.C.4 for shear stress.

Similarly to the von Mises comparison, concentrations for the axial stress, the stress distributions and the locations of the maximum concentrations are similar to the global model, shown in Table.C.2. The differences compared to the global model for different strategies vary from -6.1% to 7.3%.

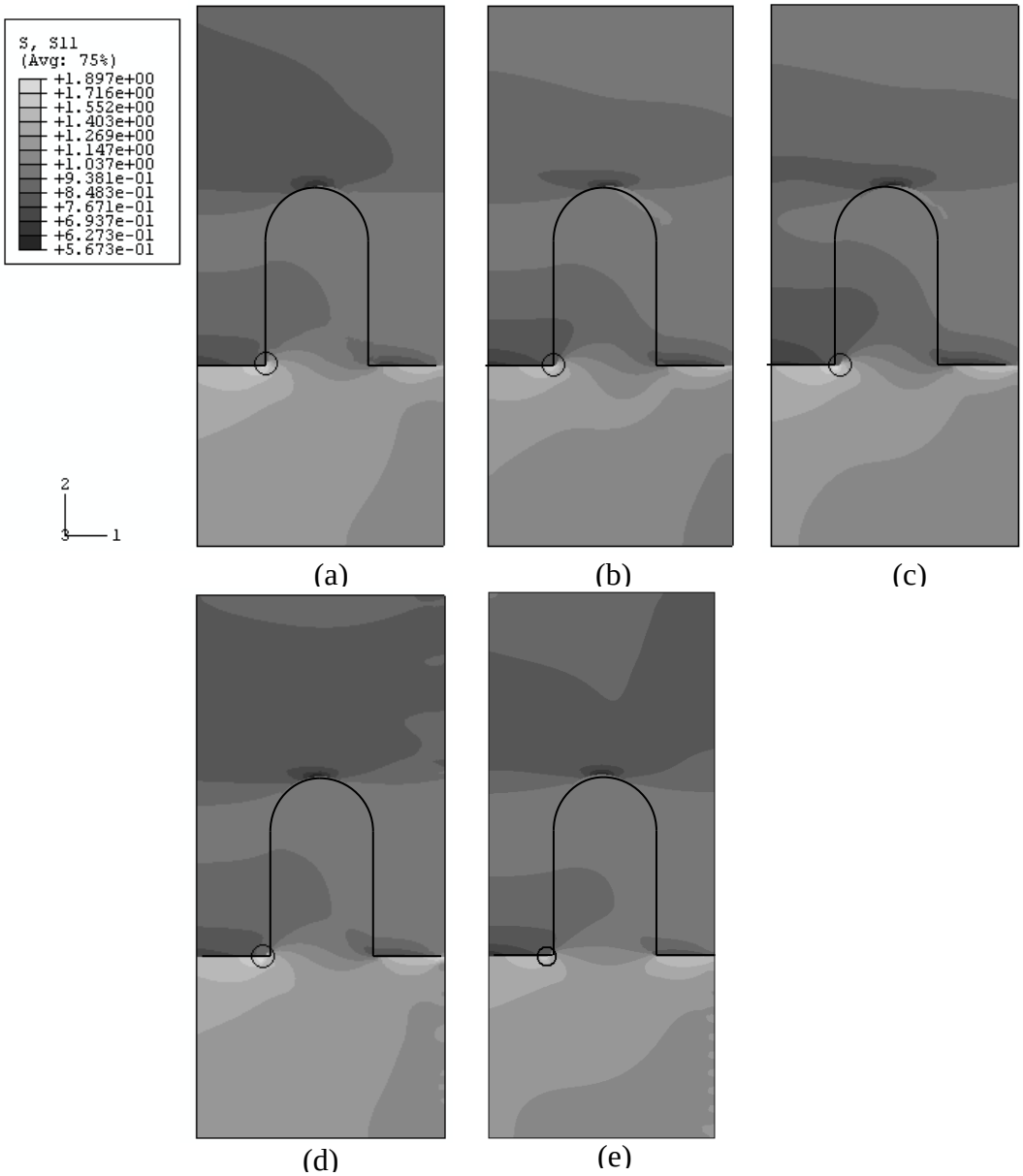

Fig.C.2 *Axial stress concentration contour results of the end protrusion for the global model with detailed geometries (a); Strategy A Model 1 (b); Strategy A Model 2 (c); Strategy B (d); Strategy C (e)*

Table.C.2 *Maximum concentration of axial stresses for various models*

Global Model	Strategy A Model 1	Strategy A Model 2	Strategy B	Strategy C
1.768	1.770	1.889	1.897	1.660
% compare to the global model	+0.1%	+6.8%	+7.3%	-6.1%

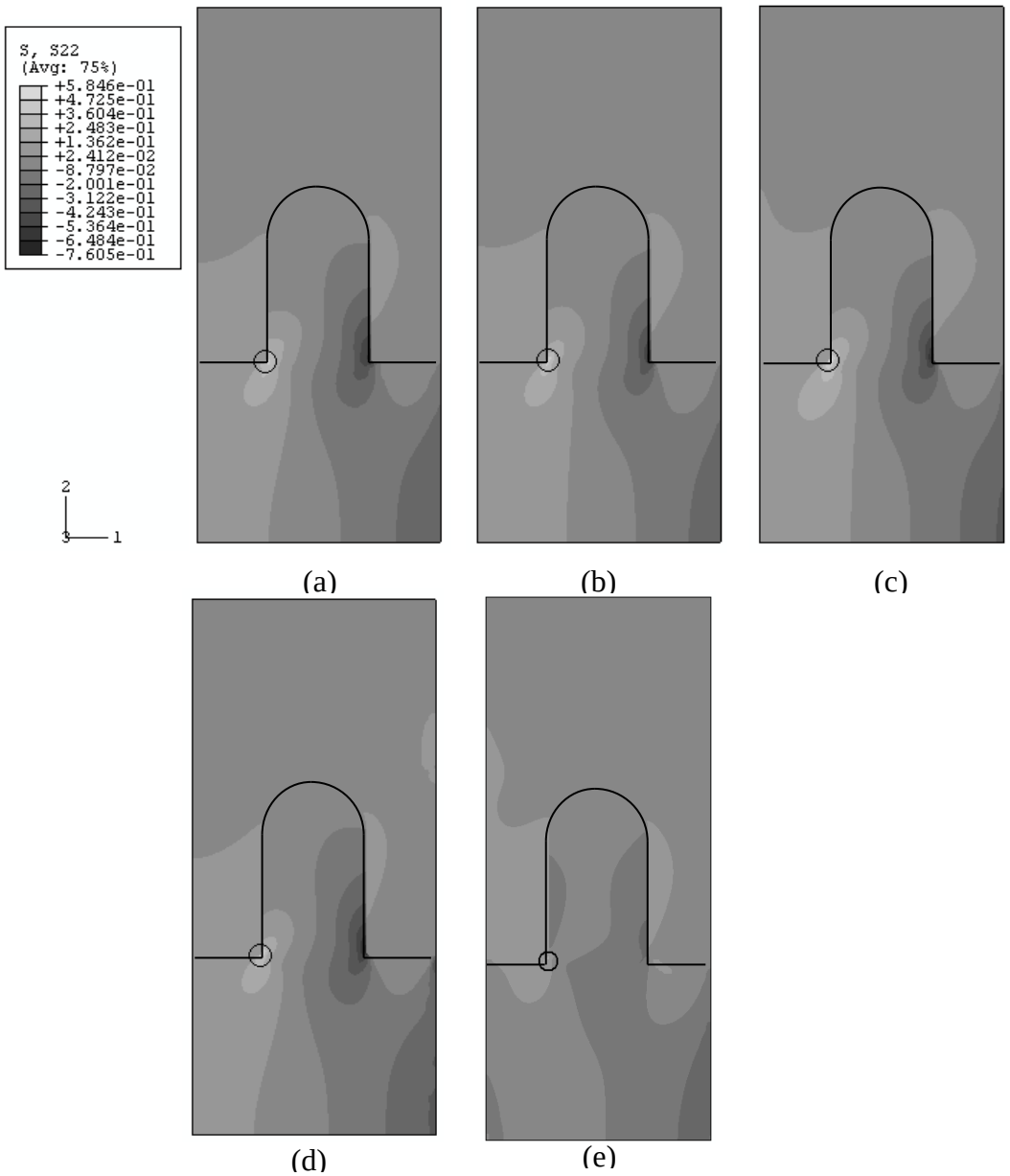

Fig.C.3 *Peel stress concentration contour results of the end protrusion for global model with detailed geometries (a); Strategy A Model 1 (b); Strategy A Model 2 (c); Strategy B (d); Strategy C (e)*

For the peel stress, see Fig.C.3, all stress distributions are similar as well as the maximum stress locations. The maximum concentrations are listed in Table.C.3. The maximum stress concentration for Fig.C.3 (e) is less than half of the global model result, indicating the accuracy for Strategy C is low.

Table.C.3 *Maximum concentration of peel stresses for various models*

Global Model	Strategy A Model 1	Strategy A Model 2	Strategy B	Strategy C
0.4505	0.5052	0.5846	0.5172	0.1962
% compare to the global model	+12.1%	+29.8%	+14.8%	-56.4%

For the shear stress, see Fig.C.4, stress distributions are again similar to the global model result except Strategy C, Fig.C.4 (e). The maximum stress concentrations are much more different than the previous comparisons ranging from -30.3% to 32.7%, listed in Table.C.4.

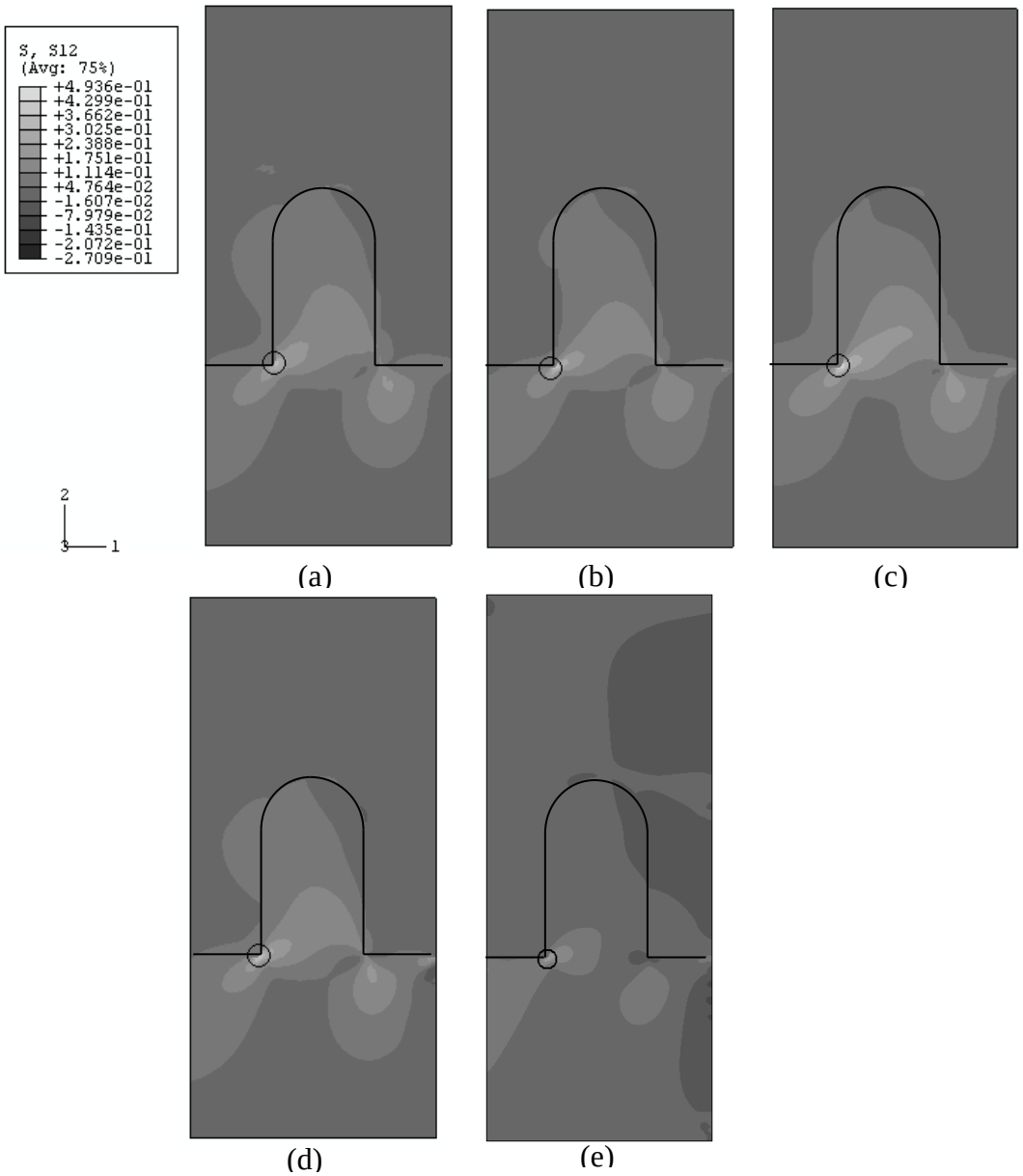

Fig.C.4 *Shear stress concentration contour results of the end protrusion for global model with detailed geometries (a); Strategy A Model 1 (b); Strategy A Model 2 (c); Strategy B (d); Strategy C (e)*

Table.C.4 *Maximum concentration of shear stresses for various models*

Global Model	Strategy A Model 1	Strategy A Model 2	Strategy B	Strategy C
0.3719	0.4247	0.4936	0.4484	0.2592
% compare to the global model	+14.2%	+32.7%	+20.6%	-30.3%

After the examination of the whole model, according to the stress distributions displayed in Fig.C.1 to Fig.C.4, Strategy A Model 1 shows a stronger agreement with the global model results for the end protrusion. However, as failure occurs in the composite region of the joining system, the conclusion should not be made according to the whole model comparisons. Therefore, composite region of the end protrusion and its peel and shear stress should be examined further.

Appendix C.2 Stress concentration profiles for perpendicular protrusions models on the model side edges

To further compare all strategies with the global model, both left and right sides of the end protrusion region were selected. Axial, peel and shear stress concentrations profiling were along each side from top to bottom, see Fig.C.5 to Fig.C.7. The Y axis is stress and the X axis is distance from top of the joint surface. Two on the X axis indicate the joint step surface.

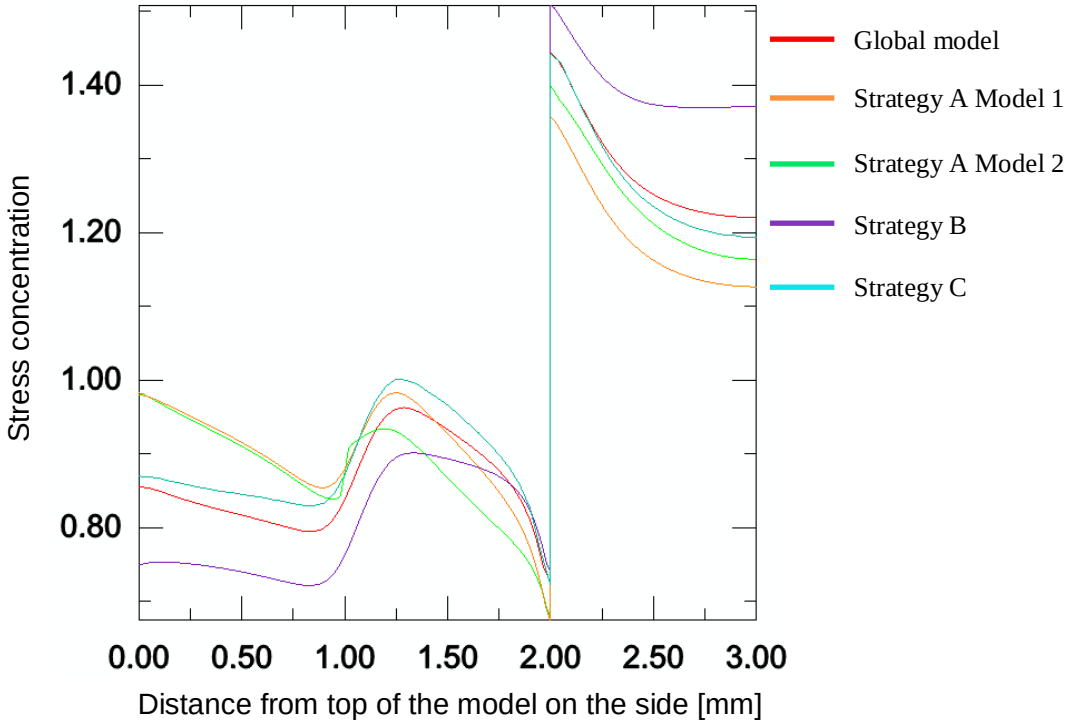

Fig.C.5 *Axial stress concentration on the left side of the end protrusion for the global model and all the strategies*

Axial stress concentration on both sides are examined in Fig.C.5 and Fig.C.6. On the left side, reasonable agreement with the global model case was found for all strategies except Strategy B, which shows larger variations especially in the titanium alloy region. On the right side, Strategy B and C show larger variations.

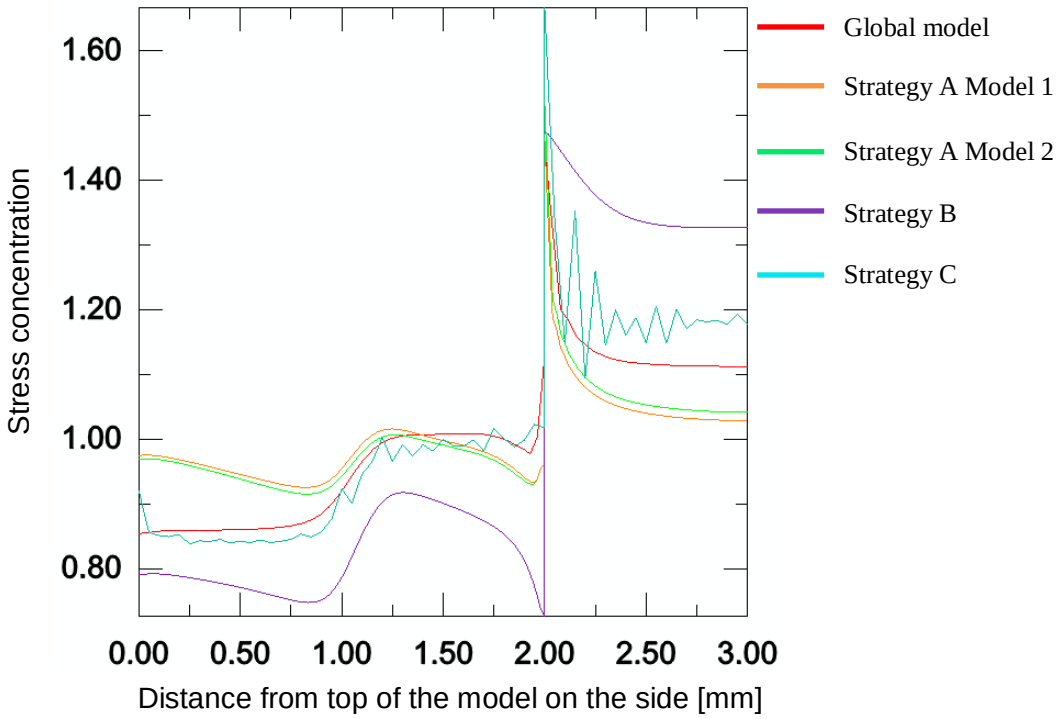

Fig.C.6 *Axial stress concentration on the right side of the end protrusion for the global model and all the strategies*

Peel stress concentration on both sides were examined in Fig.C.7 and Fig.C.8. On the left side, before the joint step except for Strategy A Model 2, all other strategies were close to the global model result. When it reached the titanium alloy region, stress for Strategy A Model 1 has a similar shape with the global model, but shows higher concentrations, whereas Strategy B shows lower concentrations with a similar shape. Strategy C shows a kink at close to 3mm, i.e. bottom of the end protrusion model. This may be caused by the loading of the protrusion model. Strategy A Model 2 displays a very different stress concentration on the left side of the model. This is considered due to the homogenised composite region for simplification.

On the right side, Strategy A models show a reasonable agreement with the global model, whereas Strategy B and C show complete different trends. Again, these are considered to be caused by the loading of the models on the right side.

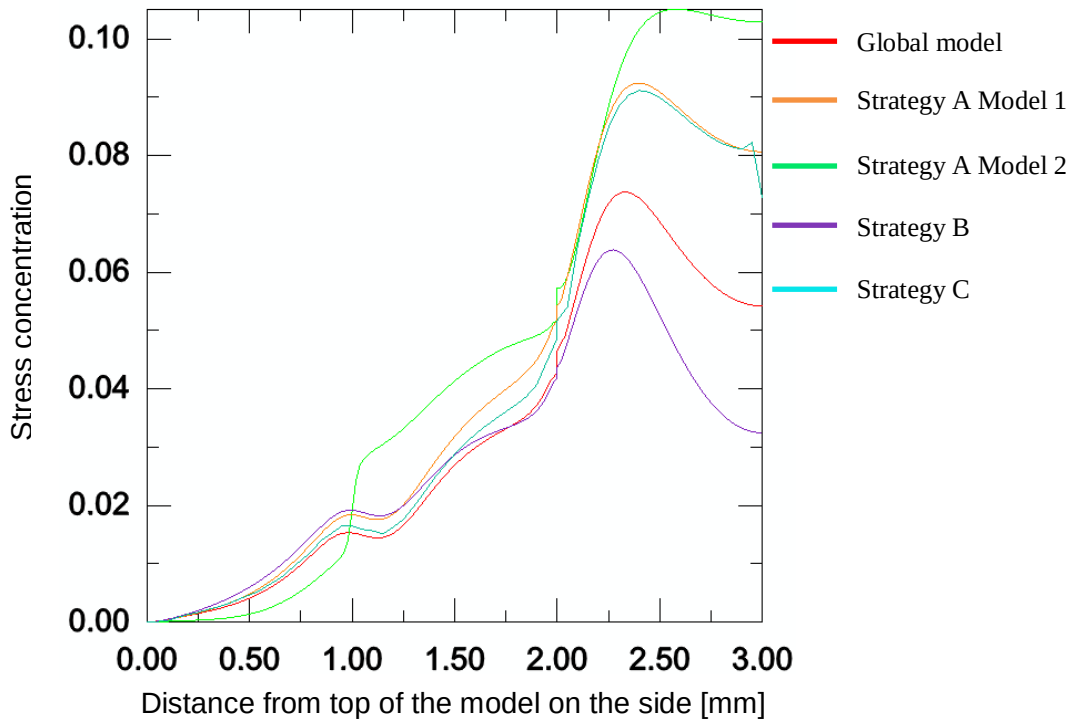

Fig.C.7 *Peel stress concentration on the left side of the end protrusion for the global model and all the strategies*

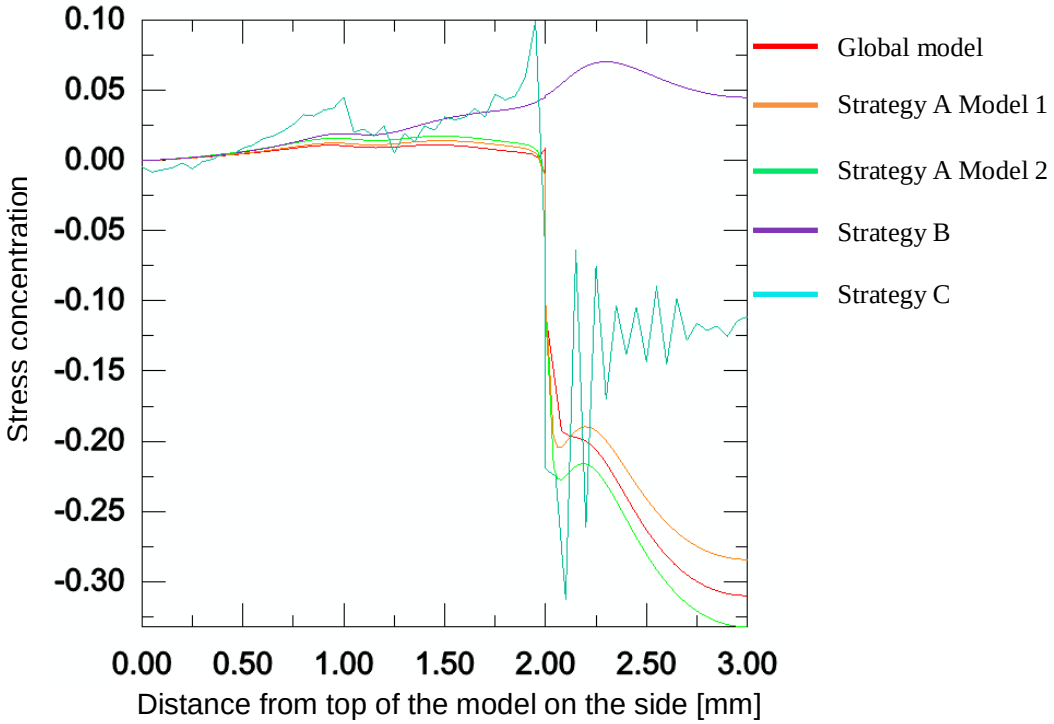

Fig.C.8 *Peel stress concentration on the right side of the end protrusion for the global model and all the strategies*

Shear stress concentration on both left and right side is shown in Fig.C.9 and Fig.C.10. On the left side, Strategy B and C shows completely different response to the load. For strategy B, the stress is far smaller than that of the global model end protrusion. Boundary conditions for Strategy C resulted in the zero shear stress nearly all through the height. Strategy A models show much closer shape and concentrations with the global model, especially Model 1, although the concentrations are smaller than the global model results.

On the right side, similar trends are observed. Strategy B and C are completely different from the globle model results. Strategy A models show very good agreement with the global model, where the Maximum concentration at around 2mm are both higher than the global model results.

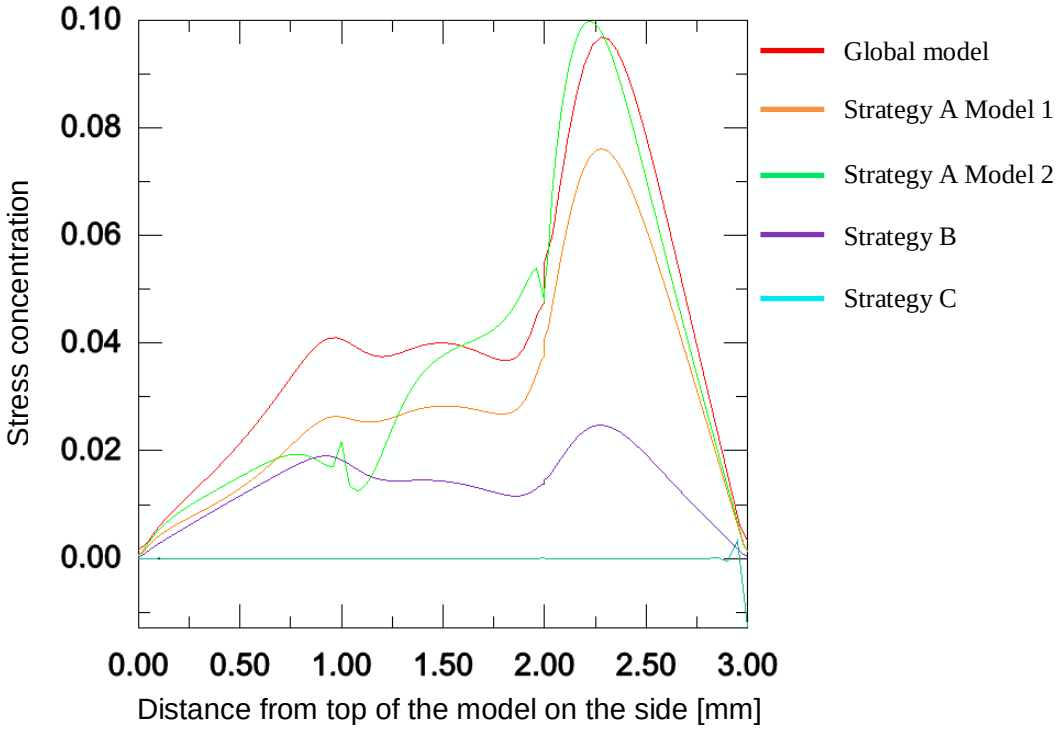

Fig.C.9 *Shear stress concentration on the left side of the end protrusion for the global model and all the strategies*

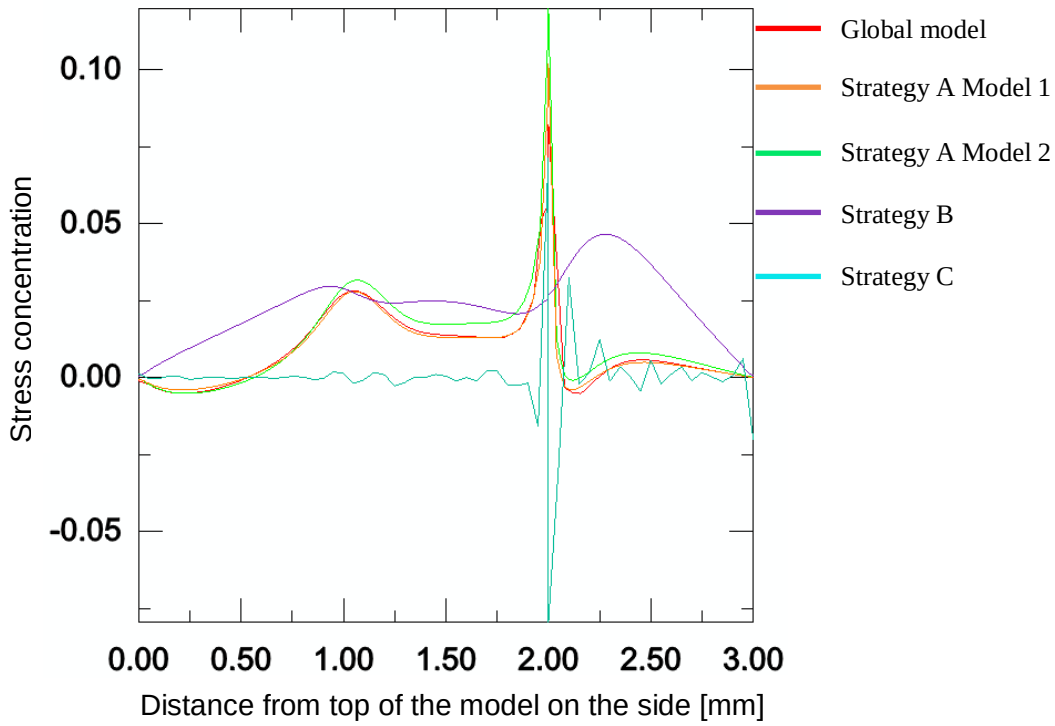

Fig.C.10 *Shear stress concentration on the right side of the end protrusion for the global model and all the strategies*

The stress profile results show that Strategy C is not suitable to represent the end protrusion from the global model; Strategy A Model 1 seems to be the best strategy to simulate the perpendicular end protrusion behaviour of the joint under tension. The question to be asked is whether this strategy is also the best to simulate angled end protrusions.

Appendix C.3 Contour results for 30 degree protrusions models

The stress concentration contour results are shown in Fig.C.11 to Fig.C.14 for the whole end protrusion in various strategies. The locations of the maximum stresses are marked with circle on each of the contour results. The maximum concentrations are listed in Table.C.5 to Table.C.14. For peel and shear stresses, minus concentrations indicate change in stress direction.

Comparisons of the end protrusion with composites

Fig.C.11 shows the von Mises stress concentration contour results for various models. These comparisons are made to assess the modelling strategy. The maximum stress concentrations shown here occurred in the titanium alloy, listed in Table.C.5, therefore the concentrations are not important for the joint failure in this work. With the same scale the stress distributions are similar to the global model. The maximum stresses occurred at the foot of the protrusion within the titanium region, except Strategy B, Fig.C.11 (d). The maximum concentrations are all in reasonable agreement with the global model end protrusion with 0.3% lower to 7.8% higher concentrations. However, the maximum stress location for Strategy B is different. In Fig.C.11 (d), for the same location of the global model maximum stress, the von Mises stress concentration is 1.663, which is 7.4% more than the global model.

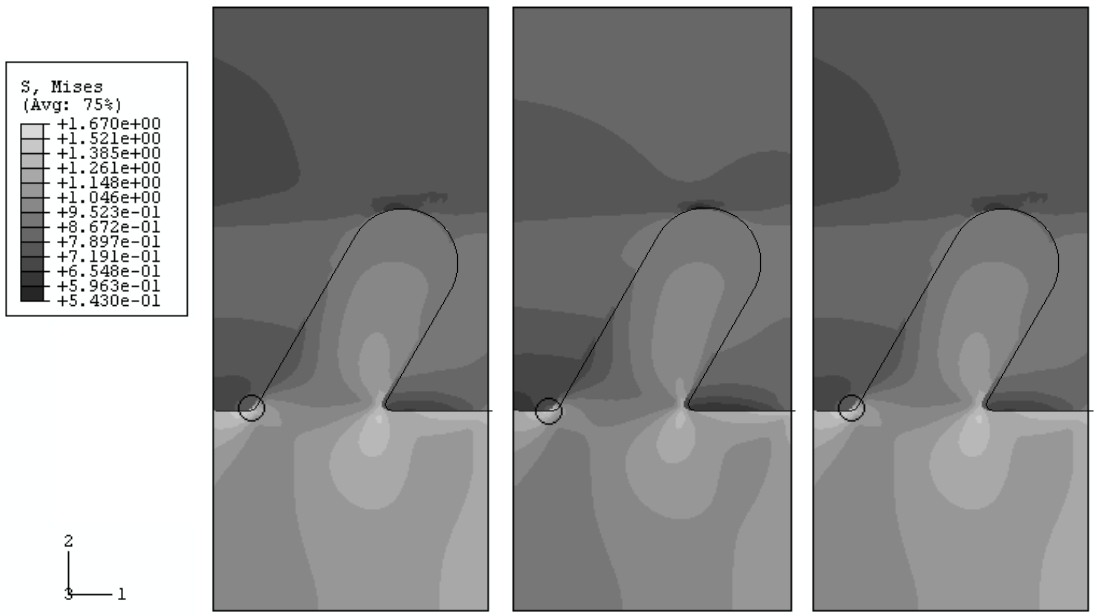

(a) (b) (c)

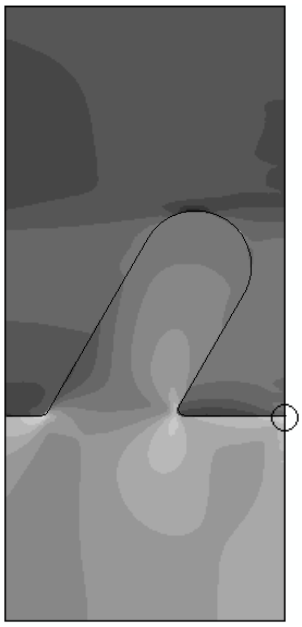

(d)

Fig.C.11 *Von Mises stress concentration contour results of the end protrusion at 30 degree for the global model with detailed geometries (a); Strategy A Model 1 (b); Strategy A Model 2 (c); Strategy B (d)*

Table.C.5 *Maximum concentration of Von Mises stresses for various models*

Global Model	Strategy A Model 1	Strategy A Model 2	Strategy B
1.549	1.545	1.638	1.670
% compare to the global model	-0.3%	+5.7%	+7.8%

Contour results of stress components are shown in Fig.C.12 for axial stress, Fig.C.13 for peel stress, and Fig.C.14 for shear stress.

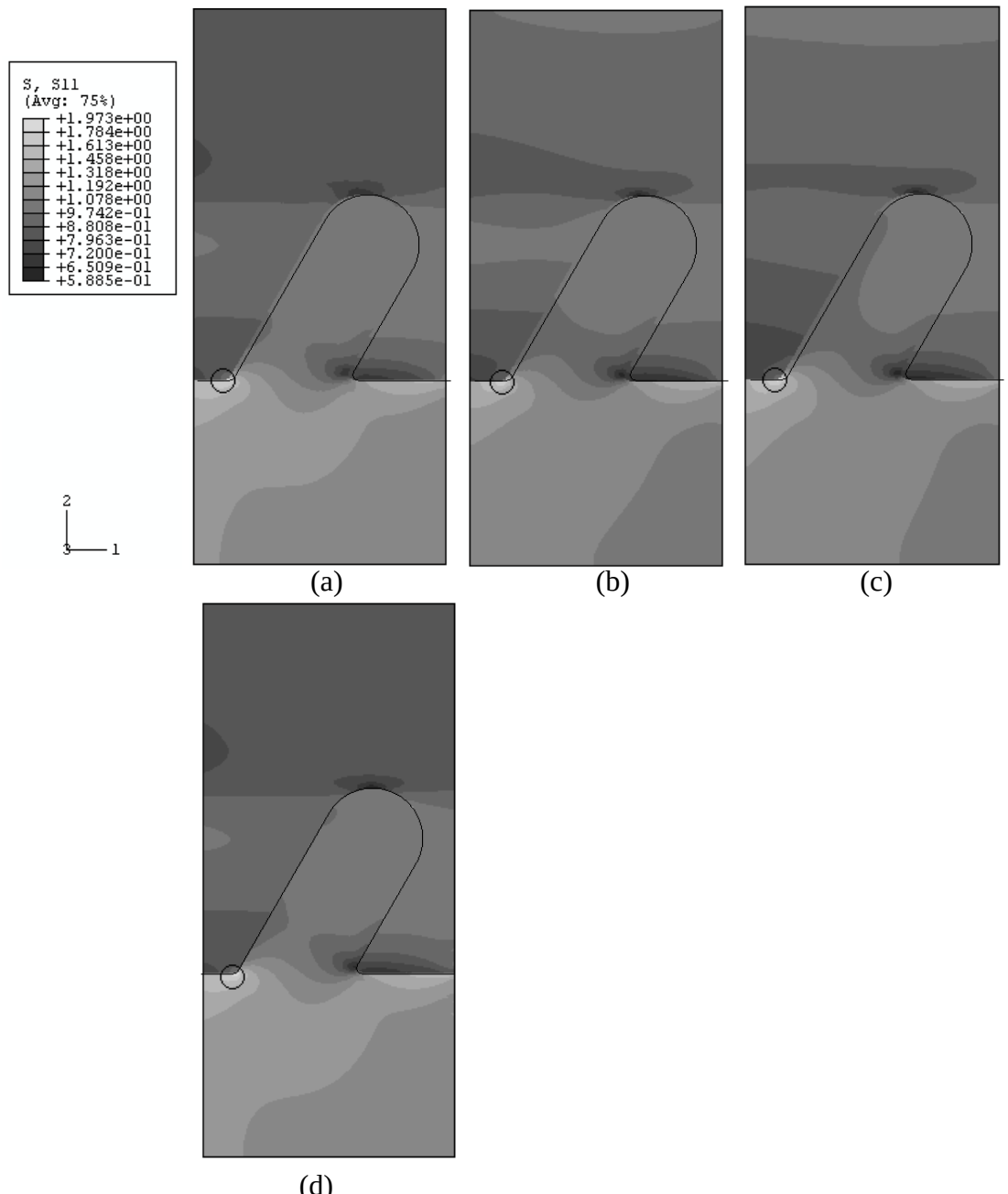

Fig.C.12 *Axial stress concentration contour results of the end protrusion at 30 degrees for the global model with detailed geometries (a); Strategy A Model 1 (b); Strategy A Model 2 (c); Strategy B (d)*

Similarly to the von Mises comparison, for the axial stress, the stress distributions and the locations of the maximum stress concentrations are similar to the global model,

shown in Table.C.6. The differences compare to the global model for different strategies vary from -1.3% to 5.7%.

Table.C.6 *Maximum concentration of axial stresses for various models*

Global Model	Strategy A Model 1	Strategy A Model 2	Strategy B
1.866	1.841	1.943	1.973
% compare to the global model	-1.3%	+4.1%	+5.7%

For the peel stress, see Fig.C.13, all stress distributions are similar as well as the maximum stress locations. The maximum concentrations are listed in Table.C.7. The maximum stress concentrations compare to the global model are much more higher than the case of axial stress, ranging from 13.1% to 29.6%.

Table.C.7 *Maximum concentration of peel stresses for various models*

Global Model	Strategy A Model 1	Strategy A Model 2	Strategy B
0.496	0.561	0.643	0.587
% compare to the global model	+13.1%	+29.6%	+18.3%

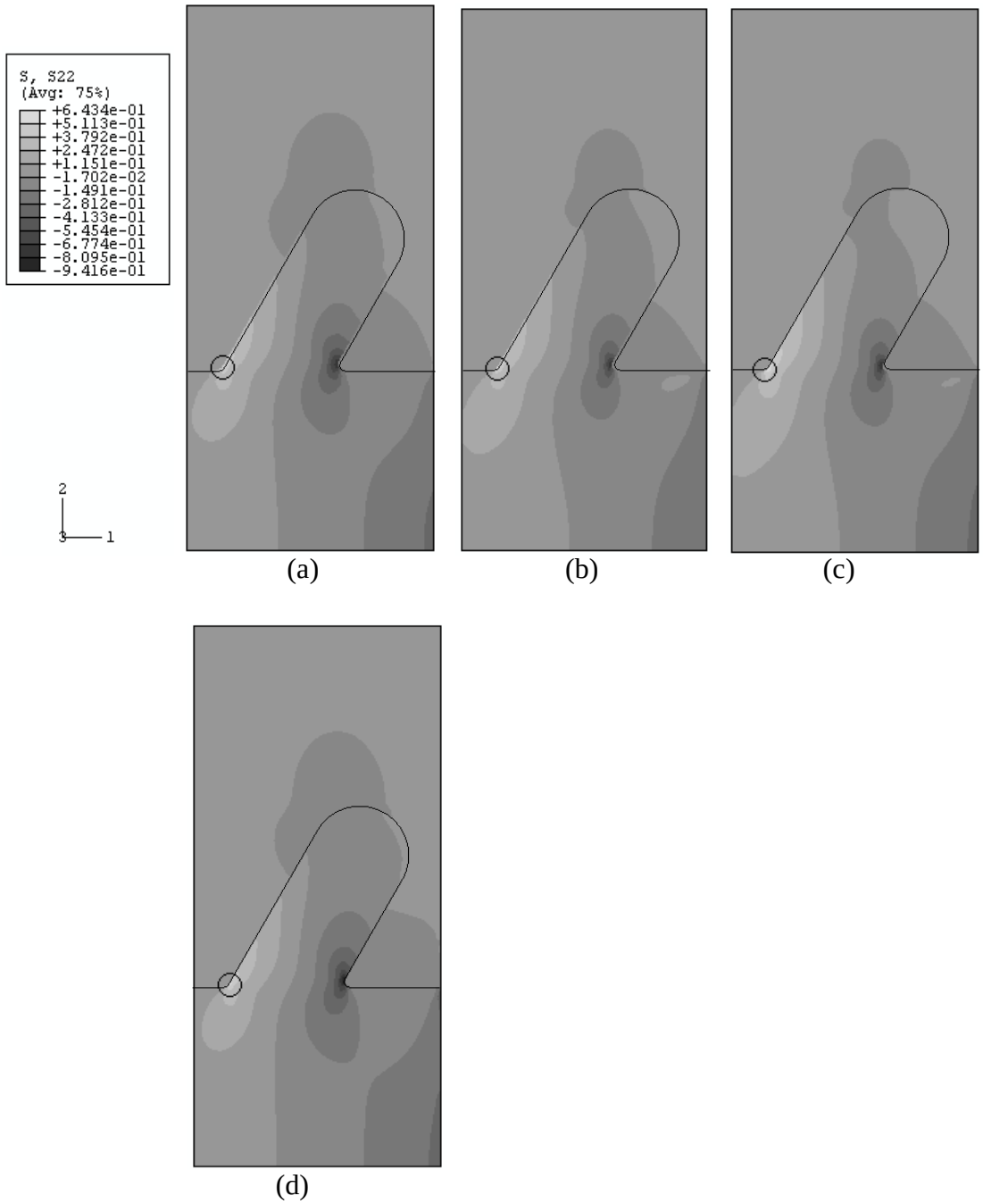

Fig.C.13 *Peel stress concentration contour results of the end protrusion at 30 degrees for the global model with detailed geometries (a); Strategy A Model 1 (b); Strategy A Model 2 (c); Strategy B (d)*

For the shear stress, see Fig.C.14, stress distributions are again similar to the global model result. The maximum stress concentrations are higher than the global model ranging from 4.3% to18.7%, listed in Table.C.8.

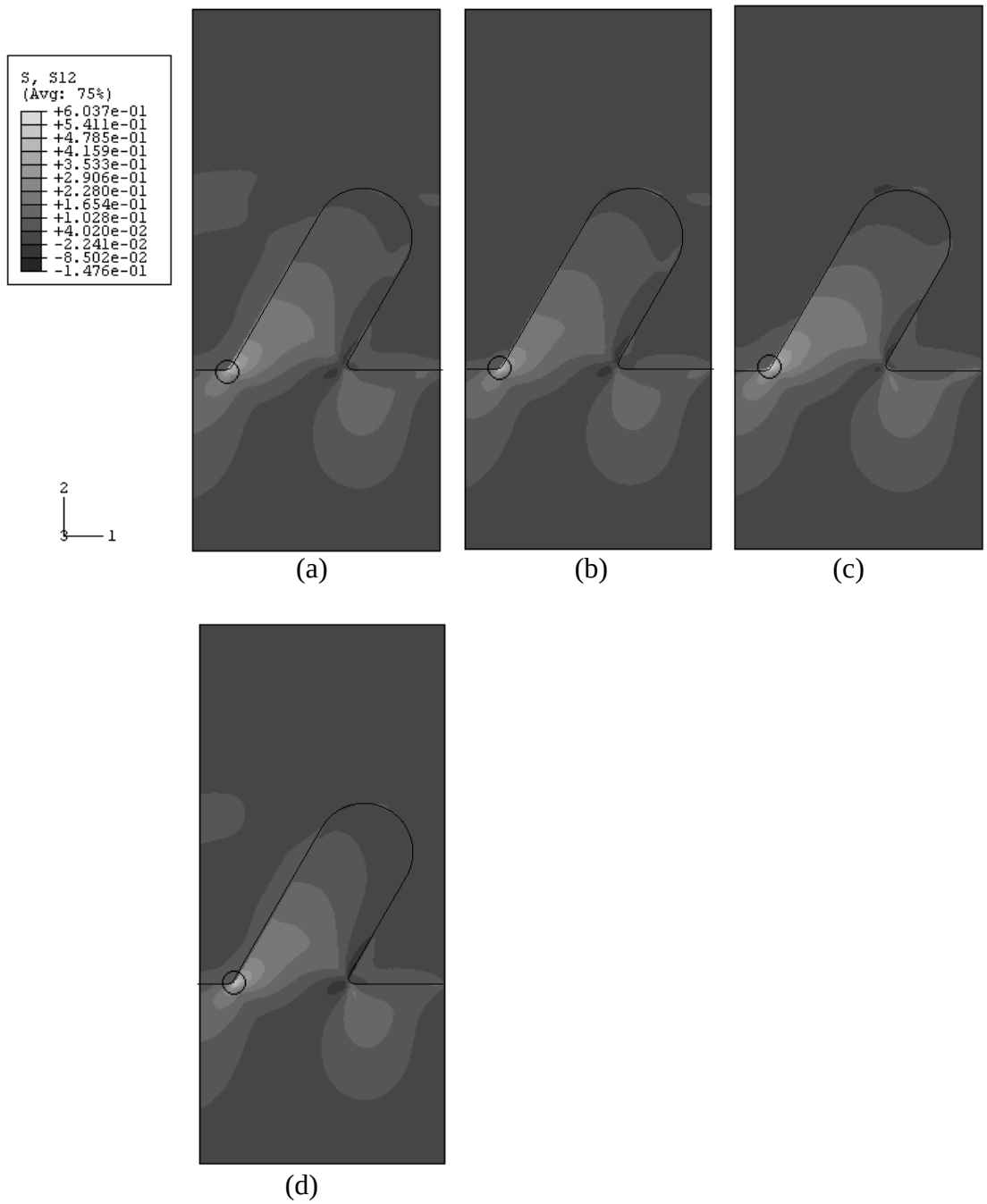

Fig.C.14 *Shear stress concentration contour results of the end protrusion at 30 degrees for the global model with detailed geometries (a); Strategy A Model 1 (b); Strategy A Model 2 (c); Strategy B (d)*

Table.C.8 *Maximum concentration of shear stresses for various models*

Global Model	Strategy A Model 1	Strategy A Model 2	Strategy B
0.509	0.531	0.604	0.569
% compare to the global model	+4.3%	+18.7%	+11.8%

All the locations of maximum stress concentration occur in the titanium alloy region, but it is observed experimentally failure occurs in the composite region of the joining system. Therefore, composite region of the end protrusion and its peel and shear stress should be examined further.

Appendix C.4 Stress concentration profiles for 30 degree protrusions models on the model side edges

Judging from the contour results for axial, peel and shear stress, there is not clear indication for the best modelling strategy. As for the perpendicular protrusion case, both left and right sides of the end protrusion region were selected. Axial, peel and shear stress concentrations were ploted against the distance from the top of the end protrusion region to the bottom on each side, see Fig.C.15 to Fig.C.20. The Y axis is stress concentration, and the X axis is distance, in mm, from top of the joint surface. From zero to two milimeter on the X axis indicates the composite and protrusion region, two milimetre on the X axis indicates the joint step surface, and from two to three milimetre on the X axis indicates the region of the joint step.

Axial stress concentration on both sides were examined in Fig.C.15 and Fig.C.16. On the left side, reasonable agreement with the global model case was found for all strategies. On the right side, Strategy B shows larger variations. From one to two milimetre, it is the region of the protrusion, the axial stress concentration on both sides is similar to the global model for Strategy A models, except for Strategy A Model 2 on the left side.

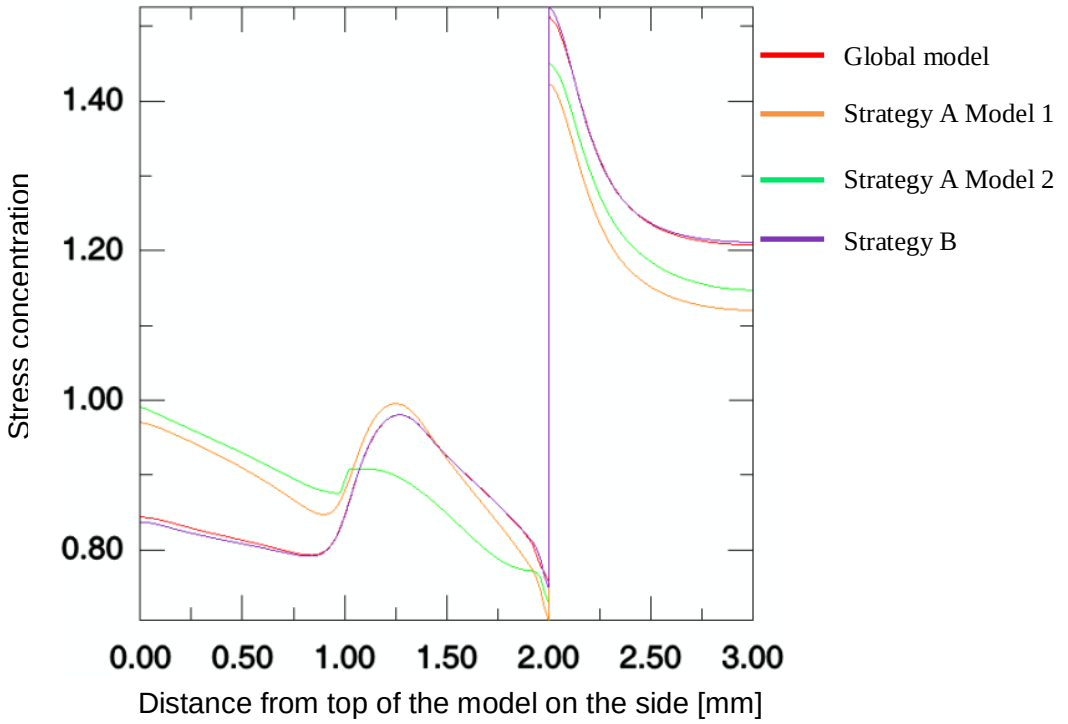

Fig.C.15 *Axial stress concentration on the left side of the end protrusion at 30 degrees for the global model and all the strategies*

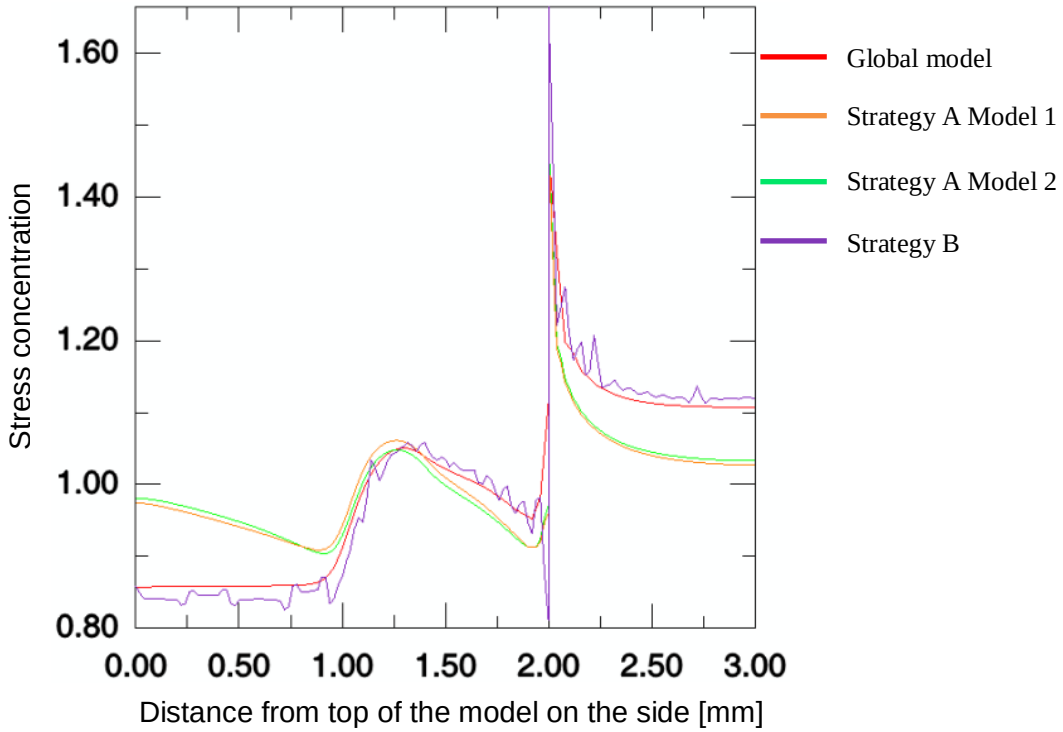

Fig.C.16 *Axial stress concentration on the right side of the end protrusion at 30 degrees for the global model and all the strategies*

Peel stress concentration on both sides were examined in Fig.C.17 and Fig.C.18. On the left side, before the joint step except for Strategy A Model 2, all other strategies were close to the global model result. When it reached the titanium alloy region, stress for Strategy A models have similar shapes compare with the global model, but show higher concentrations, whereas Strategy B shows lower concentrations with a similar shape. Stratey A Model 2 displays a very different stress concentration on the left side of the model. This is considered due to the homogenised composite region for simplification.

On the right side, Strategy A models show a reasonable agreement with the global model, whereas Strategy B shows much more variations. Again, these are considered to be caused by the loading on the right side of the model.

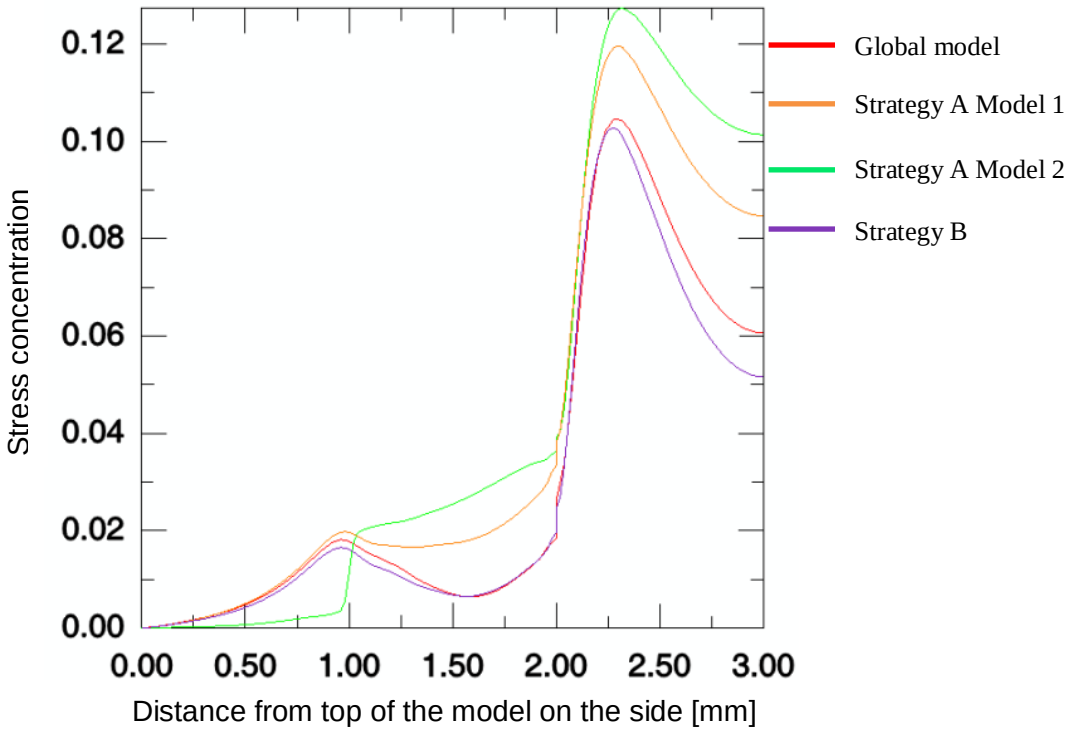

Fig.C.17 *Peel stress concentration on the left side of the end protrusion at 30 degrees for the global model and all the strategies*

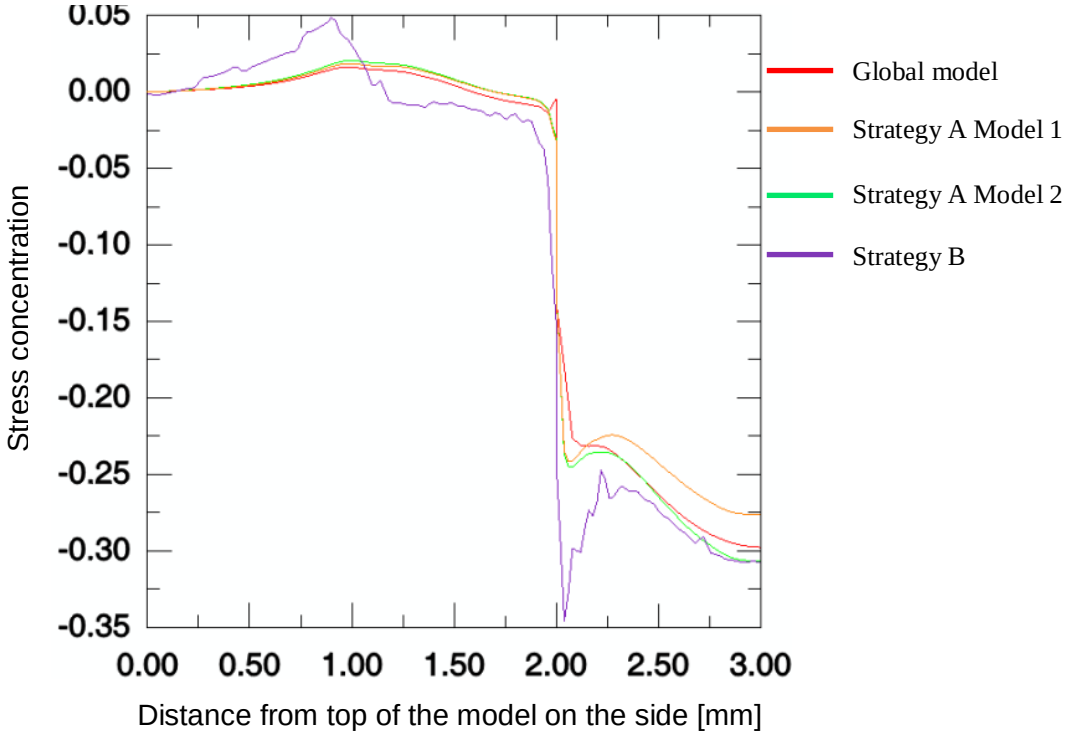

Fig.C.18 *Peel stress concentration on the right side of the end protrusion at 30 degrees for the global model and all the strategies*

Shear stress concentration on both left and right side is shown in Fig.C.19 and Fig.C.20. On the left side, Strategy A Model 2 shows a different response to the load. Strategy B shows a very close results with the global model end protrusion, and Strategy A Model 1shows a very good agreement with slight lower concentrations to the global model endprotrusion.

On the right side, Strategy B shows a very different stress profile compare with the global model results. Strategy A models show very good agreement with the global model, where the maximum concentration at around 2mm are both hgiher than the global model results.

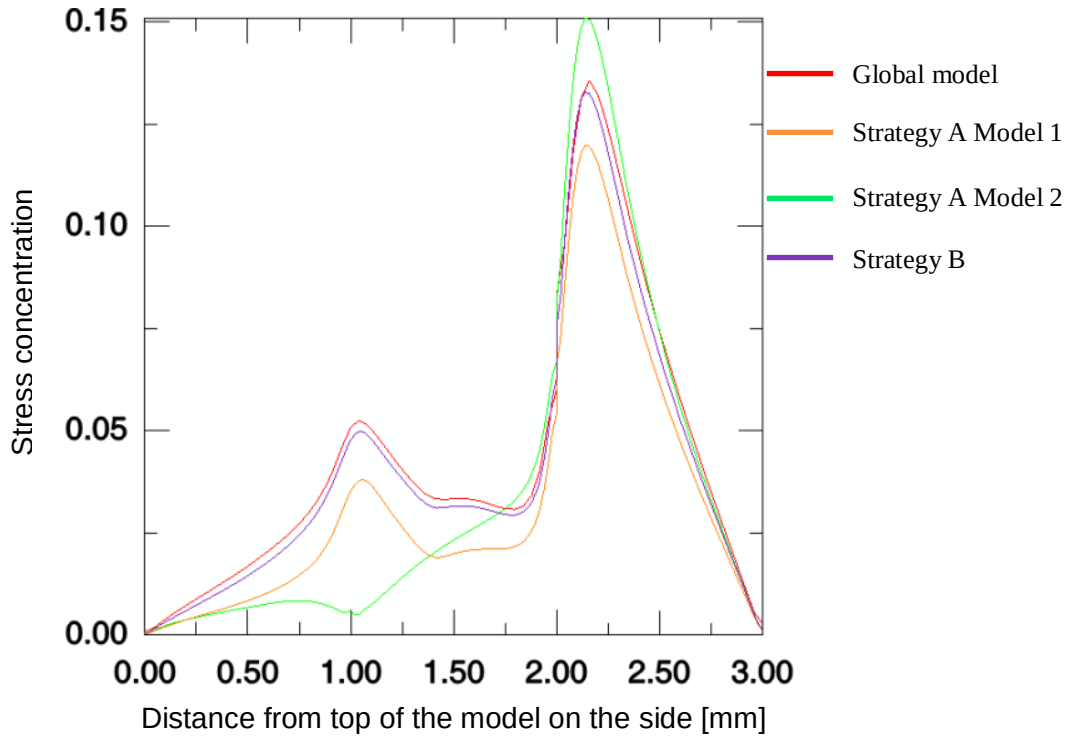

Fig.C.19 *Shear stress concentration on the left side of the end protrusion at 30 degrees for the global model and all the strategies*

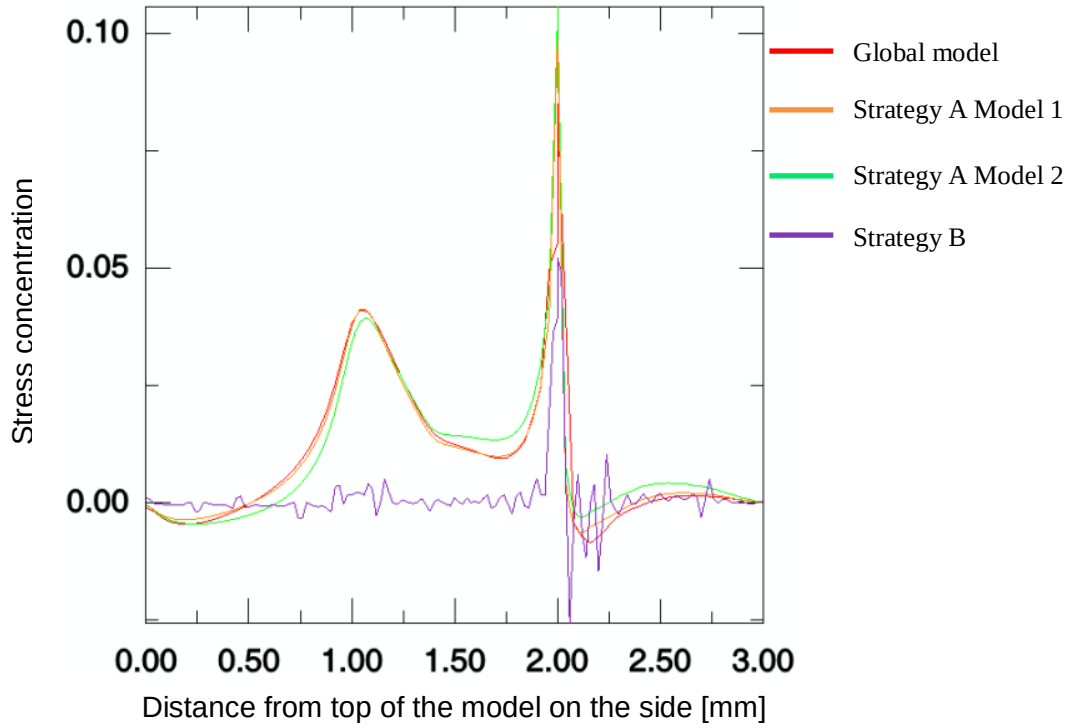

Fig.C.20 *Shear stress concentration on the right side of the end protrusion at 30 degrees for the global model and all the strategies*

APPENDIX D
2D analysis whole model results

Appendix D.1 Results for the repetitive protrusions

The effects of the geometric parameters including protrusion height, shape and angle were presented in this section.

D.1.1 Effect of the protrusion height

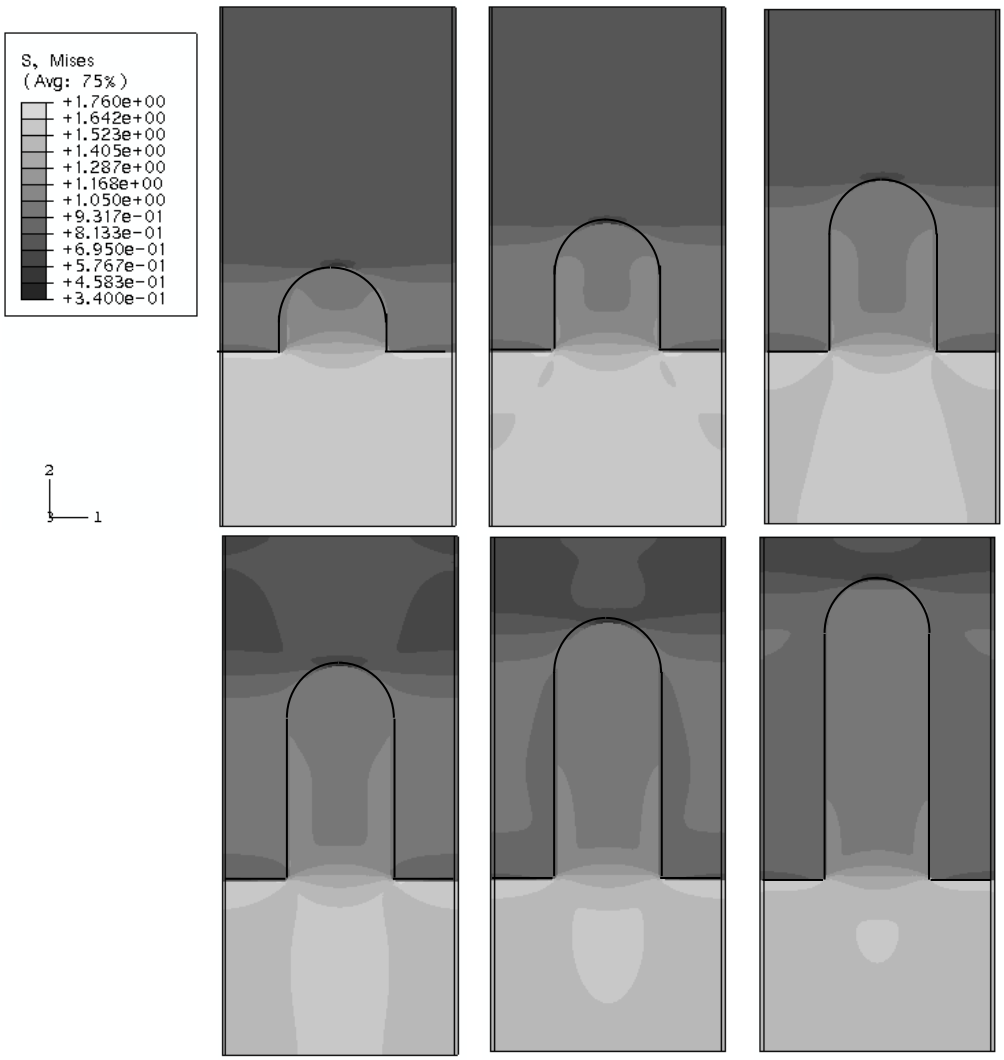

Fig.D.1 *Von Mises stress concentration contour results with different protrusion height*

The height of the protrusion was defined in Chapter 3, Fig.3.4. For the effects of the protrusion height, the cases of 0.50 mm to 1.75 mm with 0.25mm increments were analysed. The stress concentration contour results of the whole model are shown in figures, Fig.D.1 for the von Mises stress, Fig.D.2 for the axial stress, Fig.D.3 for the peel stress and Fig.D.4 for the shear stress.

For the von Mises stress, the stress concentration distributions are symmetric from left to right and the stress concentrated at the foot of the protrusions despite the height variation. The maximum stress concentrations are listed in Table.D.1. It is obvious that the stress concentration reduced with higher protrusion, and more even stress distribution across the whole model was observed for the higher protrusion unit cell model.

Table.D.1 *Maximum von Mises stress concentration with different protrusion heights*

Height [mm]	0.50	0.75	1.00	1.25	1.50	1.75
σ_m/σ	1.75e-0	1.70e-0	1.66e-0	1.63e-0	1.59e-0	1.57e-0

For the axial stress, it is similar to the case of the von Mises stress, see Fig.D.2.

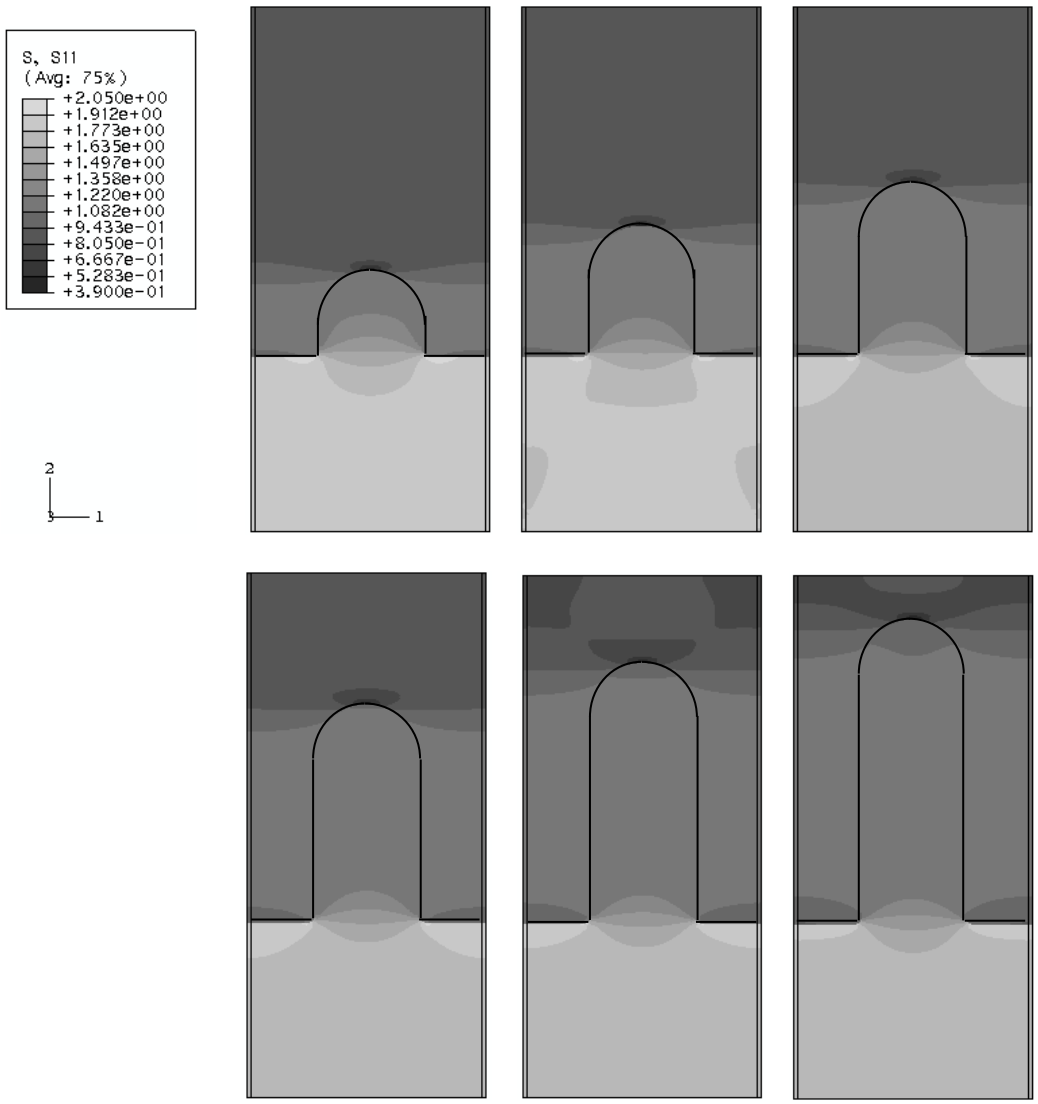

Fig.D.2 *Axial stress concentration contour results with different protrusion height*

The stress concentration distributions are symmetric from left to right and the maximum stress concentration occurs at the foot of the protrusions despite the height variation and the maximum stress concentrations are listed in Table.D.2.

Table.D.2 *Maximum axial stress concentration with different protrusion height*

Height [mm]	0.50	0.75	1.00	1.25	1.50	1.75
σ_{11}/σ	2.02e-0	1.96e-0	1.93e-0	1.88e-0	1.85e-0	1.81e-0

For the peel stress, maximum stress concentration occurs at the foot of the protrusions despite the protrusion height change, see Fig.D.3. The maximum stress concentrations are listed in Table.D.3.

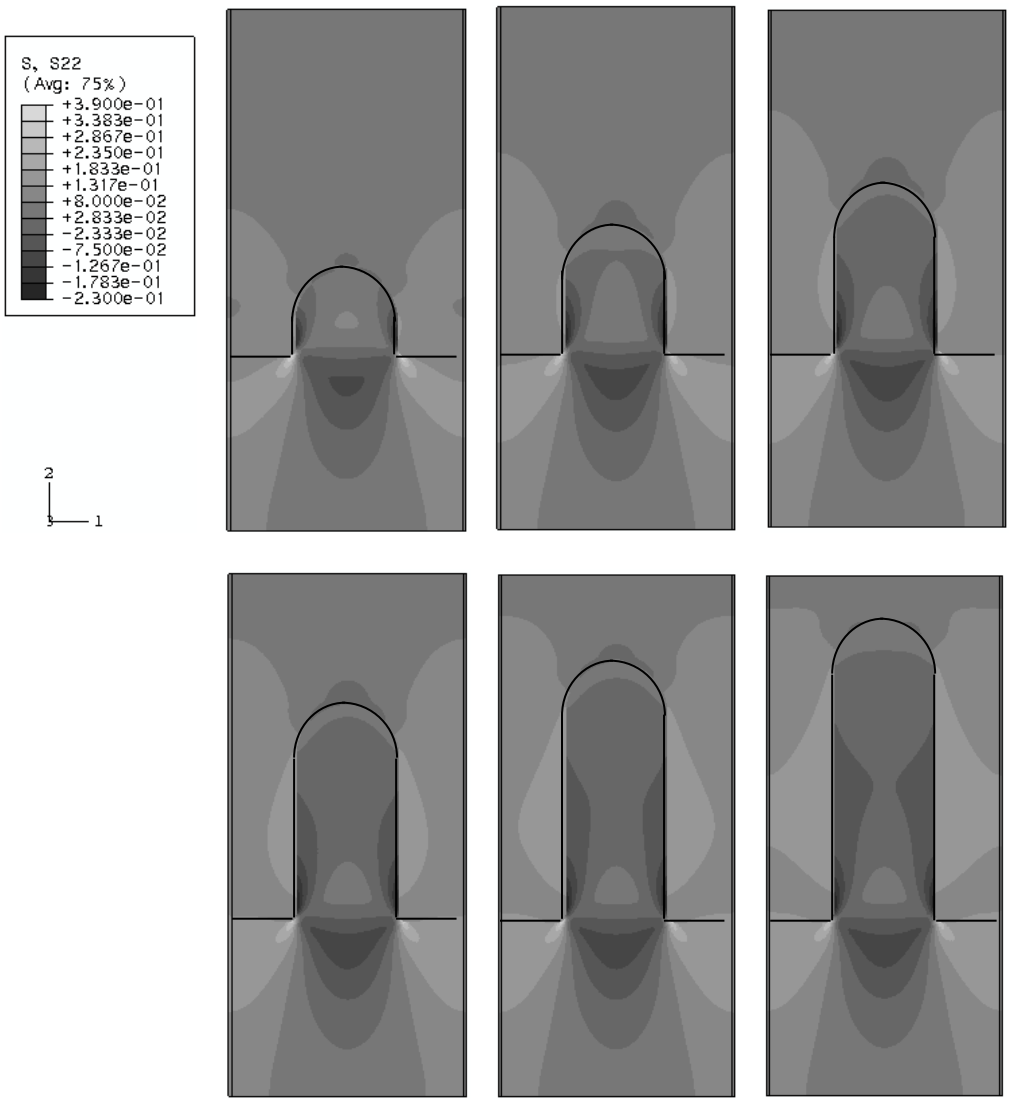

Fig.D.3 *Peel stress concentration contour results with different protrusion height*

Table.D.3 *Maximum peel stress concentration with different protrusion height*

Height [mm]	0.50	0.75	1.00	1.25	1.50	1.75
σ_{22}/σ	3.84e-1	3.31e-1	3.46e-1	3.04e-1	3.30e-1	2.94e-1

The maximum stress concentration various and there is not any obvious trend. For the stress distribution peel stress concentrated at the foot and the side of the protrusions and on the protrusion sides, the peel stress concentration region enlarges with the increase of the protrusion height. Inside the protrusion sides, compression can be

observed. This is due to the stiffness difference between the carbon fibre composite and the titanium alloy.

For the shear stress, the stress concentration contours for different height protrusion models are shown in Fig.D.4. The maximum stress concentrations are listed in Table.D.4.

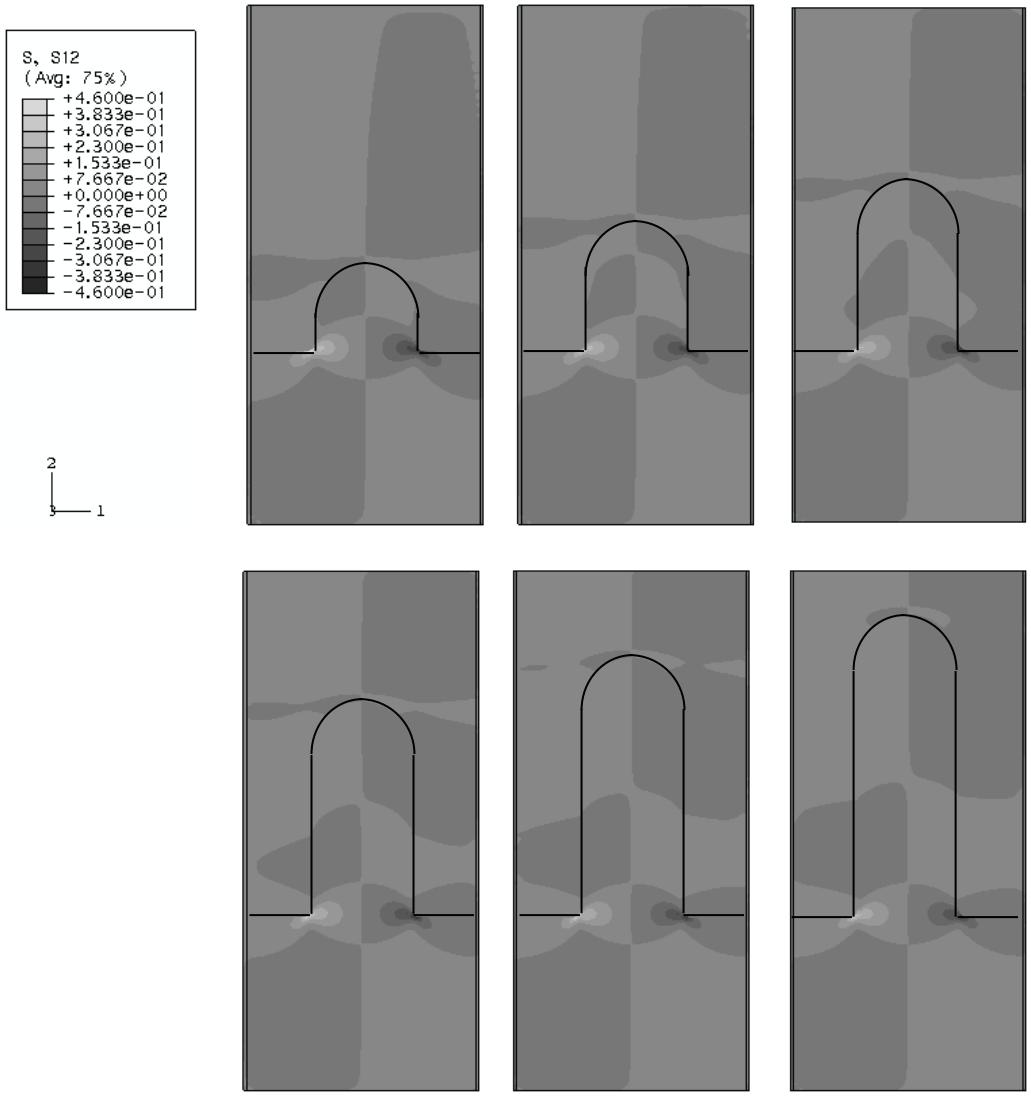

Fig.D.4 *Shear stress concentration contour results with different protrusion height*

The stress distributions are symmetric for the different height protrusion unit cell models. Maximum stress concentrations occur at the foot of the protrusions. The negative value in the contour results indicates change of directions for the shear stress.

The shortest protrusion model has the highest level of shear stress concentration at the foot of the protrusion.

Table.D.4 *Maximum shear stress concentration with different protrusion height*

Height [mm]	0.50	0.75	1.00	1.25	1.50	1.75
σ_{12}/σ	4.54e-1	4.33e-1	4.10e-1	4.04e-1	3.89e-1	3.83e-1

The maximum stress concentration oscillates with the increase of the protrusion height while the highest protrusion has lowest level of the maximum stress concentration. There is not any clear trend for the effects of protrusion height with the maximum stress concentration.

D.1.2 Effect of protrusion angle for the parallel shape protrusions

The angle of the protrusion was defined in Chapter 3, Fig.3.4. For the effects of the protrusion angle, the cases of -30 to 30 degrees with 10 degrees increments were analysed, where the minus angle stands for the protrusion leaning towards the left hand side, the titanium end of the joint, and vice versa. The stress concentration contour results of the whole model are shown in figures, Fig.D.5 for the von Mises stress, Fig.D.6 for the axial stress, Fig.D.7 for the peel stress and Fig.D.8 for the shear stress.

For the von Mises stress, the stress concentration distributions are symmetric for the same absolute protrusion angle and the stress concentrated at the foot of the protrusions despite the height variation marked with circles in Fig.D.5 and listed Table.D.5. For the perpendicular protrusion the stress distribution is symmetric and the maximum stress concentration occurs at the foot of the protrusion.

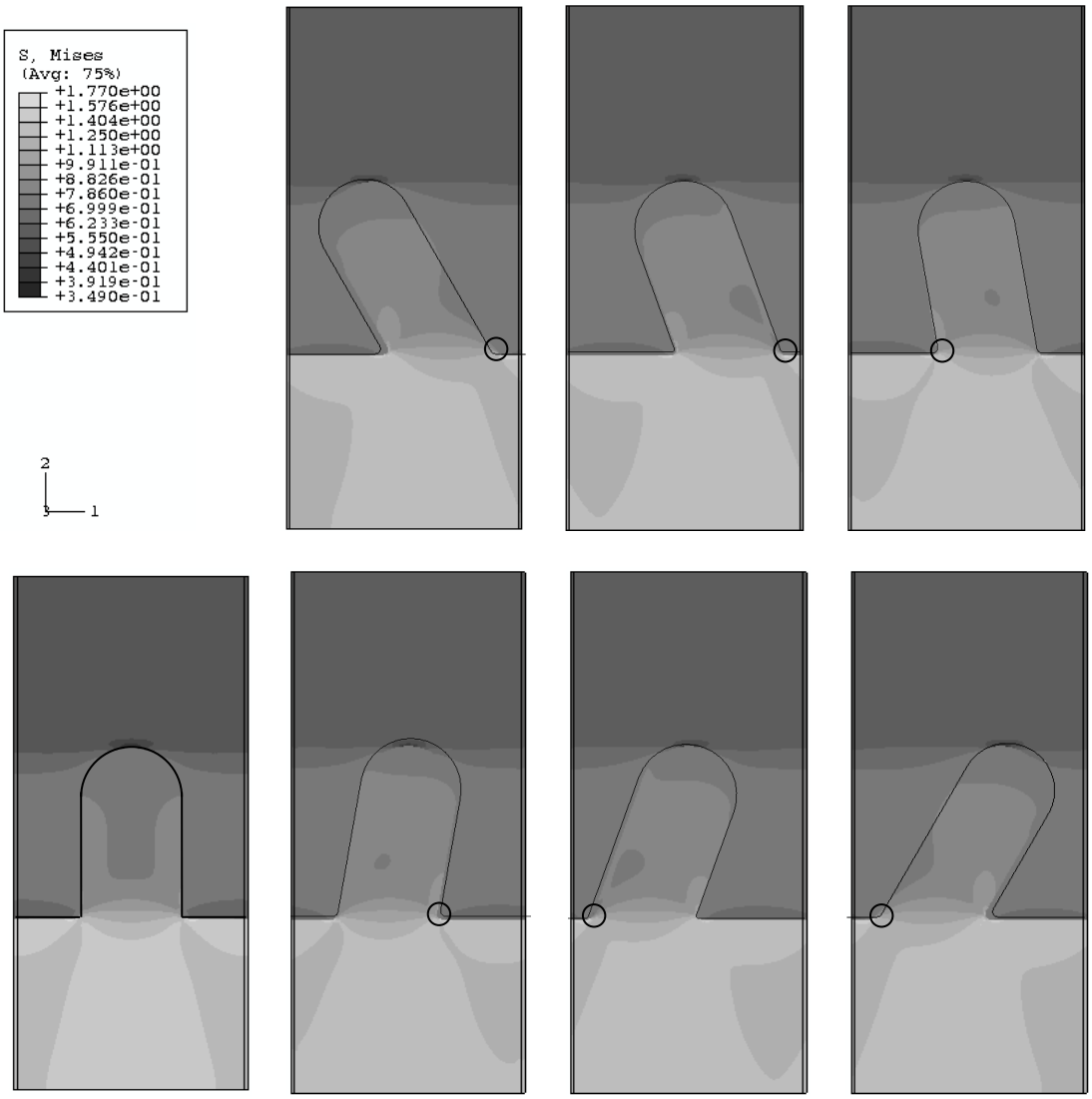

Fig.D.5 *Von Mises stress concentration contour results with different protrusion angle*

Table.D.5 *Maximum von Mises stress concentration with different protrusion angle*

Angle [°]	-30	-20	-10	0	10	20	30
σ_m/σ	1.77e-0	1.74e-0	1.65e-0	1.67e-0	1.65e-0	1.74e-0	1.77e-0

In Fig.4.12, the maximum von Mises stress concentration for the protrusion angle reduces from minus 30 degrees to minus 10 degrees and increase for the perpendicular protrusion.

Similarly for the axial and peel stress, see Fig.D.6 and Fig.D.7, the stress distributions are symmetric for the same absolute protrusion angle, and this is also true for the location of the maximum stress concentration; for the perpendicular protrusion, the

stress distribution is symmetric and maximum stress concentration occurs at the foot of the protrusion. The maximum stress concentrations are listed in Table.D.6 and Table.D.7 for the axial and peel stress. The effect of the protrusion angle on the maximum stress concentration is similar to the von Mises case despite lower or equal stress concentration for the perpendicular protrusion.

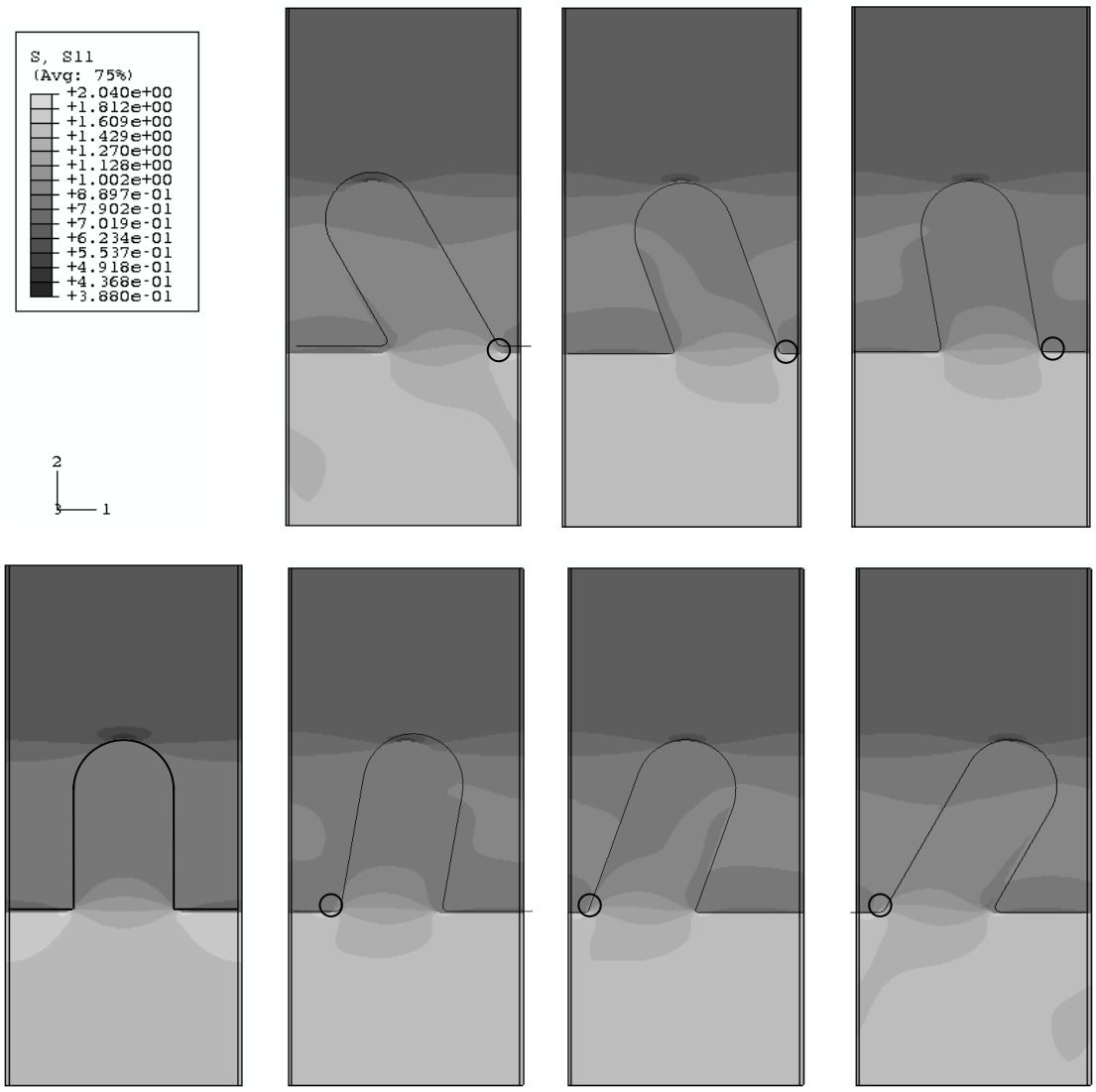

Fig.D.6 *Axial stress concentration contour results with different protrusion angle*

Table.D.6 *Maximum axial stress concentration with different protrusion angle*

Angle [°]	-30	-20	-10	0	10	20	30
σ_{11}/σ	2.04e-0	2.01e-0	1.95e-0	1.95e-0	1.95e-0	2.01e-0	2.04e-0

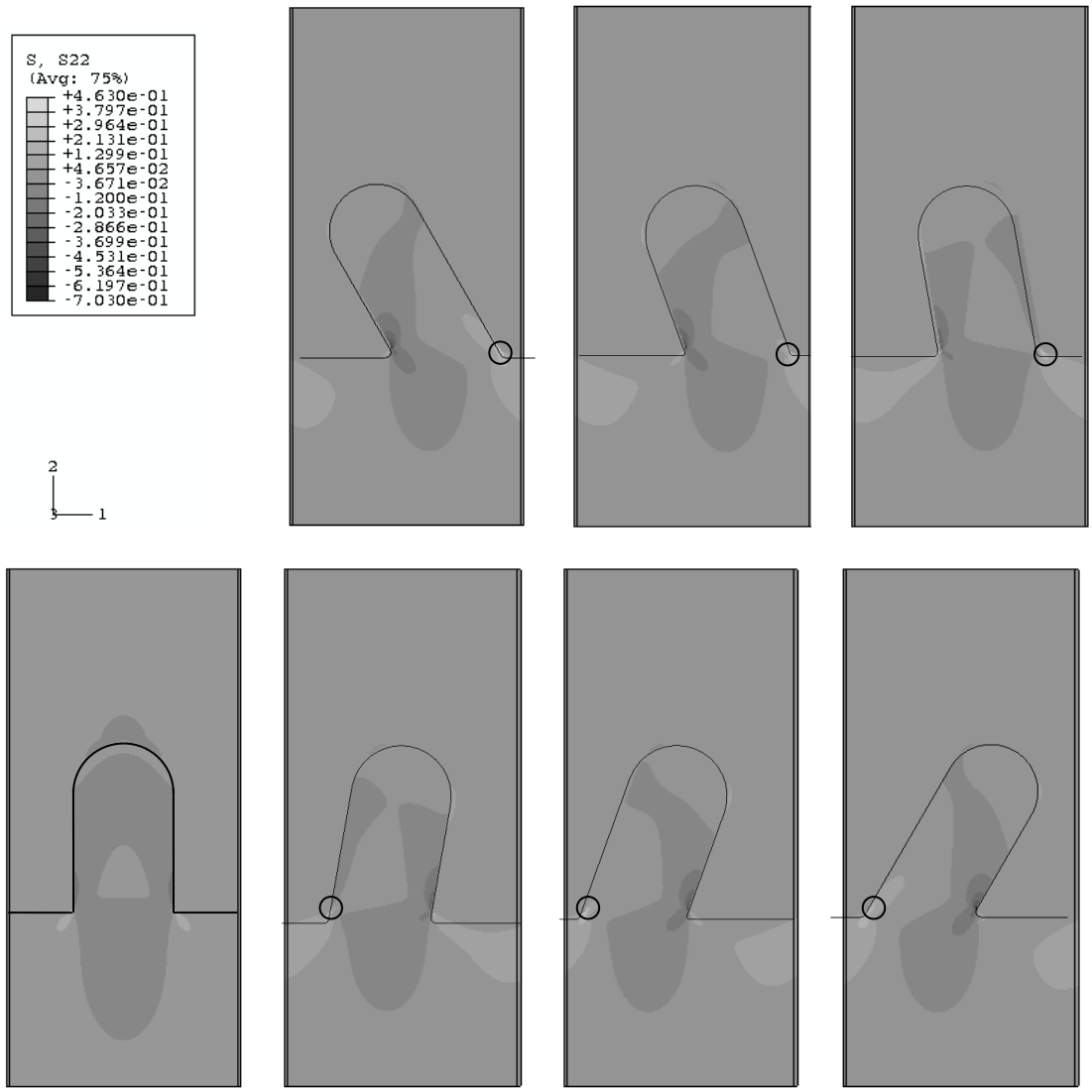

Fig.D.7 *Peel stress concentration contour results with different protrusion angle*

Table.D.7 *Maximum peel stress concentration with different protrusion angle*

Angle [°]	-30	-20	-10	0	10	20	30
σ_{22}/σ	4.63e-1	4.01e-1	3.50e-1	3.25e-1	3.50e-1	4.01e-1	4.63e-1

In Fig.D.8, for the shear stress concentration, negative value indicates the change of direction. Therefore, the stress distribution is symmetric for the same absolute protrusion angle with opposite directions. The trend for the maximum stress concentration is similar to the von Mises case, see Table.D.8.

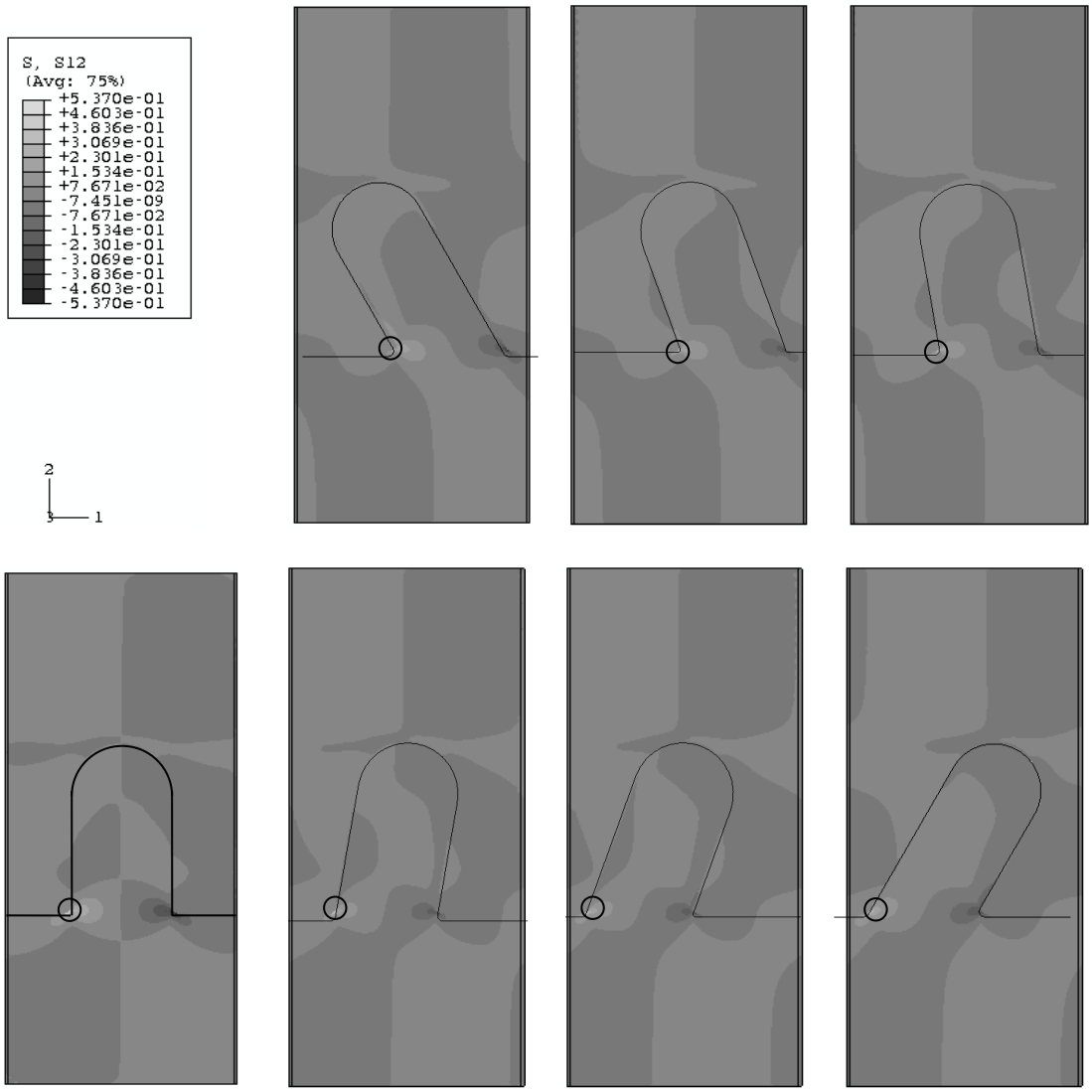

Fig.D.8 *Shear stress concentration contour results with different protrusion angle*

Table.D.8 *Maximum shear stress concentration with different protrusion angle*

Angle [°]	-30	-20	-10	0	10	20	30
σ_{12}/σ	5.37e-1	5.35e-1	4.02e-1	4.11e-1	4.02e-1	5.35e-1	5.37e-1

D.1.3 Effect of protrusion angle for the hill shape protrusions

The angle of the hill protrusion was defined in Fig.3.4. For the effects of the protrusion angle, the stress concentration contour results of the whole model were shown in figures, Fig.D.9 for the von Mises stress, Fig.D.10 for the axial stress, Fig.D.11 for the peel stress and Fig.D.12 for the shear stress.

For the whole model the stress concentration of von Mises stress, axial stress, peel stress and shear stress, the situation is similar to the parallel shape protrusions. The maximum stress concentrations for the hill shape protrusions cover a wider range than the parallel shape protrusions. And this is also true for the locations of maximum stress concentration and the angle effect for the whole model, also see Table.D.9, D.10, D.11 and D.12.

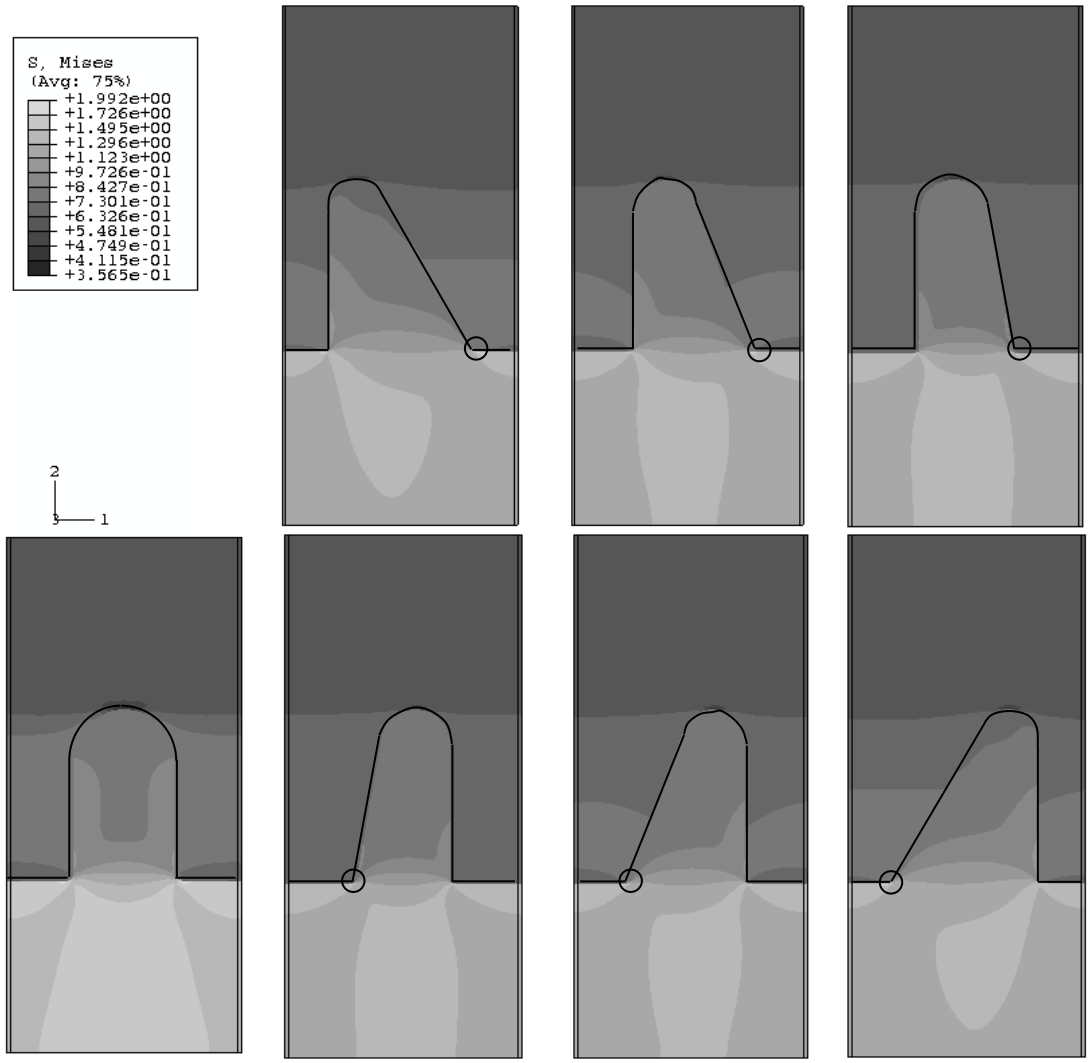

Fig.D.9 *Von Mises stress concentration contour results with different protrusion angle*

Table.D.9 *Maximum von Mises stress concentration with different protrusion angle*

Angle [°]	-30	-20	-10	0	10	20	30
σ_m/σ	1.99e-0	1.89e-0	1.77e-0	1.67e-0	1.77e-0	1.89e-0	1.99e-0

In the case of axial, peel and shear stress concentrations, the situation is similar to the parallel shape protrusions.

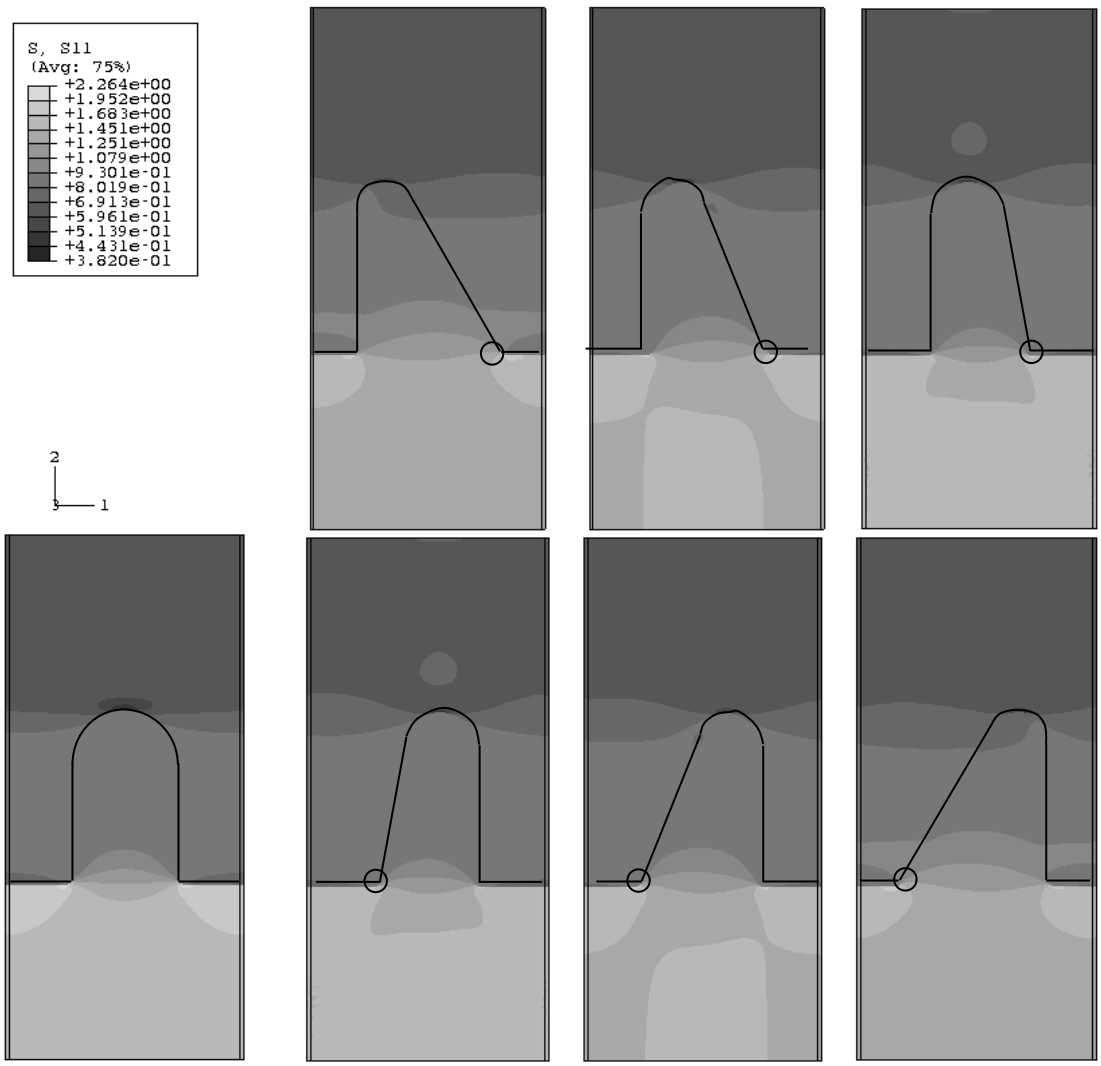

Fig.D.10 *Axial stress concentration contour results with different protrusion angle*

Table.D.10 *Axial stress concentration with different protrusion angle*

Angle [°]	-30	-20	-10	0	10	20	30
σ_{11}/σ	2.26e-0	2.15e-0	2.03e-0	1.95e-0	2.03e-0	2.15e-0	2.26e-0

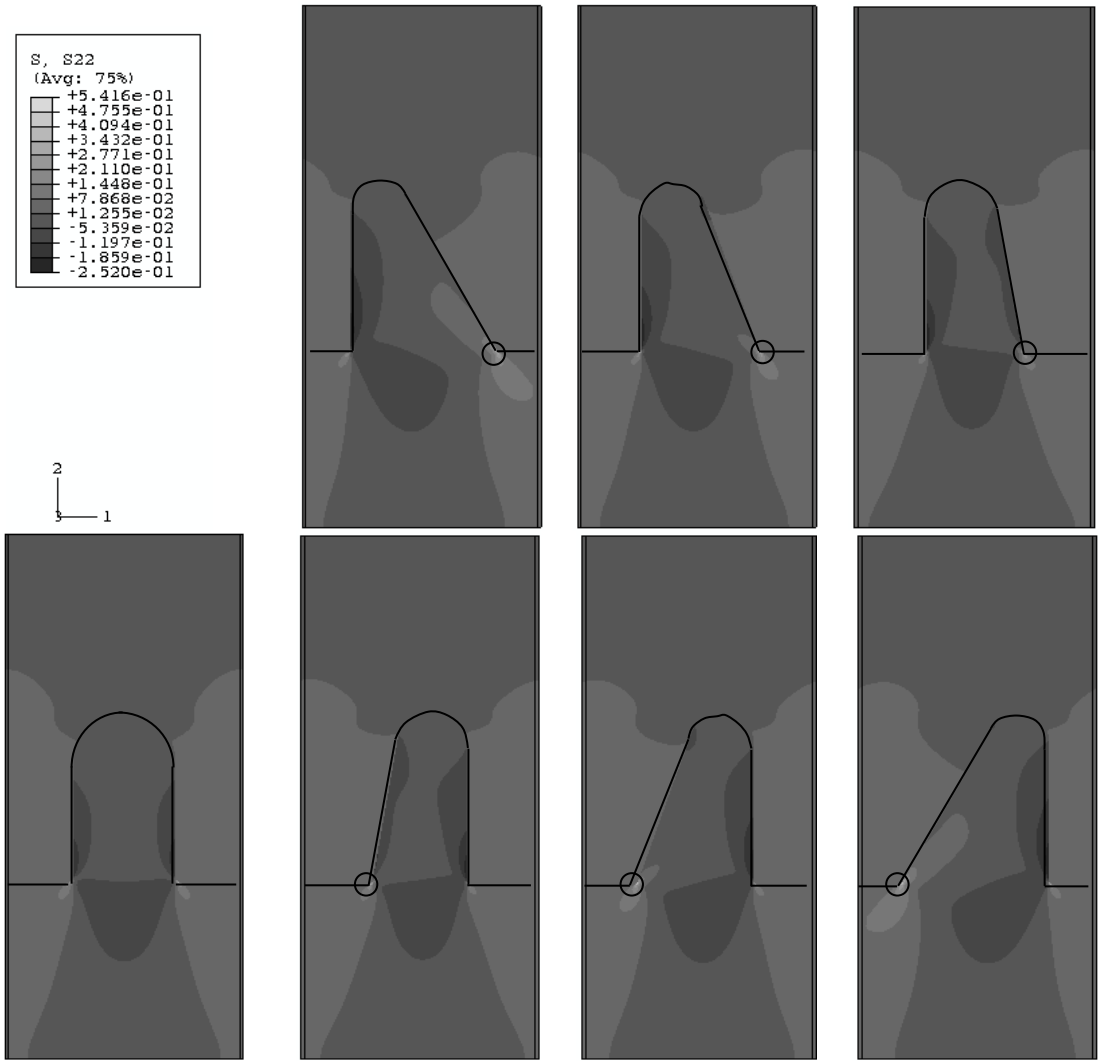

Fig.D.11 *Peel stress concentration contour results with different protrusion angle*

Table.D.11 *Peel stress concentration with different protrusion angle*

Angle [°]	-30	-20	-10	0	10	20	30
σ_{22}/σ	5.42e-1	5.18e-1	4.07e-1	3.25e-1	4.07e-1	5.18e-1	5.42e-1

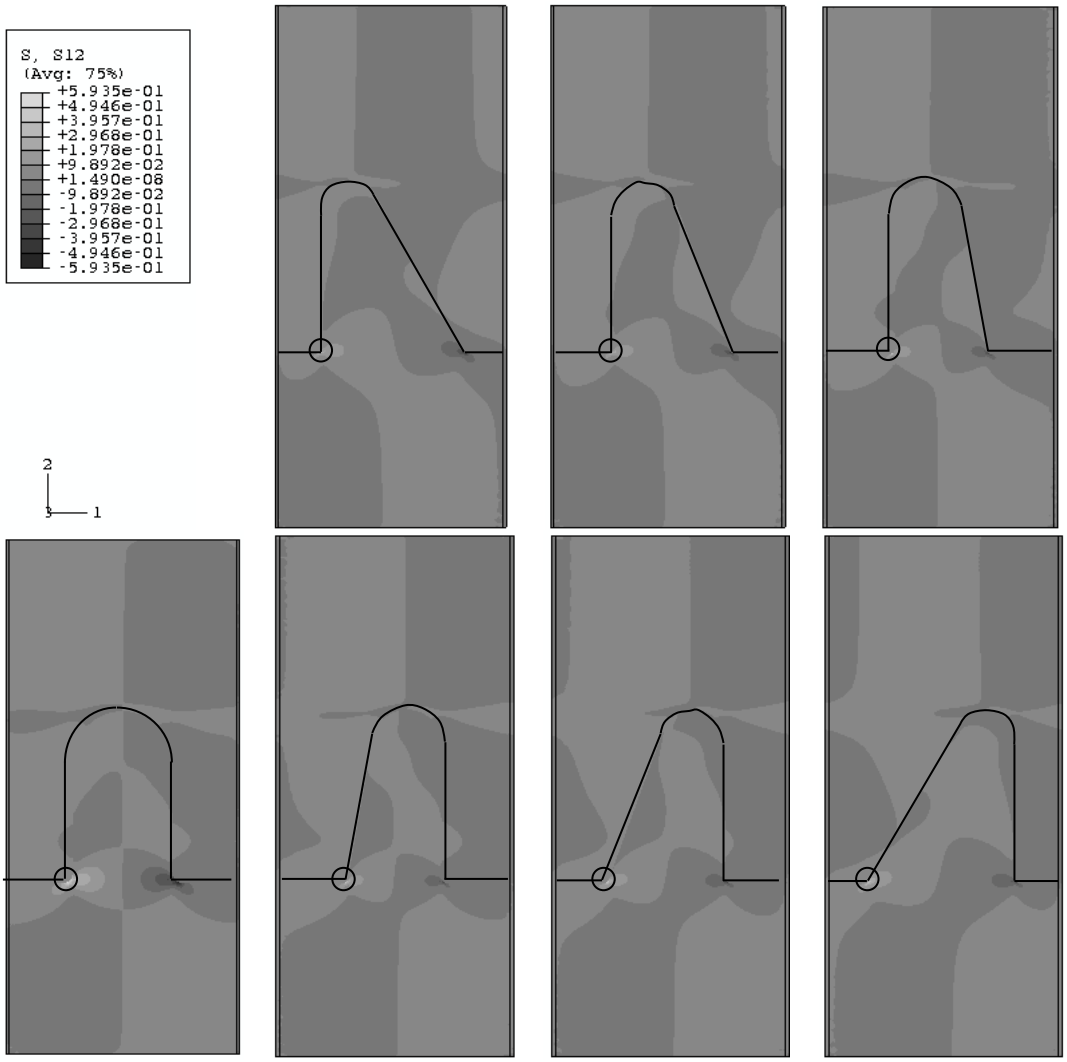

Fig.D.12 *Shear stress concentration contour results with different protrusion angle*

Table.D.12 *Shear stress concentration with different protrusion angle*

Angle [°]	-30	-20	-10	0	10	20	30
σ_{12}/σ	5.94e-1	5.74e-1	4.86e-1	4.11e-1	4.86e-1	5.74e-1	5.94e-1

Appendix D.2 Results for the protrusions on the joint step edge

The effects of the geometric parameters including protrusion height, shape and angle are presented in this section for the protrusions on the joint step edge. The model design can be found in Chapter 3, section 3.3.

D.2.1 Effect of the protrusion height

For the effects of the protrusion height, the cases of 0.50mm to 1.75mm with 0.25mm increments were analysed. The stress concentration contour results of the whole model are presented in figures, Fig.D.13, D.14, D.15 and D.16 for the von Mises stress, axial stress, peel stress and shear stress respectively.

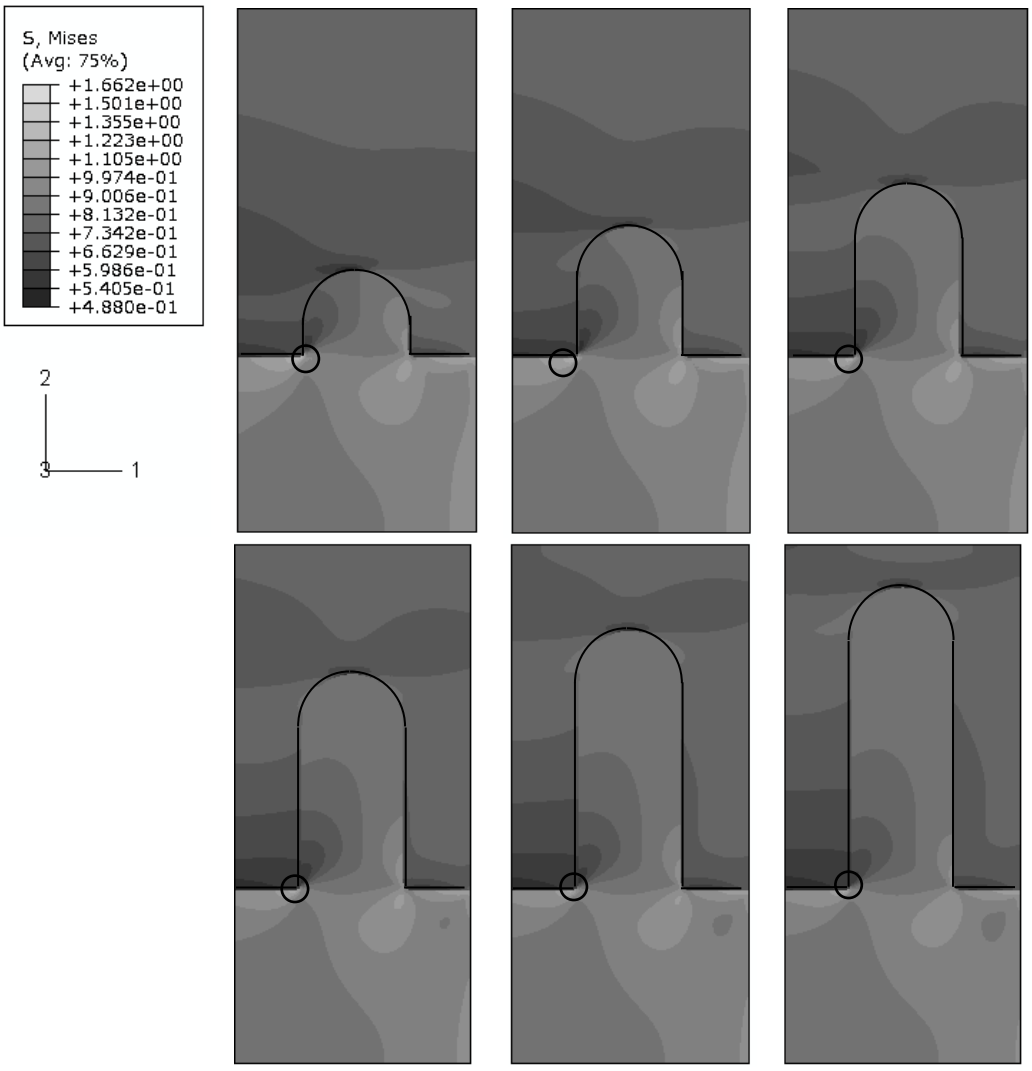

Fig.D.13 *Von Mises stress concentration contour results with different protrusion height*

For the von Mises stress, the stress concentration distributions are not symmetric from left to right. The maximum stress concentration occurs at the left foot of the protrusions, marked with circles and listed in Table.D.13. The stress concentrated at the foot of the protrusions, and the concentrated stress was spread into the composite

region due to the protrusion height change. For the maximum stress concentration, the general trend is the decrease of the maximum stress concentration with the increase of the protrusion height.

Table.D.13 *Maximum von Mises stress concentration with different protrusion heights*

Height [mm]	0.50	0.75	1.00	1.25	1.50	1.75
σ_m/σ	1.66e-0	1.57e-0	1.47e-0	1.48e-0	1.42e-0	1.43e-0

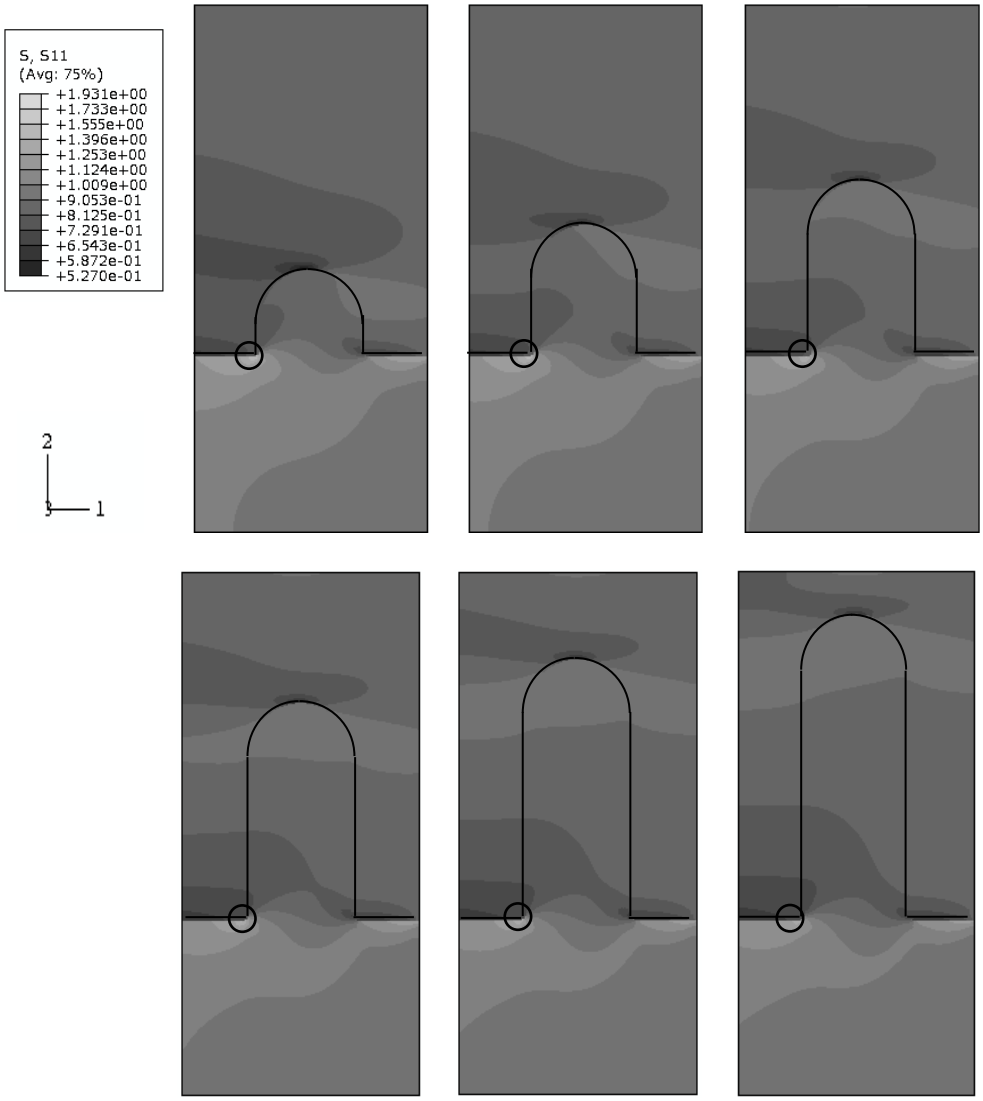

Fig.D.14 *Axial stress concentration contour results with different protrusion height*

Very similarly, for the axial stress, peel stress and shear stress, the stress concentration distributions were spread into the composite region along with the

increase of the protrusion height, the maximum stress concentration occurs at the left foot of the protrusion, and the maximum stress concentration reduced with the increase of the protrusion height, see Fig.D.14 to D.16 and Table.D.14 to D.16.

Table.D.14 *Maximum axial stress concentration with different protrusion height*

Height [mm]	0.5	0.75	1.0	1.25	1.5	1.75
σ_{11}/σ	1.93e-0	1.85e-0	1.77e-0	1.74e-0	1.69e-0	1.68e-0

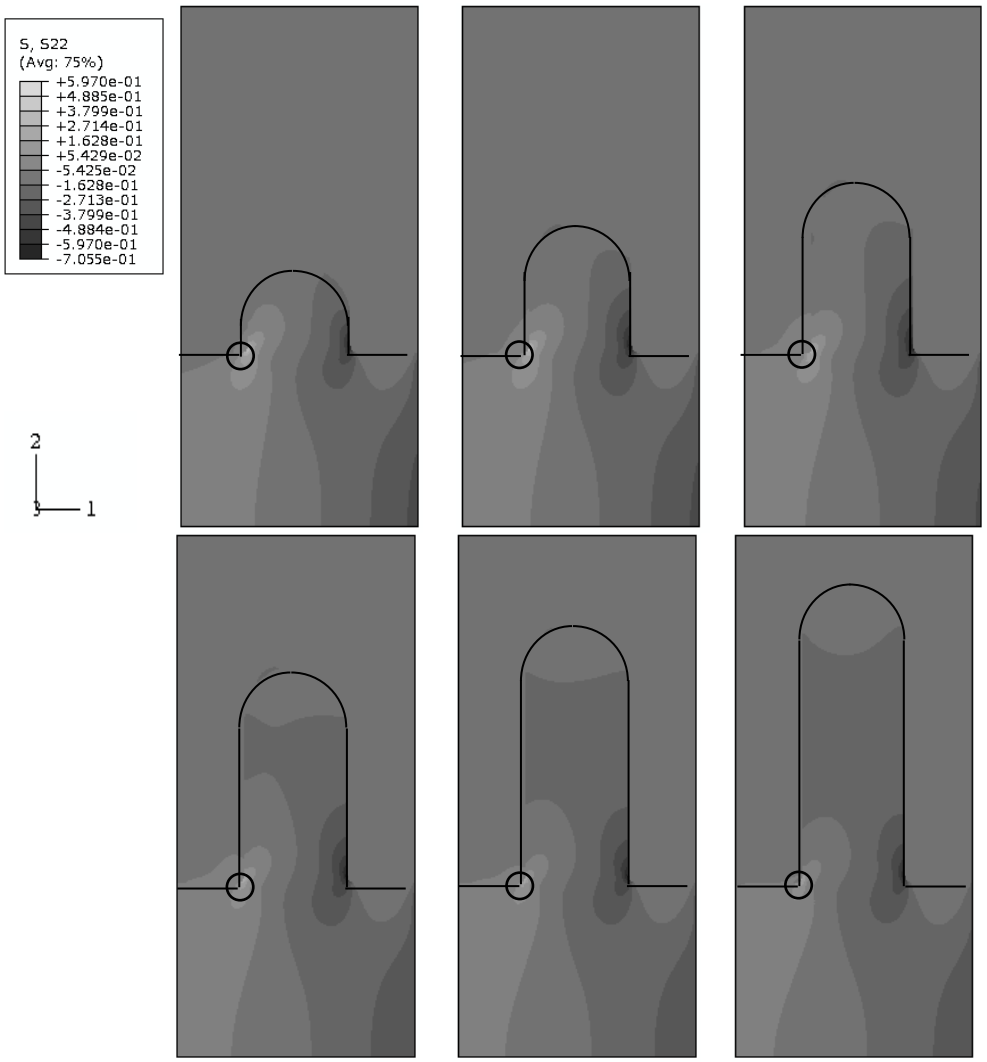

Fig.D.15 *Peel stress concentration contour results with different protrusion height*

Table.D.15 *Maximum peel stress concentration with different protrusion height*

Height [mm]	0.5	0.75	1.0	1.25	1.5	1.75
σ_{22}/σ	5.967e-1	5.864e-1	5.052e-1	4.773e-1	4.627e-1	3.981e-1

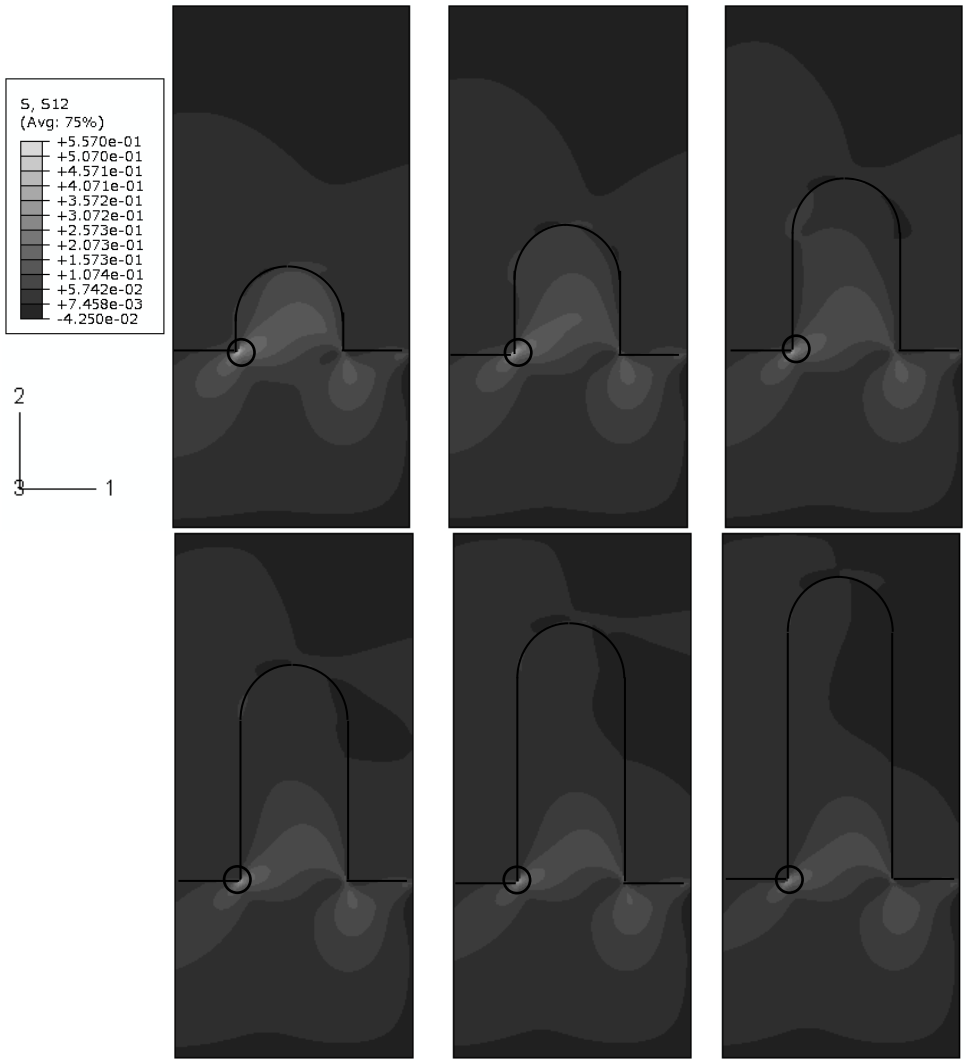

Fig.D.16 *Shear stress concentration contour results with different protrusion height*

Table.D.16 *Maximum shear stress concentration with different protrusion height*

Height [mm]	0.5	0.75	1.0	1.25	1.5	1.75
σ_{12}/σ	5.568e-1	4.997e-1	4.247e-1	4.313e-1	4.227e-1	3.865e-1

To summarise for the von Mises, axial, peel, and shear stress for the whole end protrusion region, the maximum stress concentration in the titanium at the bottom of the protrusion decreases with higher protrusion.

D.2.2 Effect of protrusion angle for the parallel shape protrusions

For the effects of the protrusion angle, the cases of -30 to 30 degrees with 10 degrees increments were analysed, where the minus angle stands for the protrusion leaning towards the metal end of the joint. The stress concentration contour results of the whole model were shown in figures, Fig.D.17 for the von Mises stress, Fig.D.18 for the axial stress, Fig.D.19 for the peel stress and Fig.D.20 for the shear stress.

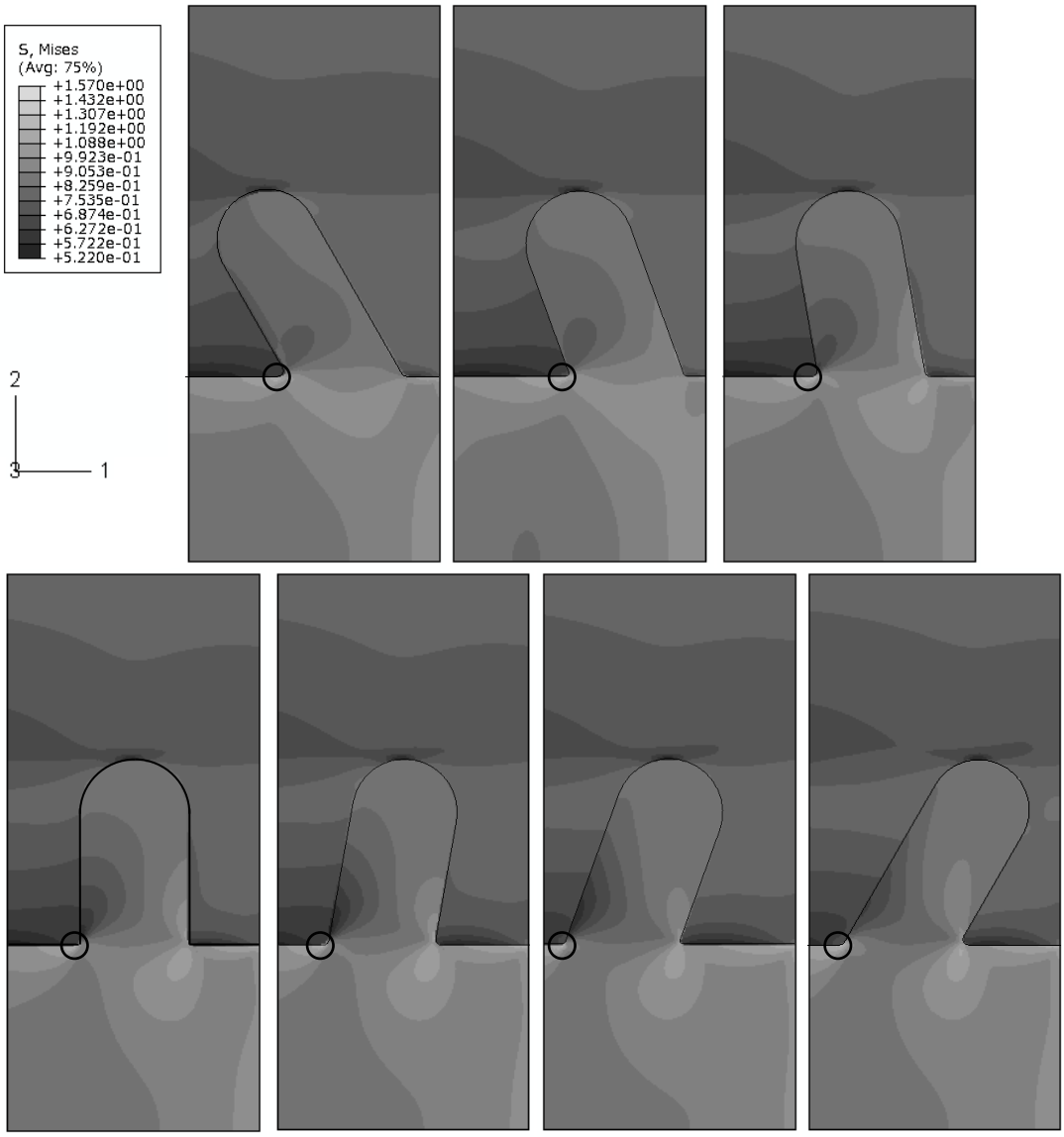

Fig.D.17 *Von Mises stress concentration contour results with different protrusion angle*

Table.D.17 *Maximum von Mises stress concentration with different protrusion angle*

Angle [°]	-30	-20	-10	0	10	20	30
σ_m/σ	1.45e-0	1.57e-0	1.58e-0	1.47e-0	1.52e-0	1.56e-0	1.56e-0

In Fig.D.17, stress distribution does not change dramatically for the top of the protrusion composite region or for the maximum stress concentrations occurred at the bottom of the protrusions within the titanium despite the protrusion angle. The maximum stress concentrations are listed in Table.D.17

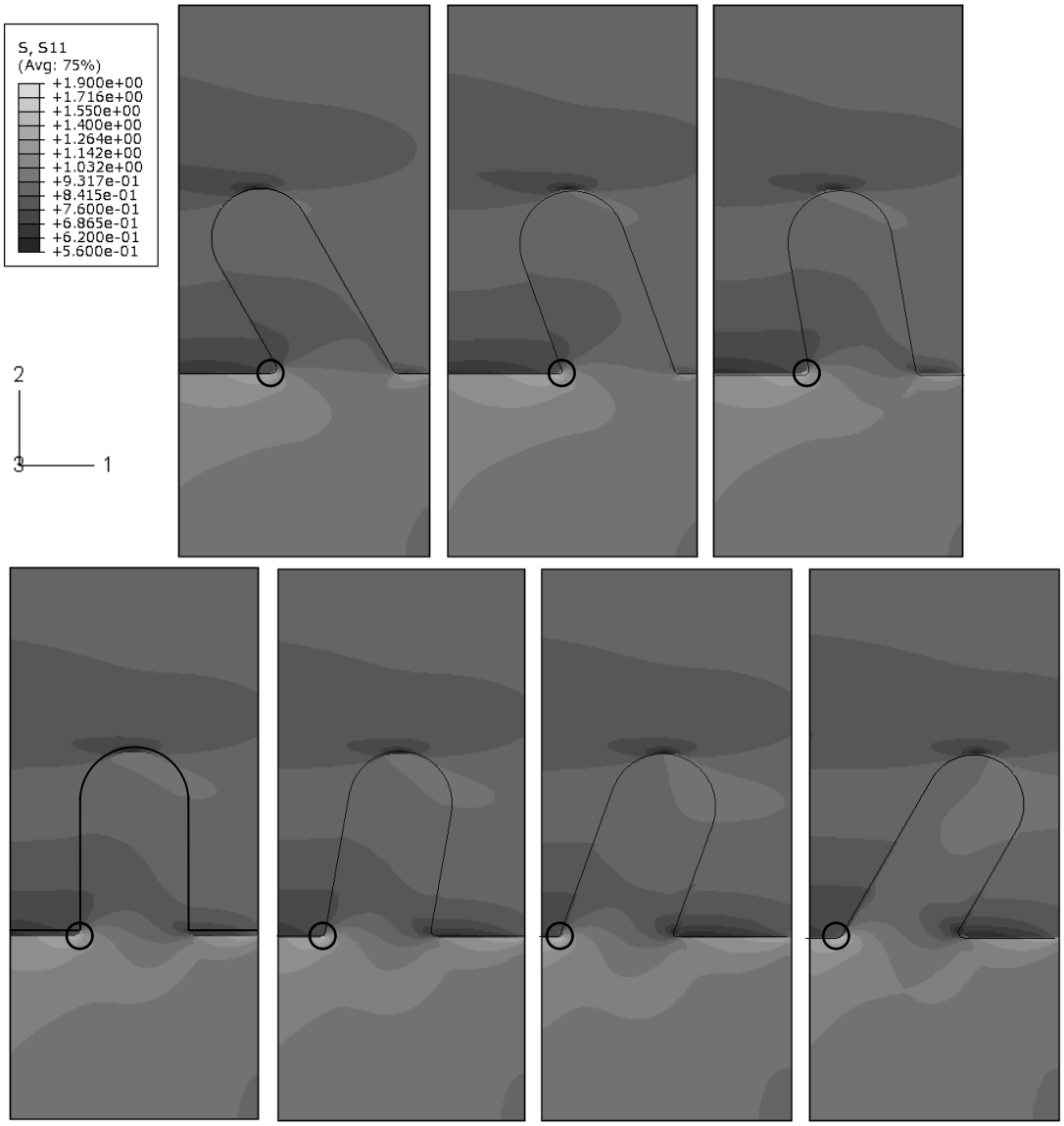

Fig.D.18 *Axial stress concentration contour results with different protrusion angle*

Table.D.18 *Maximum axial stress concentration with different protrusion angle*

Angle [°]	-30	-20	-10	0	10	20	30
σ_{11}/σ	1.71e-0	1.87e-0	1.86e-0	1.77e-0	1.86e-0	1.88e-0	1.86e-0

Similarly for the axial stress, generally, stress distributions are similar for different protrusion angle, as well as the maximum stress concentrations in the titanium at the bottom of protrusions, see Table.D.18.

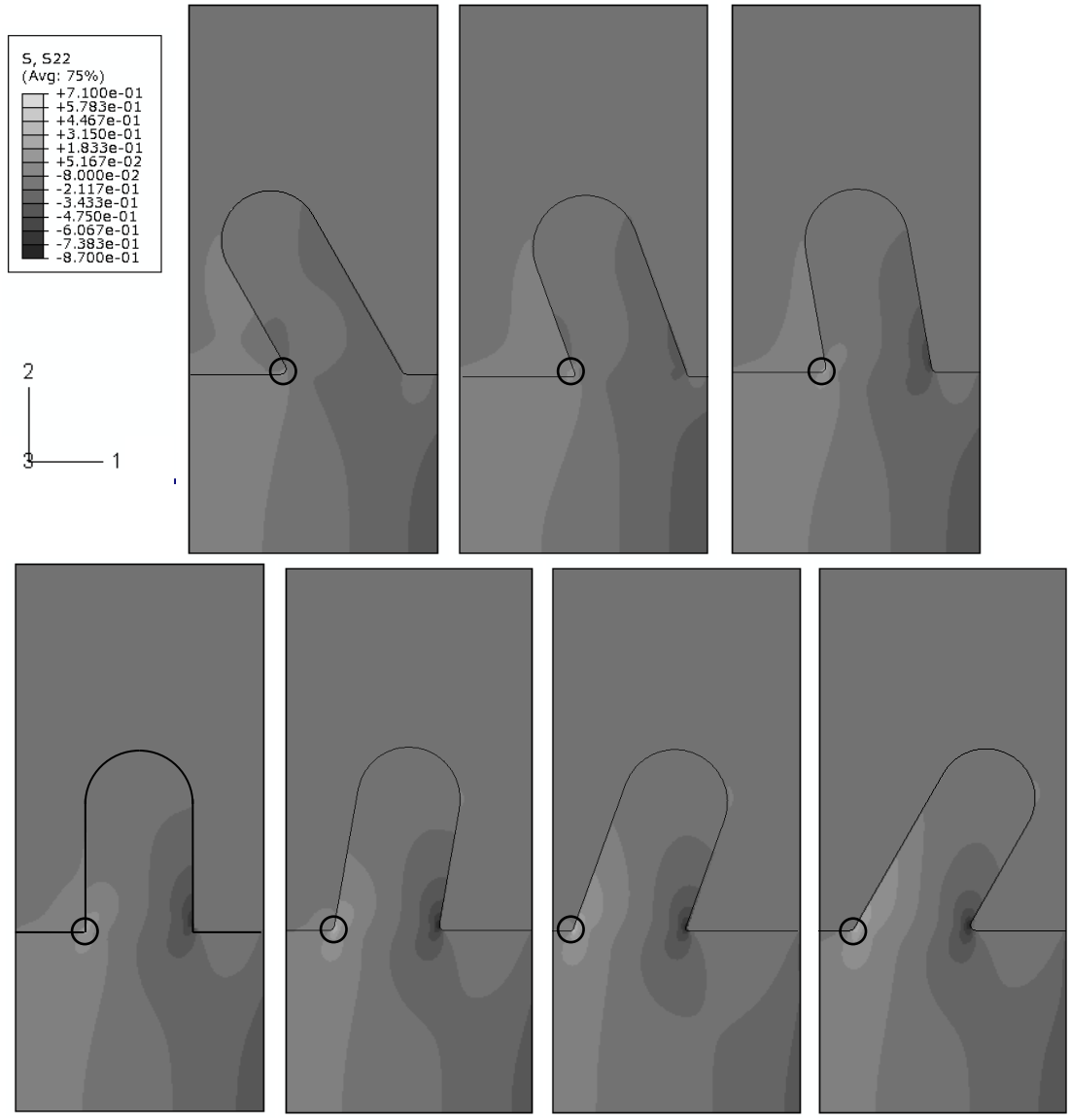

Fig.D.19 *Peel stress concentration contour results with different protrusion angle*

Table.D.19 *Maximum peel stress concentration with different protrusion angle*

Angle [°]	-30	-20	-10	0	10	20	30
σ_{22}/σ	2.22e-1	3.59e-1	4.79e-1	5.05e-1	6.53e-1	7.01e-1	5.71e-1

For the peel stress, generally, stress distributions are similar for different protrusion angle. The maximum stress concentration varies in the titanium at the bottom of protrusions, see Table.D.19.

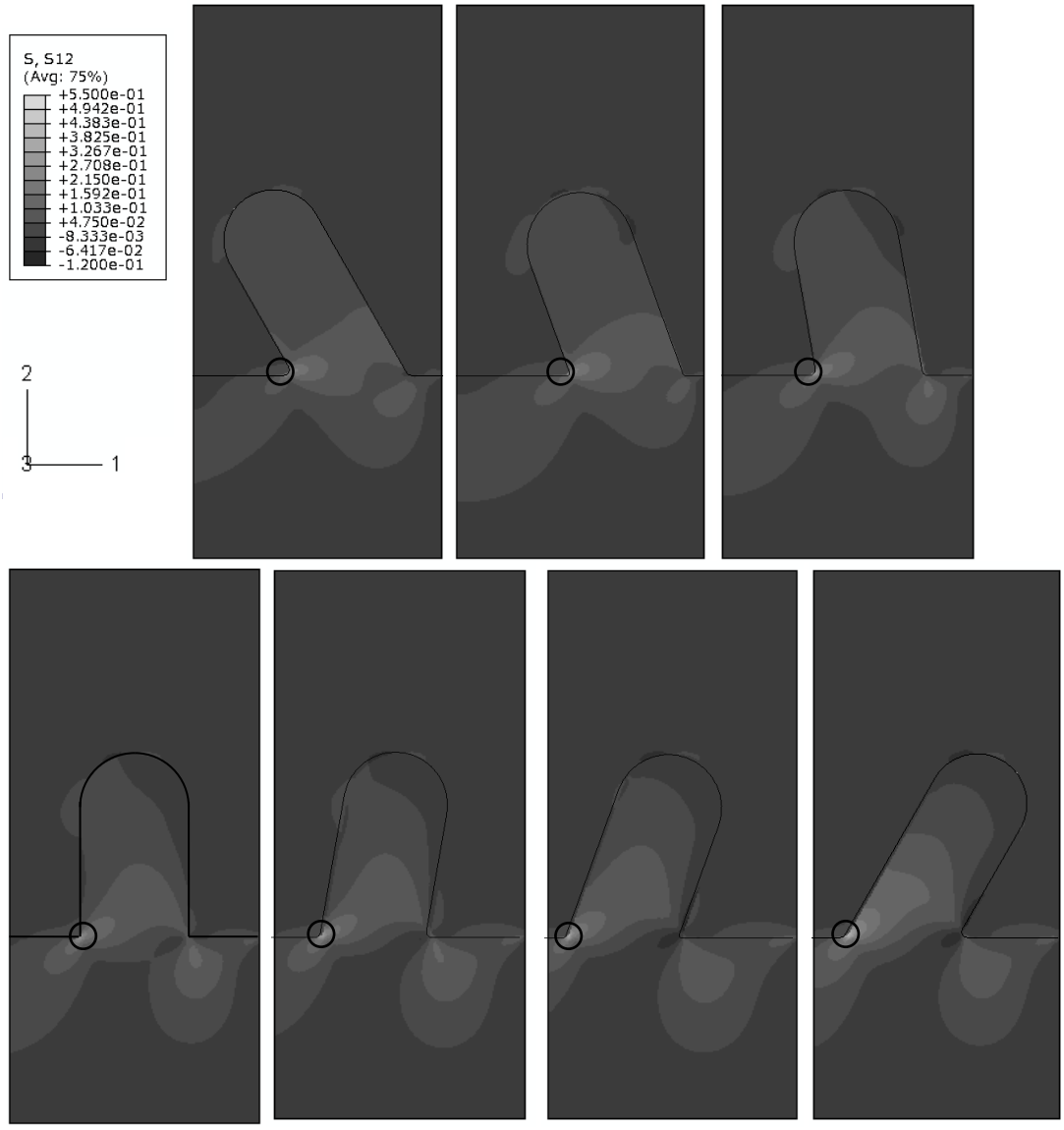

Fig.D.20 *Shear stress concentration contour results with different protrusion angle*

Table.D.20 *Maximum shear stress concentration with different protrusion angle*

Angle [°]	-30	-20	-10	0	10	20	30
σ_{12}/σ	2.92e-1	3.67e-1	4.59e-1	4.25e-1	4.80e-1	5.18e-1	5.41e-1

For the shear stress, generally, stress distributions are similar for different protrusion angle. The maximum stress concentration increases for the angle from minus to positive in the titanium at the bottom of protrusions, see Table.D.20.

To summarise, the stress concentrations are similar for all the protrusion angles; for the minus 30 degree protrusion angle, the maximum stress concentration is the lowest for all the contour results.

D.2.3 Effect of protrusion angle for the hill shape protrusions

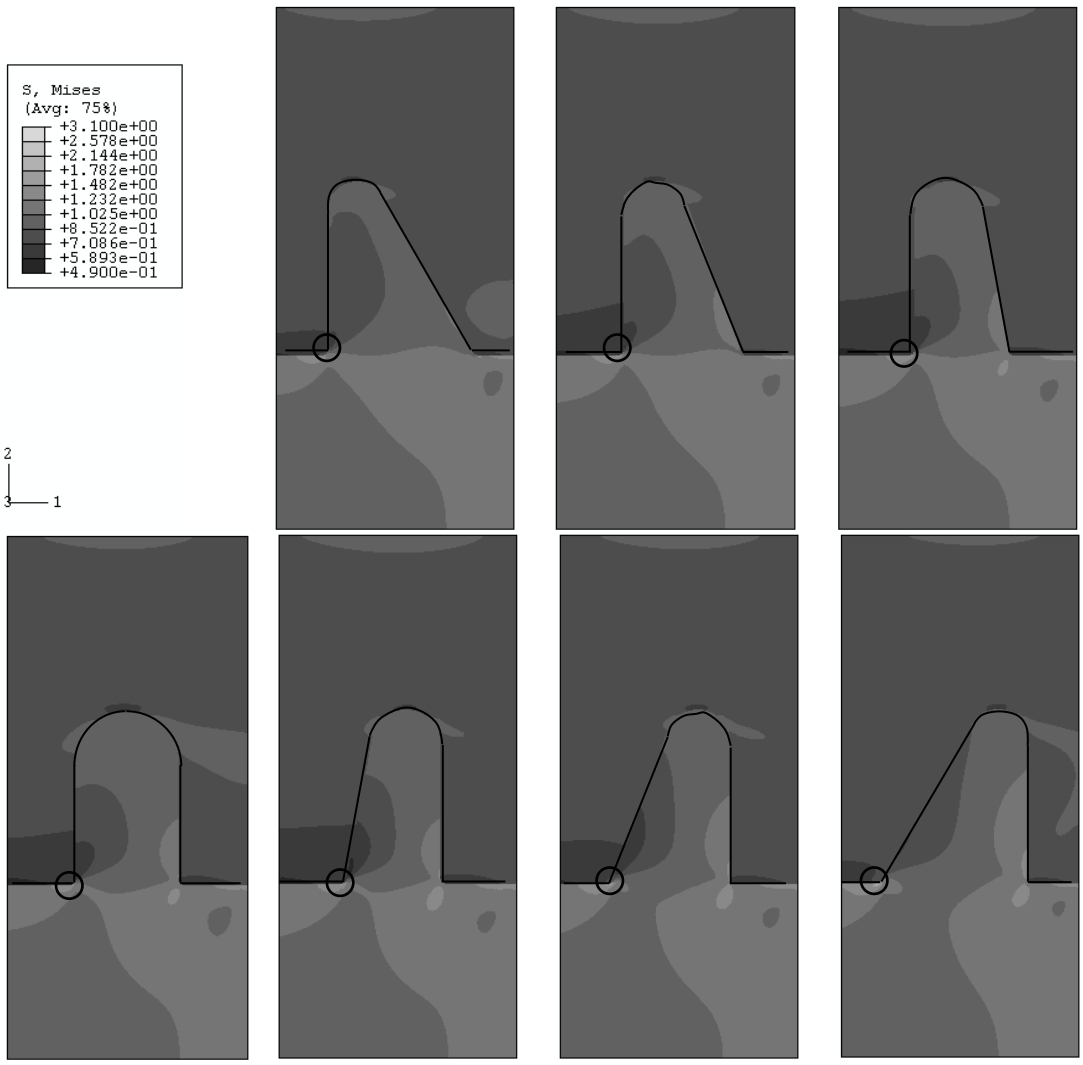

Fig.D.21 *Von Mises stress concentration contour results with different protrusion angle*

For the effects of the protrusion angle, the cases of -30 to 30 degrees with 10 degrees increments were analysed, where the minus angle stands for the protrusion leaning towards the metal end of the joint. The stress concentration contour results of the whole model were shown in figures, Fig.D.21 for the von Mises stress, Fig.D.22 for the axial stress, Fig.D.23 for the peel stress and Fig.D.24 for the shear stress.

For the von Mises stress, the maximum stress concentration occurs at the left foot of the protrusions despite the angle change. This is very similar comparing with the case of the parallel shape protrusions. The maximum stress concentrations for the different protrusion angle are listed in Table.D.21.The maximum stress concentration for the 30 degree hill shape protrusion is much larger compare to the other protrusion angles.

Table.D.21 *Maximum von Mises stress concentration with different protrusion angle*

Angle [°]	-30	-20	-10	0	10	20	30
σ_m/σ	1.43e-0	1.67e-0	1.53e-0	1.47e-0	1.55e-0	1.77e-0	3.08e-0

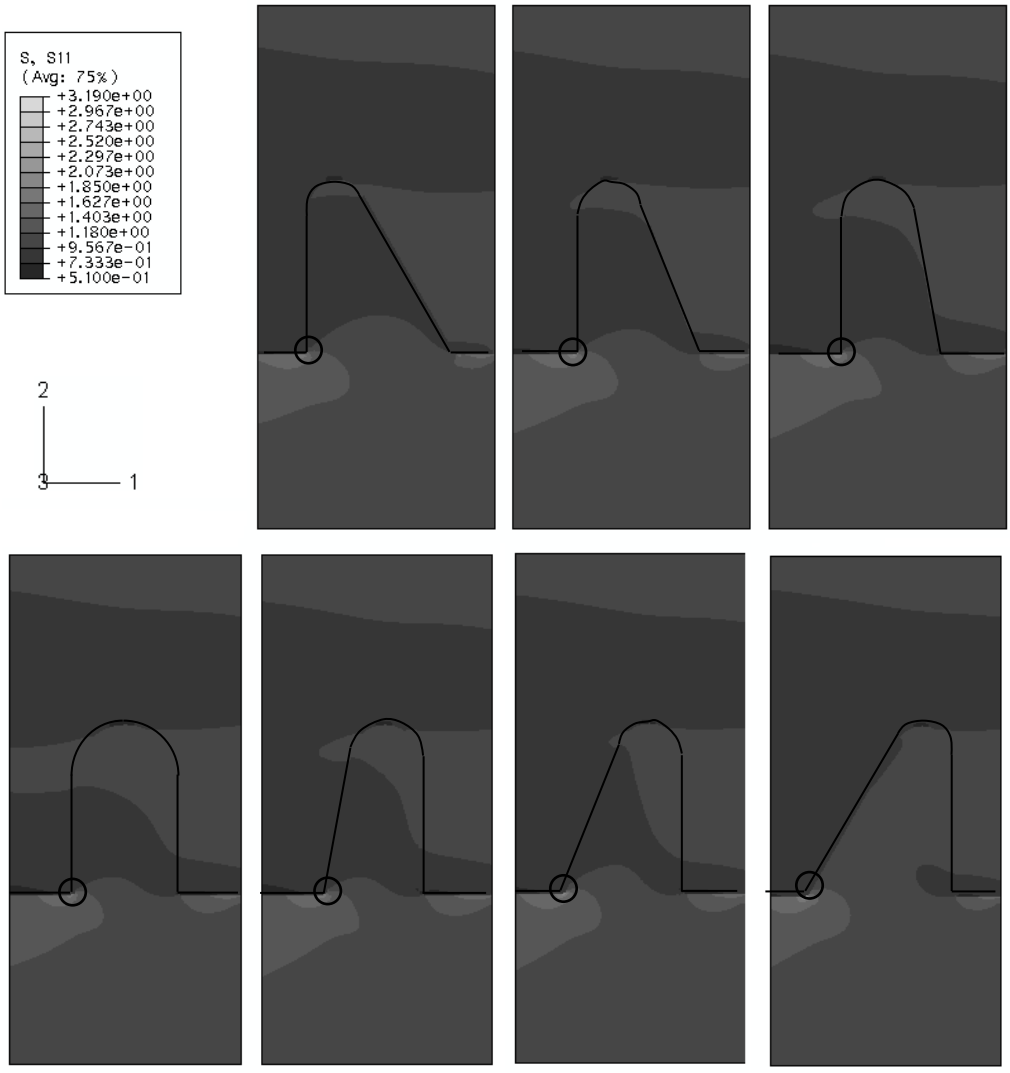

Fig.D.22 *Axial stress concentration contour results with different protrusion angle*

For the axial, peel and shear stress concentrations, it is similar to the case of von Mises stress, see Fig.D.22 to D.24, and Table.D.22 to D.24.

Table.D.22 *Maximum axial stress concentration with different protrusion angle*

Angle [°]	-30	-20	-10	0	10	20	30
σ_{11}/σ	1.75e-0	1.95e-0	1.83e-0	1.77e-0	1.85e-0	2.09e-0	3.19e-0

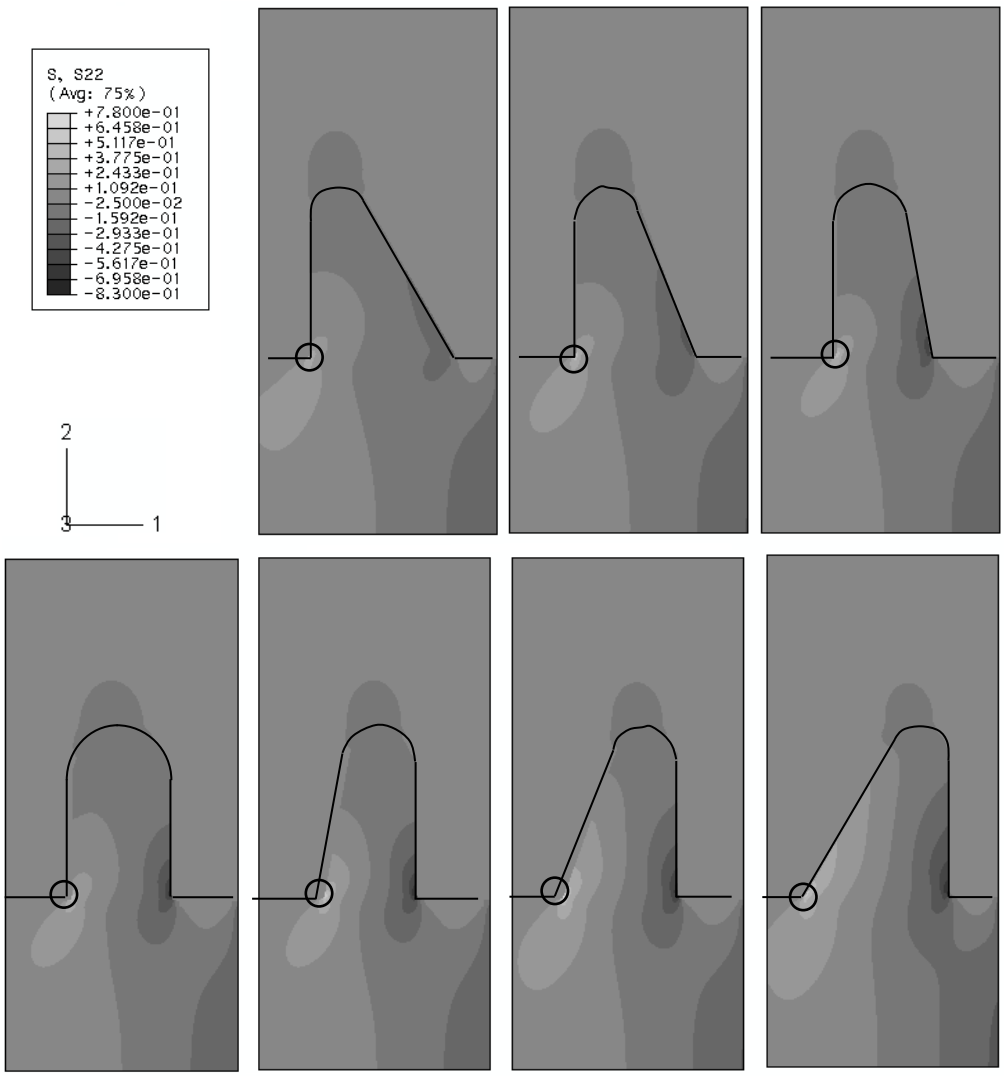

Fig.D.23 *Peel stress concentration contour results with different protrusion angle*

Table.D.23 *Maximum peel stress concentration with different protrusion angle*

Angle [°]	-30	-20	-10	0	10	20	30
σ_{22}/σ	4.94e-1	6.10e-1	5.07e-1	5.05e-1	6.31e-1	7.09e-1	7.79e-1

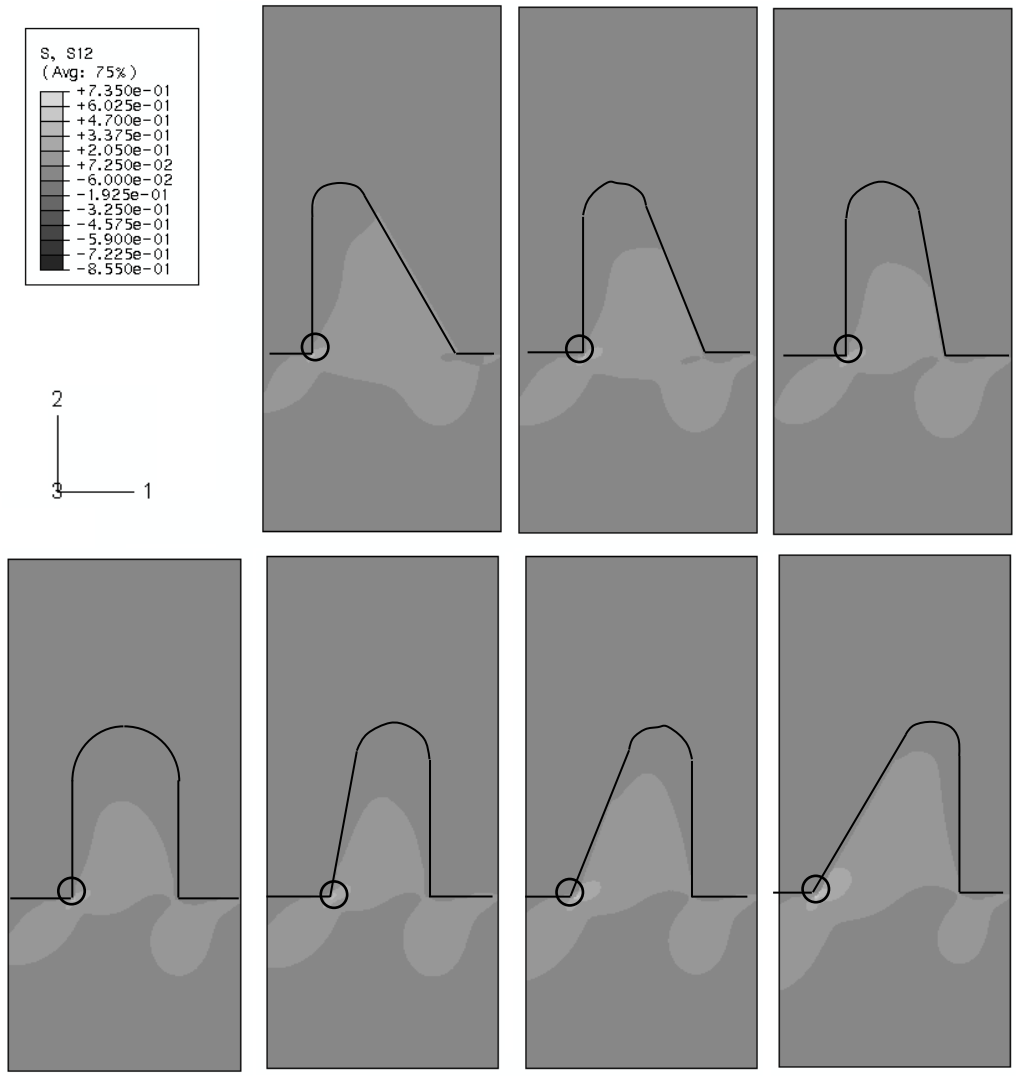

Fig.D.24 *Shear stress concentration contour results with different protrusion angle*

Table.D.24 *Maximum shear stress concentration with different protrusion angle*

Angle [°]	-30	-20	-10	0	10	20	30
σ_{12}/σ	4.19e-1	5.19e-1	4.40e-1	4.25e-1	4.79e-1	6.34e-1	7.34e-1